

Copyright  
by  
Saptaswa Basu  
2014

**The Thesis Committee for Saptaswa Basu  
Certifies that this is the approved version of the following thesis:**

**Fracture Diagnostics using Low Frequency Electromagnetic Induction**

**APPROVED BY  
SUPERVISING COMMITTEE:**

**Supervisor:**

---

Mukul M. Sharma

---

Hugh Daigle

**Fracture Diagnostics using Low Frequency Electromagnetic Induction**

**by**

**Saptaswa Basu, B.E.**

**Thesis**

Presented to the Faculty of the Graduate School of

The University of Texas at Austin

in Partial Fulfillment

of the Requirements

for the Degree of

**Master of Science in Engineering**

**The University of Texas at Austin**

**May 2014**

## **Dedication**

To my dad who taught me to be humble

## **Acknowledgements**

This work wouldn't have started without the vision and encouragement of Dr. Sharma. I remember that foggy morning in Abu Dhabi when Dr. Sharma interviewed me for being a part of his research group to build an electromagnetic well logging tool. It was an offer I couldn't refuse. I submitted my resignation letter to my then dream job, packed my bags, and came down to the Live Music Capital of the World to make my own logging tool.

Austin wouldn't have been same without a few people in my life. Somnath Mondal over the course of years has adeptly shuttled between the roles of a friend, philosopher and a chef. Jin has made the daily grind quite pleasant with her sunny smile even on the hardest days. Lionel, Rd, Anand, Eric, Sahil, Mac, and Rod have all brought a sense of belongingness in a block of red bricks. Divya and Soumava, with their warmth and kindness, have made sure that I never felt like a lone wolf in the jungle.

I wouldn't be here without the wonderful teachers I have had in my life: Hirak Mitra, DN Bhattacharya, and A.K. Sarkar to name a few. And life itself!

## **Abstract**

### **Fracture Diagnostics using Low Frequency Electromagnetic Induction**

Saptaswa Basu, M.S.E.

The University of Texas at Austin, 2014

Supervisor: Mukul M. Sharma

Currently microseismic monitoring is widely used for fracture diagnosis. Since the method monitors the propagation of shear failure events, it is an indirect measure of the propped fracture geometry. Our primary interest is in estimating the orientation and length of the ‘propped’ fractures (not the created fractures), as that is the primary driver for well productivity. This thesis presents a new Low Frequency Electromagnetic Induction (LFEI) method that has the potential to estimate the propped length, height, orientation of hydraulic fractures, and vertical distribution of proppant within the fracture.

The proposed technique involves pumping electrically conductive proppant (which is currently available) into the fracture and then using a specially built logging tool to measure the electromagnetic response of the formation. Results are presented for a proposed logging tool that consists of three sets of tri-directional transmitters and receivers at 6, 30 and 60 feet spacing respectively. The solution of Maxwell’s equations shows that it is possible to use the tool to determine both the orientation and the length of the fracture by detecting the location of these particles in the formation after hydraulic

fracturing. Results for extensive sensitivity analysis are presented in this thesis to show the effect of different propped lengths, height and orientation of planar fractures in a shale environment. Multiple numerical simulations, using a state-of-the-art electromagnetic simulator (FEKO) indicate, as this work show, that we can detect and map fractures up to 250 feet in length, 0.2 inches wide, and with a 0 to 45 degree of inclination with respect to the wellbore. Special cases such as proppant banking, non-symmetrical bi-wing fractures, and wells with steel casing in place were studied.

## Table of Contents

List of Tables .....	x
List of Figures .....	xi
Chapter 1: Introduction .....	1
1.1 Background and Motivation .....	3
1.2 Research Objective .....	7
1.3 Past Work.....	8
1.4 Overview of Chapters .....	9
Chapter 2: Induction Logging Tools.....	12
2.1 Governing Physics .....	14
2.2 Application of Electromagnetic Induction in Logging Tools .....	18
2.3 Proposed Low Frequency Electromagnetic Tool.....	24
Chapter 3: Model Description.....	28
3.1 Software .....	29
3.2 Matrix and Wellbore Formulation .....	31
3.3 Fracture Formulation .....	34
3.4 Tool Formulation .....	37
3.5 Meshing of grids .....	38
Chapter 4: Fracture Diagnosis using Low Frequency Electromagnetic Induction (LFEI) .....	41
4.1 Horizontal Well.....	43
4.1.1 Orthogonal Fractures in Open Hole .....	45
4.1.2 Orthogonal Fracture in Cased Hole .....	48
4.1.3 Oriented Fractures.....	50
4.1.4 Non-uniform distribution of proppant .....	52
4.1.5 Non Symmetrical Fractures .....	55
4.2 Vertical Well.....	57
4.2.1 Orthogonal fractures in Open Hole.....	58

4.2.2 Orthogonal Fracture in Cased Hole .....	60
4.2.3 Oriented Fractures .....	60
Chapter 5: Sensitivity Analysis.....	62
5.1 Frequency of Operation .....	64
5.2 Transmitter-Receiver Spacing .....	66
5.3 Resistivity of Rock Matrix.....	67
5.4 Resistivity of Proppant.....	68
5.5 Magnetic Permeability of Proppant .....	69
Chapter 6: Conclusion.....	71
Appendices.....	76
A1. Raw electric and magnetic field responses for an orthogonal fracture in vertical well (open hole completion) .....	76
A2.Raw electric and magnetic field responses for an orthogonal fracture in vertical well (cased hole completion) .....	102
A3. Raw electric and magnetic field responses for an orthogonal fracture in horizontal well (open hole completion) .....	126
A4. electric and magnetic field responses for an orthogonal fracture in horizontal well (cased hole completion) .....	148
A5. Raw electric and magnetic field responses for non symmetrical bi-wing fracture in horizontal well (open hole completion).....	168
<b>References .....</b>	<b>177</b>

## List of Tables

Table 1.1:	Capabilities and limitations of current fracture diagnostic tools (after Cipolla and Wright, 2000) .....	5
Table 1.2:	Summary of simulations done in FEKO for different fracture geometry and orientation using LFEI tool. ....	11
Table 4.1:	Simulations run on FEKO for different cases, and the parameters that are changed in each.....	42
Table 4.2:	Parameters used in simulations of tool, rock, proppant, and steel casing. ....	43
Table 5.1	Parameters used in sensitivity analysis .....	64

## List of Figures

Figure 1.1: U.S. petroleum and other liquid fuels supply by source (million barrels per day) (after Figure 1 of EIA’s Annual Energy Outlook 2014 Early Release Overview) .....	2
Figure 1.2: U.S. energy production by fuel, 1980-2040 (quadrillion Btu) (after Figure 11 of EIA’s Annual Energy Outlook 2014 Early Release Overview) .....	3
Figure 2.1: History of induction logging tools .....	13
Figure 2.2: Basic two coil induction electromagnetic tool .....	14
Figure 2.3: Normalized real (top) and imaginary (bottom) parts of Born response function for a two-coil system with coil spacing of L (after Anderson, 2001). .....	21
Figure 2.4: Normalized real (top) and imaginary (bottom) parts of integrated Born response function for a two-coil system with coil spacing of L (after Anderson, 2001).....	22
Figure 2.6: Maximum distance of signal penetration in a 0.01S/m matrix as a function of frequency (after Salies, 2012, Figure 3.5) .....	25
Figure 2.7: Maximum distance of signal penetration in a $10^{-6}$ S/m matrix as a function of frequency (after Salies, 2012, Figure 3.4). .....	26
Figure 2.8: Schematic representation of the technology .....	27
Figure 2.9: Schematic representation of proposed tri-directional electromagnetic induction tool where Tx, Ty and Tz represents the tri-directional transmitter and Rx, Ry and Rz represents the tri-directional receivers.	

Figure 3.1: Capability of FEKO to use different solvers based on the complexity of materials and electrical size .....	29
Figure 3.2: Model of wellbore with casing in CADFEKO .....	31
Figure 3.3: Rock formation modeled in FEKO as a series of beds of different resistivity (shown in different colors) with wellbore at the center. ...	32
Figure 3.4: Rock formation modeled as concentric cylinders of different resistivity with wellbore at the center. ....	33
Figure 3.5: Response at the receiver (Real electric field in Z direction) for homogenous case, i.e. only rock matrix and no hydraulic fracture ..	34
Figure 3.6: Model of orthogonal fracture in a horizontal wellbore .....	35
Figure 3.7: Schematic diagram of a moving tool across a orthogonal fracture in a horizontal wellbore .....	35
Figure 3.8: Schematic model of non-orthogonal fracture in a horizontal wellbore	36
Figure 3.9: Model of bi-wing fracture in a vertical wellbore .....	36
Figure 3.10: Imaginary component of magnetic field for a given fracture geometry for mesh sizes of 1.5 m (150 cm) , 2 m (200 cm) , 2.5 m (250 cm) and 3 m (300 cm) at the coarsest point. ....	40
Figure 4.1: Model of orthogonal fracture in a horizontal wellbore .....	44
Figure 4.2: Schematic diagram of a moving tool across a orthogonal fracture in a horizontal wellbore .....	44
Figure 4.3: Receiver response to fractures placed orthogonal to a horizontal well for different fracture lengths (a) 30m, (b) 50m, (c) 75m and (d) 100m.	46
Figure 4.4: Comparison of the magnitude of the electric fields in the Z direction for different fracture half lengths.....	46

Figure 4.5: Comparison of the imaginary component of the magnetic fields in the Z direction for different fracture half lengths.....	47
Figure 4.6: Comparison of the magnitude of electric field in the Z direction for different fracture half lengths.....	47
Figure 4.7: Electric Field in Z direction at long spacing receiver divided by the transmitter strength against long spacing receiver location in the borehole for different fracture half-length. ....	48
Figure 4.8: Comparison of Electric field magnitudes of different fracture lengths in a horizontal wellbore through steel casing. ....	49
Figure 4.9: Receiver response to orthogonal fracture in a horizontal well with casing installed.....	49
Figure 4.10: Electric Field in Z direction at long spacing receiver divided by the transmitter strength against long spacing receiver location in the borehole for different fracture half-length (in cased-hole). ....	50
Figure 4.11: Schematic representation of hydraulic fractures rotated in the borehole by angles of 15, 30 and 45 degrees respectively.....	51
Figure 4.12: Received Electric field signal in X-, Y- and Z- direction for changing fracture half-length and fracture angles.....	52
Figure 4.13: Orthogonal fracture in horizontal wellbore filled with proppant (in green) and water (in blue). The wellbore is across the plane of the paper (Z-axis) and the fracture half length is 50m.....	53
Figure 4.14: Different heights of proppant bank(in green), from 5m, 15m, 25m, 35m and 45m, respectively. ....	54

Figure 4.15: Magnitude of Electric Field Signal in X-, Y- and Z- direction showing the variation of Electric field in X-direction with changing height of proppant bank.....	54
Figure 4.16: Magnitude of Electric Field signal in X-,Y- and Z- direction showing changes in Electric Field signal in X direction with changes in resistivity of fracturing fluid.....	55
Figure 4.17: Non-symmetrical orthogonal fracture in a horizontal wellbore (cutting across the plane of the paper). The wing on the left side is 60m while the one of the right is 30m. ....	56
Figure 4.18: Comparison of Imaginary component of Magnetic field in Y-direction for different configurations .....	56
Figure 4.19: Comparison of Imaginary component of Magnetic field in Z-direction for different configurations .....	57
Figure 4.20: Model of bi-wing fracture in a vertical wellbore .....	58
Figure 4.21: Magnitude of received Electric field signal in the Z direction for different fracture length. ....	59
Figure 4.22: Ratio of the magnitude of the Electric Field signal in Y direction and X direction for different azimuthal angles of bi-wing hydraulic fracture in vertical wellbore.....	61
Figure 5.1: Model of orthogonal fracture in horizontal well, used for sensitivity analysis.....	63
Figure 5.2: Sensitivity analysis for Frequency of Operation.....	65
Figure 5.3: Sensitivity analysis for transmitter-receiver spacing .....	67
Figure 5.4: Sensitivity analysis for rock matrix resistivity.....	68
Figure 5.5: Sensitivity analysis for conductivity of proppant .....	69

Figure 5.6 Sensitivity analysis for changing magnetic permeability of proppant	.70
Figure 6.1: Schematic diagram of proposed tool with receiver arrays, pressure compensator section, electronic section	.....74
Figure 6.2: Array Section Subassembly showing transmitter and receiver coil, with bulkhead at the top and loading sleeve at bottom	.....74
Figure 6.3: Workflow of LFEI technology	.....75
Figure A1.1: Real component of electric field in the Z-direction for a orthogonal fracture of half-length 5 m in a vertical wellbore	.....76
Figure A1.2: Imaginary component of electric field in the Z-direction for a orthogonal fracture of half-length 5 m in a vertical wellbore	.....76
Figure A1.3: Magnitude of electric field in the Z-direction for a orthogonal fracture of half-length 5 m in a vertical wellbore	.....77
Figure A1.4: Real component of magnetic field in the Z-direction for a orthogonal fracture of half-length 5 m in a vertical wellbore	.....77
Figure A1.5: Imaginary component of magnetic field in the Z-direction for a orthogonal fracture of half-length 5 m in a vertical wellbore	.....78
Figure A1.6: Magnitude of magnetic field in the Z-direction for a orthogonal fracture of half-length 5 m in a vertical wellbore	.....78
Figure A1.7: Real component of electric field in the Z-direction for a orthogonal fracture of half-length 10 m in a vertical wellbore	.....79
Figure A1.8: Imaginary component of electric field in the Z-direction for a orthogonal fracture of half-length 10 m in a vertical wellbore	.....79
Figure A1.9: Magnitude of electric field in the Z-direction for a orthogonal fracture of half-length 10 m in a vertical wellbore	.....80

Figure A1.10: Real component of magnetic field in the Z-direction for a orthogonal fracture of half-length 10 m in a vertical wellbore .....80

Figure A1.11: Imaginary component of magnetic field in the Z-direction for a orthogonal fracture of half-length 10 m in a vertical wellbore .....81

Figure A1.12: Magnitude of magnetic field in the Z-direction for a orthogonal fracture of half-length 10 m in a vertical wellbore .....81

Figure A1.13: Real component of electric field in the Z-direction for a orthogonal fracture of half-length 15 m in a vertical wellbore .....82

Figure A1.14: Imaginary component of electric field in the Z-direction for a orthogonal fracture of half-length 15 m in a vertical wellbore .....82

Figure A1.15: Real component of magnetic field in the Z-direction for a orthogonal fracture of half-length 15 m in a vertical wellbore .....83

Figure A1.16: Imaginary component of magnetic field in the Z-direction for a orthogonal fracture of half-length 15 m in a vertical wellbore .....83

Figure A1.17: Real component of electric field in the Z-direction for a orthogonal fracture of half-length 20 m in a vertical wellbore .....84

Figure A1.18: Imaginary component of electric field in the Z-direction for a orthogonal fracture of half-length 20 m in a vertical wellbore .....84

Figure A1.19: Real component of magnetic field in the Z-direction for a orthogonal fracture of half-length 20 m in a vertical wellbore .....85

Figure A1.20: Imaginary component of magnetic field in the Z-direction for a orthogonal fracture of half-length 20 m in a vertical wellbore .....85

Figure A1.21: Real component of electric field in the Z-direction for a orthogonal fracture of half-length 25 m in a vertical wellbore .....86

Figure A1.22: Imaginary component of electric field in the Z-direction for a orthogonal fracture of half-length 25 m in a vertical wellbore .....	86
Figure A1.23: Real component of magnetic field in the Z-direction for a orthogonal fracture of half-length 25 m in a vertical wellbore .....	87
Figure A1.24: Imaginary component of magnetic field in the Z-direction for a orthogonal fracture of half-length 25 m in a vertical wellbore .....	87
Figure A1.25: Real component of electric field in the Z-direction for a orthogonal fracture of half-length 30 m in a vertical wellbore .....	88
Figure A1.26: Imaginary component of electric field in the Z-direction for a orthogonal fracture of half-length 30 m in a vertical wellbore .....	88
Figure A1.27: Real component of magnetic field in the Z-direction for a orthogonal fracture of half-length 30 m in a vertical wellbore .....	89
Figure A1.28: Imaginary component of magnetic field in the Z-direction for a orthogonal fracture of half-length 30 m in a vertical wellbore .....	89
Figure A1.29: Real component of electric field in the Z-direction for a orthogonal fracture of half-length 35 m in a vertical wellbore .....	90
Figure A1.30: Imaginary component of electric field in the Z-direction for a orthogonal fracture of half-length 35 m in a vertical wellbore .....	90
Figure A1.31: Real component of magnetic field in the Z-direction for a orthogonal fracture of half-length 35 m in a vertical wellbore .....	91
Figure A1.32: Imaginary component of magnetic field in the Z-direction for a orthogonal fracture of half-length 35 m in a vertical wellbore .....	91
Figure A1.33: Real component of electric field in the Z-direction for a orthogonal fracture of half-length 40 m in a vertical wellbore .....	92

Figure A1.34: Imaginary component of electric field in the Z-direction for a  
orthogonal fracture of half-length 40 m in a vertical wellbore .....92

Figure A1.35: Real component of magnetic field in the Z-direction for a orthogonal  
fracture of half-length 40 m in a vertical wellbore .....93

Figure A1.36: Imaginary component of magnetic field in the Z-direction for a  
orthogonal fracture of half-length 40 m in a vertical wellbore .....93

Figure A1.37: Real component of electric field in the Z-direction for a orthogonal  
fracture of half-length 45 m in a vertical wellbore .....94

Figure A1.38: Imaginary component of electric field in the Z-direction for a  
orthogonal fracture of half-length 45 m in a vertical wellbore .....94

Figure A1.39: Real component of magnetic field in the Z-direction for a orthogonal  
fracture of half-length 45 m in a vertical wellbore .....95

Figure A1.40: Imaginary component of magnetic field in the Z-direction for a  
orthogonal fracture of half-length 45 m in a vertical wellbore .....95

Figure A1.41: Real component of electric field in the Z-direction for a orthogonal  
fracture of half-length 60 m in a vertical wellbore .....96

Figure A1.42: Imaginary component of electric field in the Z-direction for a  
orthogonal fracture of half-length 60 m in a vertical wellbore .....96

Figure A1.43: Real component of magnetic field in the Z-direction for a orthogonal  
fracture of half-length 60 m in a vertical wellbore .....97

Figure A1.44: Imaginary component of magnetic field in the Z-direction for a  
orthogonal fracture of half-length 60 m in a vertical wellbore .....97

Figure A1.45: Real component of electric field in the Z-direction for a orthogonal  
fracture of half-length 75 m in a vertical wellbore .....98

Figure A1.46: Imaginary component of electric field in the Z-direction for a  
orthogonal fracture of half-length 75 m in a vertical wellbore .....98

Figure A1.47: Real component of magnetic field in the Z-direction for a orthogonal  
fracture of half-length 75 m in a vertical wellbore .....99

Figure A1.48: Imaginary component of magnetic field in the Z-direction for a  
orthogonal fracture of half-length 75 m in a vertical wellbore .....99

Figure A1.49: Real component of electric field in the Z-direction for a orthogonal  
fracture of half-length 100 m in a vertical wellbore .....100

Figure A1.50: Imaginary component of electric field in the Z-direction for a  
orthogonal fracture of half-length 100 m in a vertical wellbore .....100

Figure A1.51: Real component of magnetic field in the Z-direction for a orthogonal  
fracture of half-length 100 m in a vertical wellbore .....101

Figure A1.52: Real component of magnetic field in the Z-direction for a orthogonal  
fracture of half-length 100 m in a vertical wellbore .....101

Figure A2.1: Real component of electric field in the Z-direction for a orthogonal  
fracture of half-length 5 m in a vertical wellbore through steel casing102

Figure A2.2: Imaginary component of electric field in the Z-direction for a orthogonal  
fracture of half-length 5 m in a vertical wellbore through steel casing102

Figure A2.3: Real component of magnetic field in the Z-direction for a orthogonal  
fracture of half-length 5 m in a vertical wellbore through steel casing103

Figure A2.4: Imaginary component of magnetic field in the Z-direction for a  
orthogonal fracture of half-length 5 m in a vertical wellbore through  
steel casing .....103

Figure A2.5: Real component of electric field in the Z-direction for a orthogonal fracture of half-length 10 m in a vertical wellbore through steel casing  
104

Figure A2.6: Imaginary component of electric field in the Z-direction for a orthogonal fracture of half-length 10 m in a vertical wellbore through steel casing  
104

Figure A2.7: Real component of magnetic field in the Z-direction for a orthogonal fracture of half-length 10 m in a vertical wellbore through steel casing  
105

Figure A2.8: Imaginary component of magnetic field in the Z-direction for a orthogonal fracture of half-length 10 m in a vertical wellbore through steel casing .....105

Figure A2.9: Real component of electric field in the Z-direction for a orthogonal fracture of half-length 15 m in a vertical wellbore through steel casing  
106

Figure A2.10: Imaginary component of electric field in the Z-direction for a orthogonal fracture of half-length 15 m in a vertical wellbore through steel casing .....106

Figure A2.11: Real component of magnetic field in the Z-direction for a orthogonal fracture of half-length 15 m in a vertical wellbore through steel casing  
107

Figure A2.12: Imaginary component of magnetic field in the Z-direction for a orthogonal fracture of half-length 15 m in a vertical wellbore through steel casing .....107

Figure A2.13: Real component of electric field in the Z-direction for a orthogonal fracture of half-length 20 m in a vertical wellbore through steel casing  
108

Figure A2.14: Imaginary component of electric field in the Z-direction for a orthogonal fracture of half-length 20 m in a vertical wellbore through steel casing .....108

Figure A2.15: Real component of magnetic field in the Z-direction for a orthogonal fracture of half-length 20 m in a vertical wellbore through steel casing  
109

Figure A2.16: Imaginary component of magnetic field in the Z-direction for a orthogonal fracture of half-length 20 m in a vertical wellbore through steel casing .....109

Figure A2.17: Real component of electric field in the Z-direction for a orthogonal fracture of half-length 25 m in a vertical wellbore through steel casing  
110

Figure A2.18: Imaginary component of electric field in the Z-direction for a orthogonal fracture of half-length 25 m in a vertical wellbore through steel casing .....110

Figure A2.19: Real component of magnetic field in the Z-direction for a orthogonal fracture of half-length 25 m in a vertical wellbore through steel casing  
111

Figure A2.20: Imaginary component of magnetic field in the Z-direction for a orthogonal fracture of half-length 25 m in a vertical wellbore through steel casing .....111

Figure A2.21: Real component of electric field in the Z-direction for a orthogonal fracture of half-length 30 m in a vertical wellbore through steel casing  
112

Figure A2.22: Imaginary component of electric field in the Z-direction for a orthogonal fracture of half-length 30 m in a vertical wellbore through steel casing .....112

Figure A2.23: Real component of magnetic field in the Z-direction for a orthogonal fracture of half-length 30 m in a vertical wellbore through steel casing  
113

Figure A2.24: Imaginary component of magnetic field in the Z-direction for a orthogonal fracture of half-length 30 m in a vertical wellbore through steel casing .....113

Figure A2.25: Real component of electric field in the Z-direction for a orthogonal fracture of half-length 35 m in a vertical wellbore through steel casing  
114

Figure A2.26: Imaginary component of electric field in the Z-direction for a orthogonal fracture of half-length 35 m in a vertical wellbore through steel casing .....114

Figure A2.27: Real component of magnetic field in the Z-direction for a orthogonal fracture of half-length 35 m in a vertical wellbore through steel casing  
115

Figure A2.28: Imaginary component of magnetic field in the Z-direction for a orthogonal fracture of half-length 35 m in a vertical wellbore through steel casing .....115

Figure A2.29: Real component of electric field in the Z-direction for a orthogonal fracture of half-length 40 m in a vertical wellbore through steel casing  
116

Figure A2.30: Imaginary component of electric field in the Z-direction for a orthogonal fracture of half-length 40 m in a vertical wellbore through steel casing .....116

Figure A2.31: Real component of magnetic field in the Z-direction for a orthogonal fracture of half-length 40 m in a vertical wellbore through steel casing  
117

Figure A2.32: Imaginary component of magnetic field in the Z-direction for a orthogonal fracture of half-length 40 m in a vertical wellbore through steel casing .....117

Figure A2.33: Real component of electric field in the Z-direction for a orthogonal fracture of half-length 45 m in a vertical wellbore through steel casing  
118

Figure A2.34: Imaginary component of electric field in the Z-direction for a orthogonal fracture of half-length 45 m in a vertical wellbore through steel casing .....118

Figure A2.35: Real component of magnetic field in the Z-direction for a orthogonal fracture of half-length 45 m in a vertical wellbore through steel casing  
119

Figure A2.36: Imaginary component of magnetic field in the Z-direction for a orthogonal fracture of half-length 45 m in a vertical wellbore through steel casing .....119

Figure A2.37: Real component of electric field in the Z-direction for a orthogonal fracture of half-length 60 m in a vertical wellbore through steel casing  
120

Figure A2.38: Imaginary component of electric field in the Z-direction for a orthogonal fracture of half-length 60 m in a vertical wellbore through steel casing .....120

Figure A2.39: Real component of magnetic field in the Z-direction for a orthogonal fracture of half-length 60 m in a vertical wellbore through steel casing  
121

Figure A2.40: Imaginary component of magnetic field in the Z-direction for a orthogonal fracture of half-length 60 m in a vertical wellbore through steel casing .....121

Figure A2.41: Real component of electric field in the Z-direction for a orthogonal fracture of half-length 75 m in a vertical wellbore through steel casing  
122

Figure A2.42: Imaginary component of electric field in the Z-direction for a orthogonal fracture of half-length 75 m in a vertical wellbore through steel casing .....122

Figure A2.43: Real component of magnetic field in the Z-direction for a orthogonal fracture of half-length 75 m in a vertical wellbore through steel casing  
123

Figure A2.44: Imaginary component of magnetic field in the Z-direction for a orthogonal fracture of half-length 75 m in a vertical wellbore through steel casing .....123

Figure A2.45: Real component of electric field in the Z-direction for a orthogonal fracture of half-length 100 m in a vertical wellbore through steel casing  
124

Figure A2.46: Imaginary component of electric field in the Z-direction for a orthogonal fracture of half-length 100 m in a vertical wellbore through steel casing .....124

Figure A2.47: Real component of magnetic field in the Z-direction for a orthogonal fracture of half-length 100 m in a vertical wellbore through steel casing .....125

Figure A2.48: Imaginary component of magnetic field in the Z-direction for a orthogonal fracture of half-length 100 m in a vertical wellbore through steel casing .....125

Figure A3.1: Real component of electric field in the Z-direction for a orthogonal fracture of half-length 5 m in a horizontal wellbore .....126

Figure A3.2: Imaginary component of electric field in the Z-direction for a orthogonal fracture of half-length 5 m in a horizontal wellbore .....126

Figure A3.3: Real component of magnetic field in the Z-direction for a orthogonal fracture of half-length 5 m in a horizontal wellbore .....127

Figure A3.4: Imaginary component of magnetic field in the Z-direction for a orthogonal fracture of half-length 5 m in a horizontal wellbore.....127

Figure A3.5: Real component of electric field in the Z-direction for a orthogonal fracture of half-length 10 m in a horizontal wellbore .....128

Figure A3.6: Imaginary component of electric field in the Z-direction for a orthogonal fracture of half-length 10 m in a horizontal wellbore .....128

Figure A3.7: Real component of magnetic field in the Z-direction for a orthogonal fracture of half-length 10 m in a horizontal wellbore .....129

Figure A3.8: Imaginary component of magnetic field in the Z-direction for a orthogonal fracture of half-length 10 m in a horizontal wellbore...129

Figure A3.9: Real component of electric field in the Z-direction for a orthogonal fracture of half-length 15 m in a horizontal wellbore .....130

Figure A3.10: Imaginary component of electric field in the Z-direction for a orthogonal fracture of half-length 15 m in a horizontal wellbore...130

Figure A3.11: Real component of magnetic field in the Z-direction for a orthogonal fracture of half-length 15 m in a horizontal wellbore .....131

Figure A3.12: Imaginary component of magnetic field in the Z-direction for a orthogonal fracture of half-length 15 m in a horizontal wellbore...131

Figure A3.13: Real component of electric field in the Z-direction for a orthogonal fracture of half-length 20 m in a horizontal wellbore .....132

Figure A3.14: Imaginary component of electric field in the Z-direction for a orthogonal fracture of half-length 20 m in a horizontal wellbore...132

Figure A3.15: Real component of magnetic field in the Z-direction for a orthogonal fracture of half-length 20 m in a horizontal wellbore .....133

Figure A3.16: Imaginary component of magnetic field in the Z-direction for a orthogonal fracture of half-length 20 m in a horizontal wellbore...133

Figure A3.17: Real component of electric field in the Z-direction for a orthogonal fracture of half-length 25 m in a horizontal wellbore .....134

Figure A3.18: Imaginary component of electric field in the Z-direction for a orthogonal fracture of half-length 25 m in a horizontal wellbore...134

Figure A3.19: Real component of magnetic field in the Z-direction for a orthogonal fracture of half-length 25 m in a horizontal wellbore .....135

Figure A3.20: Imaginary component of magnetic field in the Z-direction for a orthogonal fracture of half-length 25 m in a horizontal wellbore...135

Figure A3.21: Real component of electric field in the Z-direction for a orthogonal fracture of half-length 30 m in a horizontal wellbore .....136

Figure A3.22: Imaginary component of electric field in the Z-direction for a orthogonal fracture of half-length 30 m in a horizontal wellbore...136

Figure A3.23: Real component of magnetic field in the Z-direction for a orthogonal fracture of half-length 30 m in a horizontal wellbore .....137

Figure A3.24: Imaginary component of magnetic field in the Z-direction for a orthogonal fracture of half-length 30 m in a horizontal wellbore...137

Figure A3.25: Real component of electric field in the Z-direction for a orthogonal fracture of half-length 35 m in a horizontal wellbore .....138

Figure A3.26: Imaginary component of electric field in the Z-direction for a orthogonal fracture of half-length 35 m in a horizontal wellbore...138

Figure A3.27: Real component of magnetic field in the Z-direction for a orthogonal fracture of half-length 35 m in a horizontal wellbore .....139

Figure A3.28: Imaginary component of magnetic field in the Z-direction for a orthogonal fracture of half-length 35 m in a horizontal wellbore...139

Figure A3.29: Real component of electric field in the Z-direction for a orthogonal fracture of half-length 40 m in a horizontal wellbore .....140

Figure A3.30: Imaginary component of electric field in the Z-direction for a orthogonal fracture of half-length 40 m in a horizontal wellbore...140

Figure A3.31: Real component of magnetic field in the Z-direction for a orthogonal fracture of half-length 40 m in a horizontal wellbore .....141

Figure A3.32: Imaginary component of magnetic field in the Z-direction for a orthogonal fracture of half-length 40 m in a horizontal wellbore...141

Figure A3.33: Real component of electric field in the Z-direction for a orthogonal fracture of half-length 45 m in a horizontal wellbore .....142

Figure A3.34: Imaginary component of electric field in the Z-direction for a orthogonal fracture of half-length 45 m in a horizontal wellbore...142

Figure A3.35: Real component of magnetic field in the Z-direction for a orthogonal fracture of half-length 45 m in a horizontal wellbore .....143

Figure A3.36: Imaginary component of magnetic field in the Z-direction for a orthogonal fracture of half-length 45 m in a horizontal wellbore...143

Figure A3.37: Real component of electric field in the Z-direction for a orthogonal fracture of half-length 60 m in a horizontal wellbore .....144

Figure A3.38: Imaginary component of electric field in the Z-direction for a orthogonal fracture of half-length 60 m in a horizontal wellbore...144

Figure A3.39: Real component of magnetic field in the Z-direction for a orthogonal fracture of half-length 60 m in a horizontal wellbore .....145

Figure A3.40: Imaginary component of magnetic field in the Z-direction for a orthogonal fracture of half-length 60 m in a horizontal wellbore...145

Figure A3.41: Real component of magnetic field in the Z-direction for a orthogonal fracture of half-length 75 m in a horizontal wellbore .....146

Figure A3.42: Imaginary component of magnetic field in the Z-direction for a orthogonal fracture of half-length 75 m in a horizontal wellbore...146

Figure A3.43: Real component of electric field in the Z-direction for a orthogonal fracture of half-length 75 m in a horizontal wellbore .....	147
Figure A3.44: Imaginary component of electric field in the Z-direction for a orthogonal fracture of half-length 75 m in a horizontal wellbore...	147
Figure A4.1: Real component of electric field in the Z-direction for a orthogonal fracture of half-length 5 m in a horizontal wellbore in steel casing	148
Figure A4.2: Imaginary component of electric field in the Z-direction for a orthogonal fracture of half-length 5 m in a horizontal wellbore in steel casing	148
Figure A4.3: Real component of magnetic field in the Z-direction for a orthogonal fracture of half-length 5 m in a horizontal wellbore in steel casing	149
Figure A4.4: Imaginary component of magnetic field in the Z-direction for a orthogonal fracture of half-length 5 m in a horizontal wellbore in steel casing .....	149
Figure A4.5: Real component of electric field in the Z-direction for a orthogonal fracture of half-length 10 m in a horizontal wellbore in steel casing	150
Figure A4.6: Imaginary component of electric field in the Z-direction for a orthogonal fracture of half-length 10 m in a horizontal wellbore in steel casing	150
Figure A4.7: Real component of magnetic field in the Z-direction for a orthogonal fracture of half-length 10 m in a horizontal wellbore in steel casing	151
Figure A4.8: Imaginary component of magnetic field in the Z-direction for a orthogonal fracture of half-length 10 m in a horizontal wellbore in steel casing .....	151
Figure A4.9: Real component of electric field in the Z-direction for a orthogonal fracture of half-length 15 m in a horizontal wellbore in steel casing	152

Figure A4.10: Imaginary component of electric field in the Z-direction for a  
orthogonal fracture of half-length 15 m in a horizontal wellbore in steel  
casing .....152

Figure A4.11: Real component of magnetic field in the Z-direction for a orthogonal  
fracture of half-length 15 m in a horizontal wellbore in steel casing153

Figure A4.12: Imaginary component of magnetic field in the Z-direction for a  
orthogonal fracture of half-length 15 m in a horizontal wellbore in steel  
casing .....153

Figure A4.13: Real component of electric field in the Z-direction for a orthogonal  
fracture of half-length 20 m in a horizontal wellbore in steel casing154

Figure A4.14: Imaginary component of electric field in the Z-direction for a  
orthogonal fracture of half-length 20 m in a horizontal wellbore in steel  
casing .....154

Figure A4.15: Real component of magnetic field in the Z-direction for a orthogonal  
fracture of half-length 20 m in a horizontal wellbore in steel casing155

Figure A4.16: Imaginary component of magnetic field in the Z-direction for a  
orthogonal fracture of half-length 20 m in a horizontal wellbore in steel  
casing .....155

Figure A4.17: Real component of electric field in the Z-direction for a orthogonal  
fracture of half-length 25 m in a horizontal wellbore in steel casing156

Figure A4.18: Imaginary component of electric field in the Z-direction for a  
orthogonal fracture of half-length 25 m in a horizontal wellbore in steel  
casing .....156

Figure A4.19: Real component of magnetic field in the Z-direction for a orthogonal  
fracture of half-length 25 m in a horizontal wellbore in steel casing157

Figure A4.20: Imaginary component of magnetic field in the Z-direction for a  
orthogonal fracture of half-length 25 m in a horizontal wellbore in steel  
casing .....157

Figure A4.21: Real component of electric field in the Z-direction for a orthogonal  
fracture of half-length 30 m in a horizontal wellbore in steel casing158

Figure A4.22: Imaginary component of electric field in the Z-direction for a  
orthogonal fracture of half-length 30 m in a horizontal wellbore in steel  
casing .....158

Figure A4.23: Real component of magnetic field in the Z-direction for a orthogonal  
fracture of half-length 30 m in a horizontal wellbore in steel casing159

Figure A4.24: Imaginary component of magnetic field in the Z-direction for a  
orthogonal fracture of half-length 30 m in a horizontal wellbore in steel  
casing .....159

Figure A4.25: Real component of electric field in the Z-direction for a orthogonal  
fracture of half-length 35 m in a horizontal wellbore in steel casing160

Figure A4.26: Imaginary component of electric field in the Z-direction for a  
orthogonal fracture of half-length 35 m in a horizontal wellbore in steel  
casing .....160

Figure A4.27: Real component of magnetic field in the Z-direction for a orthogonal  
fracture of half-length 35 m in a horizontal wellbore in steel casing161

Figure A4.28: Imaginary component of magnetic field in the Z-direction for a  
orthogonal fracture of half-length 35 m in a horizontal wellbore in steel  
casing .....161

Figure A4.29: Real component of electric field in the Z-direction for a orthogonal  
fracture of half-length 40 m in a horizontal wellbore in steel casing162

Figure A4.30: Imaginary component of electric field in the Z-direction for a orthogonal fracture of half-length 40 m in a horizontal wellbore in steel casing .....	162
Figure A4.31: Real component of magnetic field in the Z-direction for a orthogonal fracture of half-length 40 m in a horizontal wellbore in steel casing	163
Figure A4.32: Imaginary component of magnetic field in the Z-direction for a orthogonal fracture of half-length 40 m in a horizontal wellbore in steel casing .....	163
Figure A4.33: Real component of electric field in the Z-direction for a orthogonal fracture of half-length 45 m in a horizontal wellbore in steel casing	164
Figure A4.34: Imaginary component of electric field in the Z-direction for a orthogonal fracture of half-length 45 m in a horizontal wellbore in steel casing .....	164
Figure A4.35: Real component of magnetic field in the Z-direction for a orthogonal fracture of half-length 45 m in a horizontal wellbore in steel casing	165
Figure A4.36: Imaginary component of Magnetic field in the Z-direction for a orthogonal fracture of half-length 45 m in a horizontal wellbore in steel casing .....	165
Figure A4.37: Real component of magnetic field in the Z-direction for a orthogonal fracture of half-length 60 m in a horizontal wellbore in steel casing	166
Figure A4.38: Imaginary component of magnetic field in the Z-direction for a orthogonal fracture of half-length 60 m in a horizontal wellbore in steel casing .....	166
Figure A4.39: Real component of electric field in the Z-direction for a orthogonal fracture of half-length 60 m in a horizontal wellbore in steel casing	167

Figure A4.40: Imaginary component of electric field in the Z-direction for a orthogonal fracture of half-length 60 m in a horizontal wellbore in steel casing .....	167
Figure A5.1: Imaginary component of magnetic field in Y- direction for a non- symmetrical fracture of wings of half length 5m and 10m on either side .....	168
Figure A5.2: Imaginary component of magnetic field in Z- direction for a non- symmetrical fracture of wings of half length 5m and 10m on either side .....	168
Figure A5.3: Imaginary component of magnetic field in Y- direction for a non- symmetrical fracture of wings of half length 5m and 15m on either side .....	169
Figure A5.4: Imaginary component of magnetic field in Z- direction for a non- symmetrical fracture of wings of half length 5m and 15m on either side .....	169
Figure A5.5: Imaginary component of magnetic field in Y- direction for a non- symmetrical fracture of wings of half length 5m and 20m on either side .....	170
Figure A5.6: Imaginary component of magnetic field in Z- direction for a non- symmetrical fracture of wings of half length 5m and 20m on either side .....	170
Figure A5.7: Imaginary component of Magnetic field in Y- direction for a non- symmetrical fracture of wings of half length 5m and 25m on either side .....	171

Figure A5.8: Imaginary component of magnetic field in Z- direction for a non-symmetrical fracture of wings of half length 5m and 25m on either side .....171

Figure A5.9: Imaginary component of magnetic field in Y- direction for a non-symmetrical fracture of wings of half length 5m and 30m on either side .....172

Figure A5.10: Imaginary component of magnetic field in Z- direction for a non-symmetrical fracture of wings of half length 5m and 30m on either side .....172

Figure A5.11: Imaginary component of magnetic field in Y- direction for a non-symmetrical fracture of wings of half length 15m and 30m on either side .....173

Figure A5.12: Imaginary component of magnetic field in Z- direction for a non-symmetrical fracture of wings of half length 15m and 30m on either side .....173

Figure A5.13: Imaginary component of magnetic field in Y- direction for a non-symmetrical fracture of wings of half length 15m and 45m on either side .....174

Figure A5.14: Imaginary component of magnetic field in Z- direction for a non-symmetrical fracture of wings of half length 15m and 45m on either side .....174

Figure A5.15: Imaginary component of magnetic field in Y- direction for a non-symmetrical fracture of wings of half length 15m and 60m on either side .....175

Figure A5.16: Imaginary component of magnetic field in Z- direction for a non-symmetrical fracture of wings of half length 15m and 60m on either side .....175

Figure A5.17: Imaginary component of magnetic field in Y- direction for a non-symmetrical fracture of wings of half length 30m and 60m on either side .....176

Figure A5.18: Imaginary component of magnetic field in Z- direction for a non-symmetrical fracture of wings of half length 30m and 60m on either side .....176

## **Chapter 1: Introduction**

Global energy demand has galloped to over 500 quadrillion BTUs along with explosive population growth spurred by relative world peace and better health care (Exxon Mobil Energy Outlook, 2013). An immediate need to find energy solutions for the future is necessary. Over the last decade hydraulic fracturing has become increasingly prevalent, especially in USA, to recover hydrocarbons from tight rocks. Hydraulic fracturing has a market of over \$20 billion in the US with over 100,000 fracturing jobs per year. In 2009, shale gas represented 16% of domestic gas production. By 2035, shale gas is estimated to represent 47% of domestic gas production, becoming the “largest source of natural gas supply” (the Energy Information Administration (EIA), 2009). The forward-looking statement appears more realistic in the projected reduction of net petroleum imports and increase in natural gas and tight oil production, as shown in Figure 1.1, in EIA’s Annual Energy Outlook 2014 Early Release Overview. The same document also projects an increase in production of natural gas from 31%-38% as shown in Figure 1.2. In addition to the shale plays in the US, there are large shale plays in South America, China, Mexico, and Russia that can also be produced from, using hydraulic fracturing.

Shale plays are the future for the ever increasing demand for energy in the US. King (2010) identifies the four biggest technological advances responsible for the enhanced recovery of hydrocarbons: (a) “slick water” fracturing, (b) horizontal wells of length exceeding 5000ft, (c) increased number of fracture stages ranging from 10-20 per well, and (d) simultaneous or sequential fracturing. Since hydraulic fracturing is one of the critical components of enhanced hydrocarbon recovery, it is necessary to determine

the drivers of productivity of these fractures. The dimensions of hydraulic fractures, especially the propped length, width and height, determine the productivity of a particular well. These dimensions, if measured accurately, can be used in reservoir simulations to predict recovery from a particular well or a reservoir. Moreover, we can use fracture diagnosis as a tool to design more effective treatment of hydraulic fractures.

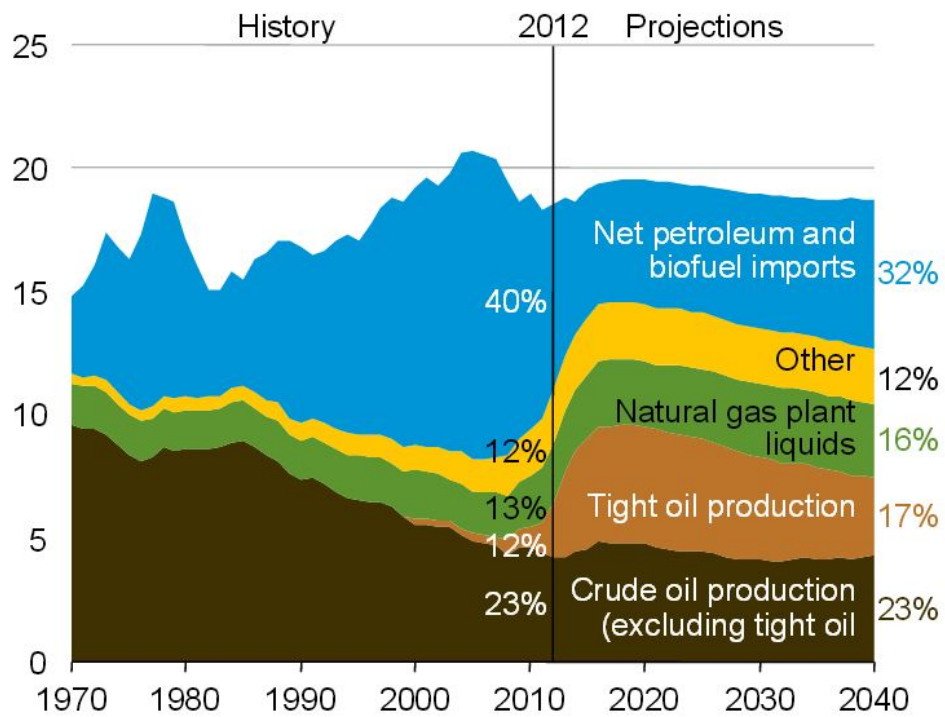


Figure 1.1: U.S. petroleum and other liquid fuels supply by source (million barrels per day) (after Figure 1 of EIA's Annual Energy Outlook 2014 Early Release Overview)

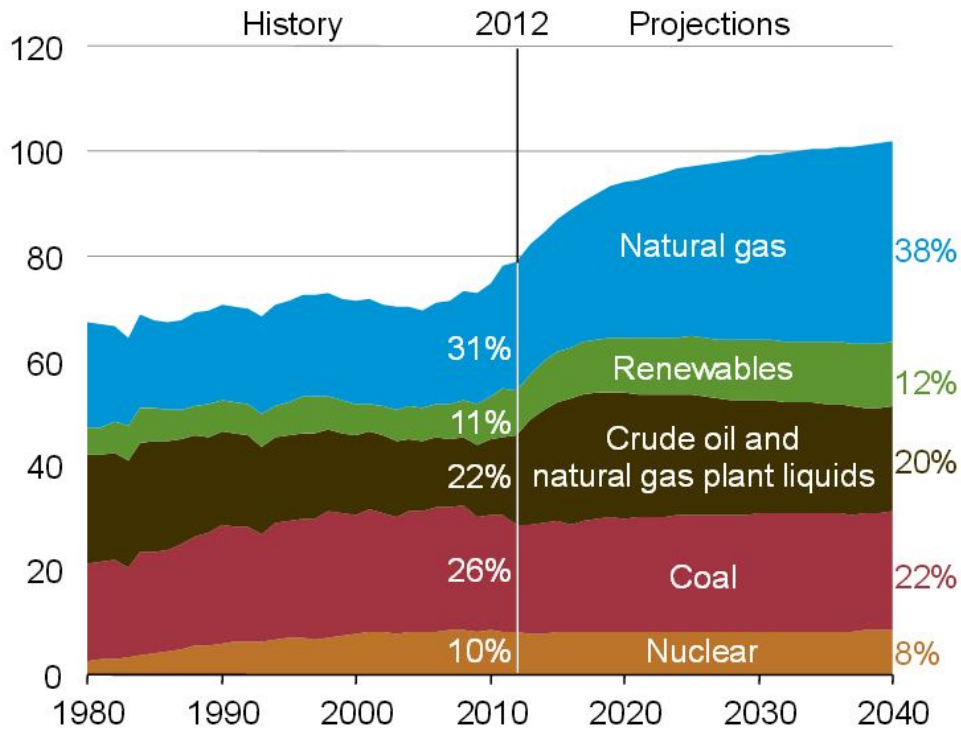


Figure 1.2: U.S. energy production by fuel, 1980-2040 (quadrillion Btu) (after Figure 11 of EIA's Annual Energy Outlook 2014 Early Release Overview)

### 1.1 BACKGROUND AND MOTIVATION

Presently, there are many fracture diagnostic methods available in the market. Based on their depth of investigation and when they are used in the sequence of operations, these methods can be broadly divided in three groups (Cipolla and Wright, 2000), as shown in Table 1.1:

- a. Far field, during fracturing
- b. Near wellbore, after fracturing
- c. Model Based

Of these, the first two are direct methods while the last one gives us the inferred or indirect measurement of fracture dimensions. Each of these approaches has their own advantages and limitations. The most popular far field method of fracture diagnosis is microseismic monitoring. Sometimes tiltmeters are also used for far field fracture diagnosis. Tiltmeters typically measure deformation. The measured deformation is analyzed to compute volume and direction of created hydraulic fractures. Surface tiltmeters are installed on surface, while downhole tiltmeters need a monitoring well. The resolution of tiltmeters decreases as the distance from surface or monitoring well increases. Tiltmeters provide no information about proppant distribution or fracture geometry. Hence, they are seldom the preferred choice for hydraulic fracture diagnostics.

On the other hand, the second broad category, near wellbore diagnostics is executed after fracturing is done. Near wellbore diagnostic's limitation is that it can only analyze hydraulic fractures only up to a few inches of the wellbore. Radioactive tracers are, therefore, used to detect the location of the proppant in the wellbore. Further, since the photomultiplier tube (PMT) of the logging tool measures incident gamma ray radiation from the tracers over the entire 360-degree of the borehole, direction of the fracture cannot be inferred using this technique. The tracers only provide a lower limit for fracture height if fracture and well path are aligned. Thus, we have no information of the propped length, which is the most important factor controlling the productivity of a well. Temperature and production logging is frequently used after the well starts producing. However, it only tells us where the flow is coming from, and in what quantity, at a particular instant. For this reason, production logs need to be run multiple times to obtain a time lapse analysis of production trends. Borehole imagers and downhole video cameras are also used to image the wellbore. Essentially, these tools give us information about the locations of natural, drilling induced, and hydraulic fractures where they

intersect the wellbore. They do not provide any information about the lateral extent of the fractures.

**Capabilities and Limitations of Fracture Diagnostics**

Techniques ■ can determine ■ may determine  cannot determine

Group	Fracture Diagnostic Method	Main Limitations	Ability to Estimate							
			Length	Height	Asymmetry	Width	Azimuth	Dip	Volume	Conductivity
Far field, during fracturing	Surface tiltmeter mapping	<ul style="list-style-type: none"> <li>Cannot resolve individual and complex fracture dimensions</li> <li>Mapping resolution decreases with depth (fracture azimuth <math>\pm 3^\circ</math> at 3,000-ft depth and <math>\pm 10^\circ</math> at 10,000-ft depth)</li> </ul>								
	Downhole tiltmeter mapping	<ul style="list-style-type: none"> <li>Resolution in fracture length and height decreases as monitoring-well distance increases</li> <li>Limited by the availability of potential monitoring wells</li> <li>No information about proppant distribution and effective fracture geometry</li> </ul>								
	Microseismic mapping	<ul style="list-style-type: none"> <li>Limited by the availability of potential monitoring wells</li> <li>Dependent on velocity-model correctness</li> <li>No information about proppant distribution and effective fracture geometry</li> </ul>								
Near wellbore, after fracturing	Radioactive tracers	<ul style="list-style-type: none"> <li>Measurement in near-wellbore volume</li> <li>Provides only a lower limit for fracture height if fracture and well path are not aligned</li> </ul>								
	Temperature logging	<ul style="list-style-type: none"> <li>Thermal conductivity of different formations can vary, skewing temperature log results</li> <li>Post-treatment log requires multiple passes within 24 h after the treatment</li> <li>Provides only a lower limit for fracture height if fracture and well path are not aligned</li> </ul>								
	Production logging	<ul style="list-style-type: none"> <li>Provides only information about zones or perforations contributing to production in cased-hole applications</li> </ul>								
	Borehole image logging	<ul style="list-style-type: none"> <li>Run only in open hole</li> <li>Provides fracture orientation only near the wellbore</li> </ul>								
	Downhole video	<ul style="list-style-type: none"> <li>Run mostly in cased holes and provides information only about zones and perforations contributing to production</li> <li>May have openhole applications</li> </ul>								
Model based	Net-pressure fracture analysis	<ul style="list-style-type: none"> <li>Results depend on model assumptions and reservoir description</li> <li>Requires "calibration" with direct observations</li> </ul>								
	Well testing	<ul style="list-style-type: none"> <li>Results dependent on model assumptions</li> <li>Requires accurate permeability and reservoir pressure estimates</li> </ul>								
	Production analysis	<ul style="list-style-type: none"> <li>Results dependent on model assumptions</li> <li>Requires accurate permeability and reservoir pressure estimates</li> </ul>								

Table 1.1: Capabilities and limitations of current fracture diagnostic tools (after Cipolla and Wright, 2000)

The primary model based approach for fracture diagnosis is pressure transient test analysis. Post fracture production data is easily available at the wellhead. This data can be fed into various fracture models to determine the height, width, and length of created fractures. It involves history-matching production and pressure data to the simulated fracture model. In-situ stresses, permeability, and conductivity of fractures can be varied to match field data. The major limitation of this method is that it can only provide non-unique solutions. Also, data over a substantial period of time is required to obtain an accurate history match.

Owing to the limitations of other methods microseismic monitoring has emerged as the most preferred method of fracture diagnostic. As a hydraulic fracture is created, it causes shear slippage and tensile deformation within a rock that are detected as microseisms (Le Calvez et al., 2006). The microseisms give rise to p- and s- waves that can be detected by sensors in a monitoring well or on the surface. These waves are reflected, refracted, and transmitted as they move through the rock matrix, depending on the material properties of the rocks. The locations of the source of these microseisms are obtained through triangulation by using an appropriate velocity model. An improper velocity model can give rise to errors of 20-40% (Castano, et al, 2010). Once the locations are established they are used to estimate the simulated reservoir volume (SRV). Traditionally, microseismic inversion models assume that all events are due to pure shear failures (shear source models) without accounting for fluid and proppant. Therefore, the simulated rock volume (SRV) map doesn't provide any information about the proppant location. To address this issue, moment tensor (MT) models have been developed. The tensor matrix takes into account three source mechanisms: a. pure shear, b. tensile and c. explosive/implosive. However, at least 2 monitor wells recording both p- and s- waves are required to resolve the full 6 parameters (Warpinski and Du, 2010). When only one

well is available, as it is in most cases, only 5 components can be effectively recovered. Also, the presence of other challenges like signal-to-noise ratios of receiver arrays, inherent uncertainties in the location of the microseismic events, may increase uncertainty in the results. It is important to understand that while these maps tell us about the location of microseismic events, they do not provide any insight into their hydraulic connectivity. Therefore, it is essential to investigate further, and find a technology that estimates the propped length of hydraulic fracture that contributes to the production in a fractured well.

## **1.2 RESEARCH OBJECTIVE**

The primary objective of this research is to design and investigate the feasibility of a logging tool that can determine propped length of a hydraulic fracture. The following objectives are specifically addressed in this thesis:

1. Designing of a Low Frequency Electromagnetic Induction (LFEI) logging tool that can determine propped length of hydraulic fracture.
2. Modeling of wellbore, rock matrix, and different geometries of hydraulic fractures in FEKO electromagnetic simulator.
3. Studying the response of real and imaginary component of electric and magnetic fields, as well as their magnitudes, to different fracture geometries. Both cased-hole and open-hole completions need to be investigated in vertical and horizontal wells.
4. Analyzing special cases such as signal through steel casing, proppant banking, non-symmetrical fractures in horizontal well.

5. Sensitivity analysis of i. frequency of operation, ii. transmitter-receiver spacing, iii. resistivity of rock matrix and iv. resistivity of proppant.

### **1.3 PAST WORK**

This research is a continuation of the work done by Salies (2012). Her thesis explored two different ways of developing a fracture diagnostic tool capable of measuring propped length of a hydraulic fracture. Although both her methods used electrically conductive proppants, one method used antenna resonance (frequency of operation: 0.2 – 3 MHz) and the other used low frequency electromagnetic induction (frequency of operation: 100-1000Hz). Due to the dispersive nature of rock matrix (resistivity: 0.1-1000 Ohm-m), the antenna resonance approach was abandoned in favor of electromagnetic induction. In her research, simulations were performed using FEKO of bi-wing fractures 20m-100m in length. Salies's thesis explored numerical schemes for canceling primary magnetic field in order to extract secondary magnetic field, which contains information about the fracture geometry. Her conclusions were:

- a. The resultant magnetic field increases with increasing fracture size.
- b. Medium and long spaced tool are more sensitive to length of fracture than short spaced tool.
- c. The proposed electromagnetic logging tool should be built with the largest transmitter-receiver spacing.

Salies (2012) also evaluated current low frequency electromagnetic hardware that is used in cross-well electromagnetic tomography (XW-EMT) and concluded that it can be applied to the proposed Low Frequency Electromagnetic (LFEI) tool, and

recommended further of exhausting all the possible forward simulations for different fracture geometries before attempting an inversion scheme.

Following Salies, Pardo and Torres-Verdin (2013) also investigated the possibility of using low frequency electromagnetic induction as a means to diagnose penny-shaped hydraulic fractures. Their work provided a cross validation of Salies (2012) as the simulation uses 2D hp-Finite Element (FE) discretization of the EM problem for the same geometry. Pardo and Torres-Verdin concluded that it is possible to quantify both the thickness and length of disc shaped hydraulic fractures using this technique. They compared solenoid and toroid based transmitters, and also assessed the effect of steel casing in these problems.

Low-frequency electromagnetic induction has also been used for anomaly detection outside the energy industry. For instance, Milesevic et al (2011) used low frequency electromagnetic induction (50 Hz) to calculate induced voltages in underground pipelines (240 m) using their in-house EMTP-ATP software. Dorn (2002) also used low frequency electromagnetic induction (1 kHz) for shape reconstruction at a depth of investigation of 200 m. His method involved using level sets and adjoint fields to solve Maxwell's equation in the frequency domain. Therefore, exploring applications of low frequency electromagnetic induction, as this thesis proposes, for far field imaging (up to 100m) of fractured rock formation can be a promising prospect.

#### **1.4 OVERVIEW OF CHAPTERS**

The next chapter of this thesis delves into the physics of induction logging measurement. It starts with the Maxwell's equation of electromagnetism and explains its application in solving the problem at hand. The chapter then sifts through various

numerical methods that can be used to solve Maxwell's equation in the frequency domain. It further explains how electromagnetic induction is applied to determine petrophysical properties of rocks. Current high frequency induction logging tools and along with low frequency cross-well electromagnetic tomography (XW-EMT) are also studied in the chapter. The chapter ends with the design of the proposed Low Frequency Electromagnetic Induction Tool (LFEI) that includes specifications of frequency of operation, transmitter-receiver spacing and expected depth of penetration.

Chapter 3 justifies the choice of EM simulator, FEKO, by comparing it with other commercial electromagnetic simulators and analyzes the capabilities and limitation of each. Modeling and formulation of wellbore, formation matrix, casing and hydraulic fracture is also discussed. Modeling of dielectric and magnetic properties of each component is explained in the chapter. Simplest cases of geometry and dielectric properties are considered first and then more complex cases are analyzed. Chapter 3 also formulates the proposed tool by using a vertical magnetic dipole (VMD) as a source, and short, medium and long spaced receivers. The chapter ends with a simple sensitivity analysis of the meshing grid for a given fracture geometry.

Chapter 4 presents results of various simulations done as summarized in Table 1.2. Simulations were done for fracture half-length of 5 m, 10 m, 15 m, 20 m, 25 m, 30m, 35 m, 40 m, 45 m, 60 m, 75 m and 100 m. The real and the imaginary part of the electric and magnetic fields are plotted for each of these cases. In some cases, the magnitude of the same is also shown in the plots. Although significant plots are presented in this thesis, some plots have been excluded for the sake of brevity. The chapter concludes with the analysis of various special cases. It also highlights how the proposed tool can be used in more complex situations.

		Open Hole	Cased Hole	Uniform proppant distribution	Non-uniform proppant distribution
Vertical Well	Vertical fractures	<input type="checkbox"/>	<input type="checkbox"/>	<input type="checkbox"/>	<input type="checkbox"/>
	Oriented fractures	<input type="checkbox"/>	<input type="checkbox"/>	<input type="checkbox"/>	<input type="checkbox"/>
Horizontal Well	Orthogonal fractures	<input type="checkbox"/>	<input type="checkbox"/>	<input type="checkbox"/>	<input type="checkbox"/>
	Non-orthogonal fractures	<input type="checkbox"/>	<input type="checkbox"/>	<input type="checkbox"/>	<input type="checkbox"/>

Table 1.2: Summary of simulations done in FEKO for different fracture geometry and orientation using LFEI tool.

Chapter 5 delves into the sensitivity analysis of the i. frequency of operation, ii. transmitter-receiver spacing, iii. dielectric property of matrix, and iv. dielectric property of proppant. This particular section of the thesis lists out the conditions under which the proposed technology can be successfully applied.

The final chapter tabulates the main findings of this thesis. It also charts out the two-pronged approach that needs to be taken for continuing this work. The chapter ends with a flowchart of how this tool will improve fractures diagnostics and reservoir management in general.

## **Chapter 2: Induction Logging Tools**

Induction logging for subsurface prospecting is an old science. The earliest patent for eddy current measurement in borehole dates back in the early 19<sup>th</sup> century. The first electrical surface prospecting job was executed by Conrad Schlumberger in 1912. He did this by sending current between two metallic rods driven in the earth's surface and mapping the current paths. H.G. Doll found the first practical downhole application by using a two-coil induction logging tool over a jeep-mounted mine detector that he had developed for the U.S. War Department during the World War II. Induction logging tools have become the backbone of any well logging suite as a hydrocarbon detector. In simplest of terms, high resistivity indicates presence of oil or gas, whereas low resistivity indicates water in pores of rocks. Resistivity can also be measured using Laterolog tools and micro-resistivity devices. However, induction logging remains the most popular method, primarily due to its versatility at being able to operate in a wide variety of environments.

Induction logging, nevertheless, has come a long way from the first two-coil tool to the multi-coil array, as depicted in Figure 2.1(Anderson and Barber, 1995). Modern induction logging tools use sophisticated electronic equipment and computational methods to arrive at the final answer product. The simple two-coil tool has given way to arrays of coils that utilize signal deconvolution, phasor processing, and a wide range of environmental corrections(Anderson and Barber, 1999 and Barber, 1985).. This study focus on the simplest case of two-coil sonde as it aims to become a proof of concept.

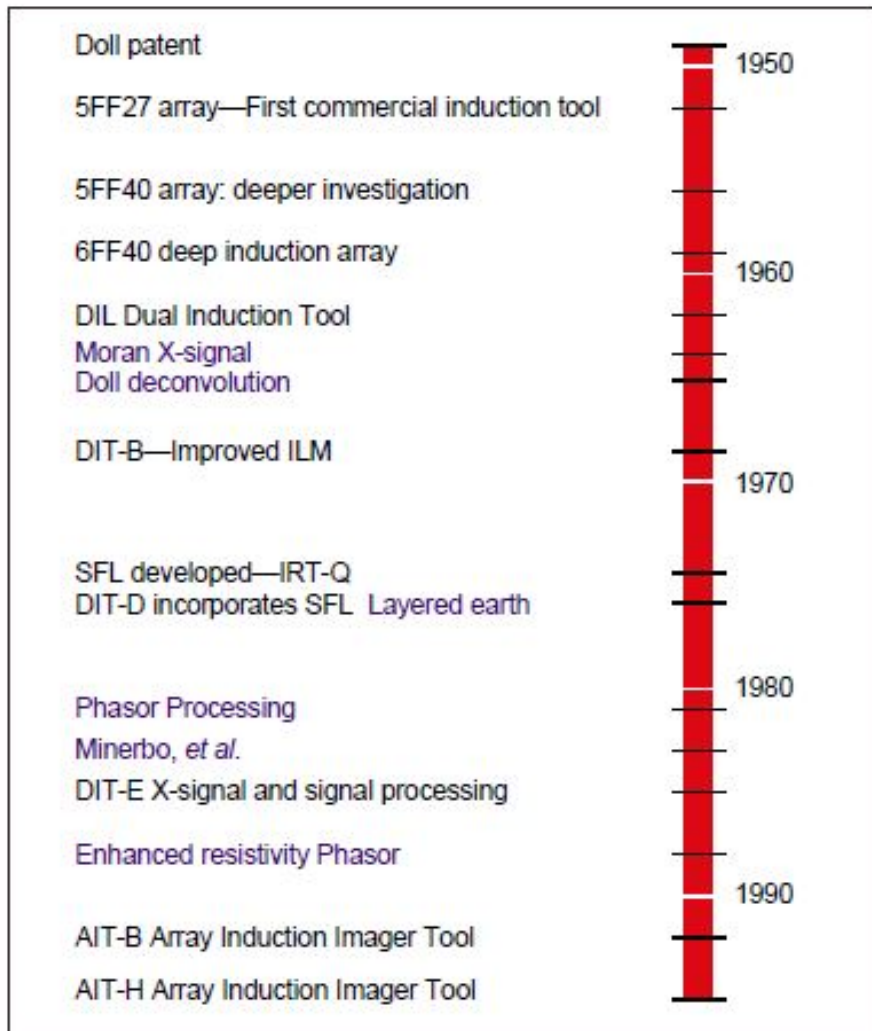


Figure 2.1: History of induction logging tools

Induction logging tools, fundamentally, consists of a two-coil sonde mounted coaxially on a mandrel, as shown in Figure 2.2. Each coil can be designed to have many turns. One coil acts as a transmitter because it emits electromagnetic waves that interact with the rock matrix. The transmitter induces a current loop in the formation, which in turn induces a current in the receiver coil. The electromagnetic waves interact with the

rock matrix and the fluids in the pores of the rock to produce different signals that are interpreted and presented on a log.

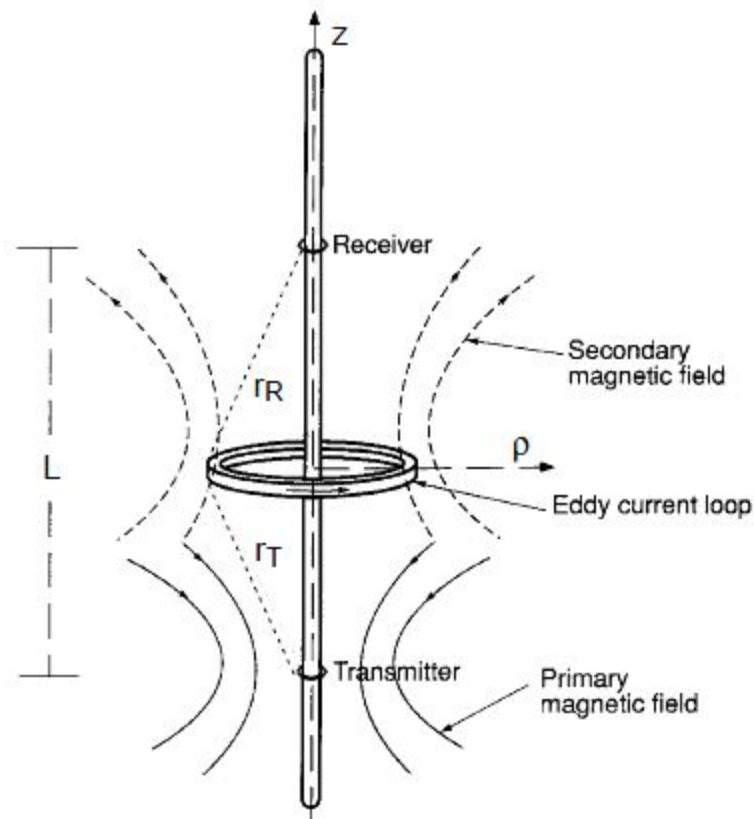


Figure 2.2: Basic two coil induction electromagnetic tool

## 2.1 GOVERNING PHYSICS

Maxwell's equations are used to interpret response at the receiver for electromagnetic tools used in well logging. By applying appropriate source and boundary conditions, the correct dielectric permittivity, relative magnetic permeability, and conductivity (resistivity) of the medium we can model both magnetic and electric fields in space and time using Maxwell's equations.

Maxwell's equation can be represented both in time and frequency domain. The equations in time domain are:

$$-\nabla \times H + \partial_t D + J = -J^e \quad (2.1)$$

$$\nabla \times E + \partial_t B = -K^e \quad (2.2)$$

$E$  = electric field strength (V/m)

$H$  = magnetic field strength (A/m)

$J^e$  = volume density of external (source) electric current (A/m<sup>2</sup>)

$J$  = volume density of electric current (A/m<sup>2</sup>)

$K^e$  = volume density of external (source) magnetic current (V/m<sup>2</sup>)

$K^m$  = volume density of material magnetic current (V/m<sup>2</sup>)

$D$  = electric flux density (C/m<sup>2</sup>)

$B$  = magnetic flux density (T)

$\rho$  = volume density of electric charge (C/m<sup>3</sup>)

$j^s$  = surface current density (A/m)

$\sigma^s$  = surface charge density (C/m<sup>3</sup>)

$\sigma$  = conductivity (S/m)

$\epsilon$  = dielectric permittivity =  $\epsilon_r \epsilon_0$  (F/m)

$\epsilon_0$  = dielectric permittivity of free space =  $8.85 \times 10^{-12}$  (F/m)

$\epsilon_r$  = relative dielectric permittivity

$\mu$  = magnetic permeability =  $\mu_r \mu_0$  (H/m)

$\mu_0$  = magnetic permeability of free space =  $4\pi \times 10^{-7}$  (H/m)

$\mu_r$  = relative magnetic permeability

In Equation 2.2, hypothetical magnetic current,  $K^e$  has been introduced for convenience. Applying the divergence operator to both sides of the previous equations, we obtain:

$$\partial_t \nabla \cdot D + \nabla \cdot J = -\nabla \cdot J^e \quad (2.3)$$

$$\partial_t \nabla \cdot B = -\nabla \cdot K^e \quad (2.4)$$

Historically volume density of charge is introduced as  $\rho = \nabla \cdot D$ . Also there are constitutive relations that carry information about the properties of the media.

$$D = \varepsilon \cdot E \quad (2.5)$$

$$B = \mu \cdot H \quad (2.6)$$

$$J = \sigma \cdot E \quad (2.7)$$

Maxwell's equations can also be represented and solved in the frequency domain. In the frequency domain these equations are written as:

$$-\nabla \times H - i\omega D + J = -J^e \quad (2.8)$$

$$\nabla \times E - i\omega B = -K^e \quad (2.9)$$

In most practical cases we encounter anisotropic media in well logging problems. In this case, electromagnetic properties of the media are characterized by tensors of rank two:  $\sigma_{ij}$ ,  $\varepsilon_{ij}$  and  $\mu_{ij}$ . These tensors can be mathematically represented by real, symmetric 3X3 matrices, and geometrically by second-degree surfaces. The highest tensor symmetry is obtained when main diagonal elements (principal values) are equal - this happens when the media is isotropic. Let us take the example of the material property, conductivity:

$$\sigma = \begin{pmatrix} \sigma_x & 0 & 0 \\ 0 & \sigma_y & 0 \\ 0 & 0 & \sigma_z \end{pmatrix} = \begin{pmatrix} \sigma_h & 0 & 0 \\ 0 & \sigma_h & 0 \\ 0 & 0 & \sigma_v \end{pmatrix} \quad (2.10)$$

In most logging conditions the principal directions (axes) do not match with the chosen coordinate system. So, frequently, we need to transform our chosen coordinate system along the tool axis to match that of the principal directions of the media properties. A rotation matrix  $R$  can be used to transform and express the elements of the principal tensors in the Cartesian coordinate system:

$$R = \begin{pmatrix} \cos \theta \cos \phi & \cos \theta \sin \phi & -\sin \theta \\ -\sin \phi & \cos \phi & 0 \\ \sin \theta \cos \phi & \sin \theta \sin \phi & \cos \theta \end{pmatrix} \quad (2.11)$$

Judicious choice of boundary conditions is necessary for solving these equations. Boundary conditions relate the electromagnetic fields on either side of an interface. For example, let  $S$  denote an interface with a unique tangential plane that has a unit vector  $\nu$  normal to  $S$ . In the absence of any surface charge, the boundary conditions on  $S$  are:

$$\nu \times H_1 = \nu \times H_2 \quad (2.12)$$

$$\nu \times E_1 = \nu \times E_2 \quad (2.13)$$

If a surface charge exists on  $S$ , then the boundary conditions become:

$$\nu \times H_2 - \nu \times H_1 = j^S \quad (2.14)$$

$$\nu \times E_2 - \nu \times E_1 = 0 \quad (2.15)$$

If the region is electrically impenetrable then  $E \cdot \nu = 0$ , Therefore:

$$\nu(x) \times E(x) \rightarrow 0 \quad (2.16)$$

where  $x \rightarrow S$ .

An electrically impenetrable medium is either perfectly conducting (i.e.  $\sigma \rightarrow \infty$ ) or  $\epsilon \rightarrow \infty$ . Applying these conditions to Maxwell's equation we get  $H(x) = 0$ . Hence:

$$\nu(x) \times H(x) \rightarrow j^S(x) \quad (2.17)$$

$$\nu(x) \cdot B(x) \rightarrow 0 \quad (2.18)$$

where  $x \rightarrow S$ .

For an isotropic medium, electric field lines are locally perpendicular to  $S$ , while magnetic field lines are tangential to  $S$ . The tangential component of magnetic field has a surface current density  $j^S$  as a limiting value on  $S$ .

## 2.2 APPLICATION OF ELECTROMAGNETIC INDUCTION IN LOGGING TOOLS

The most common induction-logging tool in the market is the Array Induction Tool or variations of the same. There is a single transmitter that operates at a frequency of 26.325Hz. In phase (R) and quadrature (X) signals are measurement for each of the mutually balanced eight arrays. After post-processing of these signals to correct for borehole and environmental effects, the tools gives resistivity readings for median depths of investigation of 10, 20, 30, 60 and 90 inches (Anderson and Barber,1995).

To understand any multi-array induction tool we need to start from two-coil sonde. A two-coil sonde has two coaxial coils mounted on a mandrel. The transmitter current is usually fed an alternating current of frequency  $\omega$ :

$$I_T = I_o \times \cos(\omega t) \quad (2.19)$$

or 
$$I_T = I_o \times e^{-i\omega t} \quad (2.20)$$

By Faraday's law the voltage induced in one circular loop element is

$$V_f = M_{TF} i\omega I_o e^{-i\omega t} \quad (2.21)$$

and

$$M_{TF} = \left( \frac{\mu T A_T \rho}{2r_T^3} \right) \quad (2.22)$$

where, T is number of transmitter turns,  $A_T$  is the area of the transmitter coil,  $\rho$  is the radius of formation loop, and  $r_T$  is the distance between transmitter and formation loop.

$M_{TF}$  is the mutual inductance between the transmitter coil and loop of conductive earth. We assume that current in each loop is unaffected by other loops, therefore  $M_{TF}$  is only a function of geometry ( $r_T$ ).

This voltage induced in the circular loop of earth would give rise to a current (eddy current), as given by:

$$I_f = V_f \frac{\delta A}{2\pi\rho} \sigma = i\omega M_{TF} \frac{\delta A}{2\pi\rho} \sigma e^{-i\omega t} \quad (2.23)$$

This current acting in the loop of earth acts as a secondary source and contributes to an induced voltage across the receiver, as given by:

$$V_R = i\omega M_{FR} I_f = -\omega^2 M_{FR} M_{TF} \frac{\delta A}{2\pi\rho} \sigma e^{-i\omega t} \quad (2.24)$$

and

$$M_{FR} = \frac{\mu R A_R \rho^2}{2r_R^3} \quad (2.25)$$

where R is the number of receiver turns,  $A_R$  is the area of the receiver coil,  $r_R$  is the distance between the receiver and the formation loop, and  $M_{FR}$  is the mutual inductance between the receiver coil and loop of conductive earth.

The received voltage can be written as:

$$V_R = \left( \frac{-\omega^2 \mu^2 TR Q I_o A_T A_R}{4\pi L} \right) \left( \frac{L \rho^3}{2r_T^3 r_R^3} \right) \delta A \sigma \quad (2.26)$$

$$V_R = Kg \delta A \sigma \quad (2.27)$$

It is useful to note that the first parenthesis in the above term contains tool parameters (K) where the second one contains information about the geometry of the media (g). Often the voltage at the receiver coil is expressed as a function of the geometric factor  $g(r,z)$ , tool constant K, and the conductivity of the earth  $\sigma$ . It essentially means different parts of the formation have different weights that give rise to the voltage in the receiver. In most inversion algorithm the geometric factor is modeled (kernel) while the conductivity is solved for. In this research, it is assumed that the conductivity of the formation where we deploy the proposed tool is known (kernel), and we solve for the geometry.

$$V_R = K \iint g(r,z) \sigma(r,z) dr dz \quad (2.28)$$

Interestingly, it is possible to add an equal and opposite quadrature (X) voltage to the receiver coil to cancel out the direct coupling between the two coil (mutual coupling). In practice this is achieved through bucking coils. At low conductivity the R-signal is 180° out of phase with the transmitter current while the remaining imaginary part, or the X-signal, is 90° out of phase with the transmitter current.

Doll(1949) introduced the concept of geometric factor ( $g_D$ ) by calculating the contribution of single loop of currents to the voltage at the receiver using Biot-Savart law. However, one should remember that Doll's geometric factor theory is valid only at the zero conductivity limits. The most commonly used technique today was introduced by Moran. The solution of Moran (1962) is analogous to Born approximation in quantum scattering. He derived an expression for the complex Born response function,  $g_B(Q,z)$ :

$$g_B(\rho, z, \sigma) = g_D(1 - ikr_T)e^{ikr_T}(1 - ikr_R)e^{ikr_R} \quad (2.29)$$

The measured complex conductivity signal is obtained by integrating over the entire space:

$$\sigma_R + i\sigma_X = \iint g_B(\rho, z, \rho)\sigma(\rho, z)d\rho dz \quad (2.30)$$

Over time studying the response of thin shells has given way to studying cylindrical volume of the formation (such as invaded zone). The integrated radial response of these cylinders is given by:

$$G_\rho(\rho, \sigma) = \iint g_B(\rho, z, \sigma)d\rho dz \quad (2.31)$$

Normalized Born response function of a two-coil sonde of imaginary and real parts is shown in Figure 2.3. Integrated Born response function for the same system is shown in Figure 2.4 (Anderson, 2001).

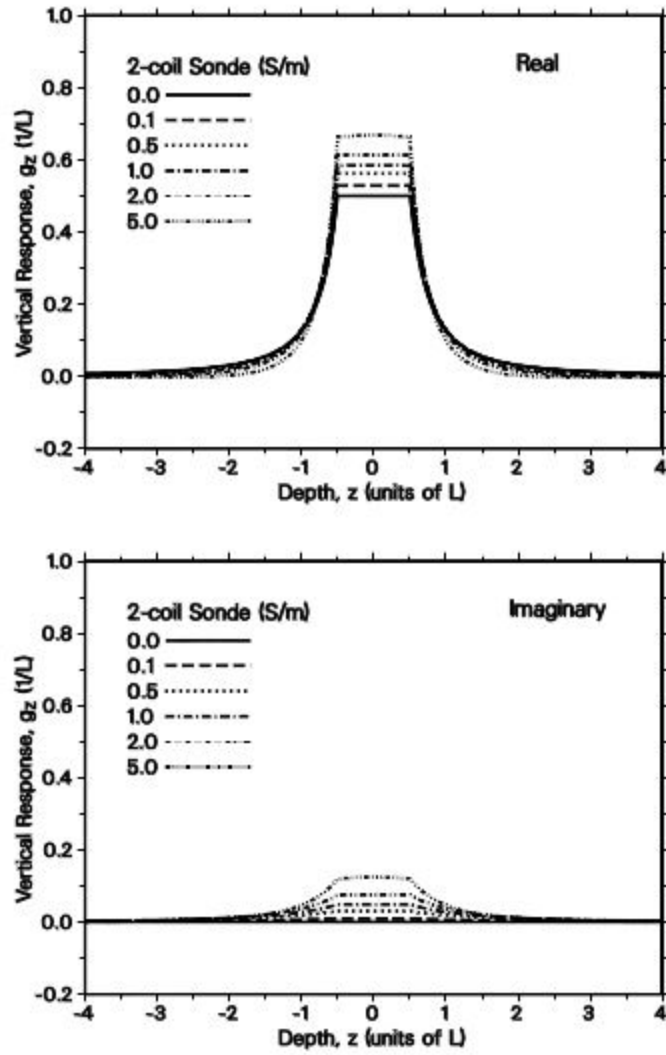


Figure 2.3: Normalized real (top) and imaginary (bottom) parts of Born response function for a two-coil system with coil spacing of  $L$  (after Anderson, 2001).

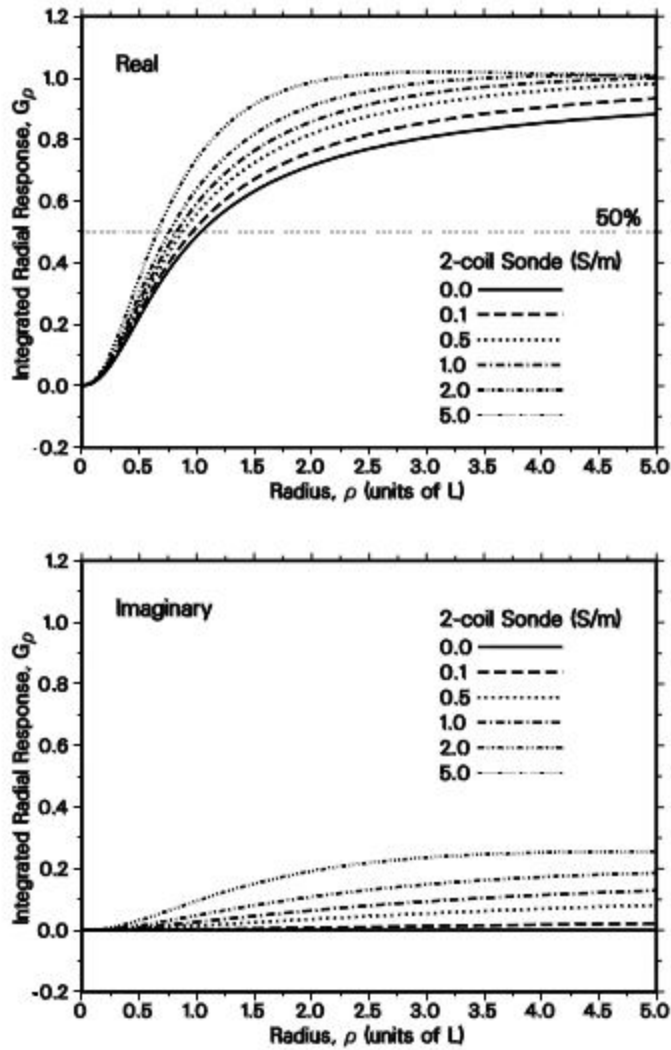


Figure 2.4: Normalized real (top) and imaginary (bottom) parts of integrated Born response function for a two-coil system with coil spacing of  $L$  (after Anderson, 2001).

The total tool response in a multi-coil tool is the normalized summation of an individual two-coil response as given by:

$$\sigma_{aTotal} = \frac{\sum_{i,j} \frac{T_i R_j \sigma_{ai,j}}{L_{i,j}}}{\sum_{i,j} \frac{T_i R_j}{L_{i,j}}} \quad (2.32)$$

Addition of auxiliary coils to the basic two-coil structure helps to focus more on a particular zone of interest.

A variety of induction logging tools are routinely used to find conductivity of the rock formation. Since resistivity is a commonly used term, conductivity is inverted to obtain resistivity. Commonly deployed induction logging tools include: Array Induction Tool (AIT) by Schlumberger, Hostile Dual Induction Log (HDIL) by Halliburton, Compact Array Induction Tool (MAI) by Weatherford, or High Definition Induction Log Tool (HDILTM) by Baker Hughes. In all these tools, the basic physics and governing principles remain the same. Most of these tools operate at a frequency range of a few kilohertz and have a depth of investigation of a few meters in the formation.

In the past, far-field application of this technology (low frequency electromagnetic induction) in geosystems engineering has been studied. Cross-well Electromagnetic Tomography (XW-EMT) is one such application. The process involves deploying a string of transmitter array (4-6) in one well and a string of receiver arrays (4-6) in another well, as shown in Figure 2.5. Each tool may be 10 meter to 20 meter long. Surface recording equipment connects the receiver and transmitters to map the space between the wells. The frequency of operation of these tools is between 5-1000Hz. Higher frequencies gives better resolution but demand smaller well spacing and lower conductivity, owing to the dispersive nature of the earth as a dielectric medium. XW-EMT needs thorough pre-planning because there are significant challenges in operational environment, faulting in rocks, water/hydrocarbon fronts, among others. Therefore, the

solution obtained is highly non-unique. Another disadvantage of this method is the frequent inability to find two closely spaced wells where this technology can be appropriately deployed.

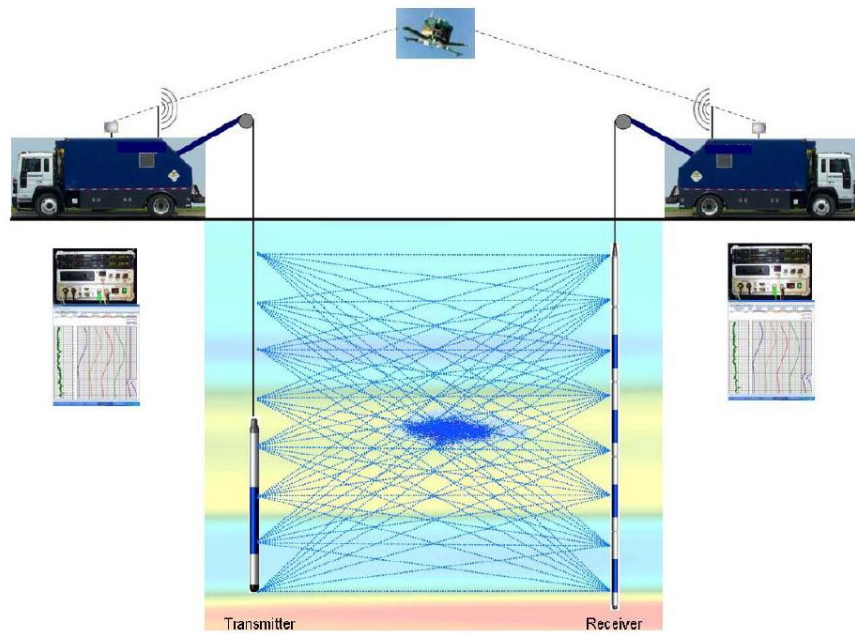


Figure 2.5: Schematic of XW-EMT system (DePavia et al 2008, Fig.1)

### 2.3 PROPOSED LOW FREQUENCY ELECTROMAGNETIC TOOL

After studying the current induction tools used for downhole prospecting, it can be seen that the proposed technology in this thesis has the potential to diagnose far field effects of hydraulic fractures. Salies (2012) had studied the depth of penetration with changing frequency for a fixed conductivity, as shown in Figures 2.6 and 2.7. One of the primary findings in her thesis was that the signal penetration decreases with an increasing frequency and conductivity. Therefore, for typical shale formations with resistivity values

from 1 ohm-m to 500 ohm-m, a signal penetration of a few hundred meters is expected if a low frequency of 100 Hz is used.

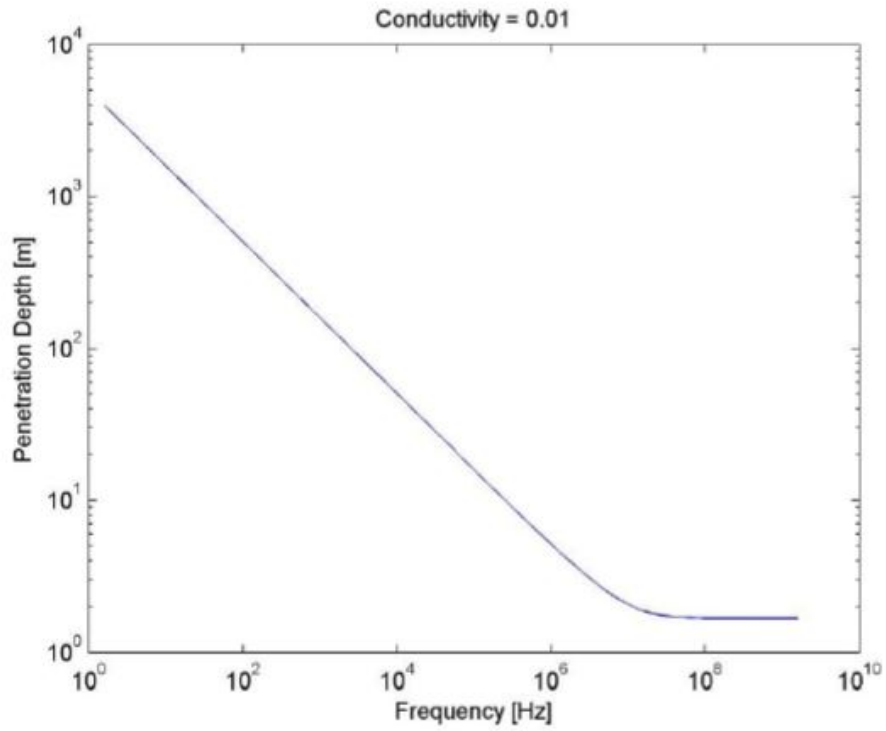


Figure 2.6: Maximum distance of signal penetration in a 0.01S/m matrix as a function of frequency (after Salies, 2012, Figure 3.5)

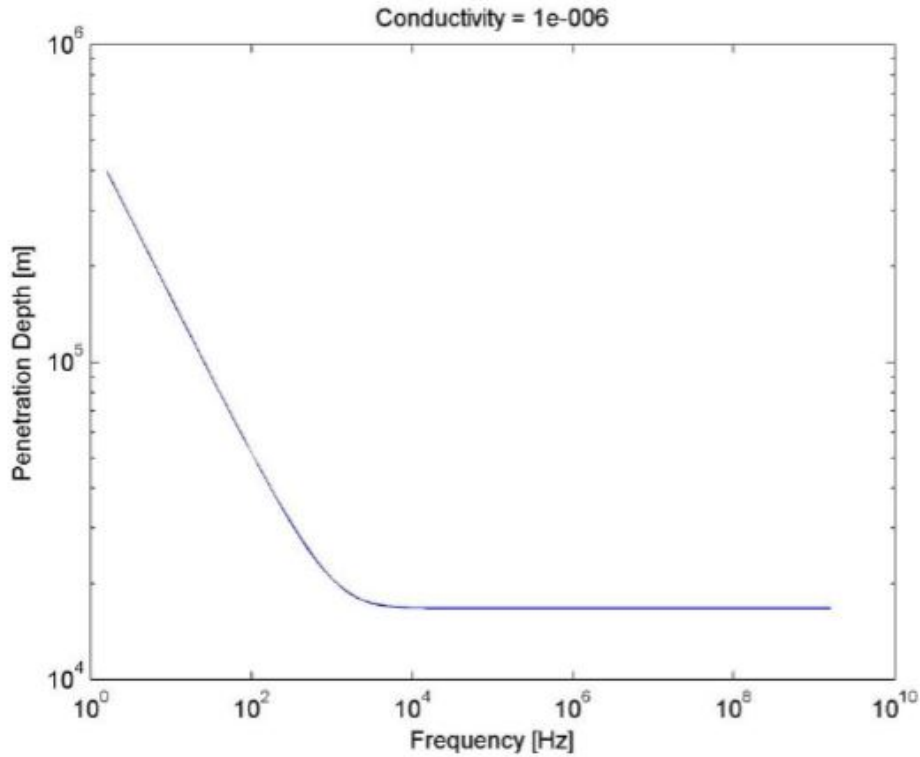


Figure 2.7: Maximum distance of signal penetration in a  $10^{-6}$ S/m matrix as a function of frequency (after Salies, 2012, Figure 3.4).

In this thesis a low frequency electromagnetic induction tool is used to detect far field anomalies in the rock matrix from a single borehole. The proposed tool has one tri-directional transmitter and three tri-directional receiver sets, each with a bucking coil to cancel out direct coupling. A basic schematic diagram of the tool is shown in Figure 2.8. A more detailed description of the tool, (Figure 2.9), is developed by incorporating tri-directional receivers and a tri-directional transmitter. Also, bucking coils for each receiver sets is envisioned. In this conceptual tool, there are 3 transmitter sets: a deep reading, a medium reading, and a shallow reading. The nominal diameter of the tool can be 3.625”, which is sufficient to house the receiver and transmitter coils.

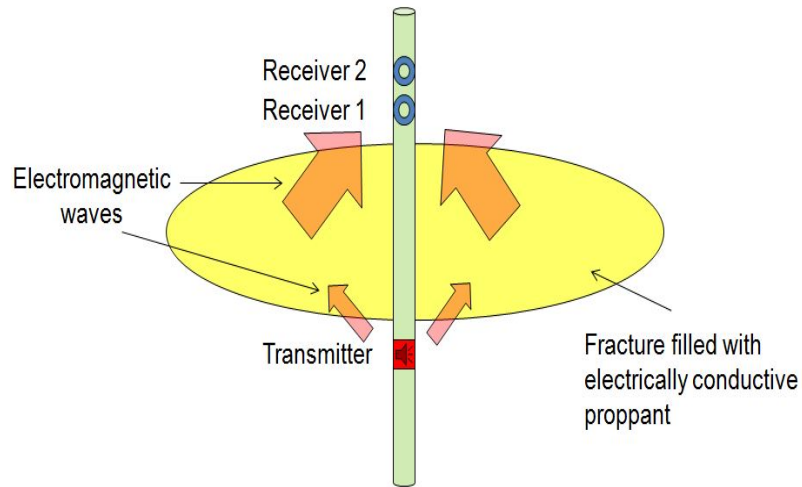


Figure 2.8: Schematic representation of the technology

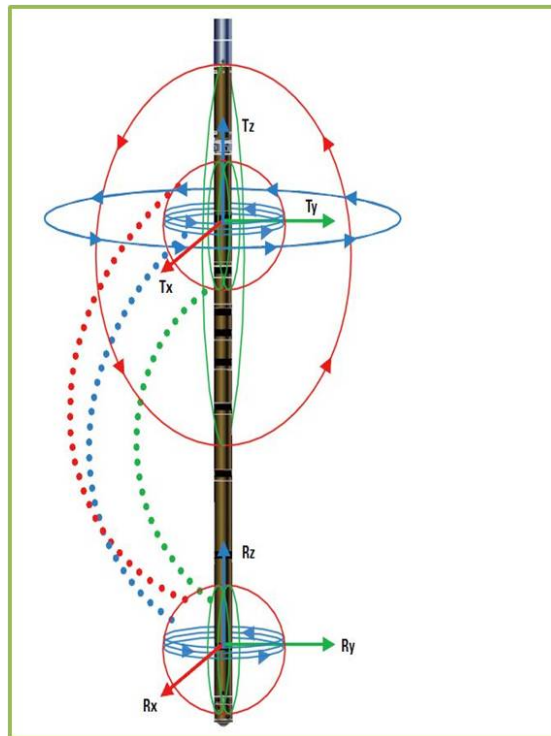


Figure 2.9: Schematic representation of proposed tri-directional electromagnetic induction tool where Tx, Ty and Tz represents the tri-directional transmitter and Rx, Ry and Rz represents the tri-directional receivers.

### **Chapter 3: Model Description**

As described in Chapter 2, the basic purpose of our simulation is to solve Maxwell's equation in the frequency domain for this problem. Since this thesis studies the feasibility of the proposed technology, various commercial electromagnetic simulators in the market were compared. But there are various issues with commercial software that limit its efficiency in producing accurate results. Hence for instance, i. sometime even simple geometries are tough to model, ii: software attempts to model configuration that it cannot model, iii: geometries analyzed are not always what the user is led to believe. Moreover, with commercial electromagnetic simulators users are expected to understand EM theory and limitations of numerical methods needed to solve it. Various electromagnetic simulation packages were researched in order to choose something that might suit this thesis's purpose. FEKO was finally chosen because:

- FEKO makes the analysis of very low frequency problems possible by automatically decomposing the problem space with special basis functions.
- In test problems FEKO accurately computed the current distribution on the object under test for frequencies as low as 0.001 Hz.
- FEKO uses hierarchical basis functions to increase the order of any triangle (of the mesh) as necessary.
- Small geometric details of a model will still be meshed with electrically small mesh elements, while larger details may be meshed with coarser mesh elements

In the following sections, the methods used to model the wellbore, rock matrix, tool and fracture is discussed.

### 3.1 SOFTWARE

We have used FEKO 6.0 for our research. CADFEKO was used to design the model, while POSTFEKO was used to analyze the results of the simulation runs. FEKO can be used for solving a variety of electromagnetic problems using different numerical methods. Applications range from antenna design, microstrip antennas and circuits, dielectric media, scattering analysis among others, as shown in Figure 3.1.

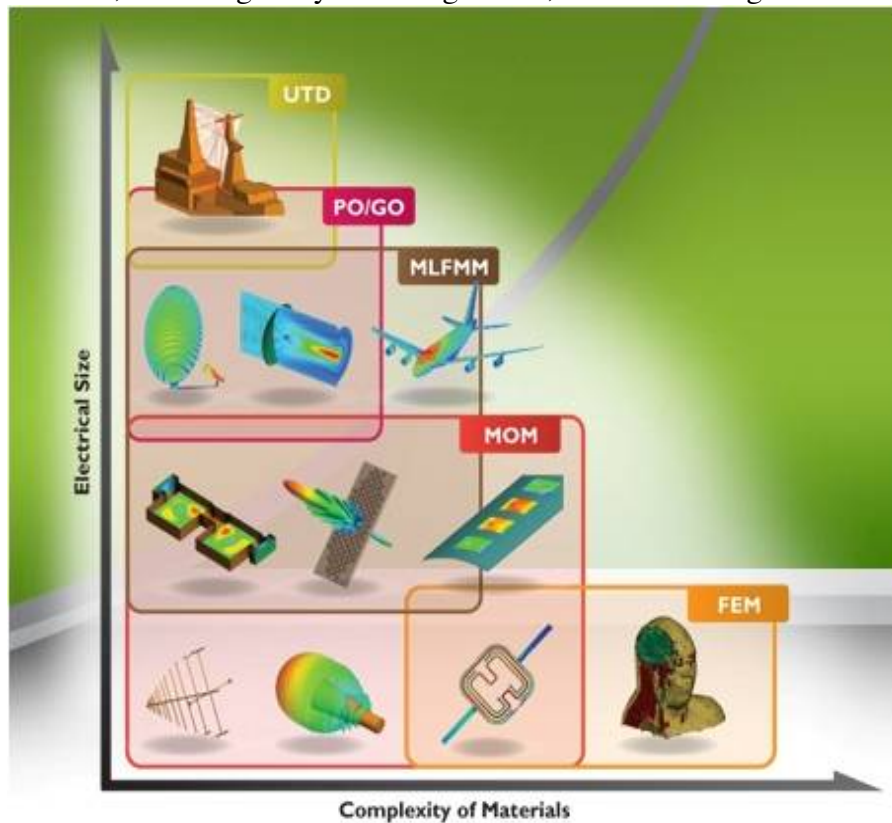


Figure 3.1: Capability of FEKO to use different solvers based on the complexity of materials and electrical size

There are various solvers embedded in the FEKO kernel: Method of Moments (MoM), Multilevel Fast Multipole Method (MLFMM), Finite Element Method (FEM), Uniform Theory of Diffraction (UTD), Geometrical optics (GO) and Physical Optics (PO). In our simulations MoM was selected as the preferred solver since it is a full wave

solution of Maxwell's integral equation in the frequency domain. FEKO's MoM has different extensions to enable modeling of dielectric and magnetic media: Surface Equivalence Principle (SEP), Volume Equivalence Principle (VEP), Planar Green's Function for Multilayered Media, Thin Dielectric Sheets, Dielectrically Coated Wires, Windscreen and Planar Green's function aperture. Since VEP allows creation of dielectric bodies from cuboids, VEP was selected as the chosen solution method. It needs more basis functions than SEP, i.e. computationally more expensive, but offers a more robust answer at low frequencies. Low frequency stabilization was also used since the simulations were run at 100 Hz.

As in all numerical solvers, meshing of geometrical elements plays a key role in the precision and accuracy of the solution. The FEKO guidelines inform that when meshing the region into tetrahedral volume elements, it is imperative that the edge length of the tetrahedral should be less than a fifth of the wavelength inside the dielectric medium in question. On the interface a finer mesh with edge length less than one-tenth of the wavelength is recommended. A factor of safety (of at least 2) is needed for low frequency solutions. In all the meshes it was ensured that these criteria were met.

Geometric models were constructed in CADFEKO. The model information was saved in \*.cfx file and the workspace layout in \*.cfs file. The program workflow required running PREFEKO which validated the model, and processed the \*.cfm and \*.pre files and generated a \*.fek file. The \*.fek file was fed into the solution kernel, FEKO. POSTFEKO was used to view the FEKO output, which was stored as a binary file \*.bof. The results were also stored in \*.out file. POSTFEKO results can be exported via an \*.ascii or \*.txt file to a different graphical application like MS Excel or MATLAB.

### 3.2 MATRIX AND WELLBORE FORMULATION

The wellbore was designed as a cylinder of length much larger than the transmitter-receiver spacing. When designing a cased-hole model a concentric cylinder of 7 inch external diameter and 6.184 inch internal diameter was created, as shown in Figure 3.2. Since steel casing is most commonly encountered, the dielectric properties of steel in medium properties were modeled. The conductivity of steel was taken as  $1 \times 10^7$  S/m and the relative magnetic permeability as 17.834. Both dielectric and magnetic modeling of the casing was assumed to be frequency independent.

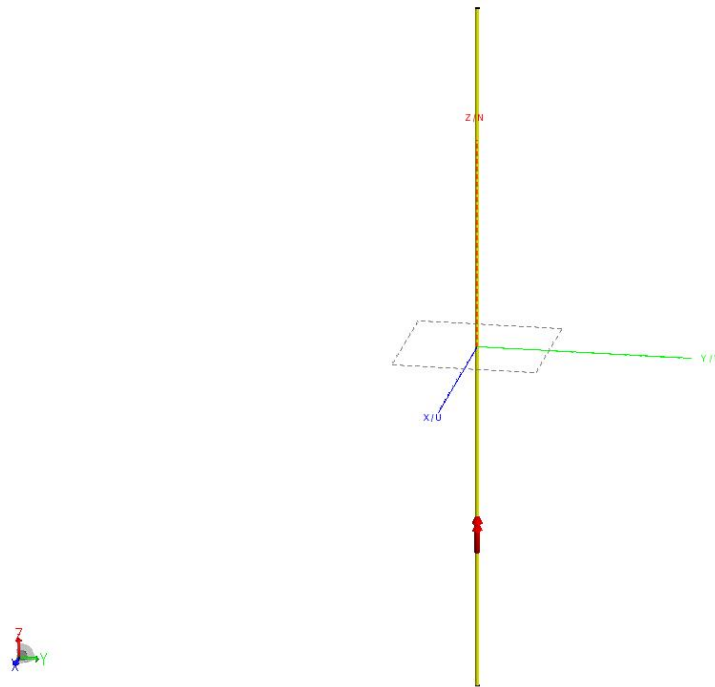


Figure 3.2: Model of wellbore with casing in CAFEKO

Similarly, we modeled the rock matrix as cylinders around the wellbore. There can be multiple cylinders stacked on top of each other as shown in Figure 3.3, to denote formations of different resistivity. Also it can be multiple concentric cylinders, as shown in Figure 3.4, to model mud-cake, invaded zone and virgin zone of the formation, or

changes in formation resistivity in radial direction owing to other reasons. Depending on the application of the problem, we can choose either approach or a combination of both. Also, while meshing we ensured that the mesh elements are finer near the source and the borehole, and they become coarser as we move further away.

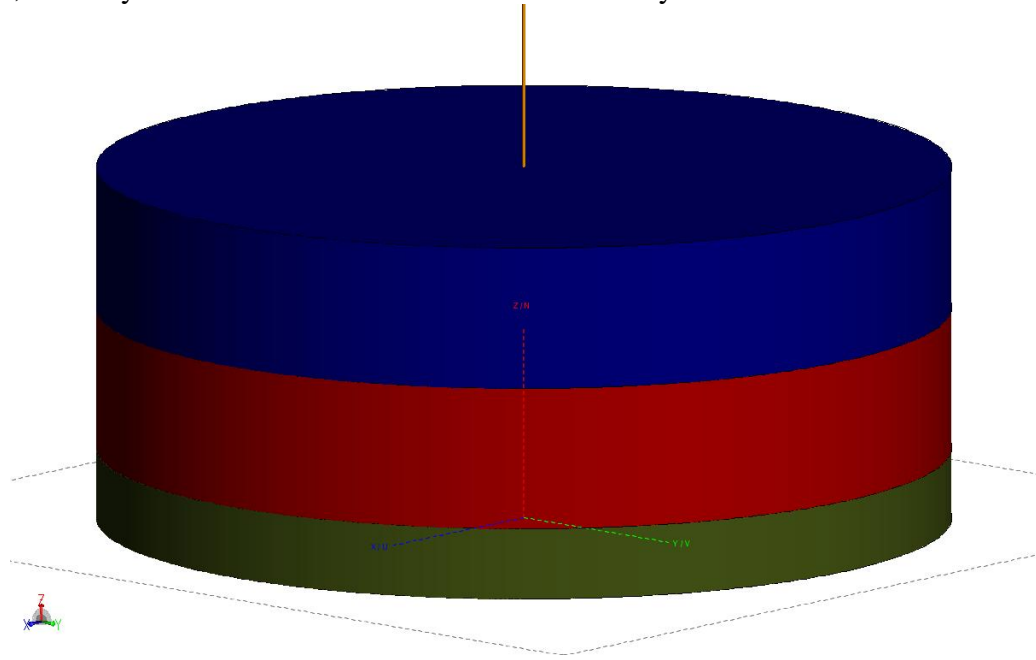


Figure 3.3: Rock formation modeled in FEKO as a series of beds of different resistivity (shown in different colors) with wellbore at the center.

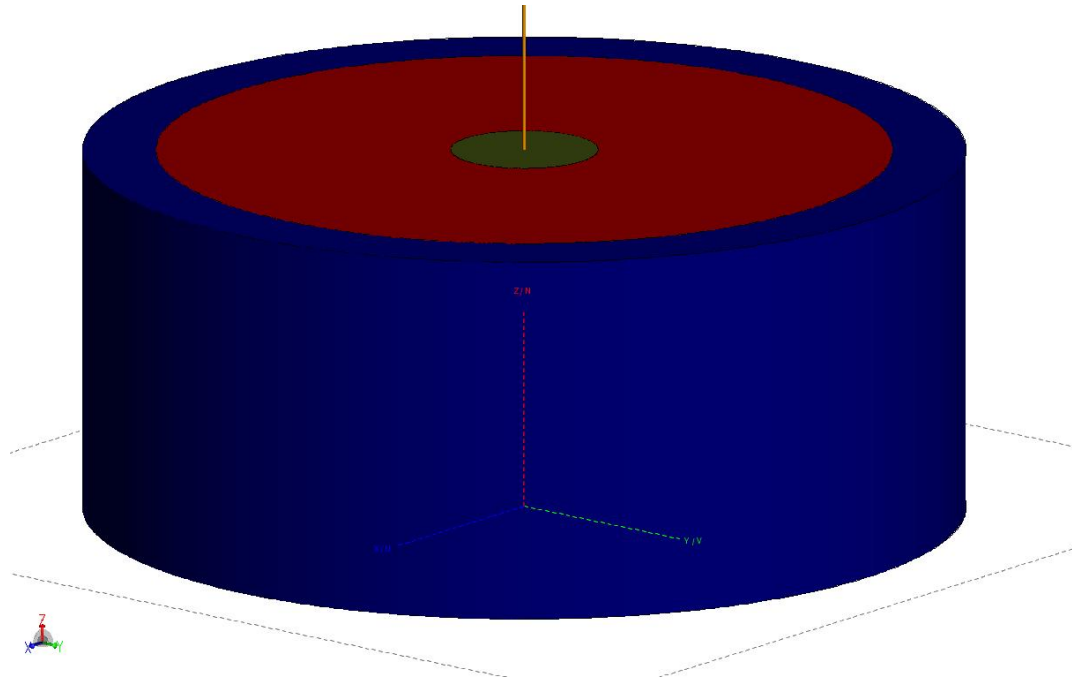
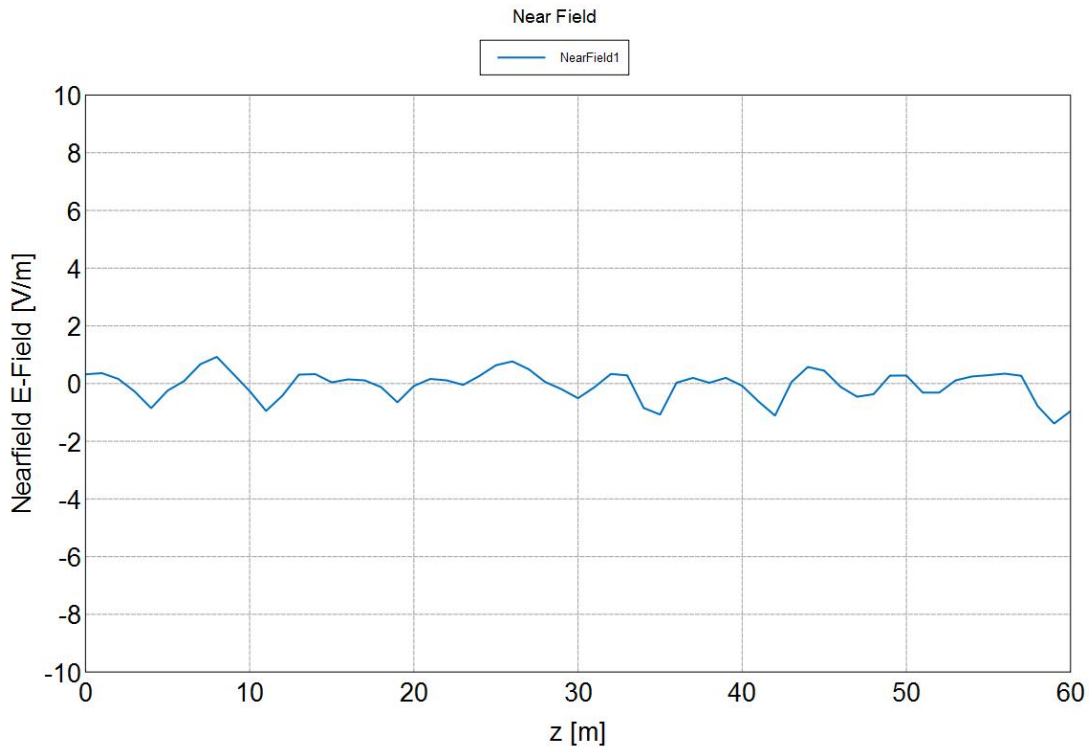


Figure 3.4: Rock formation modeled as concentric cylinders of different resistivity with wellbore at the center.

It is also possible to model dipping beds of a fixed angle using CADFEKO. However, for the purpose of the simulations that were run for this work, that approach was not used. The dielectric and magnetic modeling was kept as frequency independent. The formation was assumed to be non-magnetic, and the conductivity value changed based on the formation resistivity.

The magnetic and electric field response for the homogenous case, i.e. formation matrix without any fracture was tested for consistency of signal, as shown in Figure 3.5. It is evident that no signal was received without the presence of a fracture. It was concluded that there was no signal without a fracture. In other words, if any signal was obtained it must be due to a dielectric anomaly in the rock matrix. In this case, that anomaly was the modeled hydraulic fracture.



Real Z E-Field [Frequency = 100 Hz; rho = 0 m; phi = 0 deg] - disc\_100hz\_homogeneous case

Figure 3.5: Response at the receiver (Real electric field in Z direction) for homogenous case, i.e. only rock matrix and no hydraulic fracture

### 3.3 FRACTURE FORMULATION

After the wellbore and the rock matrix modeling, we focused on the modeling of the hydraulic fractures. The hydraulic fracture was designed as a cylinder also, embedded in a rock matrix of defined dielectric properties. First, orthogonal fracture in horizontal well was modeled. Then, oriented fracture in horizontal well was modeled. Likewise, in vertical wells, orthogonal and non-orthogonal fractures were modeled.

For orthogonal fractures in horizontal well, the hydraulic fracture was modeled as a disk embedded in the rock matrix. Typically, the width of the fractures was kept at 0.2 inch to 6 inches, while the half-length (radius) of the fracture was varied from 15 m to

100 m. A typical fracture model is shown in Figure 3.6. A schematic of the wellbore and moving tool with fracture in horizontal well is shown in Figure 3.7.

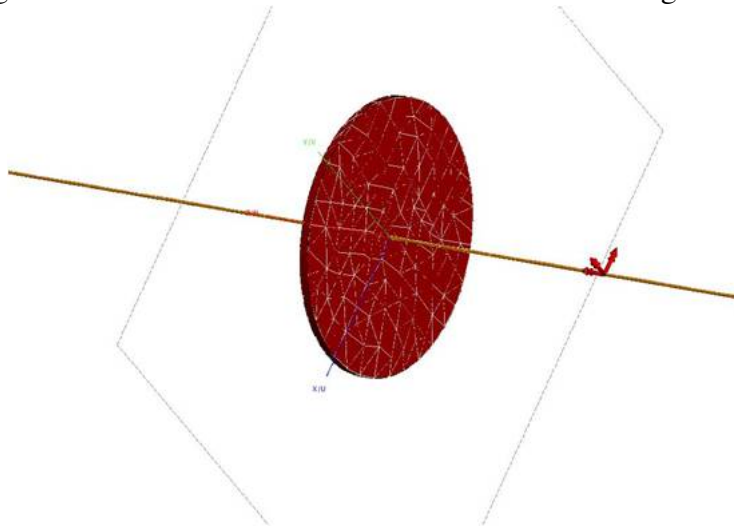


Figure 3.6: Model of orthogonal fracture in a horizontal wellbore

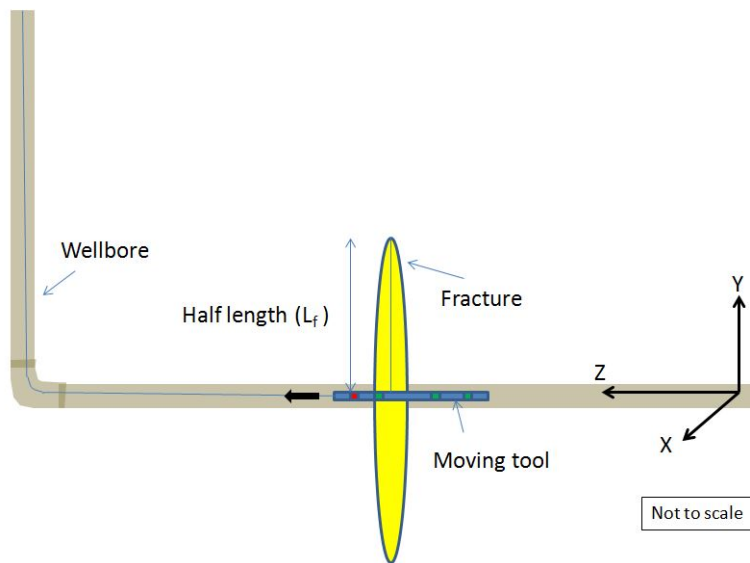


Figure 3.7: Schematic diagram of a moving tool across a orthogonal fracture in a horizontal wellbore

For non-orthogonal fractures in horizontal well, we rotated the cylindrical fracture in the well bore, as shown in Figure 3.8. In this model, both the angle of rotation and the half-length of the fracture could be changed.

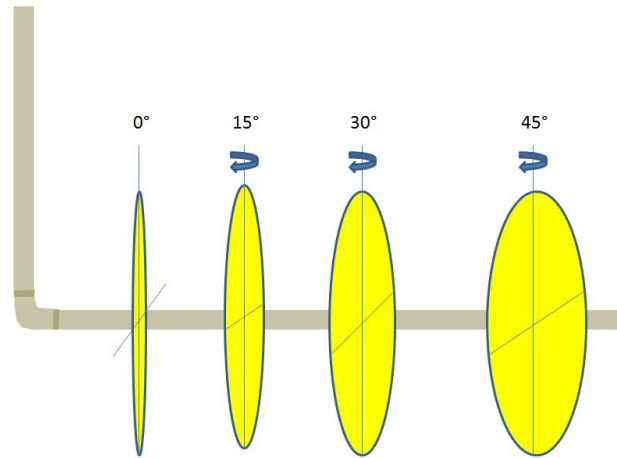


Figure 3.8: Schematic model of non-orthogonal fracture in a horizontal wellbore

For orthogonal fractures in vertical well, we modeled a bi-wing fracture, as shown in Figure 3.9. In this model, both the height and the half-length of the fracture could be changed. In most of the cases, the width was kept fixed. The bi-wing fracture could be rotated over the axis of the borehole, too.

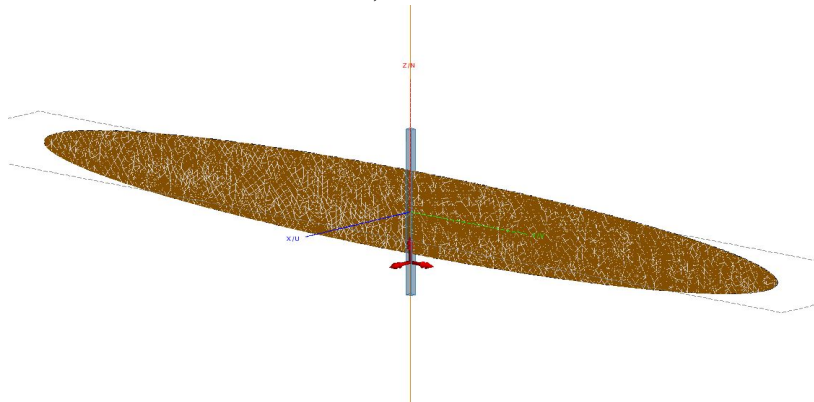


Figure 3.9: Model of bi-wing fracture in a vertical wellbore

In all the above cases, the electric and magnetic properties of the fracture can change. It could change according to the magnetic and electric properties of the chosen proppant. For simple cases, uniform distribution of proppant in the fracture was assumed. However, cases simulating non-uniform distribution of proppant were also considered, and mentioned, where applicable.

### **3.4 TOOL FORMULATION**

Alumbaugh and Wilt (2002) mention that, for most practical purposes, the source of an induction tool can be approximated to a vertical magnetic dipole (VMD). Most commercial electromagnetic (EM) induction tools are modeled in this fashion. However, older generation tools had only a unidirectional source (VMD) and measured the vertical field in offsets of 2m or less. Alumbaugh and Wilt (2002), in the same paper, recognize the need for both horizontal and vertical magnetic dipole sources to account for complexities of a heterogeneous reservoir, such as fractures and faults. In our study, we use tri-directional magnetic dipole source, which are orthogonal to each other. In this way we can study the far field effects of fracture geometry in much greater detail.

The proposed tool has one tri-directional transmitter and three tri-directional receivers at spacing of 6 ft (1.828 m), 30ft (9.144 m) and 60 ft (18.28 m) from the transmitter source. In all the plots, the hydraulic fracture was assumed to intersect the borehole at 0 ft. The short spacing response was computed keeping the transmitter-receiver spacing at 6 ft while the source moved from -60 ft to + 60 ft in the Z-direction (axis of the borehole). The electromagnetic signal was expected to react to the intersecting hydraulic fracture at 0 ft. Similarly, for the medium spacing coil, the transmitter receiver spacing was kept at 30 ft and for the long spacing coil, it was kept at 60 ft.

In all individual receivers, a bucking coil was also incorporated. Bucking coil cancels out the direct coupling between the transmitter and receiver. This is simulated by following the cancellation scheme illustrated by Salies (2012), where we removed the homogenous response from the signal obtained using the fracture. Bucking coil is a necessary feature of all commercial electromagnetic (EM) induction tools.

In some of the simulated cases, the signal obtained in the receiver could be quite noisy. The highest signal is typically obtained when the tool crosses the hydraulic fracture. So, on the graphs that show the receiver response to other parameters, such as fracture half length, conductivity of proppant, azimuth or dip, this signal is plotted. For receiver signal, the real and imaginary part of the electrical field in X, Y and Z direction was noted. Also the magnitude and phase of these signal was stored in the POSTFEKO session for further analysis. Similarly, the tri-directional real and imaginary components of the magnetic field were also plotted, and the magnitude and phase were stored in FEKO.

The strength of the magnetic dipoles was taken as 1000 A-m. Commercial electromagnetic tools use sources of the same order of magnitude. Given the cross-sectional area of the proposed tool and advances in mechanical engineering, fabricating such a source does not appear daunting. However, exact specifications of coil turns and material of magnetic core material are not discussed in this thesis.

### **3.5 MESHING OF GRIDS**

All the simulations run were checked for repeatability and accuracy of the results. To get a consistent result in FEKO, the edge length of the tetrahedral grid should be less than a fifth of the wavelength inside the dielectric medium. Also, on the interface, a finer

mesh with edge length less than one-tenth of the wavelength was needed. Obviously, a finer mesh would be computationally more expensive while a coarser mesh would give faster but a less precise solution. As stated previously, the Method of Moments (MOM) with a Volume Equivalence Principle (VEP) as the solution method was used. VEP is one implementation of MOM that is more accurate at low frequencies. It discretizes the volumes into tetrahedrons, which is computationally more expensive, but gives a more accurate solution. Low-frequency stabilization and double precision were incorporated in the numerical solution. Mesh refinement was used to create a finer mesh near the tri-directional sources, where the field gradient was higher. Since MOM forms a dense matrix as part of its solution process, the traditional implementation of MOM scaled poorly both in memory and runtime requirements. Therefore, the simulation implemented an Adaptive Cross-Approximation (ACA) method.

Figure 3.10 shows the imaginary component of the magnetic field in Z-direction of the same fracture geometry for different mesh size. The maximum mesh size was 1.75 m, 2 m, 2.5 m and 3.0 m, respectively at the coarsest point. It was observed that although there was a presence of some mesh noise over the rock matrix, the response near the fracture (where the spike is) was same for mesh sizes of 1.5 m, 2.0 m and 2.5 m. For mesh size of 3.0 m the response was different. Therefore, in most of the models, the mesh size of 1.5 m at the coarsest point was maintained. However, for very large fracture sizes (over 60 m half-length) a mesh size of 2.5 m at the coarsest point was employed. Whenever a different mesh size was used, it was noted appropriately.

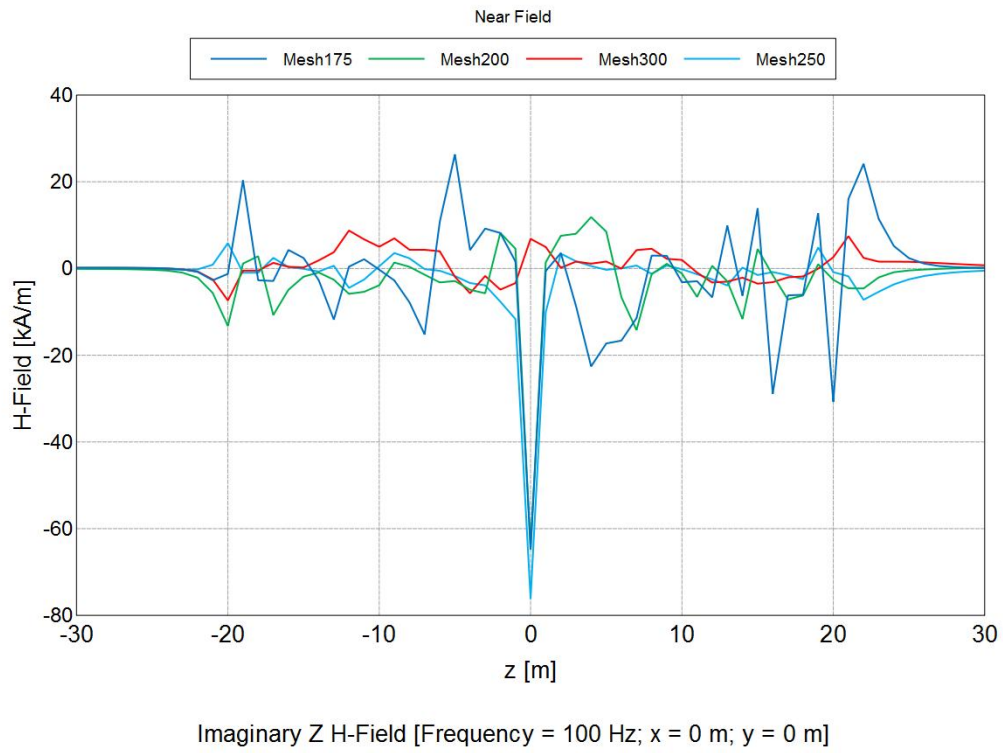


Figure 3.10: Imaginary component of magnetic field for a given fracture geometry for mesh sizes of 1.5 m (150 cm) , 2 m (200 cm) , 2.5 m (250 cm) and 3 m (300 cm) at the coarsest point.

## **Chapter 4: Fracture Diagnosis using Low Frequency Electromagnetic Induction (LFEI)**

The preceding chapters have discussed how wellbore, rock matrix, tool and hydraulic fractures were modeled, and the rationale behind it. In this chapter, various simulations that were run are shown. Simplest cases are presented first, then more complex ones. The simulations primarily investigate the forward problem of the electrical and magnetic signals received for a given fracture geometry. The electric and magnetic field response was noted for each depth as the tool moved up the borehole. The hydraulic fracture was assumed to be at 0 ft in all the simulation, while the tool moved from -30 m to 30 m in depth. Specifically, we noted the real and imaginary part of the electric field and the magnetic field, at each location of the borehole as the tool moves past it.

Various parameters of fracture geometry such as fracture half-length, azimuth, and dip, were changed one at a time. The electric and magnetic field response to the changes of these parameters were also plotted. In some cases, like an orthogonal fracture, trends were very apparent. In more complex cases, the inverse solutions could be more non-unique. The plots here are presented and analyzed for each of these cases. Table 4.1 shows the rubric of the simulations done. The rows contain the different cases that were run, while the columns define the parameters that were changed for each case. For Cased Hole (CH) cases, the casing is assumed to be of steel.

The representative plots are presented in this chapter. The detailed magnetic and electric field responses are given in the Appendices.

			Half- Length	Angle	Resistivity of proppant	Resistivity of Matrix
Vertical Well	Vertical fractures	OH	<input type="checkbox"/>	N/A	<input type="checkbox"/>	<input type="checkbox"/>
		CH	<input type="checkbox"/>	N/A	<input type="checkbox"/>	<input type="checkbox"/>
	Oriented fractures	OH	<input type="checkbox"/>	<input type="checkbox"/>	<input type="checkbox"/>	<input type="checkbox"/>
		CH	<input type="checkbox"/>	<input type="checkbox"/>	<input type="checkbox"/>	<input type="checkbox"/>
Horizontal Well	Orthogonal fractures	OH	<input type="checkbox"/>	N/A	<input type="checkbox"/>	<input type="checkbox"/>
		CH	<input type="checkbox"/>	N/A	<input type="checkbox"/>	<input type="checkbox"/>
	Non- orthogonal fractures	OH	<input type="checkbox"/>	<input type="checkbox"/>	<input type="checkbox"/>	<input type="checkbox"/>
		CH	<input type="checkbox"/>	<input type="checkbox"/>	<input type="checkbox"/>	<input type="checkbox"/>

Table 4.1: Simulations run on FEKO for different cases, and the parameters that are changed in each.

For each of the cases, unless otherwise mentioned, the parameters are defaulted according to Table 4.2.

<b>Parameter</b>	<b>Value</b>
Matrix resistivity	5 Ohm-m
Proppant resistivity	0.001 Ohm-m
Steel casing resistivity	$7 \times 10^{-7}$ Ohm-m
Strength of VMD	1000 A-m
Frequency of operation	100 Hz
Relative magnetic permeability of steel	17.834
Relative magnetic permeability of proppant	1

Table 4.2: Parameters used in simulations of tool, rock, proppant, and steel casing.

#### 4.1 HORIZONTAL WELL

A horizontal well was modeled using the method described in Chapter 3. A disk shaped fracture was designed across the horizontal wellbore, as shown in Figure 4.1. Dielectric properties of rock matrix and hydraulic fracture are mentioned in Table 4.2. In this set of simulations, we first simulated cases of orthogonal fractures and then non-orthogonal fractures, for both open-hole and cased-hole cases. In cased-hole cases, the parameter of casing is as shown in Table 4.2. A schematic of the moving tool across the fracture is shown in Figure 4.2. The tool is shown moving up the borehole (the Z axis) with the transmitter (shown in red in the schematic) travelling upward first followed by the short spacing receiver, then the medium spacing receiver and finally the long spacing

receiver. All the subsequent plots indicate the fields as seen by the respective receiver when they pass a particular depth.

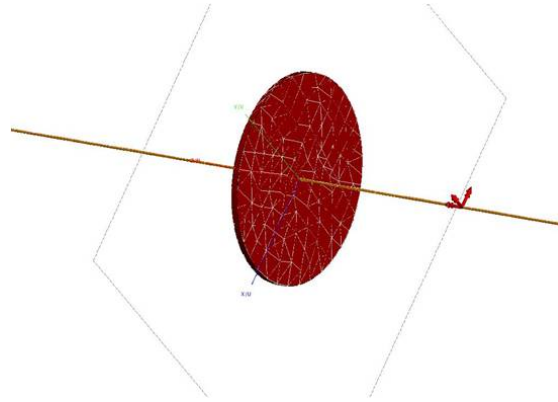


Figure 4.1: Model of orthogonal fracture in a horizontal wellbore

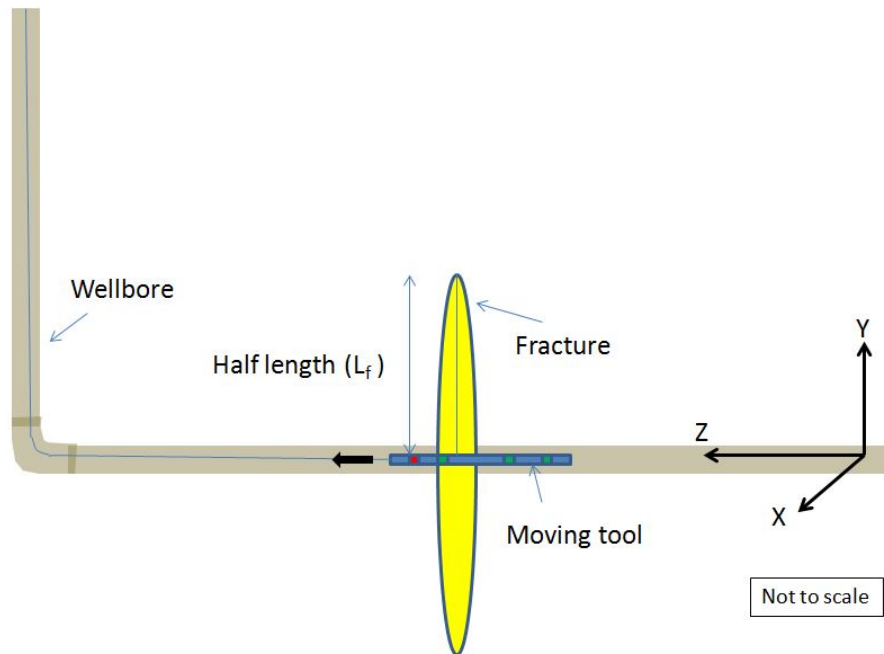


Figure 4.2: Schematic diagram of a moving tool across a orthogonal fracture in a horizontal wellbore

#### 4.1.1 Orthogonal Fractures in Open Hole

A disc shaped orthogonal fracture intersected the wellbore perpendicularly in the following set of simulations. The hydraulic fracture had a width of 0.1 m and had the dielectric and magnetic properties, as discussed in the previous chapter. The half-length of this disc was taken as 5m, and the receiver signal at the far spacing receiver (60 ft) was noted. The real and imaginary part of the electric and magnetic field were plotted. Similarly, we simulated a disc-shaped fracture of 10 m and noted the electric and magnetic field. The magnitude of electric field and imaginary part of the magnetic field increases, in this case. In an attempt to find trends in the electric and magnetic fields generated by the orthogonal fractures, we simulated fractures of half-length 15m, 20m, 25m, 30m, 35m, 40m, 45 m, 60m and 75m. Figure 4.3 shows the magnitude of the received electric field signal for 30m, 50m, 75m and 100m fractures. The key observations are: (a) a monotonic increase in received signal as fracture half-length increases and (b) the short and medium spacing receiver signals disintegrate for higher fracture half-lengths, whereas the long spacing signal remains consistent. Therefore the subsequent analysis, we only plot the long spacing receiver signals. Figure 4.4 shows the magnitude of the electric field in the long-spacing receiver as the tool moves along the borehole (z axis). Different curves represent different fracture half-lengths. In this representation also, it is easy to discern an increasing trend of received signal with increasing fracture half length. Figure 4.5 shows is a similar plot, where the imaginary part of the magnetic field at the long spacing receiver is plotted instead of electric field. We observe similar trends here also.

Therefore, from the results, magnitude of electric field and the imaginary part of the magnetic field appears to be key signals for determining the half-length of hydraulic fractures.

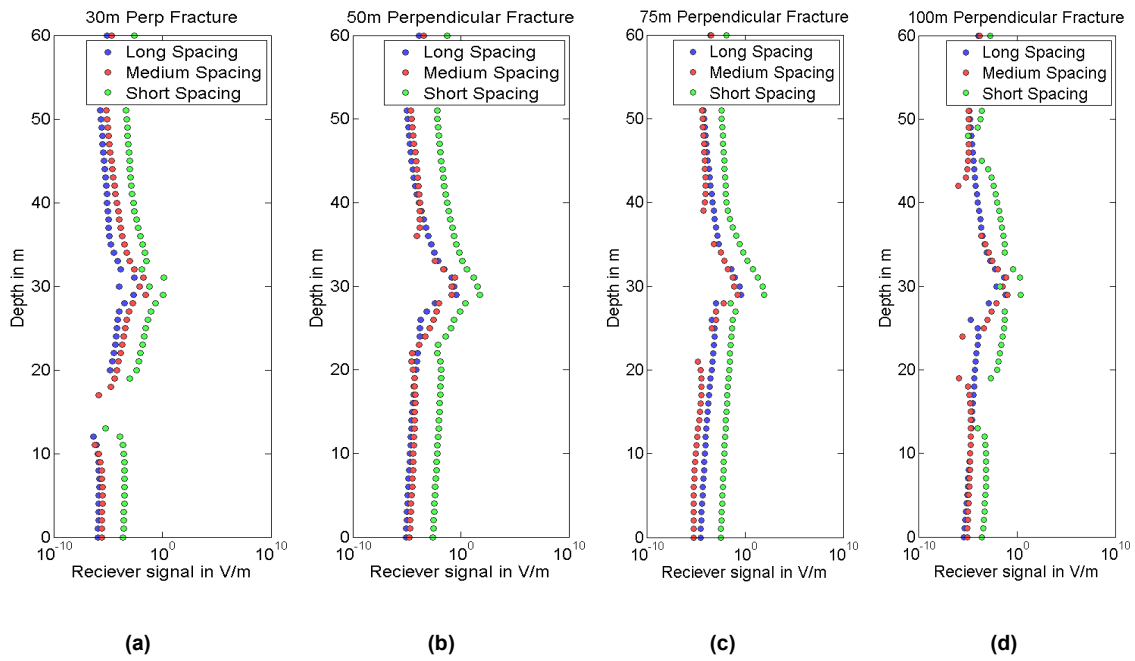


Figure 4.3: Receiver response to fractures placed orthogonal to a horizontal well for different fracture lengths (a) 30m, (b) 50m, (c) 75m and (d) 100m.

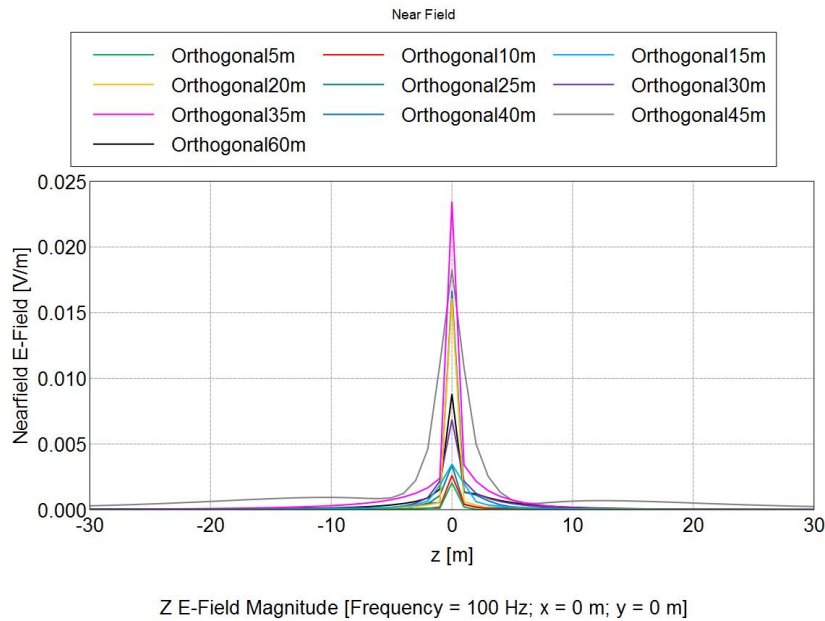


Figure 4.4: Comparison of the magnitude of the electric fields in the Z direction for different fracture half lengths.

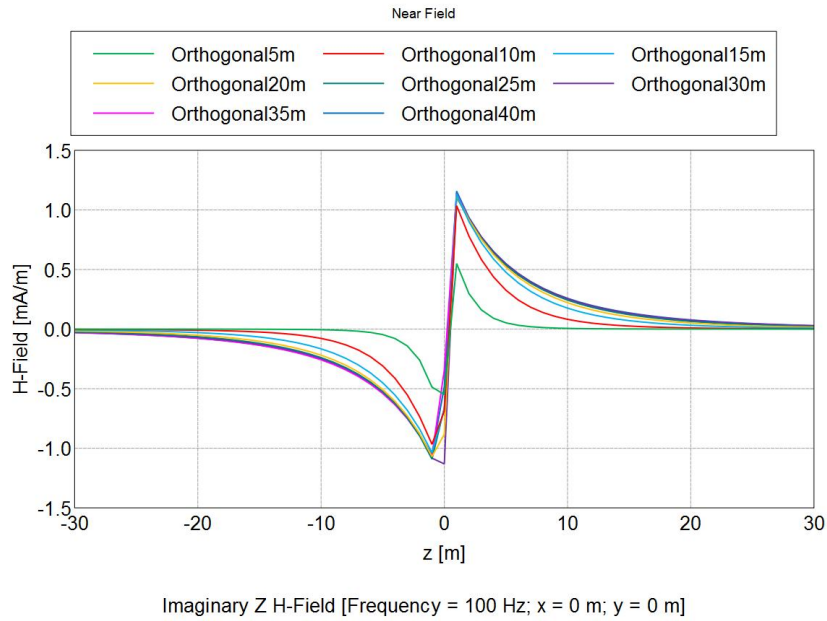


Figure 4.5: Comparison of the imaginary component of the magnetic fields in the Z direction for different fracture half lengths.

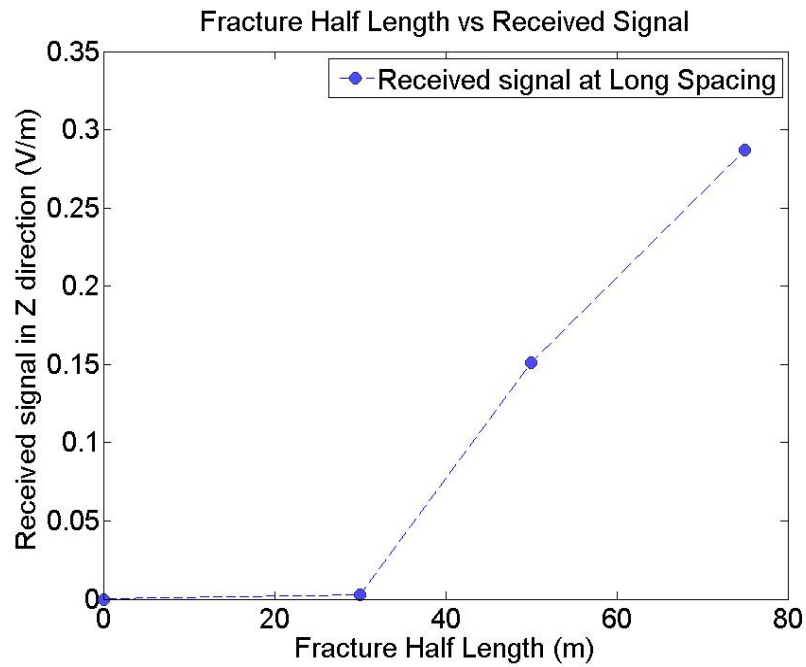


Figure 4.6: Comparison of the magnitude of electric field in the Z direction for different fracture half lengths.

The receiver response was normalized for the transmitter strength (1000 Am). Figure 4.7 shows the electric field in the Z-direction for different fracture lengths normalized for transmitter strength.

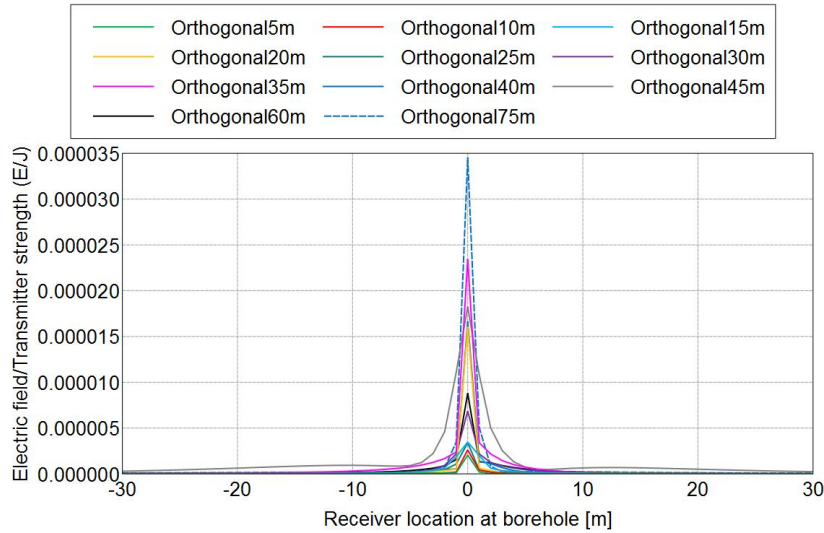


Figure 4.7: Electric Field in Z direction at long spacing receiver divided by the transmitter strength against long spacing receiver location in the borehole for different fracture half-length.

#### 4.1.2 Orthogonal Fracture in Cased Hole

We repeated the set of simulations of orthogonal fractures in open-hole for cased-hole cases. Fracture half-lengths of 5 m, 10 m, 15 m, 20 m, 25 m, 30 m, 35 m, 40 m and 45 m were simulated with a mesh size of 1.5 m at the coarsest point. 60 m fractures were modeled with a maximum mesh size of 2.5 m. We observed the signal to be noisier but also heavily attenuated due to the presence of casing. The results of electric field magnitude at the far receiver as the tool moves up the borehole are presented in Figure 4.8. Figure 4.9 gives a plot of fracture half-length against received signal.

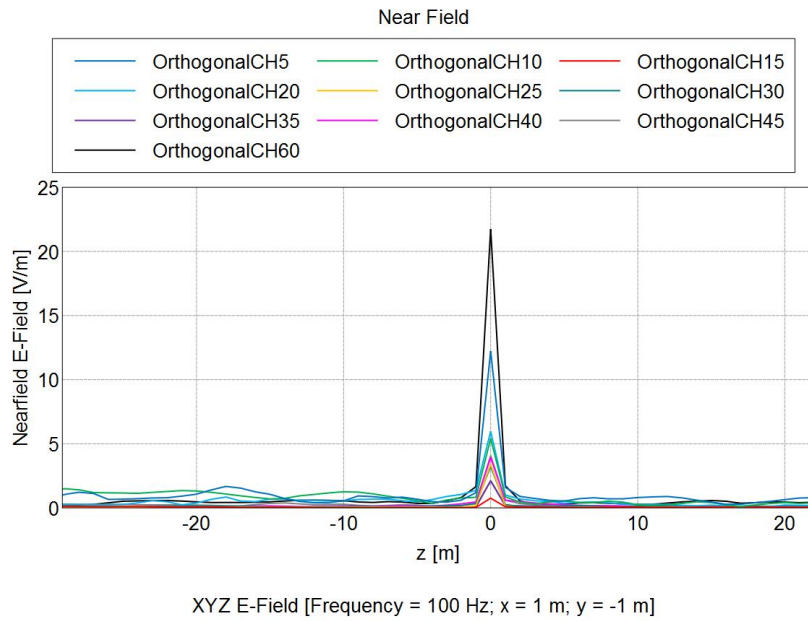


Figure 4.8: Comparison of Electric field magnitudes of different fracture lengths in a horizontal wellbore through steel casing.

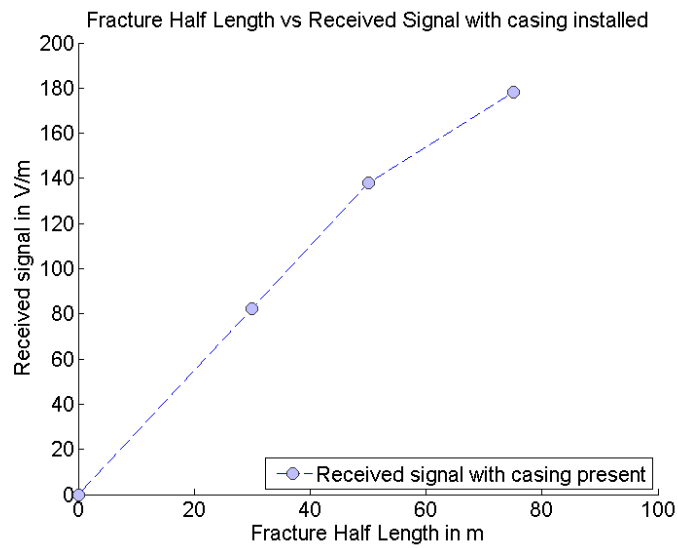


Figure 4.9: Receiver response to orthogonal fracture in a horizontal well with casing installed.

The receiver response was normalized for the transmitter strength (1000 Am). Figure 4.10 shows the electric field in the Z-direction for different fracture lengths normalized for transmitter strength.

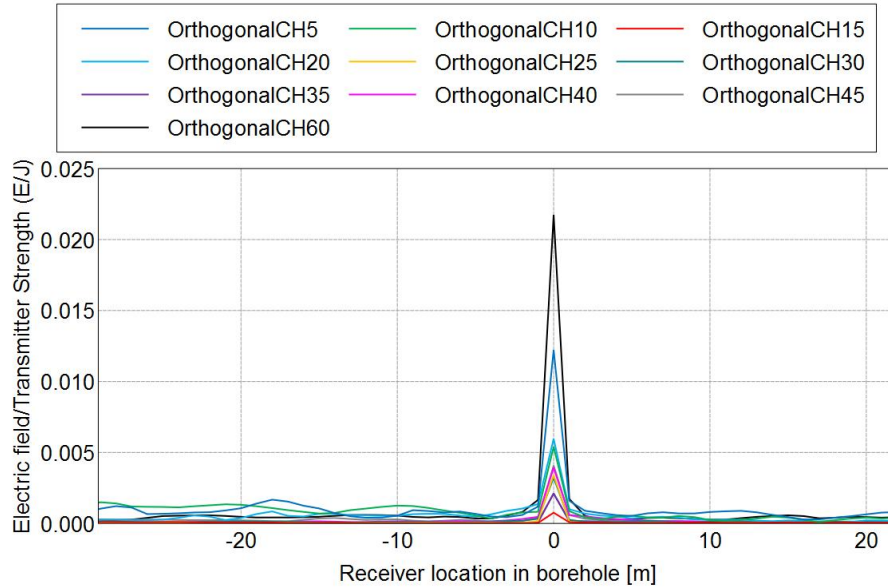


Figure 4.10: Electric Field in Z direction at long spacing receiver divided by the transmitter strength against long spacing receiver location in the borehole for different fracture half-length (in cased-hole).

### 4.1.3 Oriented Fractures

After exhausting the cases of orthogonal fractures in a horizontal wellbore, we moved on to oriented fractures. The fractures were oriented by 4 distinct angles, as shown in Figure 4.11. In the case of oriented fractures we analyzed the X-, Y-, and Z-signal individually and investigate for trends for changing angles (15 degrees, 30 degrees and 45 degrees). The real and imaginary parts of the electric and magnetic fields in X-, Y- and Z-direction were noted. Also the half-length was varied (15m, 30m, 45m and 60 m) for

each of these angles and the receiver signals were analyzed for trends. It is obvious that for each angle, the received signal followed a distinct curve for increasing half-length, as shown in Figure 4.12. Therefore, this gave confidence in the fact that the non-uniqueness of the reading won't be irresolvable through inversion. The short and the medium spacing receivers would also help in reducing the non-uniqueness. Independent measurements from other technology, like microseismic and knowledge of the geology of the reservoir (the direction of principal stresses) can help in solving this issue.

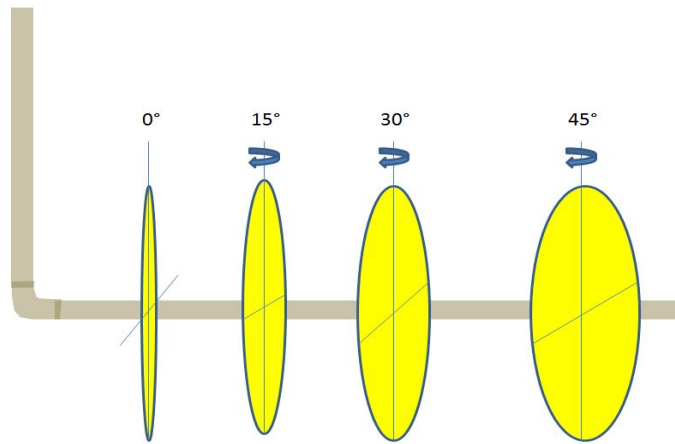


Figure 4.11: Schematic representation of hydraulic fractures rotated in the borehole by angles of 15, 30 and 45 degrees respectively

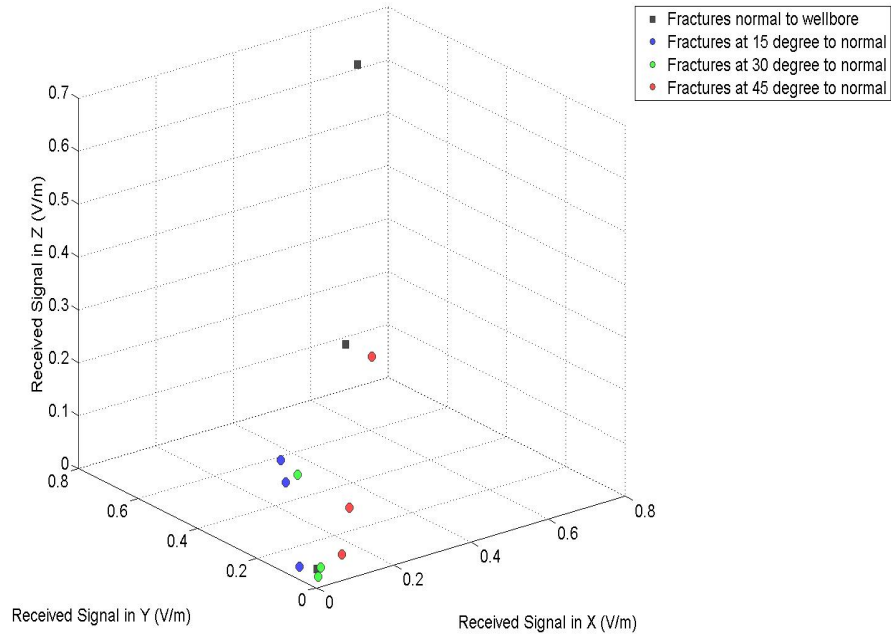


Figure 4.12: Received Electric field signal in X-, Y- and Z- direction for changing fracture half-length and fracture angles

#### 4.1.4 Non-uniform distribution of proppant

At present no fracture diagnostic method can detect proppant distribution in fractures. Proppant banking is frequently encountered in most horizontal, and sometimes in vertical completions. Since electrically conductive proppants are used in this method of fracture diagnostics, the received signal is a direct measure of where the proppant is. Therefore, it is only logical to think that location of the proppant can be deduced from the measured electric and magnetic field signal. We devised a simple model to test this hypothesis. We changed the height of the proppant bank in five different cases, as shown in Figure 4.13. Also, in a different set of simulation the resistivity of the fracturing fluid was also changed. To detect if the electric and magnetic field responded to changes in the height of the proppant bank, we modeled 5 other configurations, as shown in Figure

4.14. We compared the readings of the 5 different configurations and plotted our findings in Figure 4.15. It is evident that the Electric field in X-direction responded to the different height of the proppant bank. Figure 4.16 shows the changes in the Electric field signal in X-direction with a change in resistivity of the fracturing fluid. These set of simulations indicate that it is possible to detect proppant banking (or proppant distribution, in general) using this technique.

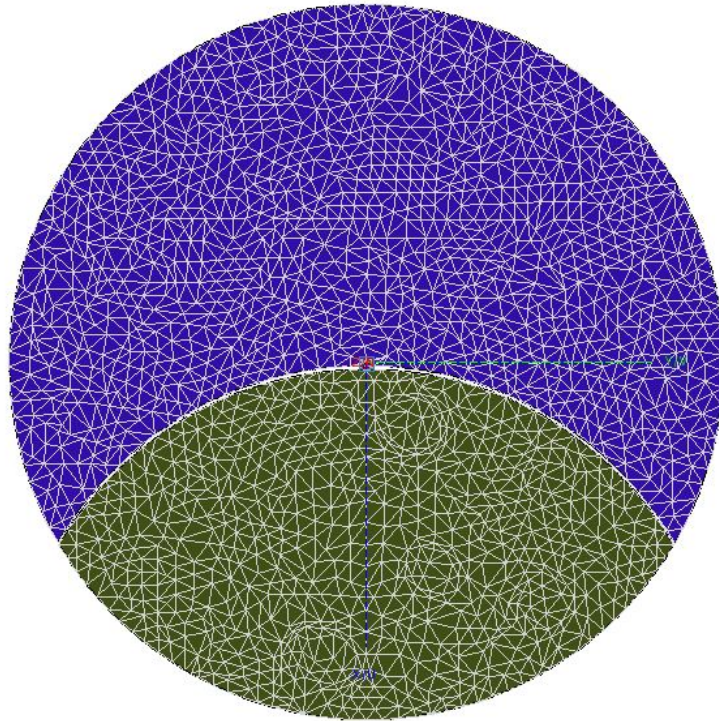


Figure 4.13: Orthogonal fracture in horizontal wellbore filled with proppant (in green) and water (in blue). The wellbore is across the plane of the paper (Z-axis) and the fracture half length is 50m.

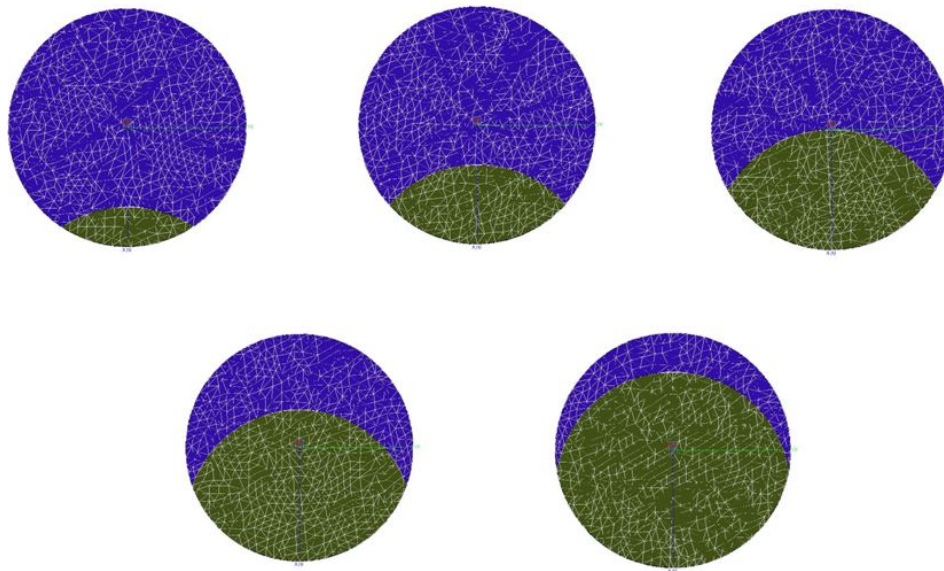


Figure 4.14: Different heights of proppant bank(in green), from 5m, 15m, 25m, 35m and 45m, respectively.

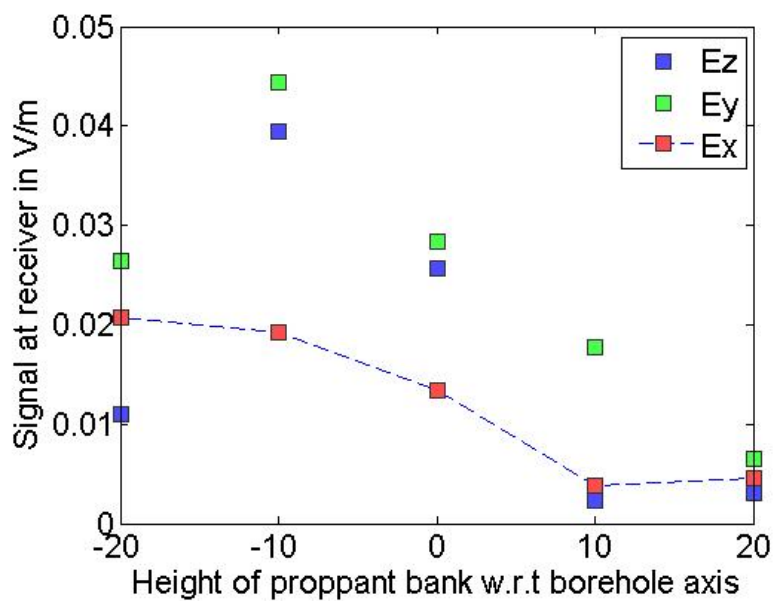


Figure 4.15: Magnitude of Electric Field Signal in X-, Y- and Z- direction showing the variation of Electric field in X-direction with changing height of proppant bank

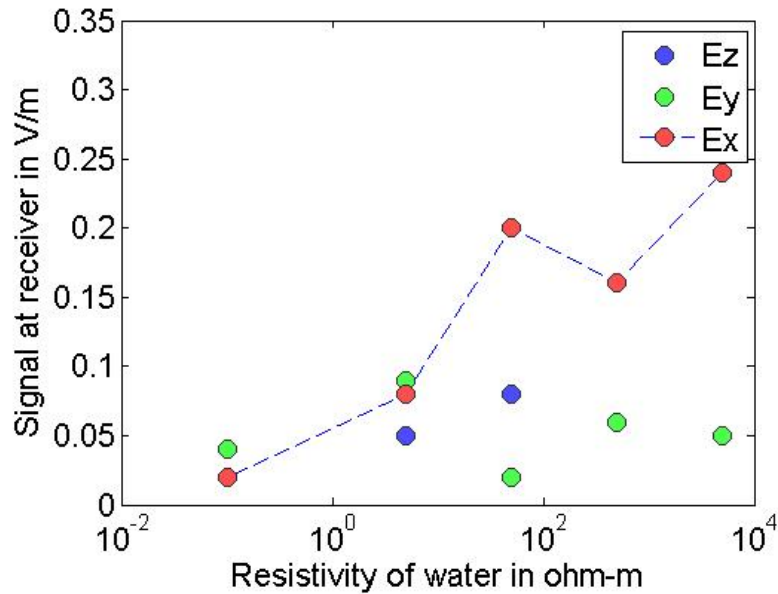


Figure 4.16: Magnitude of Electric Field signal in X-,Y- and Z- direction showing changes in Electric Field signal in X direction with changes in resistivity of fracturing fluid.

#### 4.1.5 Non Symmetrical Fractures

In most real world scenarios, hydraulic fractures are not created perfectly symmetrically across the borehole. This is caused by differences in rock properties in either side of the borehole. To model this situation, we modified the orthogonal fracture in horizontal well to have ellipsoidal fractures of different sizes on either side of the borehole, as shown in Figure 4.17. To observe the differences in received signal we started with a wing size of 5m which is kept fixed, while we increased the length of the other wing from 10m to 30m in increments of 5m. We plotted the imaginary component of the magnetic field signals in Y-and Z-direction. The imaginary component of the magnetic field in the Z-direction remained more or less constant, whereas the signal in Y-direction responded to changes in the size of the wings, as shown in Figure 4.18 and Figure 4.19.

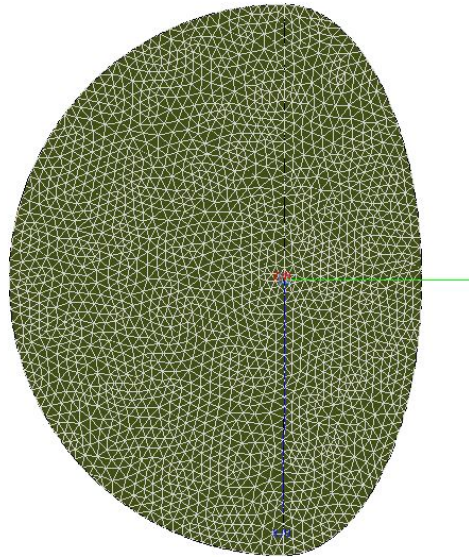


Figure 4.17: Non-symmetrical orthogonal fracture in a horizontal wellbore (cutting across the plane of the paper). The wing on the left side is 60m while the one of the right is 30m.

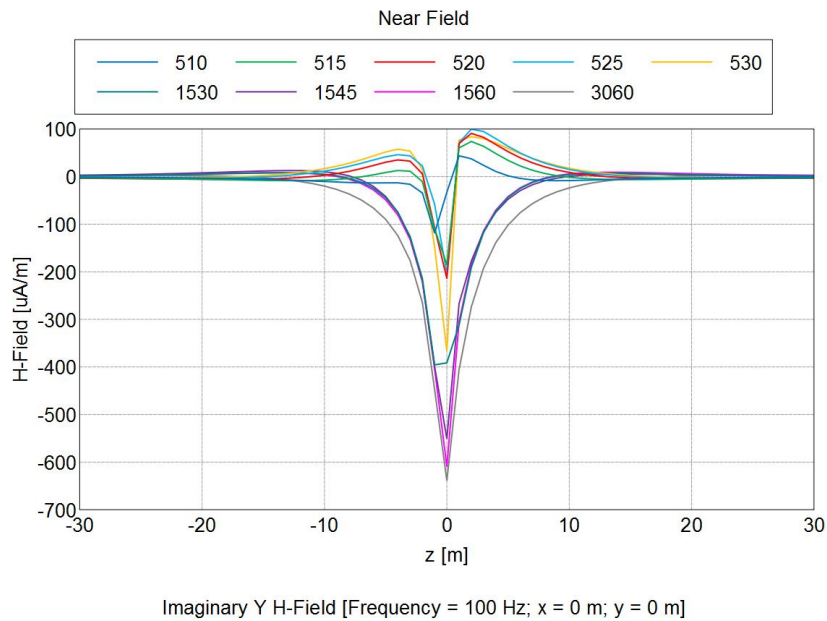


Figure 4.18: Comparison of Imaginary component of Magnetic field in Y-direction for different configurations

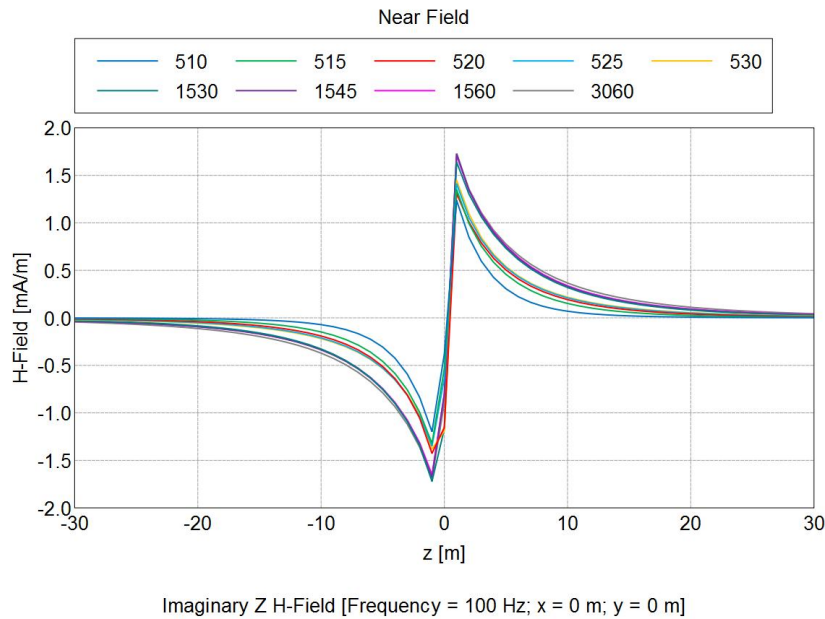


Figure 4.19: Comparison of Imaginary component of Magnetic field in Z-direction for different configurations

## 4.2 VERTICAL WELL

A vertical wellbore was designed with a wellbore of inner diameter of 7 inch. A vertical fracture intersected the vertical wellbore, as shown in Figure 4.20. The fracture was ellipsoidal and bi-wing. The width of the fracture was 0.1 m for all the case, and the height was also fixed at 20 m. Since far field effects of the propped length of the hydraulic fractures were a concern, the height was fixed and the half-length of the fracture was varied. In a separate case, both the half-length and the height are kept fixed, and the fracture was rotated across the wellbore by 4 distinct angles. The final study in vertical wellbore case involved changing the height of the fractures, while keeping the azimuth and half-length of the fracture constant. In all the above cases, the receiver response at the near, medium and far spacing receivers were analyzed for the various components of magnetic and electric field.

### 4.2.1 Orthogonal fractures in Open Hole

A hydraulic fracture of 5m half-length, 0.1 m width and 15 m height was modeled following the method outlined in Chapter 3. The dielectric and magnetic properties of the fracture, rock matrix, and wellbore as seen, are also outlined in the same chapter. The fracture was bi-wing and oriented orthogonally to the wellbore as shown in Figure 4.20. The long spacing response for real part of electric field in Z direction was analyzed as in the previous cases.

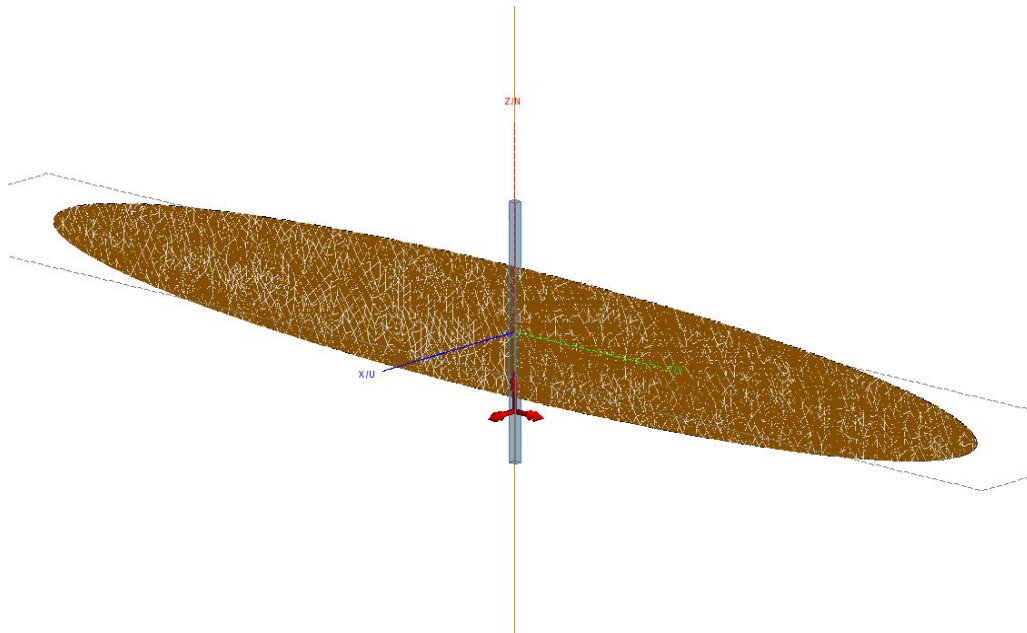


Figure 4.20: Model of bi-wing fracture in a vertical wellbore

Keeping the other parameters same, we varied the half-length to 10m. From the above cases it can be observed that the imaginary part of the magnetic field is more for 10 m than 5m. Further, the real component of the electric field also shows an increase with the half-length. In order to verify if there indeed is a correlation between these two quantities and the half-length of the fractures, fracture half-length of 15 m, 20 m, 25 m,

30 m, 35 m, 40 m and 45 m was simulated. The real and imaginary components of the electric and magnetic field are presented in the Appendix.

From the previous simulation, it was realized that there is indeed a trend of increasing imaginary magnetic field in Z direction, and increasing real electric field in Z direction with increasing fracture half-length. In order to find the limits of this trend, we also simulated 75m and 100m fractures. It was observed that at 100 m, the signal starts disintegrating and that the incremental increase in signal is very minimal.

Figure 4.21 shows the increase in magnitude of the Electric Field signal across the fracture for different fracture length.

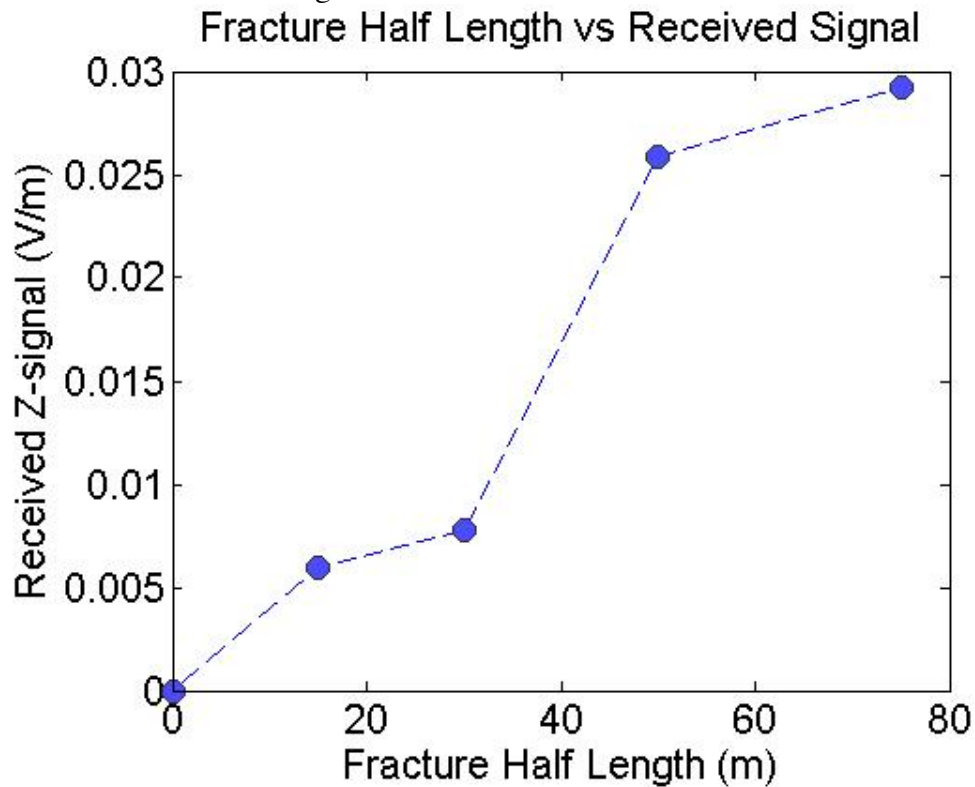


Figure 4.21: Magnitude of received Electric field signal in the Z direction for different fracture length.

### **4.2.2 Orthogonal Fracture in Cased Hole**

The above set of simulation was repeated for a cased hole. The casing was made of steel with dielectric properties defined in Chapter 3. We simulated fracture half-lengths of 5m to 45m in increments of 5m. In addition to that, we simulated hydraulic fractures of 60m, 75m and 100m. The results of these simulations, the respective magnetic and electric field in Z-direction were noted, as shown in the Appendix. When the readings of the cased-hole cases with the open-hole ones were compared, it was evident that the reading through casing was noisier but also heavily accentuated. Also, there was a very noisy signature in the near receiver antenna that rendered this measurement inaccurate. However, the magnetic field at the long spacing receiver gave a monotonically increasing signature. Therefore, if we have a robust inversion algorithm that can handle this noise, we can infer fracture dimensions through casing using this method. Current commercial induction tools can't be used through casing cases. However, these simulations point at the possibility of diagnosing fracture dimensions through casing. Pardo and Verdin (2013) also came to the same conclusion using their own independent code. They claimed that at these low frequencies (around 100Hz) the casing acted like a long electrode and accentuate the signal.

### **4.2.3 Oriented Fractures**

After exhausting the cases of orthogonal fractures, the bi-wing fracture azimuthally across the axis of the borehole was rotated. The fracture height and width were the same as the previous set of simulations. In this case, though, the fracture half-length was fixed at 30m. Now, the fracture was rotated by three angles: 15 degree, 30 degree and 45 degree respectively. Since it has been already established that the signal in the Z direction varies with fracture half-length, and the half-length was fixed, we did not

expect any change in the signal in Z-direction. Therefore, we monitored the X and Y signal as we changed the azimuthal angle. Electric field signal at the long spacing receiver in X and Y direction for an angle of 15 degrees was noted. The electric field signal for X and Y direction are also presented for 30 and 45 degrees were also calculated. On closer examination, we discovered a trend between the azimuthal angle and the ratio of the X and Y signal, as shown in figure 4. 22. Although the results were non-unique, it gave us a method for resolving changes in azimuthal angles in bi-wing fractures. Needless to say, other measurements like microseismic monitoring can be combined with this analysis to give a less uncertain solution that either method alone can.

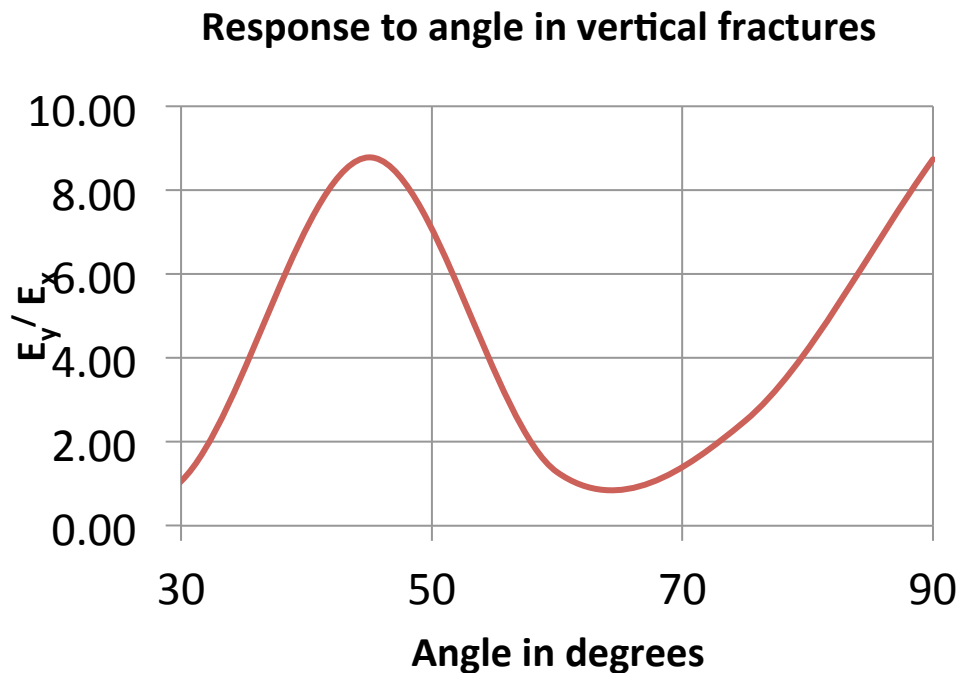


Figure 4.22: Ratio of the magnitude of the Electric Field signal in Y direction and X direction for different azimuthal angles of bi-wing hydraulic fracture in vertical wellbore

## Chapter 5: Sensitivity Analysis

After running the simulations for the forward problem as documented in the previous chapter, it is necessary to find the limits under which the proposed LFEI tool would be functionally operational. It is important to isolate the critical factors that have a first order effect on tool response. For example, as discussed in Chapter 2, frequency has an immense impact on the response at the receiver. From the analytical solutions, a greater depth of signal penetration is expected at lower frequency. However, at the same time, due to the dispersive nature of earth as a dielectric media, more noise is introduced in the signal. So, in order to find the appropriate frequency of operation for this proposed tool, the receiver signal is monitored for six different frequencies, keeping all other factors constant. Another factor that has a first order effect on the tool response is the dielectric property of the material through which the electromagnetic waves propagate.

In our research, we have two different mediums to take into account. The first medium is the rock matrix. The conductivity and magnetic permeability can vary across the rock matrix in three different directions, giving rise to anisotropy. As discussed in Chapter 2, this can be addressed through a 3X3 conductivity tensor. However, for the simplicity in modeling and numerical calculations, as well as setting the minimum safe working limits of the tool, we assume an isotropic rock medium. The second dielectric medium is the fracture itself, which is propped by a conductive proppant. We constraint all other factors, as the resistivity of the rock matrix is varied to find the limits under which this tool would be operable. Most importantly, we desire to check if this tool would operate in the shale environments of United States where most hydraulic fracturing is done. Then, we change the resistivity and magnetic permeability of the proppant to observe how these properties affect the received signal.

Transmitter receiver spacing can also have a first order impact on the depth of penetration and quality of the received signal. More importantly, it will have a tremendous impact on the resolution of the signal received. This issue is addressed by changing the transmitter receiver spacing keeping all other factors constant. However, it should be kept in mind that there are various other practical considerations while choosing transmitter receiver spacing, as discussed in subsequent section.

We designed our base case for the sensitivity analysis as tabulated in Table 5.1. A simple orthogonal fracture in a horizontal well was chosen as the template, as shown in Figure 5.1. In each of the subsequent section, we varied one parameter at a time. Also, the mesh size was kept constant for all the simulations.

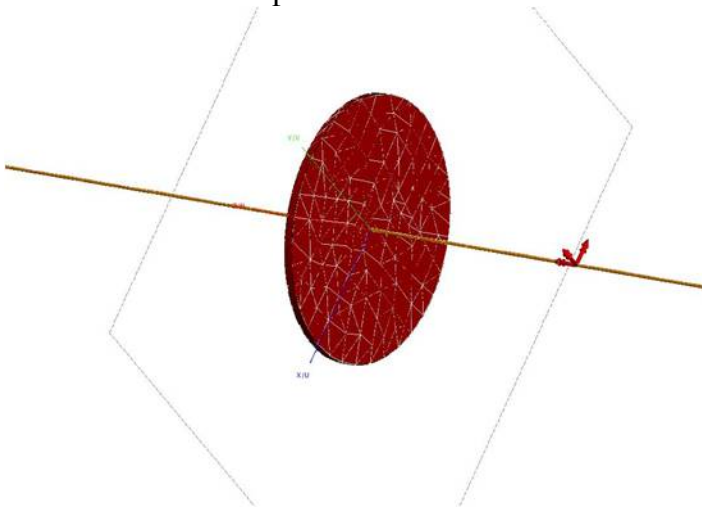


Figure 5.1: Model of orthogonal fracture in horizontal well, used for sensitivity analysis

Parameters	Value
Fracture half length	30 m
Conductivity of fracture	1000 S/m
Relative magnetic permeability of fracture	1
Conductivity of rock matrix	0.01 S/m
Transmitter receiver spacing	18.2 m

Table 5.1 Parameters used in sensitivity analysis

### 5.1 FREQUENCY OF OPERATION

Salies (2012) used the analytical solution of Huang and Boyle (2008) to calculate signal penetration as a function of frequency, given by the equation:

$$\varepsilon_M = \varepsilon \left( 1 - j \left( \frac{\sigma}{\omega \varepsilon} \right) \right)$$

$$\beta = \omega \sqrt{\mu \varepsilon_M}$$

$$D_p = -\frac{1}{\text{Im } g(\beta)}$$

where  $\varepsilon_M$  is the permittivity of the matrix,  $\varepsilon$  is the permittivity in free space,  $\sigma$  is the conductivity of the matrix,  $\omega$  is the frequency of operation,  $\mu$  is the magnetic permeability of the matrix, and  $D_p$  is the depth of penetration of the signal. Salies (2012) plotted the signal penetration for different frequencies for two distinct matrix conductivities of  $10^{-6}$  S/m and  $10^{-2}$  S/m and noted the response in each case, from the analytical solution. She concluded that for lower frequency we get a higher signal penetration. Also for a more resistive medium we get a deeper volume of investigation for the same frequency. We built on these two conclusions, and devised a systematic approach to determine the appropriate frequency of operation for the chosen transmitter

receiver spacing, and the operating environment. We choose conductivity and permeability parameters that are most common in the shale plays in mainland United States, as shown in Table 5.1. The proppant conductivity was also fixed at a known value. We kept the transmitter receiver spacing at 60 ft (18.2 m). The mesh size was limited at 1.5 m at the coarsest point. Figure 5.2 shows the response at the far spaced receiver of the tool for different frequencies from 10 Hz to 1 MHz.

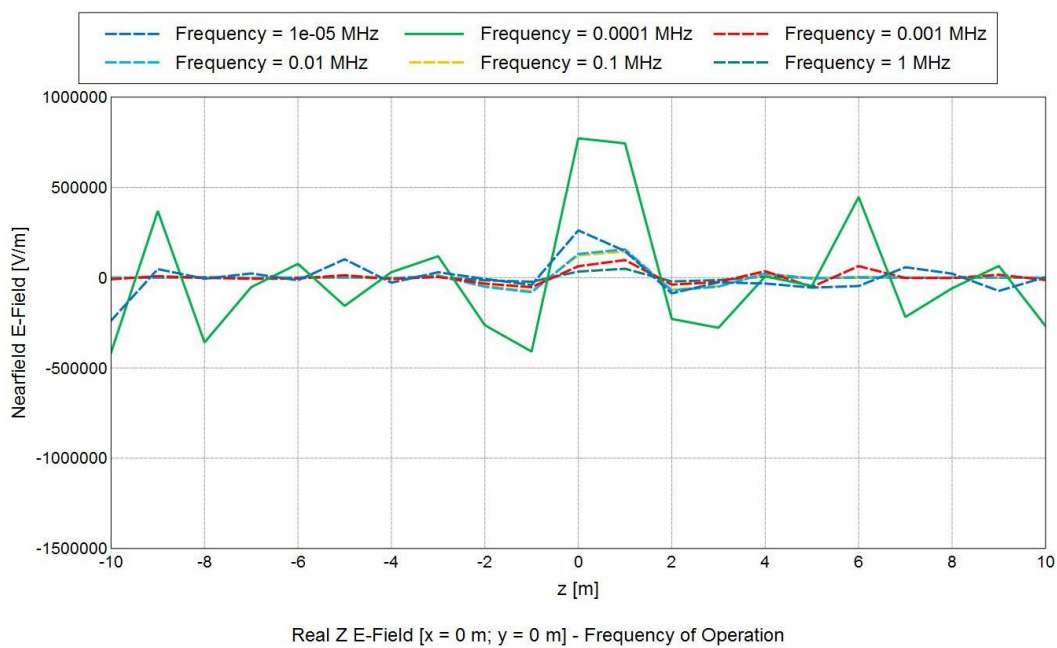


Figure 5.2: Sensitivity analysis for Frequency of Operation

We observed that for the six frequencies tested (from 10Hz to 1 MHz in logarithmic increments), 100 Hz offers the best response. Therefore, we concluded that 100 Hz is the best frequency for this application in these environments.

## 5.2 TRANSMITTER-RECEIVER SPACING

One of the final recommendations of the thesis of Salies (2012) was that the maximum transmitter receiver spacing need to be aimed for obtaining the maximum far field reading of the tool. However, there are many practical considerations while designing a tool. If the tool is expected to operate in a horizontal well, it must have a length and flexibility that allows it to pass through any dogleg to reach the lateral section. Also, conveyance of the tool downhole needs to be kept in mind. Since an induction tool would require a non-conductive housing, the alternate options of housing include fiberglass, as is used in most commercial induction tool. Wilt (2002) proposed an induction device that can be deployed through bridles. In horizontal wells, in the absence of a gravity drive, either coiled tubing or tractors can be used as conveyance. If we intend to run the tool with a tractor, it needs to be made as light as possible, so that it can be effectively pulled across the lateral. So, summing up, even though we can obtain the highest volume of investigation using high transmitter-receiver spacing, practical considerations of oilfield systems may limit the actual length of the tool. The prudent approach is, thus, to keep the transmitter-receiver spacing of the proposed tool comparable to current commercial tools in the market.

We simulated 8 different cases of transmitter-receiver spacing as shown in Fig. 13. We observed that (a) the 60 ft spacing has the highest response at the fracture but is also fairly noisy, and, (b) shorter spacing is most sensitive to the location of the fracture in the borehole. Therefore, we concluded that we need both the short and long spacing to find the location and the dimensions of the fracture. We can combine the readings for all three-receiver arrays and find the exact location of the fracture and dimensions using Phasor processing (Anderson, 2001). The shorter spacing is aimed for giving a better vertical resolution, while the long spacing is aimed at providing the maximum volume of

investigation in order to effectively determine the propped length of the fracture. A third receiver set, the medium spacing receiver, can provide redundancy of the reading, which can help in reducing the non-uniqueness of the inverse problem.

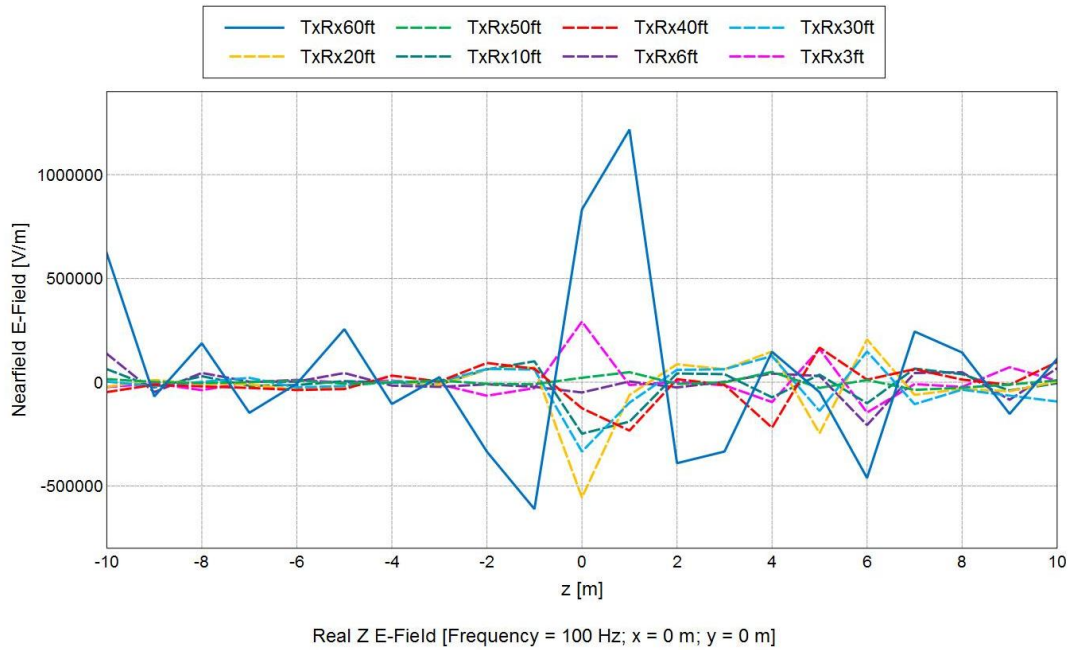


Figure 5.3: Sensitivity analysis for transmitter-receiver spacing

### 5.3 RESISTIVITY OF ROCK MATRIX

It is well established, both analytically and through practice, that the dielectric properties of the rock matrix have a tremendous impact on the response at the receivers. Equation 2.26 gives the voltage at the receiver of an induction tool. The resistivity of the medium is one of the most important factors. For the sake of simplicity we consider an isotropic medium.

Most organic shales in USA have resistivity between 1 ohm-m and 1000 ohm-m (Palacky 1987). Keeping all other parameters the same, we increased the resistivity of the matrix from 1 ohm-m to 500 ohm-m. Figure 5.5 shows that increasing the matrix

resistivity increases the received signal, implying that a higher matrix resistivity would also increase the depth of investigation. Also we can infer that the tool will not lose its functionality within this range of matrix resistivity.

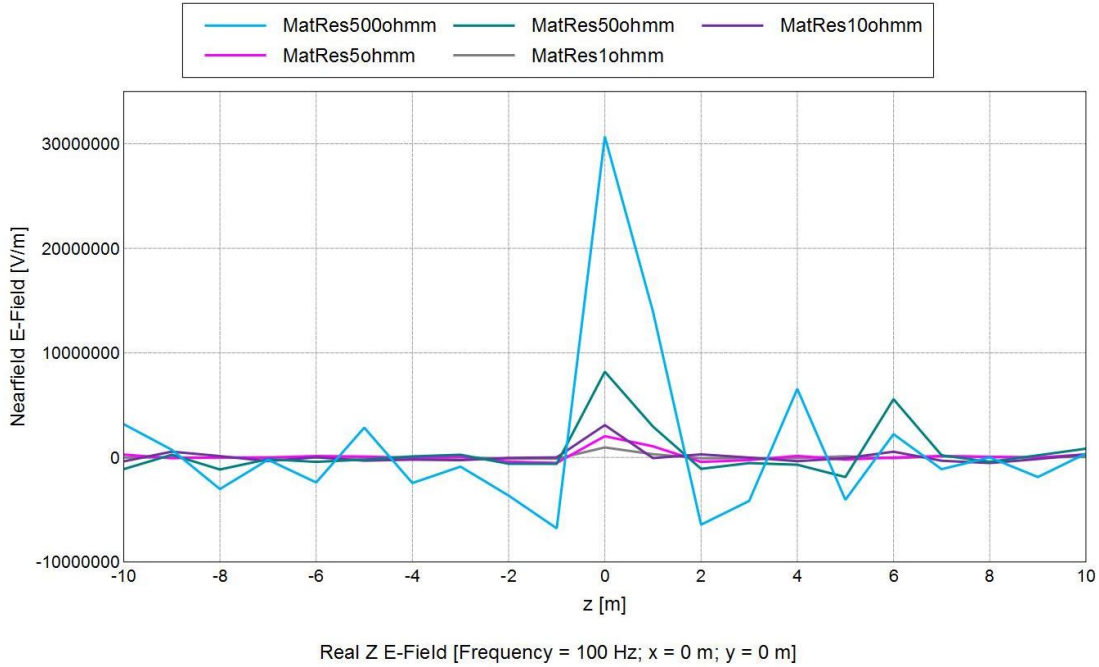


Figure 5.4: Sensitivity analysis for rock matrix resistivity.

#### 5.4 RESISTIVITY OF PROPPANT

Although we have several electrically conductive proppant available in the market, in this section we explore the possibility of finding the best proppant for our application. As demonstrated in Figure 5.6, we change the resistivity of the proppant and observe that the lower the resistivity of the proppant (higher the contrast of resistivity with matrix), the higher the received E-field signal. However, if we decrease the resistivity beyond 0.0001 ohm-m, the received signal is insufficient and cannot be recoded reliably. Moreover, increasing the resistivity beyond 1 ohm-m makes the overall signal so noisy that it is

difficult to detect the hydraulic fracture. Ideally the rock resistivity should be low enough to provide sufficient current in the rock matrix and high enough to get a sufficient resistivity contrast with the conductive proppant. Fortunately these criteria are satisfied over the entire range of resistivity for typical rocks.

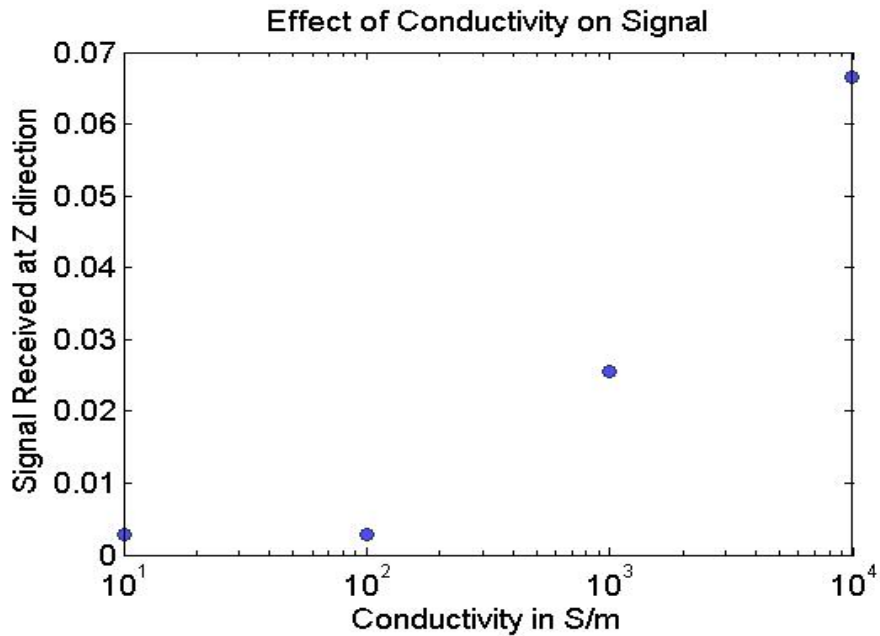


Figure 5.5: Sensitivity analysis for conductivity of proppant

### 5.5 MAGNETIC PERMEABILITY OF PROPPANT

In Maxwell's equations (Equation 2.1 and Equation 2.2), magnetic permeability has similar effect as dielectric permittivity (which is governed by conductivity at low frequencies). However magnetic permeability has a much lower variance for commonly found materials than electric conductivity. For example, steel has a relative magnetic permeability of 18, while vacuum is 1. On the other hand conductivity of commonly found materials varies over several orders of magnitude. Therefore, to obtain a sufficiently high magnetic permeability contrast with the rock matrix, special

ferromagnetic proppants need to be developed. Several research consortiums are also working on developing magnetic nanoparticles that can be used in fracturing fluids as a contrast agent. Figure 5.7 plots received signals for varying magnetic permeability of the proppant.

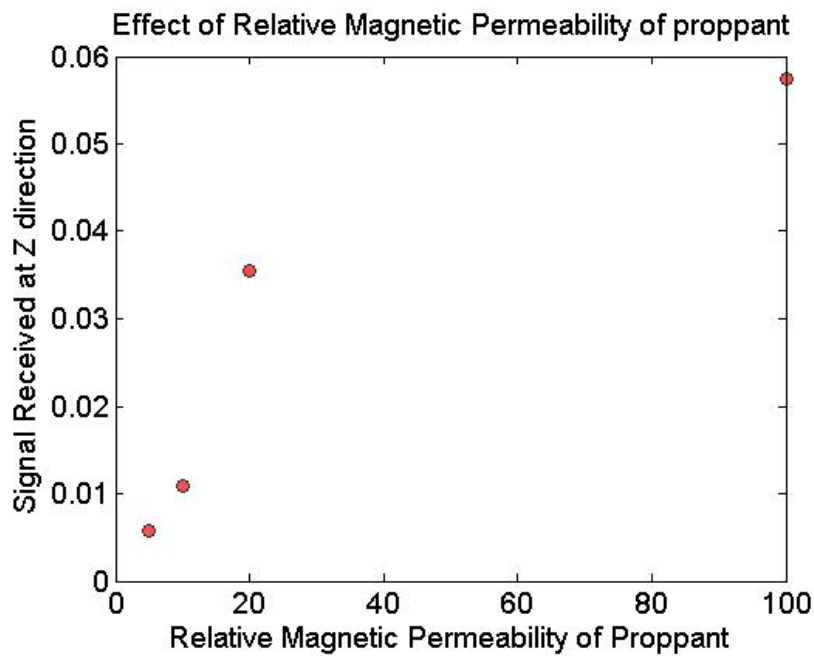


Figure 5.6 Sensitivity analysis for changing magnetic permeability of proppant

Summing up, increasing magnetic permeability will have similar impact as changing electrical conductivity. However, changing electrical conductivity of proppant is much easier than changing relative magnetic permeability over the same order of magnitude.

## Chapter 6: Conclusion

This thesis studied the feasibility of having an electromagnetic tool that is capable of measuring propped length, height and width of hydraulic fractures. In this study, we have used the principles of induction logging to devise a tool that appears to be capable of estimating fracture dimensions in controlled environments. It is too early to state that the tool is ready to be deployed in the commercial market. However, it is not a far-fetched idea to start building a prototype that can be used as a proof-of-concept in real geological environments. A lab scale prototype of this tool, however, could pose several concerns such as: (a) scaling up of electromagnetic properties is not linear, (b) finding an electrically noise free space of 200 m (100 m is the maximum half length of fracture in these simulations). It is therefore logical to attempt to build a logging tool prototype, using simple induction coils in a non-magnetic housing, that can be connected to a telemetry device and deployed through wireline cable. Once we get promising results for vertical wells, we can search for deployment options (Coiled tubing or wireline-tractor) in horizontal wells.

Nevertheless,, this study answers a few pertinent questions towards building the logging tool. The major findings are tabulated below:

1. The proposed method can estimate length, orientation and height of propped hydraulic fractures with propped length of up to 75m (250 ft) in both horizontal and vertical wells. With advances in amplifier technology, this limit can be further stretched beyond 75m.
2. In addition to fracture dimensions and orientation, this method has the potential to provide an estimate of vertical distribution of proppant.

3. We show how the use of three receivers with tri-directional antennas can be used to infer fracture dimensions in many commonly encountered fracture geometries.
4. The transmitter-receiver spacing of 60m helps us in getting a deep reading. However, we also need the shorter spacing to accurately map where the fracture intersects the wellbore. The medium spacing can provide redundancy to both the short and long spacing receivers. Also, the three receivers combined provide better resolution of the inverse problem. The tri-direction antennas are needed to ensure we can detect both the magnitude and direction of the resistive anomalies (in our problem, the orientation and half-length of hydraulic fractures).
5. Based on our simulations, 100 Hz appears to be the frequency most suitable for this application.
6. The proposed tool is tested in matrix resistivity of 1 ohm-m to 500 ohm-m, which is the range of resistivity of commonly occurring oil-bearing rocks. The technique appears to function better as the resistivity contrast of proppant and matrix increases.
7. The presence of casing increases the noise in the signal. However it also amplifies the signal, which is responsive to changes in fracture half-length. Therefore, a robust inversion algorithm that can handle the noise can be used to diagnose fracture through casing using this method.

Thus the work needed to design and implement this fracture diagnostic method is two-fold. First, we need to devise an inversion algorithm that can tackle this problem.

Although there are many inversion tools available for induction logging tools, some of them developed in-house by universities and others commercially, it needs to be understood that they all solve for resistive anomalies. In our problem, the resistivity of the proppant and the matrix is known, while we tried to find the dimensions of the hydraulic fracture. The most suitable approach appears to be devising an inversion algorithm that takes into account the forward simulations done in this study. Second, we need to develop a prototype tool that can be deployed in the field. A schematic diagram of the tool, as will be deployed in the field, is shown in Figure 6.1. Figure 6.2 gives the detail of the receiver array section with transmitter and receiver coil (each armed with its bucking coils). The design of individual receiver and transmitter is not mentioned here. But Patent no. 3,067,383 and Patent 3,329,889 can give valuable insights into the same. Also, the hardware used in XW-EMT tool can also be a starting point for the design.

The complete workflow of how this technology can be incorporated in the big picture is shown in Figure 6.3. From the base reservoir model, and existing well log, the resistivity and mechanical properties of the formation can be obtained. Using this information, a sensitivity analysis needs to be performed to ascertain if the given well is a good candidate for the proposed logging tool to be run. Once the tool is run, the field data will be inverted to obtain the exact fracture geometry. Other measurements, like flow and pressure data, as well as microseismic maps and cores, can help in reducing the non-uniqueness of the solution. Using multiple independent measurements will only enhance our confidence in our measurement. We can incorporate this is the updated reservoir model as shown in Figure 6.3 to obtain a better reservoir model. Also based on the diagnosis, we can infer if re-fracturing is needed, or if the stimulation job was good, and also how exactly does fracture dimensions impact production. All the information obtained from this tool will only enhance our understanding of our reservoirs.

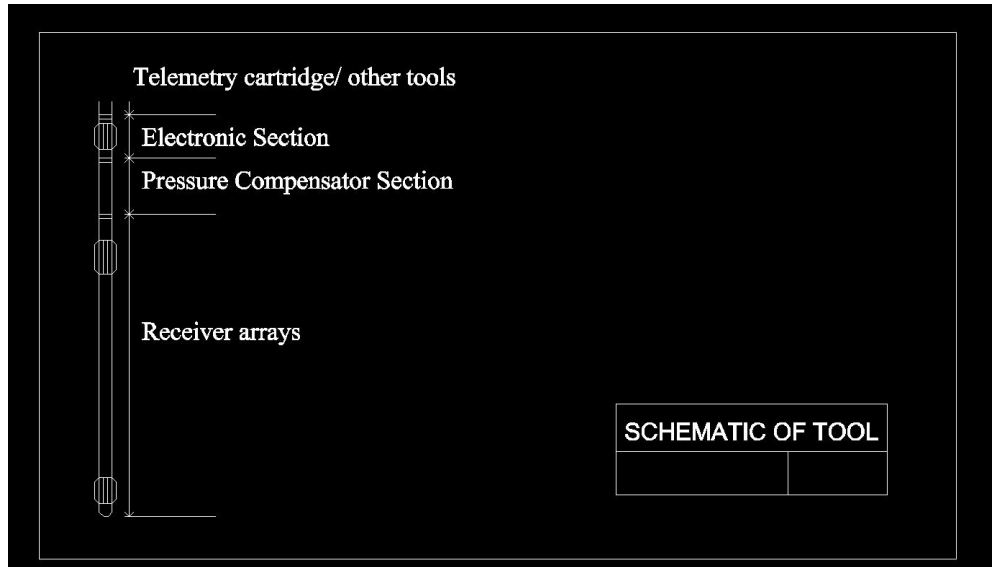


Figure 6.1: Schematic diagram of proposed tool with receiver arrays, pressure compensator section, electronic section.

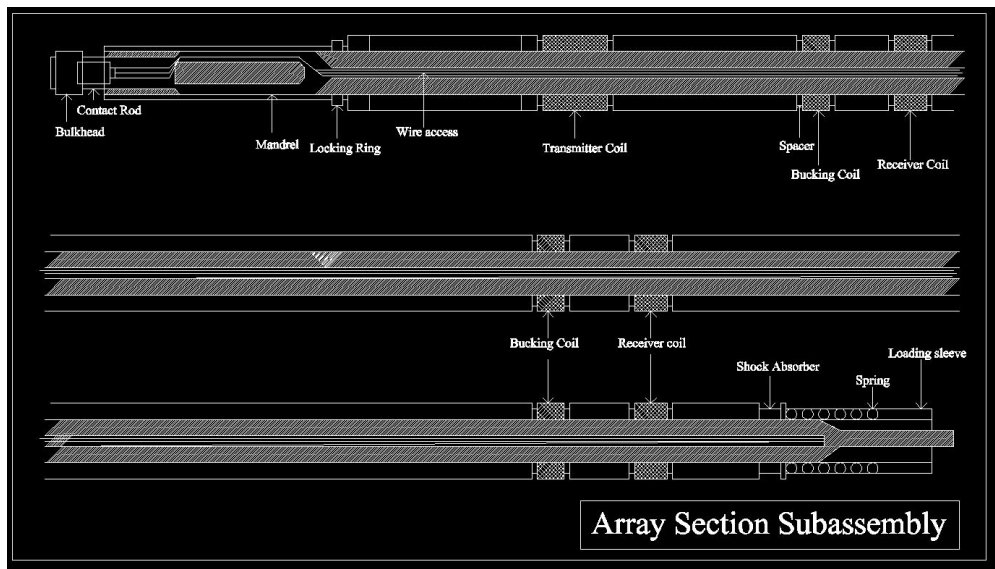


Figure 6.2: Array Section Subassembly showing transmitter and receiver coil, with bulkhead at the top and loading sleeve at bottom.

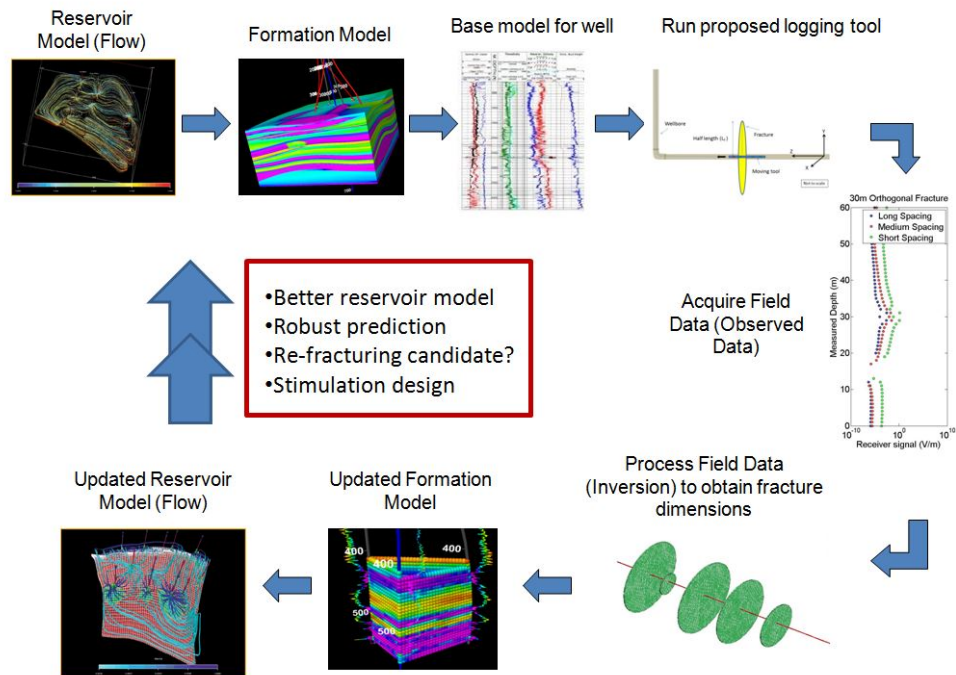


Figure 6.3: Workflow of LFEI technology

## Appendices

### A1. RAW ELECTRIC AND MAGNETIC FIELD RESPONSES FOR AN ORTHOGONAL FRACTURE IN VERTICAL WELL (OPEN HOLE COMPLETION)

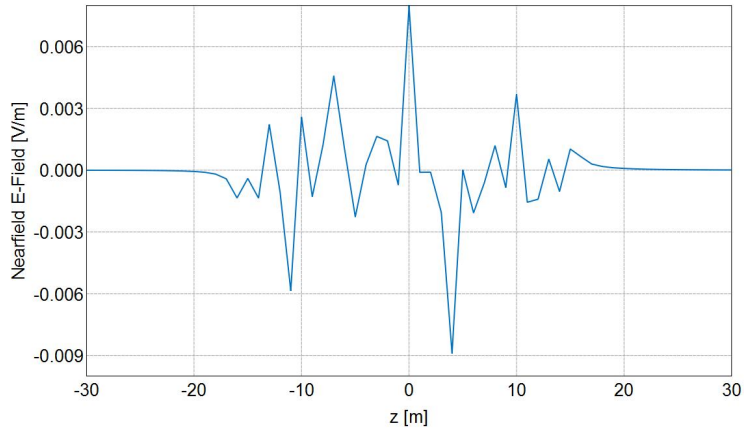


Figure A1.1: Real component of electric field in the Z-direction for a orthogonal fracture of half-length 5 m in a vertical wellbore

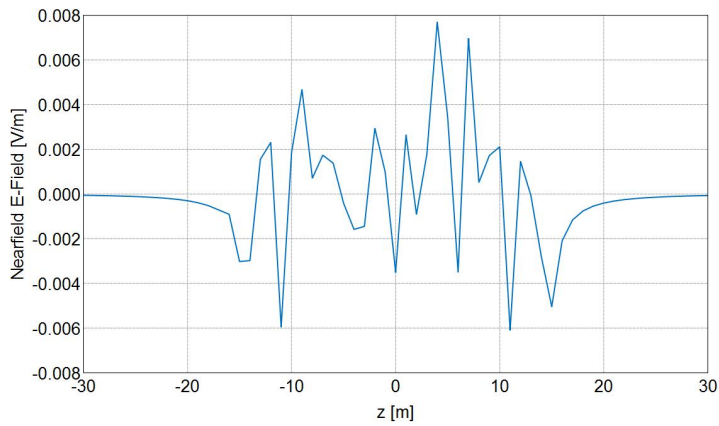
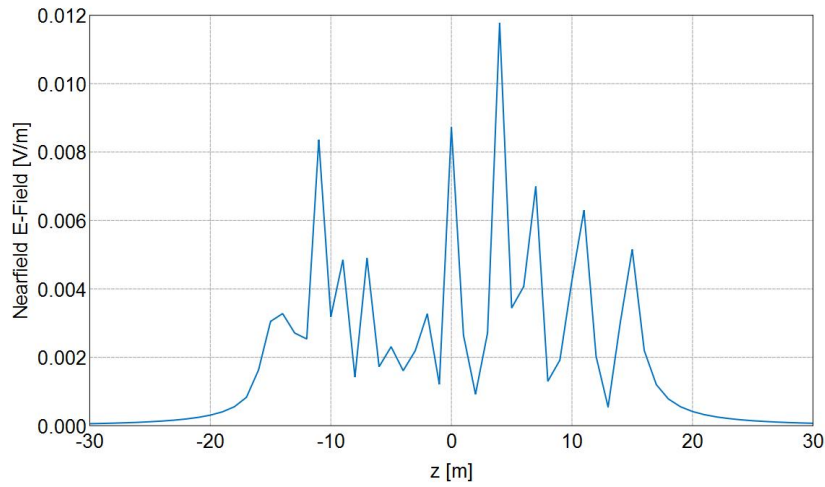
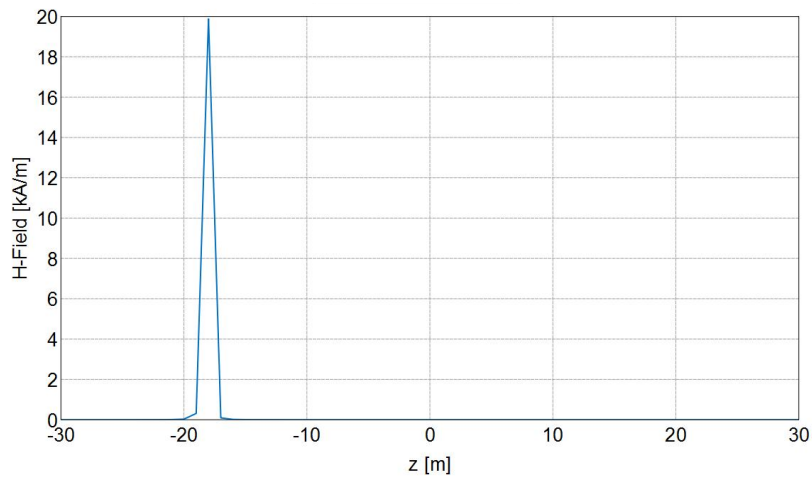


Figure A1.2: Imaginary component of electric field in the Z-direction for a orthogonal fracture of half-length 5 m in a vertical wellbore



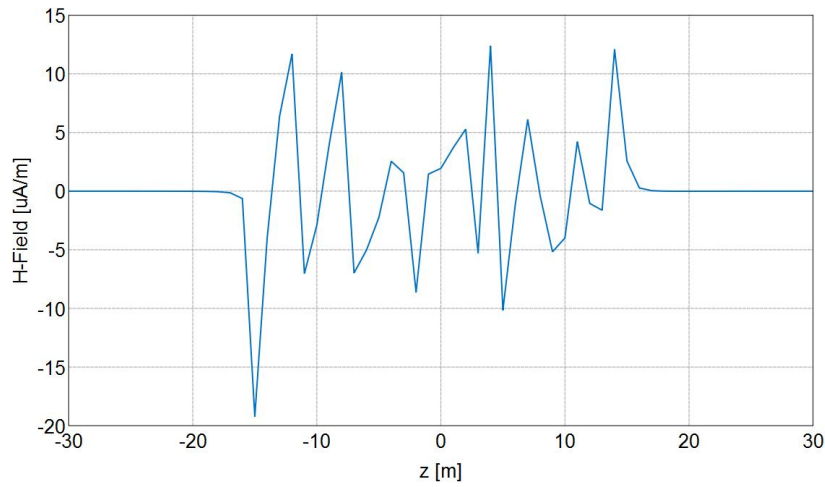
Z E-Field Magnitude [Frequency = 100 Hz; x = 0 m; y = 0 m] - Vertical well orthogonal fracture 5 m

Figure A1.3: Magnitude of electric field in the Z-direction for a orthogonal fracture of half-length 5 m in a vertical wellbore



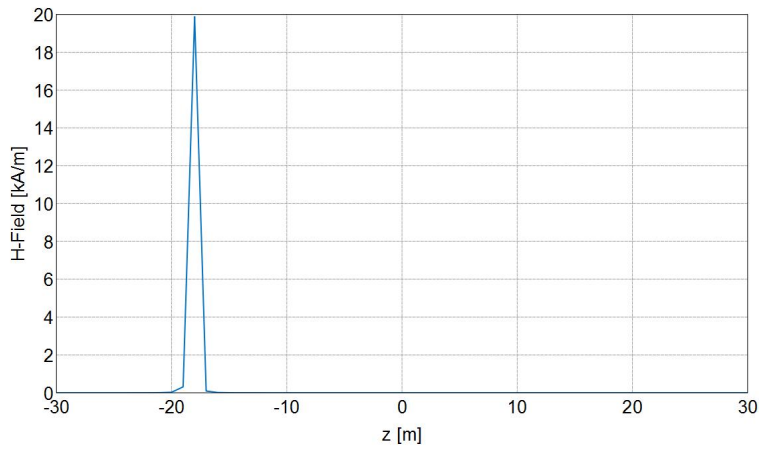
Real Z H-Field [Frequency = 100 Hz; x = 0 m; y = 0 m] - Vertical well orthogonal fracture 5 m

Figure A1.4: Real component of magnetic field in the Z-direction for a orthogonal fracture of half-length 5 m in a vertical wellbore



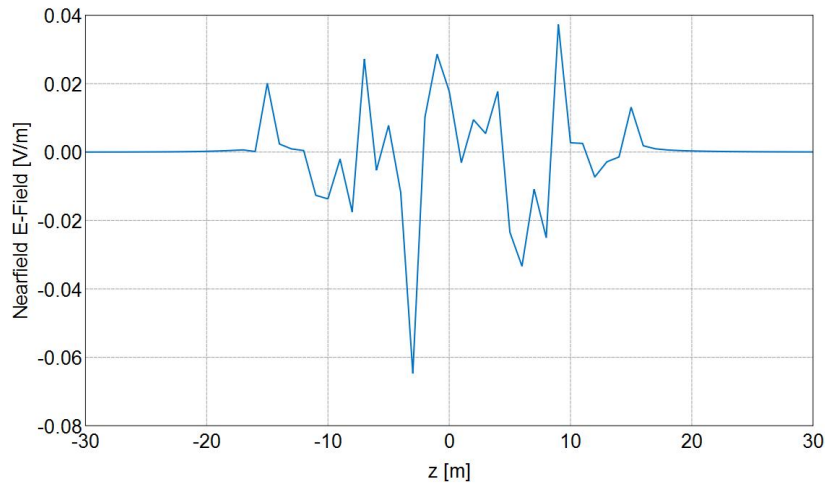
Imaginary Z H-Field [Frequency = 100 Hz; x = 0 m; y = 0 m] - Vertical well orthogonal fracture 5 m

Figure A1.5: Imaginary component of magnetic field in the Z-direction for a orthogonal fracture of half-length 5 m in a vertical wellbore



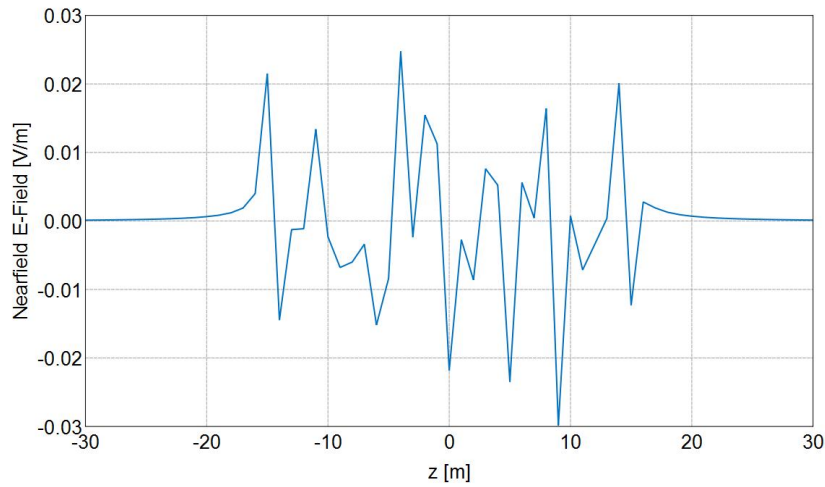
Z H-Field Magnitude [Frequency = 100 Hz; x = 0 m; y = 0 m] - Vertical well orthogonal fracture 5 m

Figure A1.6: Magnitude of magnetic field in the Z-direction for a orthogonal fracture of half-length 5 m in a vertical wellbore



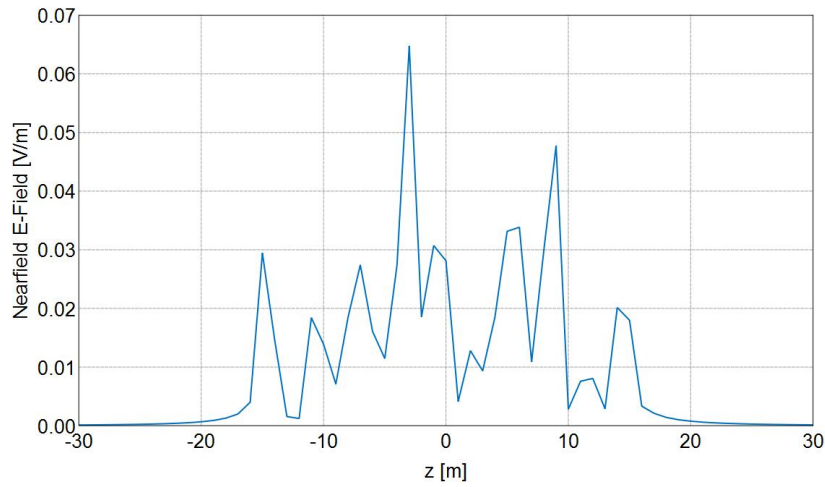
Real Z E-Field [Frequency = 100 Hz; x = 0 m; y = 0 m] - Vertical well orthogonal fracture 10 m

Figure A1.7: Real component of electric field in the Z-direction for a orthogonal fracture of half-length 10 m in a vertical wellbore



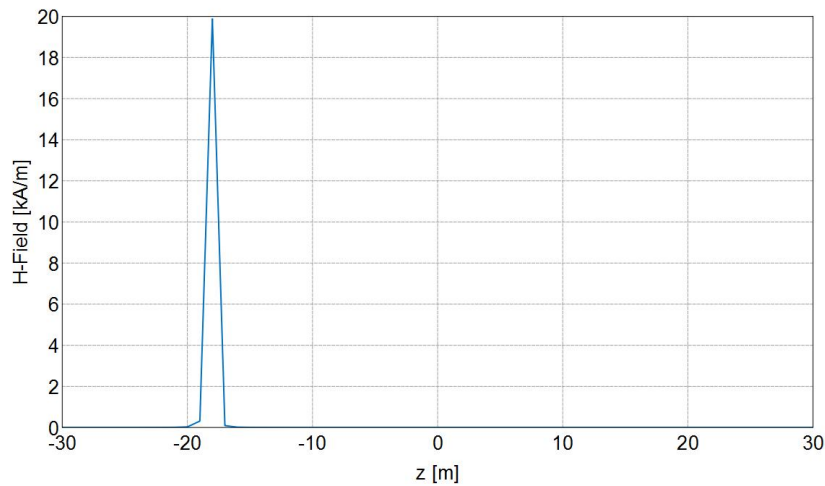
Imaginary Z E-Field [Frequency = 100 Hz; x = 0 m; y = 0 m] - Vertical well orthogonal fracture 10 m

Figure A1.8: Imaginary component of electric field in the Z-direction for a orthogonal fracture of half-length 10 m in a vertical wellbore



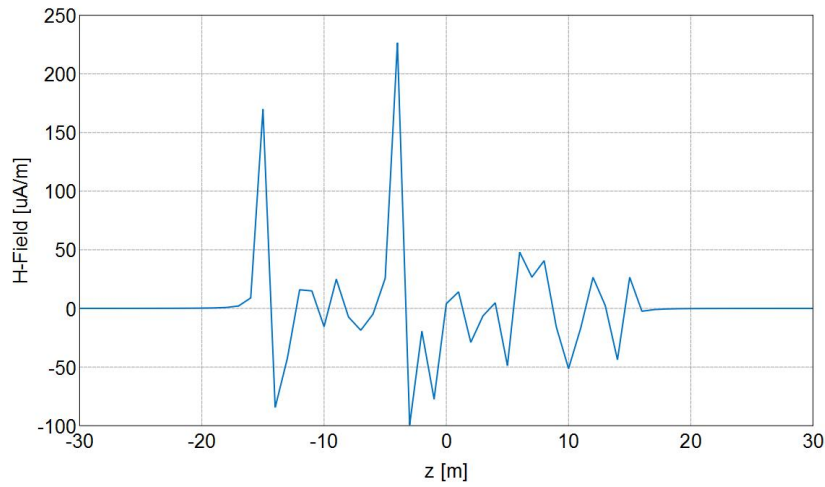
Z E-Field Magnitude [Frequency = 100 Hz; x = 0 m; y = 0 m] - Vertical well orthogonal fracture 10 m

Figure A1.9: Magnitude of electric field in the Z-direction for a orthogonal fracture of half-length 10 m in a vertical wellbore



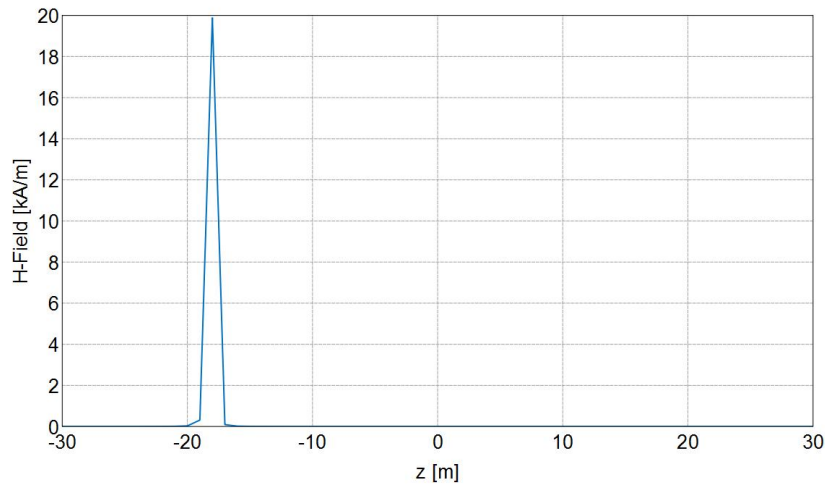
Real Z H-Field [Frequency = 100 Hz; x = 0 m; y = 0 m] - Vertical well orthogonal fracture 10 m

Figure A1.10: Real component of magnetic field in the Z-direction for a orthogonal fracture of half-length 10 m in a vertical wellbore



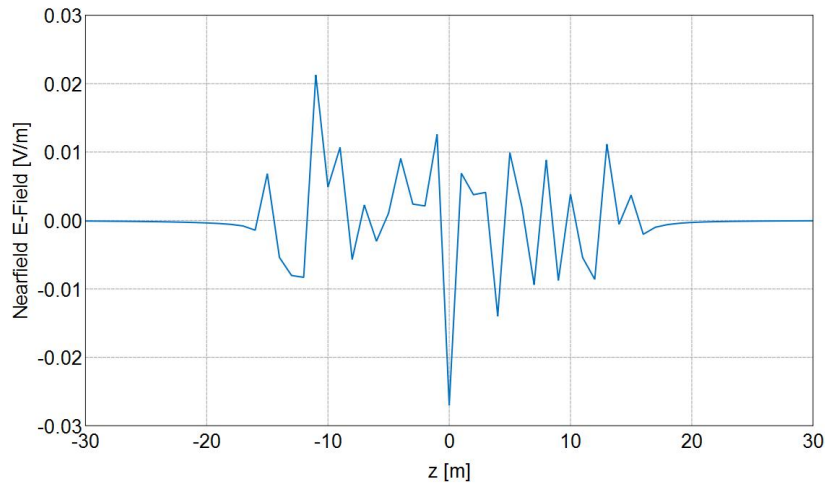
Imaginary Z H-Field [Frequency = 100 Hz; x = 0 m; y = 0 m] - Vertical well orthogonal fracture 10 m

Figure A1.11: Imaginary component of magnetic field in the Z-direction for a orthogonal fracture of half-length 10 m in a vertical wellbore



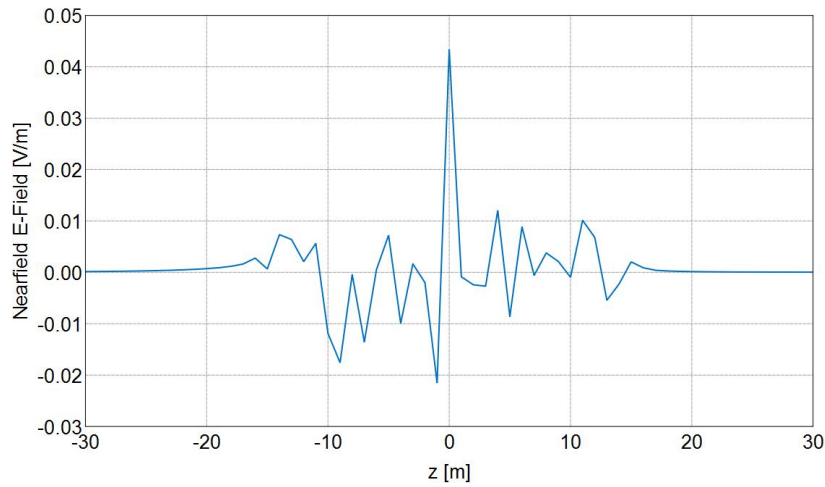
Z H-Field Magnitude [Frequency = 100 Hz; x = 0 m; y = 0 m] - Vertical well orthogonal fracture 10 m

Figure A1.12: Magnitude of magnetic field in the Z-direction for a orthogonal fracture of half-length 10 m in a vertical wellbore



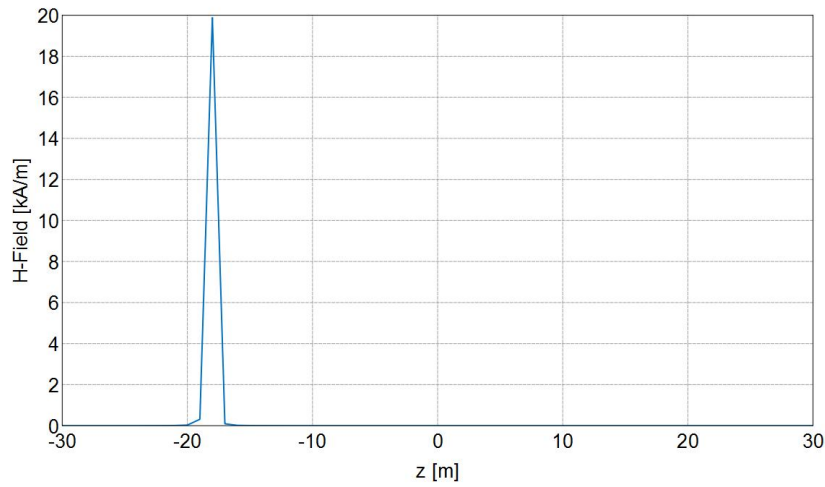
Real Z E-Field [Frequency = 100 Hz; x = 0 m; y = 0 m] - Vertical well orthogonal fracture 15 m

Figure A1.13: Real component of electric field in the Z-direction for a orthogonal fracture of half-length 15 m in a vertical wellbore



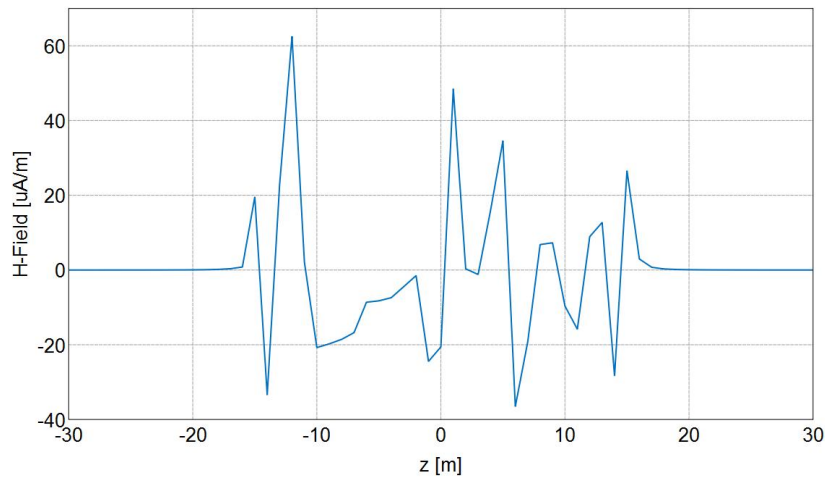
Imaginary Z E-Field [Frequency = 100 Hz; x = 0 m; y = 0 m] - Vertical well orthogonal fracture 15 m

Figure A1.14: Imaginary component of electric field in the Z-direction for a orthogonal fracture of half-length 15 m in a vertical wellbore



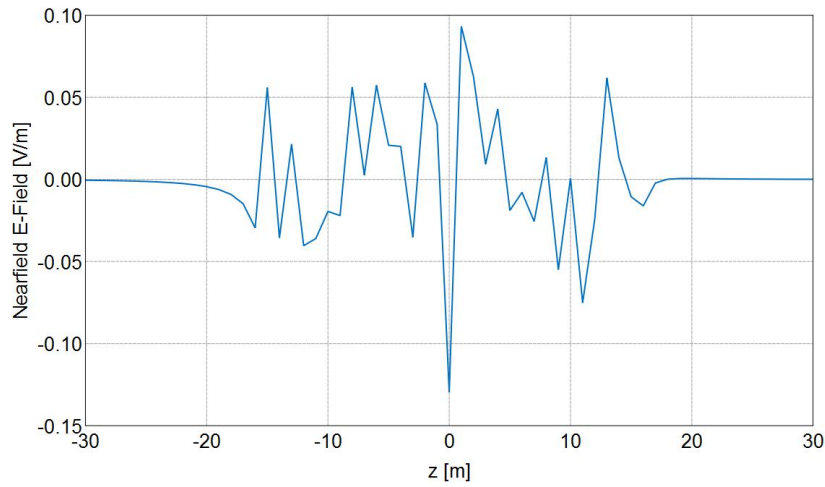
Real Z H-Field [Frequency = 100 Hz; x = 0 m; y = 0 m] - Vertical well orthogonal fracture 15 m

Figure A1.15: Real component of magnetic field in the Z-direction for a orthogonal fracture of half-length 15 m in a vertical wellbore



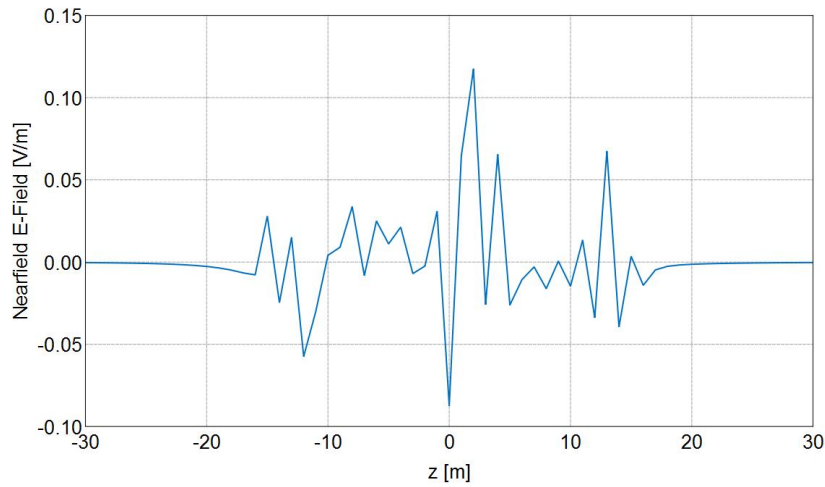
Imaginary Z H-Field [Frequency = 100 Hz; x = 0 m; y = 0 m] - Vertical well orthogonal fracture 15 m

Figure A1.16: Imaginary component of magnetic field in the Z-direction for a orthogonal fracture of half-length 15 m in a vertical wellbore



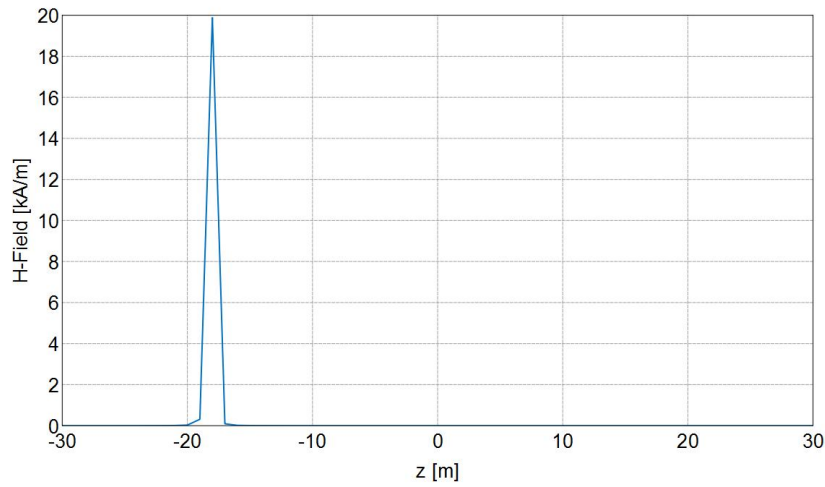
Real Z E-Field [Frequency = 100 Hz; x = 0 m; y = 0 m] - Vertical well orthogonal fracture 20 m

Figure A1.17: Real component of electric field in the Z-direction for a orthogonal fracture of half-length 20 m in a vertical wellbore



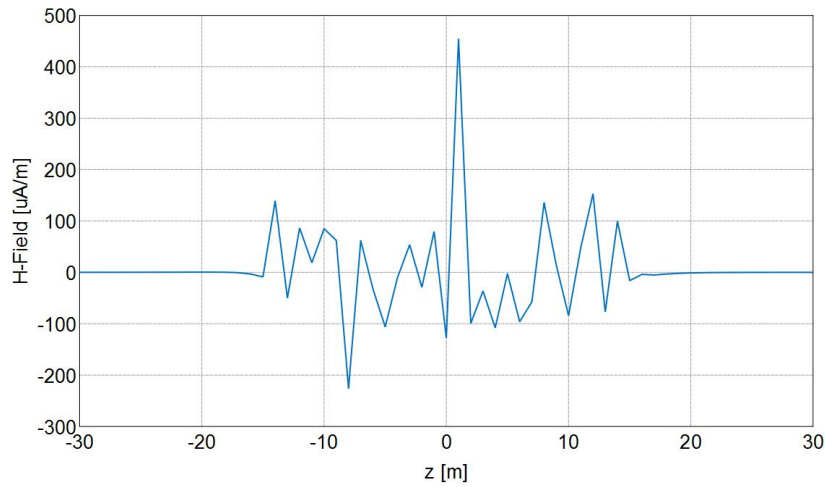
Imaginary Z E-Field [Frequency = 100 Hz; x = 0 m; y = 0 m] - Vertical well orthogonal fracture 20 m

Figure A1.18: Imaginary component of electric field in the Z-direction for a orthogonal fracture of half-length 20 m in a vertical wellbore



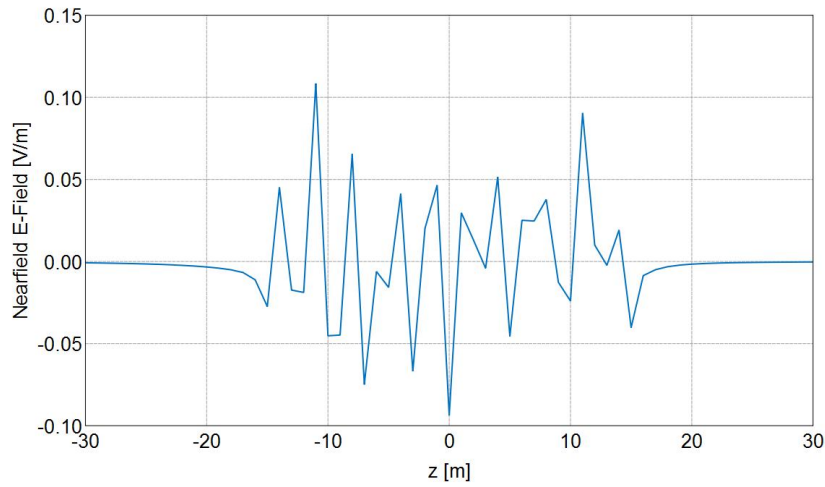
Real Z H-Field [Frequency = 100 Hz; x = 0 m; y = 0 m] - Vertical well orthogonal fracture 20 m

Figure A1.19: Real component of magnetic field in the Z-direction for a orthogonal fracture of half-length 20 m in a vertical wellbore



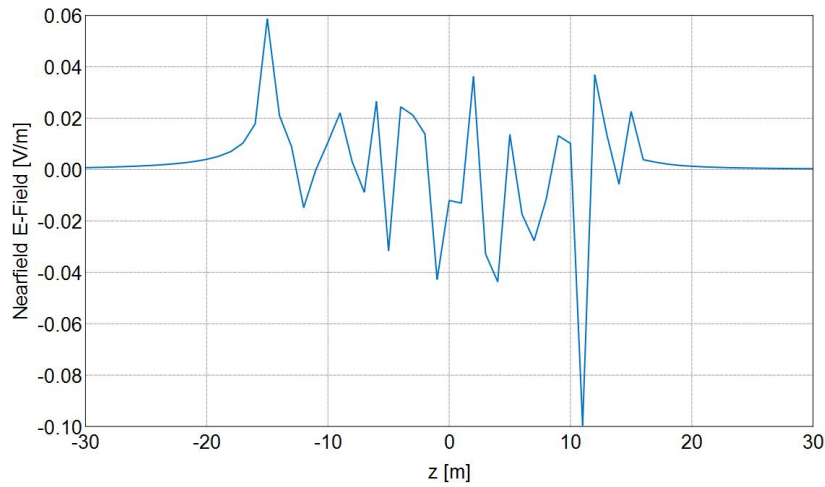
Imaginary Z H-Field [Frequency = 100 Hz; x = 0 m; y = 0 m] - Vertical well orthogonal fracture 20 m

Figure A1.20: Imaginary component of magnetic field in the Z-direction for a orthogonal fracture of half-length 20 m in a vertical wellbore



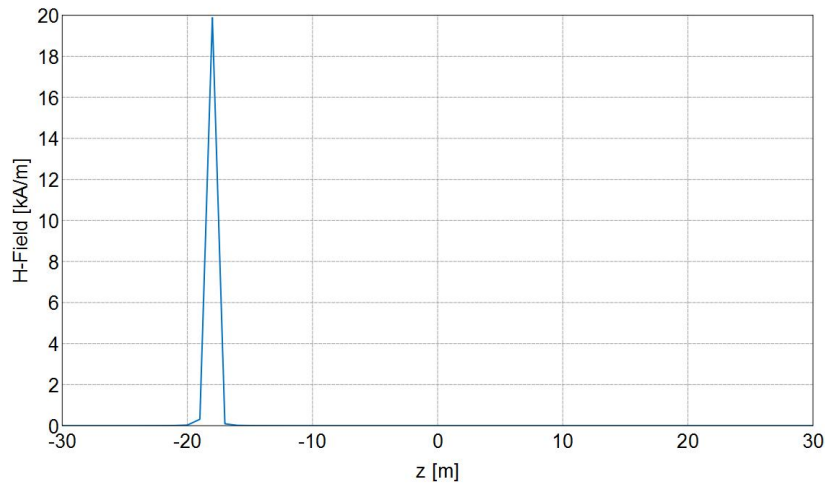
Real Z E-Field [Frequency = 100 Hz; x = 0 m; y = 0 m] - Vertical well orthogonal fracture 25 m

Figure A1.21: Real component of electric field in the Z-direction for a orthogonal fracture of half-length 25 m in a vertical wellbore



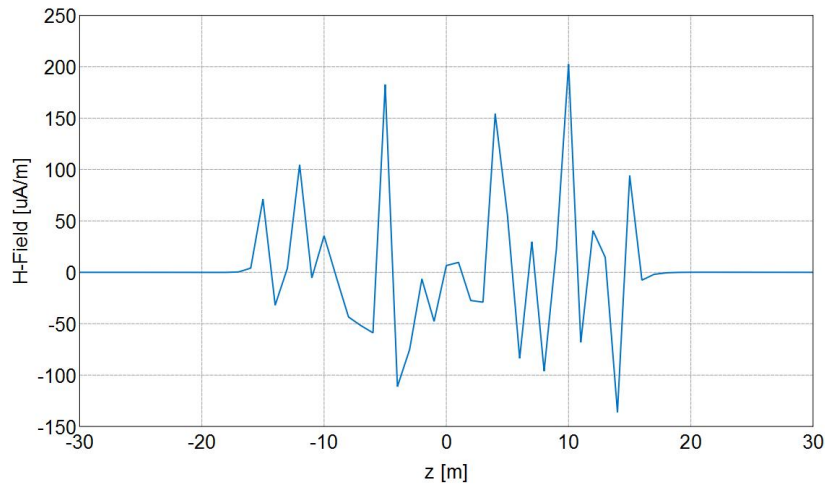
Imaginary Z E-Field [Frequency = 100 Hz; x = 0 m; y = 0 m] - Vertical well orthogonal fracture 25 m

Figure A1.22: Imaginary component of electric field in the Z-direction for a orthogonal fracture of half-length 25 m in a vertical wellbore



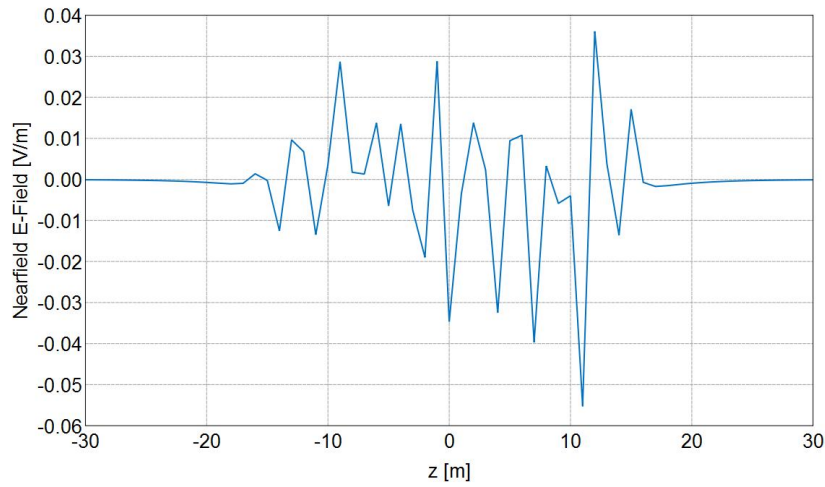
Real Z H-Field [Frequency = 100 Hz; x = 0 m; y = 0 m] - Vertical well orthogonal fracture 25 m

Figure A1.23: Real component of magnetic field in the Z-direction for a orthogonal fracture of half-length 25 m in a vertical wellbore



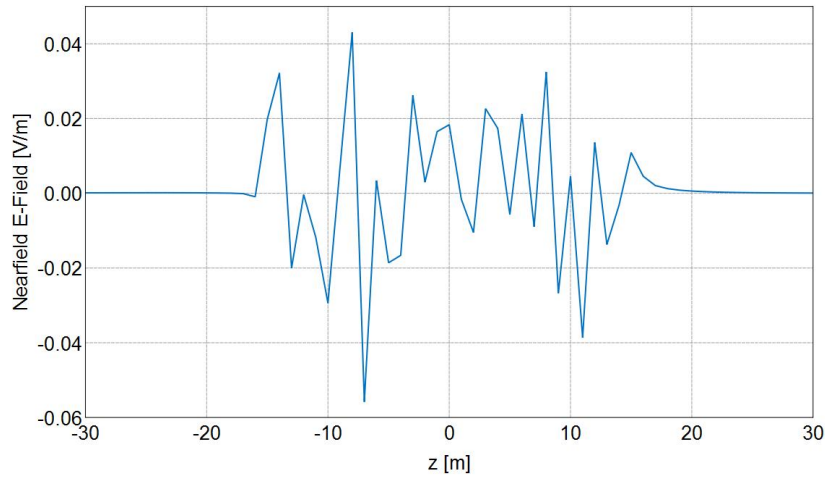
Imaginary Z H-Field [Frequency = 100 Hz; x = 0 m; y = 0 m] - Vertical well orthogonal fracture 25 m

Figure A1.24: Imaginary component of magnetic field in the Z-direction for a orthogonal fracture of half-length 25 m in a vertical wellbore



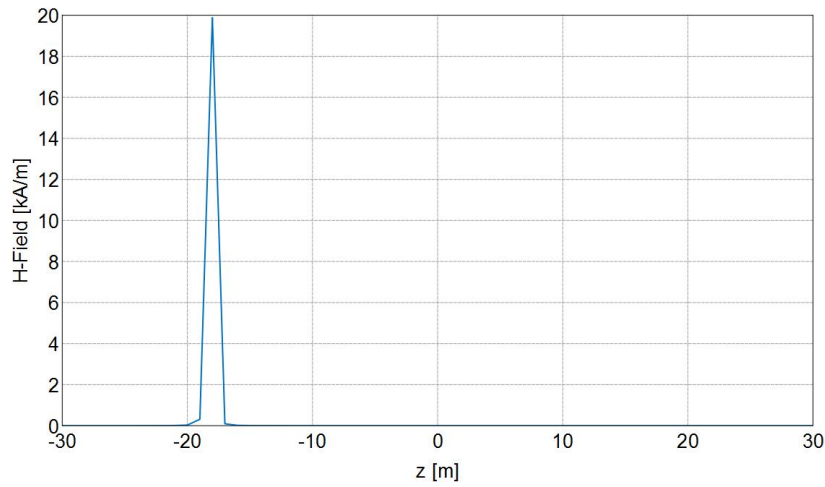
Real Z E-Field [Frequency = 100 Hz; x = 0 m; y = 0 m] - Vertical well orthogonal fracture 30 m

Figure A1.25: Real component of electric field in the Z-direction for a orthogonal fracture of half-length 30 m in a vertical wellbore



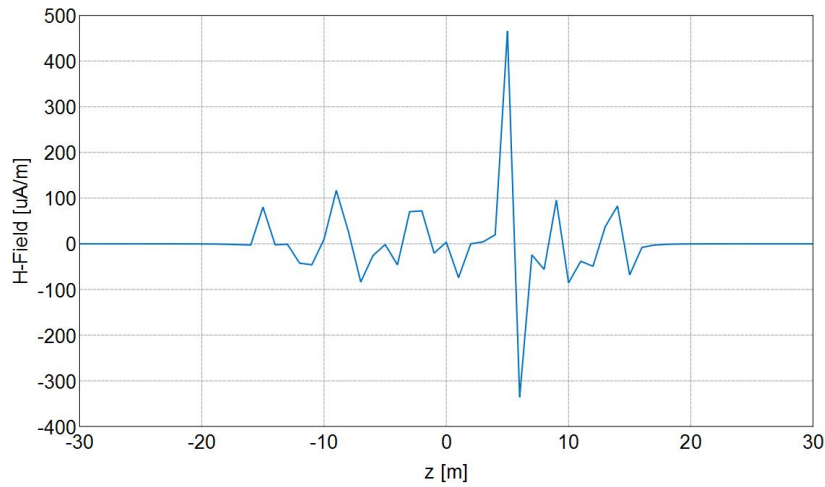
Imaginary Z E-Field [Frequency = 100 Hz; x = 0 m; y = 0 m] - Vertical well orthogonal fracture 30 m

Figure A1.26: Imaginary component of electric field in the Z-direction for a orthogonal fracture of half-length 30 m in a vertical wellbore



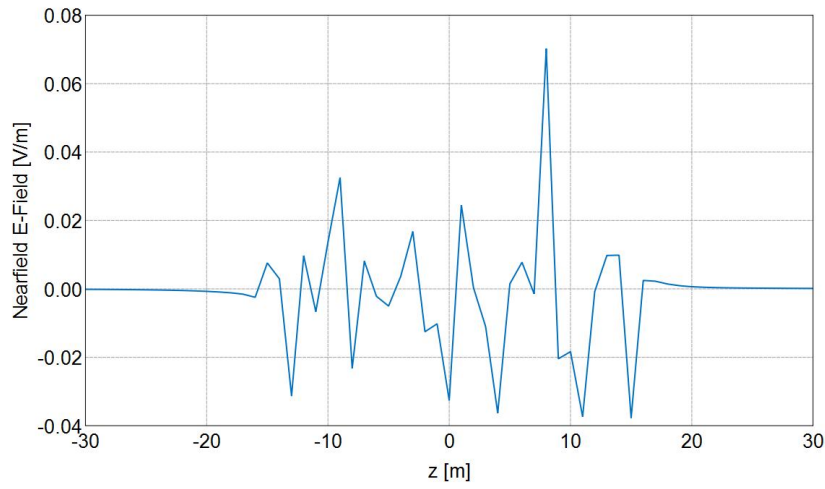
Real Z H-Field [Frequency = 100 Hz; x = 0 m; y = 0 m] - Vertical well orthogonal fracture 30 m

Figure A1.27: Real component of magnetic field in the Z-direction for a orthogonal fracture of half-length 30 m in a vertical wellbore



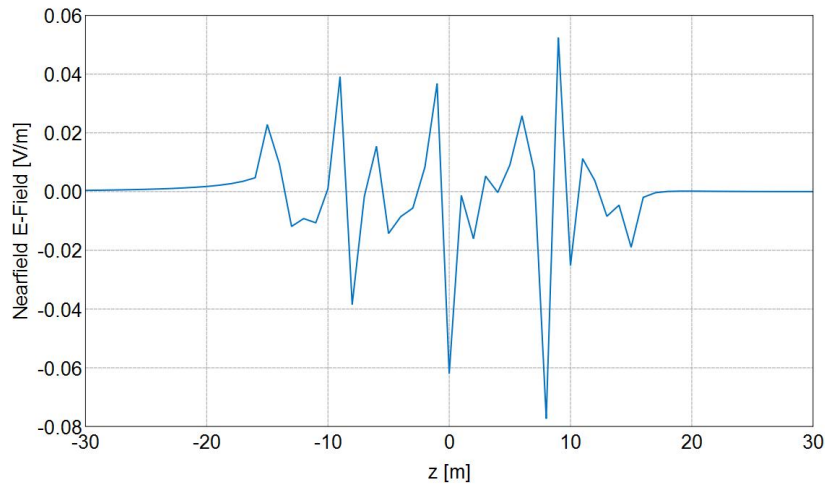
Imaginary Z H-Field [Frequency = 100 Hz; x = 0 m; y = 0 m] - Vertical well orthogonal fracture 30 m

Figure A1.28: Imaginary component of magnetic field in the Z-direction for a orthogonal fracture of half-length 30 m in a vertical wellbore



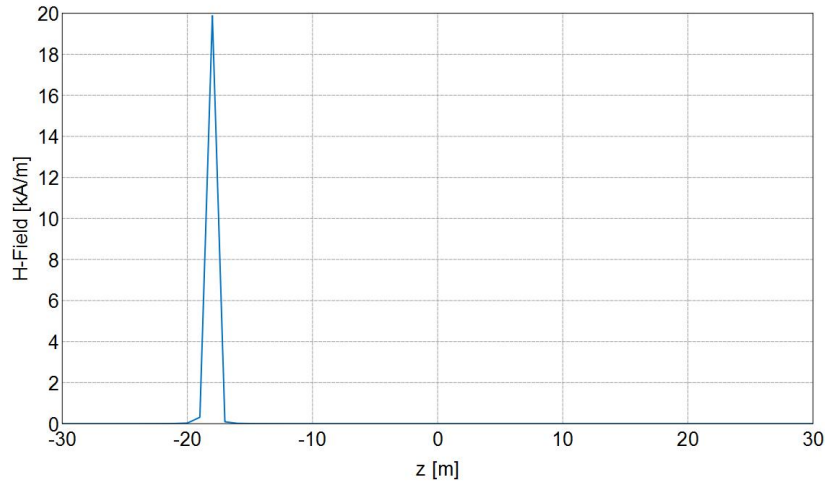
Real Z E-Field [Frequency = 100 Hz; x = 0 m; y = 0 m] - Vertical well orthogonal fracture 35 m

Figure A1.29: Real component of electric field in the Z-direction for a orthogonal fracture of half-length 35 m in a vertical wellbore



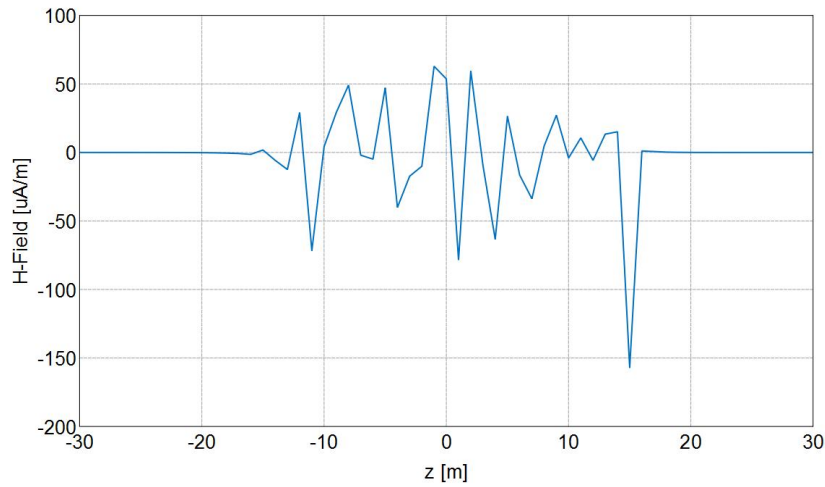
Imaginary Z E-Field [Frequency = 100 Hz; x = 0 m; y = 0 m] - Vertical well orthogonal fracture 35 m

Figure A1.30: Imaginary component of electric field in the Z-direction for a orthogonal fracture of half-length 35 m in a vertical wellbore



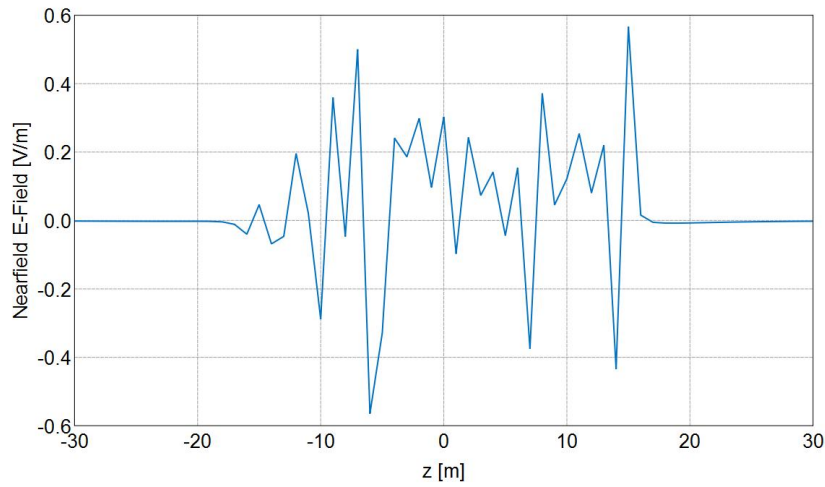
Real Z H-Field [Frequency = 100 Hz; x = 0 m; y = 0 m] - Vertical well orthogonal fracture 35 m

Figure A1.31: Real component of magnetic field in the Z-direction for a orthogonal fracture of half-length 35 m in a vertical wellbore



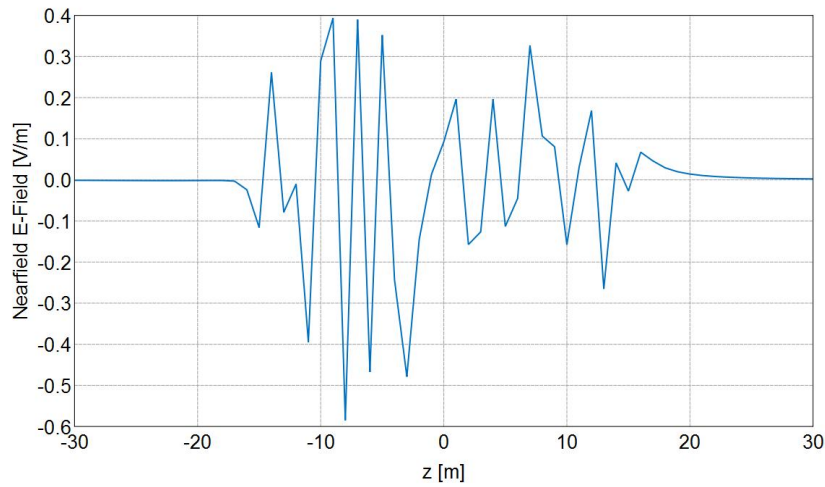
Imaginary Z H-Field [Frequency = 100 Hz; x = 0 m; y = 0 m] - Vertical well orthogonal fracture 35 m

Figure A1.32: Imaginary component of magnetic field in the Z-direction for a orthogonal fracture of half-length 35 m in a vertical wellbore



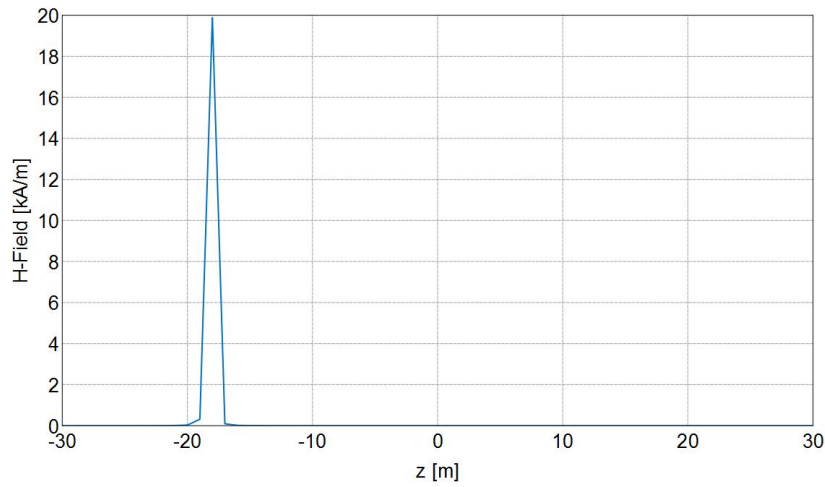
Real Z E-Field [Frequency = 100 Hz; x = 0 m; y = 0 m] - Vertical well orthogonal fracture 40 m

Figure A1.33: Real component of electric field in the Z-direction for a orthogonal fracture of half-length 40 m in a vertical wellbore



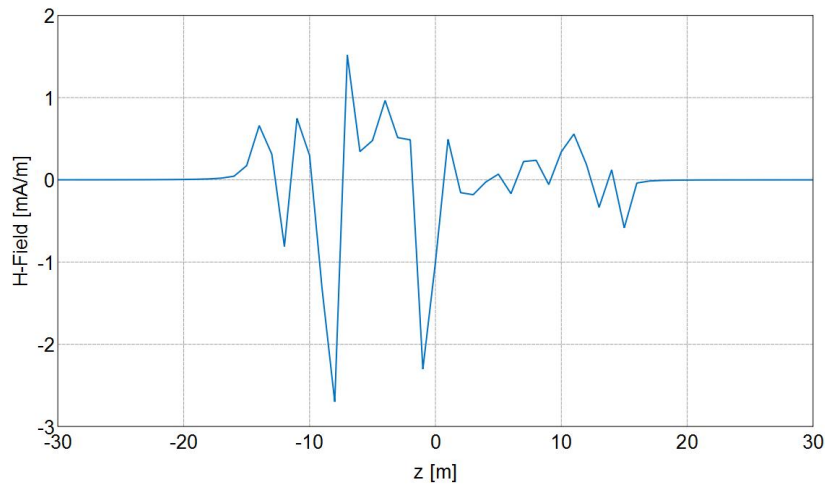
Imaginary Z E-Field [Frequency = 100 Hz; x = 0 m; y = 0 m] - Vertical well orthogonal fracture 40 m

Figure A1.34: Imaginary component of electric field in the Z-direction for a orthogonal fracture of half-length 40 m in a vertical wellbore



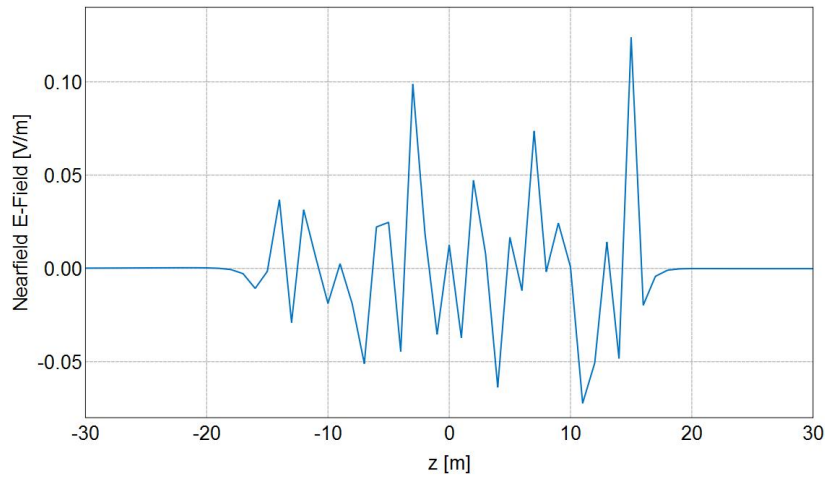
Real Z H-Field [Frequency = 100 Hz; x = 0 m; y = 0 m] - Vertical well orthogonal fracture 40 m

Figure A1.35: Real component of magnetic field in the Z-direction for a orthogonal fracture of half-length 40 m in a vertical wellbore



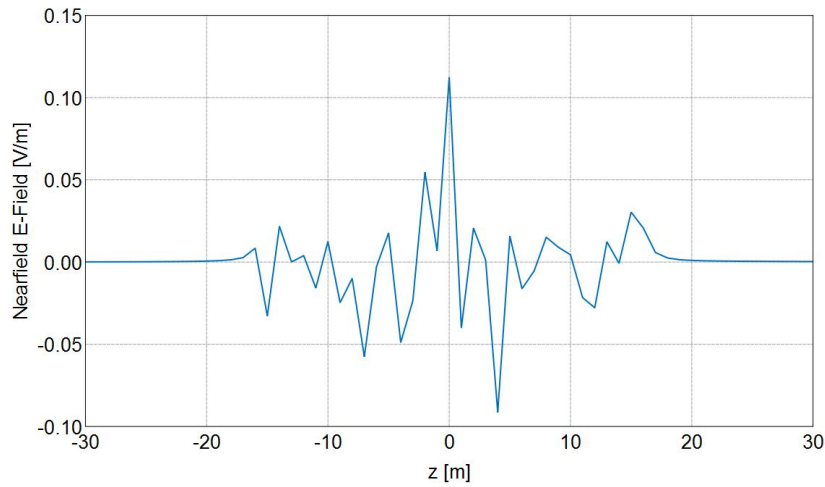
Imaginary Z H-Field [Frequency = 100 Hz; x = 0 m; y = 0 m] - Vertical well orthogonal fracture 40 m

Figure A1.36: Imaginary component of magnetic field in the Z-direction for a orthogonal fracture of half-length 40 m in a vertical wellbore



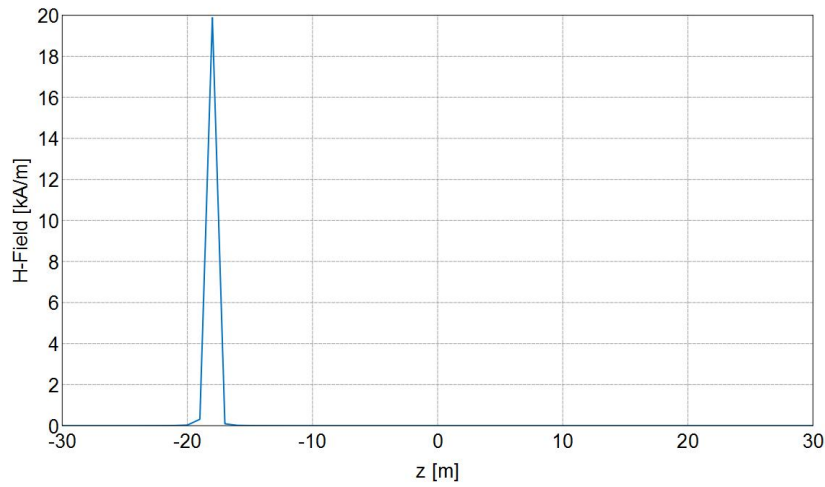
Real Z E-Field [Frequency = 100 Hz; x = 0 m; y = 0 m] - Vertical well orthogonal fracture 45 m

Figure A1.37: Real component of electric field in the Z-direction for a orthogonal fracture of half-length 45 m in a vertical wellbore



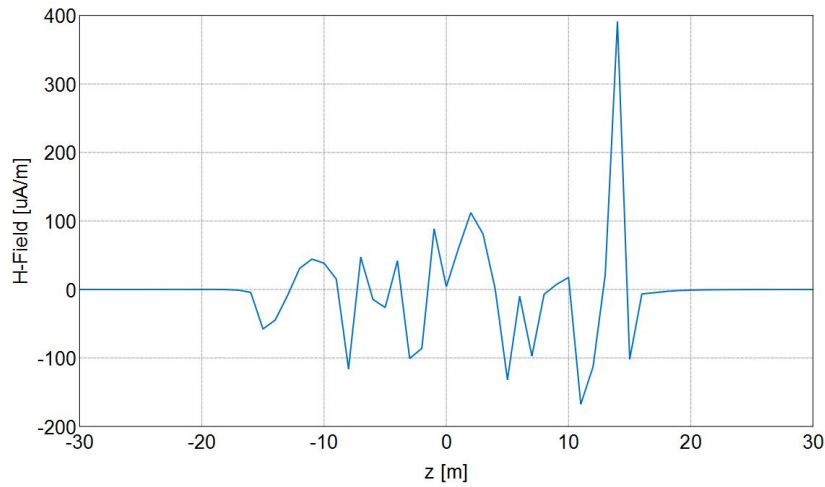
Imaginary Z E-Field [Frequency = 100 Hz; x = 0 m; y = 0 m] - Vertical well orthogonal fracture 45 m

Figure A1.38: Imaginary component of electric field in the Z-direction for a orthogonal fracture of half-length 45 m in a vertical wellbore



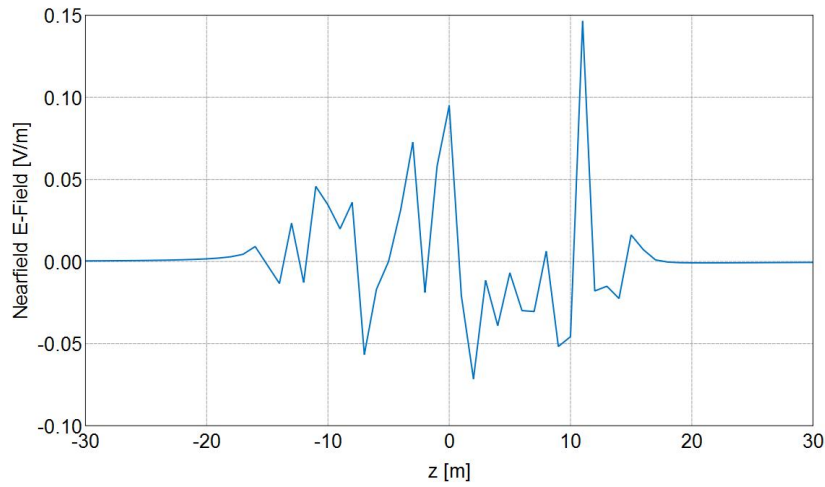
Real Z H-Field [Frequency = 100 Hz; x = 0 m; y = 0 m] - Vertical well orthogonal fracture 45 m

Figure A1.39: Real component of magnetic field in the Z-direction for a orthogonal fracture of half-length 45 m in a vertical wellbore



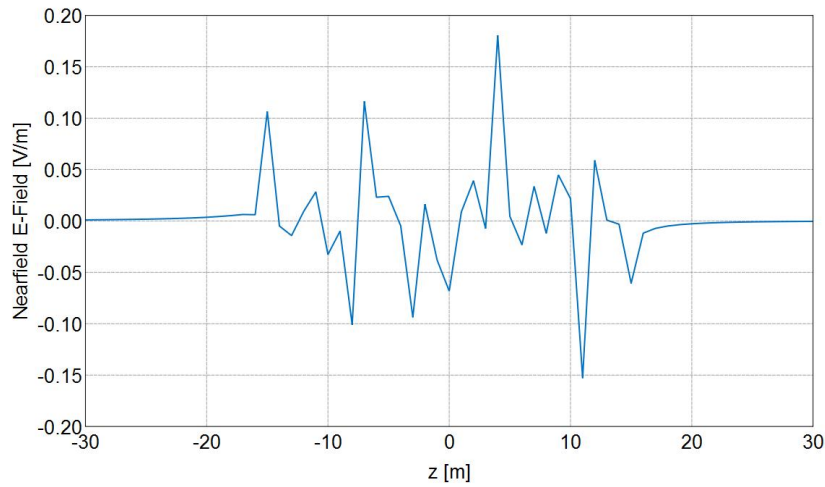
Imaginary Z H-Field [Frequency = 100 Hz; x = 0 m; y = 0 m] - Vertical well orthogonal fracture 45 m

Figure A1.40: Imaginary component of magnetic field in the Z-direction for a orthogonal fracture of half-length 45 m in a vertical wellbore



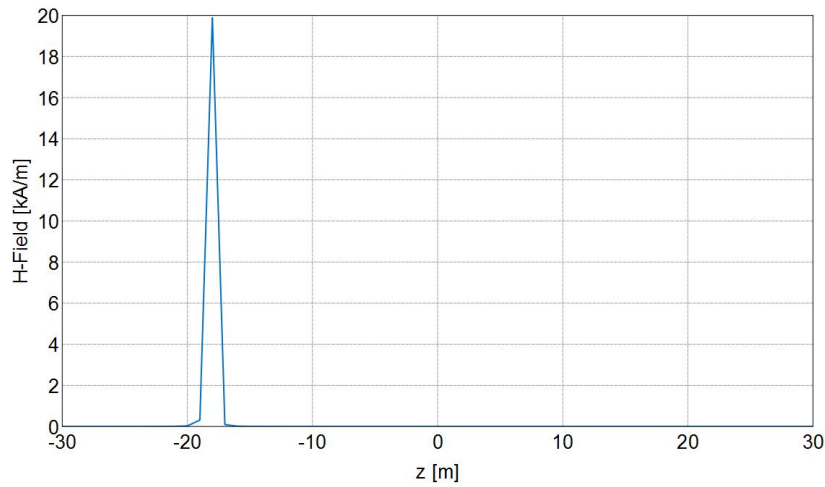
Real Z E-Field [Frequency = 100 Hz; x = 0 m; y = 0 m] - Vertical well orthogonal fracture 60 m

Figure A1.41: Real component of electric field in the Z-direction for a orthogonal fracture of half-length 60 m in a vertical wellbore



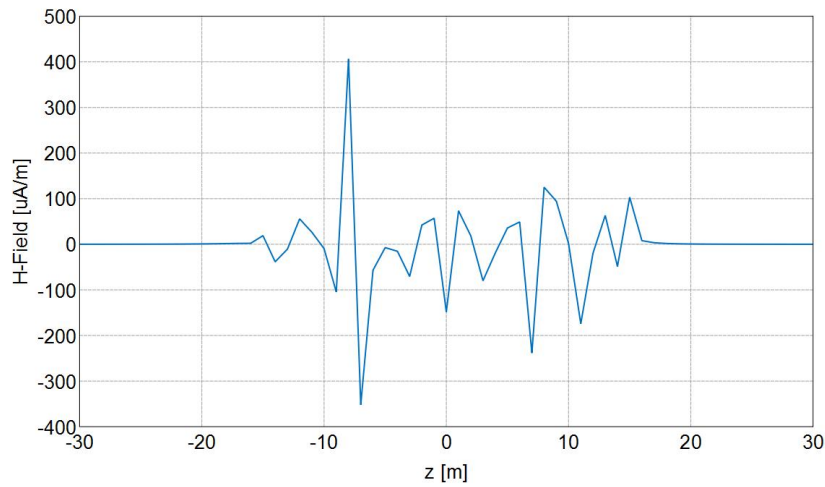
Imaginary Z E-Field [Frequency = 100 Hz; x = 0 m; y = 0 m] - Vertical well orthogonal fracture 60 m

Figure A1.42: Imaginary component of electric field in the Z-direction for a orthogonal fracture of half-length 60 m in a vertical wellbore



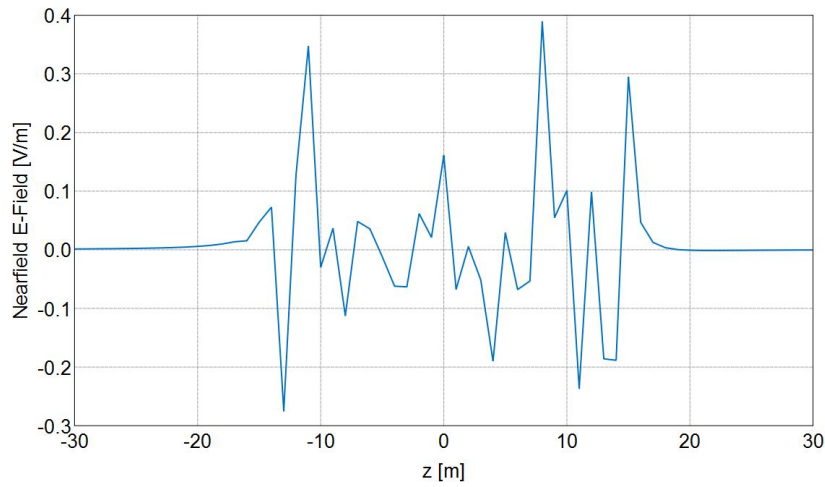
Real Z H-Field [Frequency = 100 Hz; x = 0 m; y = 0 m] - Vertical well orthogonal fracture 60 m

Figure A1.43: Real component of magnetic field in the Z-direction for a orthogonal fracture of half-length 60 m in a vertical wellbore



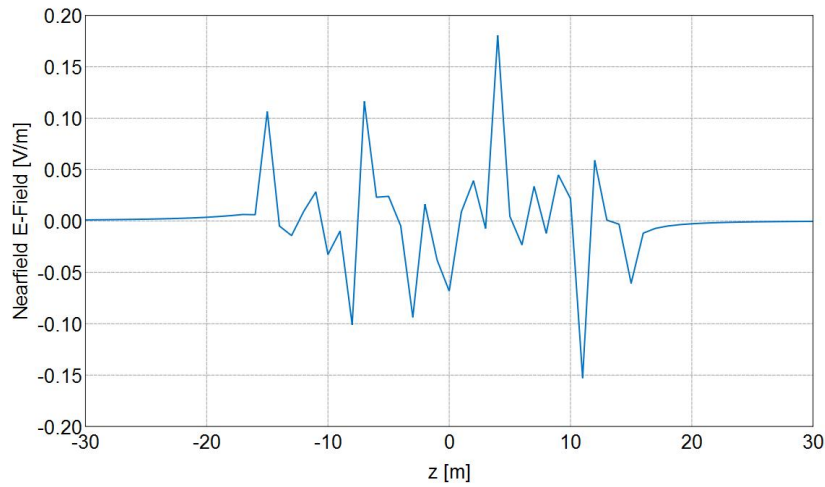
Imaginary Z H-Field [Frequency = 100 Hz; x = 0 m; y = 0 m] - Vertical well orthogonal fracture 60 m

Figure A1.44: Imaginary component of magnetic field in the Z-direction for a orthogonal fracture of half-length 60 m in a vertical wellbore



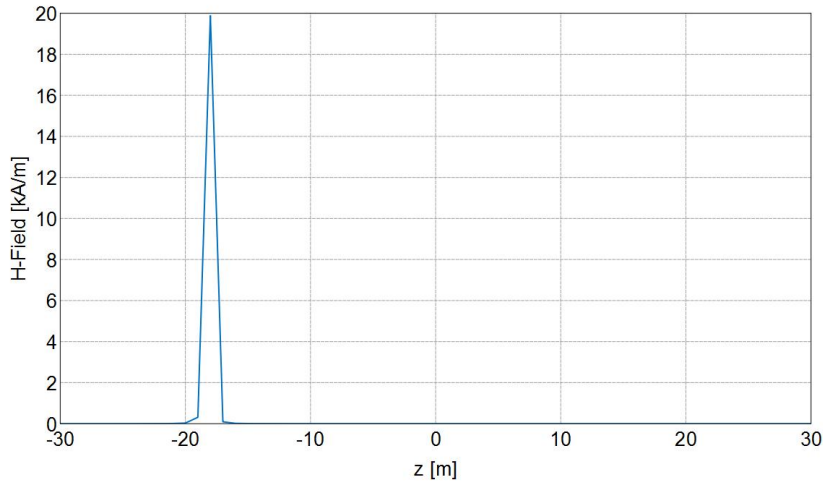
Real Z E-Field [Frequency = 100 Hz; x = 0 m; y = 0 m] - Vertical well orthogonal fracture 75 m

Figure A1.45: Real component of electric field in the Z-direction for a orthogonal fracture of half-length 75 m in a vertical wellbore



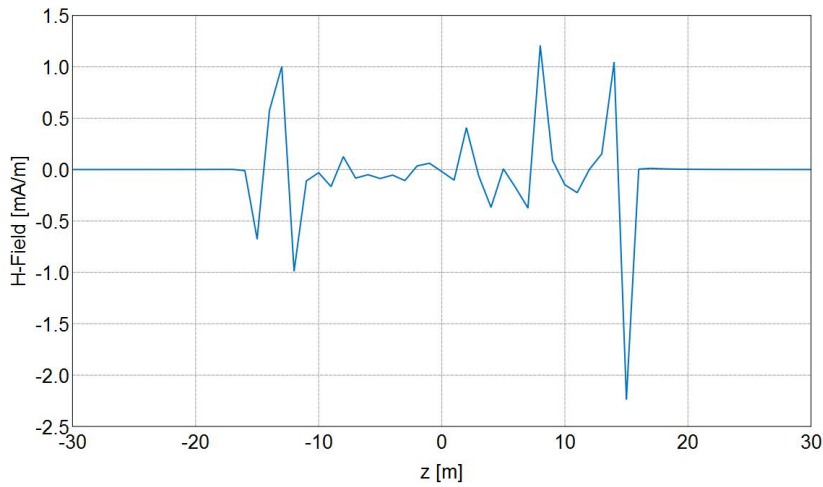
Imaginary Z E-Field [Frequency = 100 Hz; x = 0 m; y = 0 m] - Vertical well orthogonal fracture 60 m

Figure A1.46: Imaginary component of electric field in the Z-direction for a orthogonal fracture of half-length 75 m in a vertical wellbore



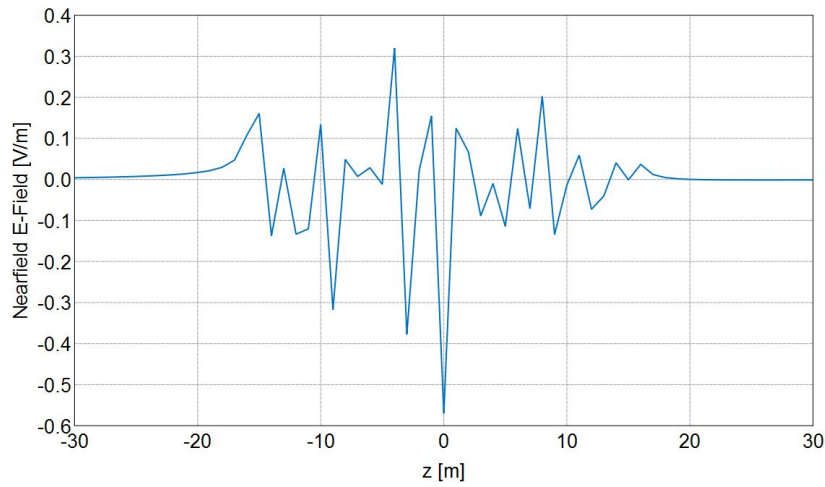
Real Z H-Field [Frequency = 100 Hz; x = 0 m; y = 0 m] - Vertical well orthogonal fracture 75 m

Figure A1.47: Real component of magnetic field in the Z-direction for a orthogonal fracture of half-length 75 m in a vertical wellbore



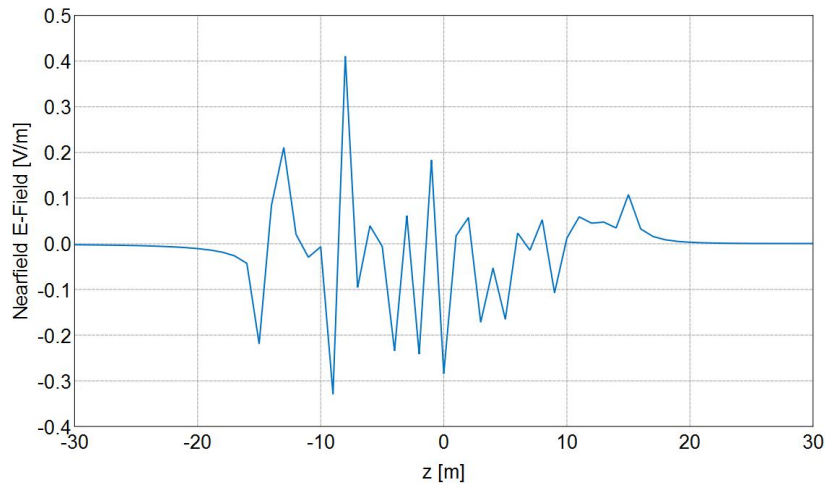
Imaginary Z H-Field [Frequency = 100 Hz; x = 0 m; y = 0 m] - Vertical well orthogonal fracture 75 m

Figure A1.48: Imaginary component of magnetic field in the Z-direction for a orthogonal fracture of half-length 75 m in a vertical wellbore



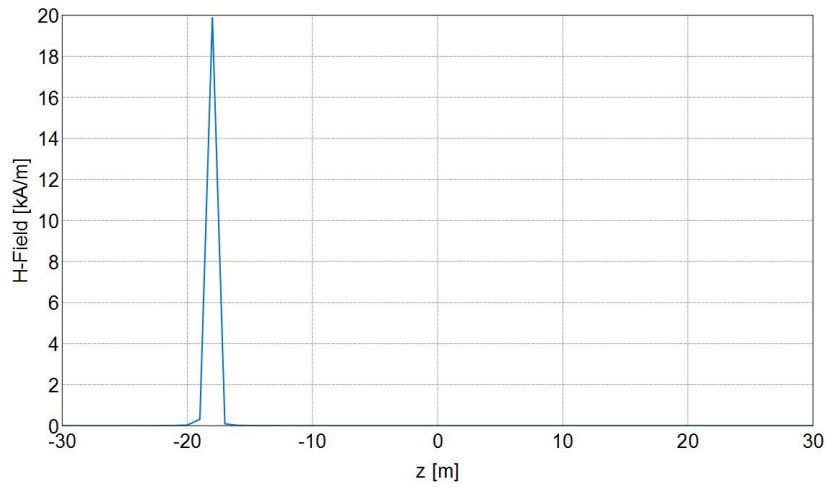
Real Z E-Field [Frequency = 100 Hz; x = 0 m; y = 0 m] - Vertical well orthogonal fracture 100 m

Figure A1.49: Real component of electric field in the Z-direction for a orthogonal fracture of half-length 100 m in a vertical wellbore



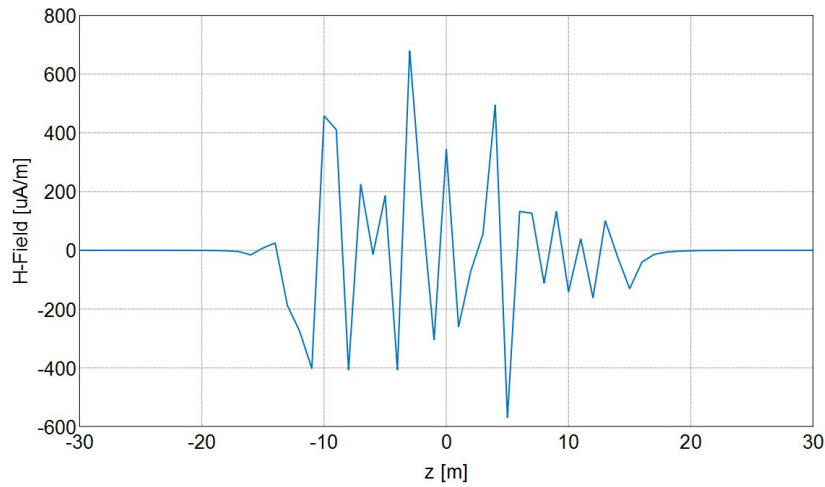
imaginary Z E-Field [Frequency = 100 Hz; x = 0 m; y = 0 m] - Vertical well orthogonal fracture 100 m

Figure A1.50: Imaginary component of electric field in the Z-direction for a orthogonal fracture of half-length 100 m in a vertical wellbore



Real Z H-Field [Frequency = 100 Hz; x = 0 m; y = 0 m] - Vertical well orthogonal fracture 100 m

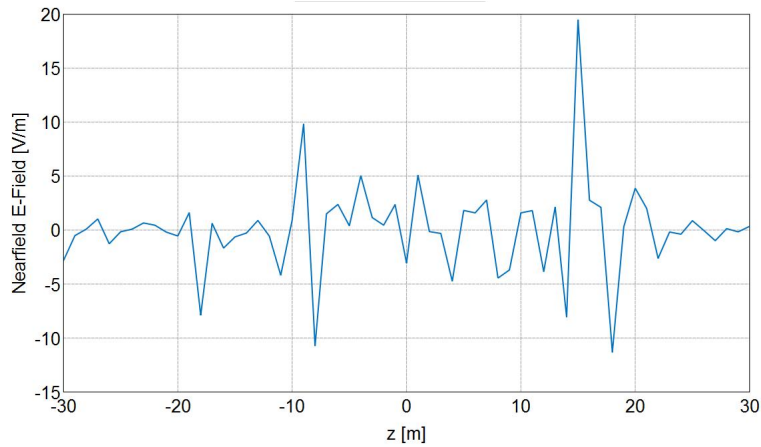
Figure A1.51: Real component of magnetic field in the Z-direction for a orthogonal fracture of half-length 100 m in a vertical wellbore



maginary Z H-Field [Frequency = 100 Hz; x = 0 m; y = 0 m] - Vertical well orthogonal fracture 100 m

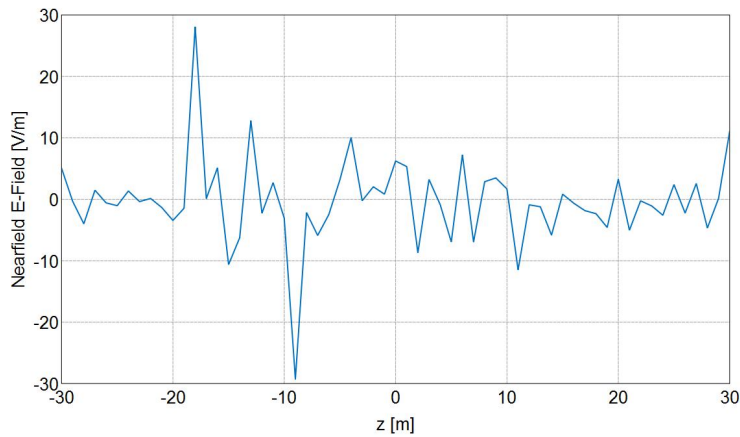
Figure A1.52: Real component of magnetic field in the Z-direction for a orthogonal fracture of half-length 100 m in a vertical wellbore

**A2.RAW ELECTRIC AND MAGNETIC FIELD RESPONSES FOR AN ORTHOGONAL FRACTURE IN VERTICAL WELL (CASED HOLE COMPLETION)**



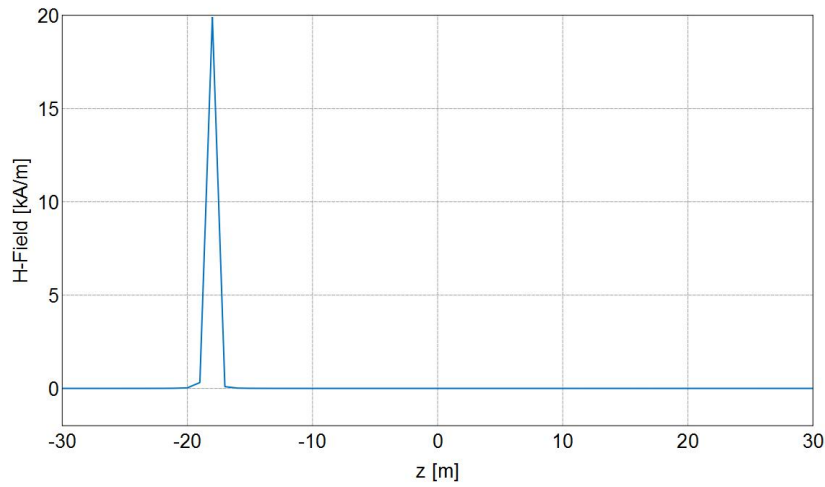
Real Z E-Field [Frequency = 100 Hz; x = 0 m; y = 0 m] - Vertical well orthogonal fracture 5 m CH

Figure A2.1: Real component of electric field in the Z-direction for a orthogonal fracture of half-length 5 m in a vertical wellbore through steel casing



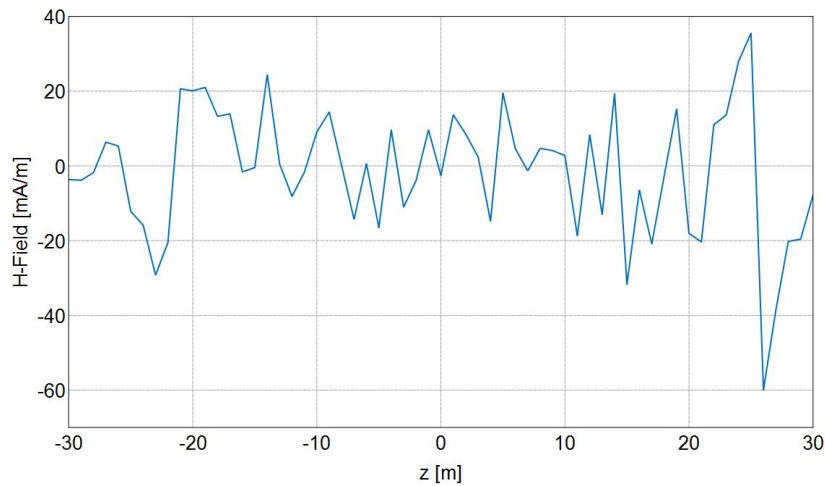
Imaginary Z E-Field [Frequency = 100 Hz; x = 0 m; y = 0 m] - Vertical well orthogonal fracture 5 m CH

Figure A2.2: Imaginary component of electric field in the Z-direction for a orthogonal fracture of half-length 5 m in a vertical wellbore through steel casing



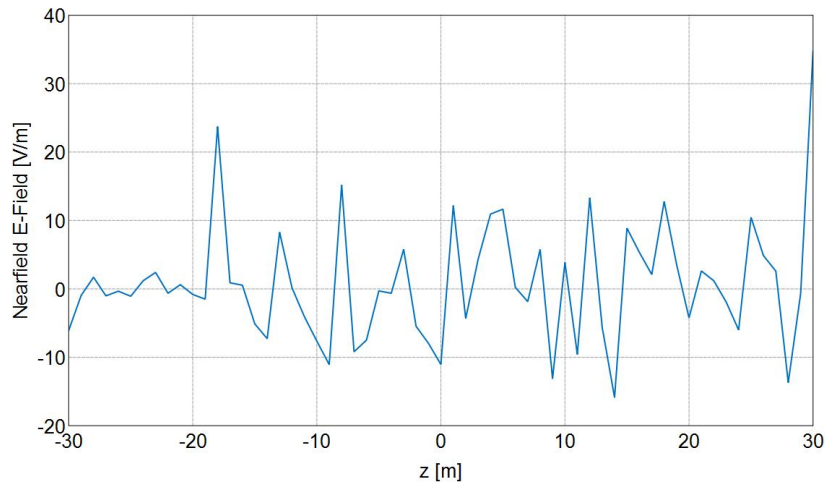
Real Z H-Field [Frequency = 100 Hz; x = 0 m; y = 0 m] - Vertical well orthogonal fracture 5 m CH

Figure A2.3: Real component of magnetic field in the Z-direction for a orthogonal fracture of half-length 5 m in a vertical wellbore through steel casing



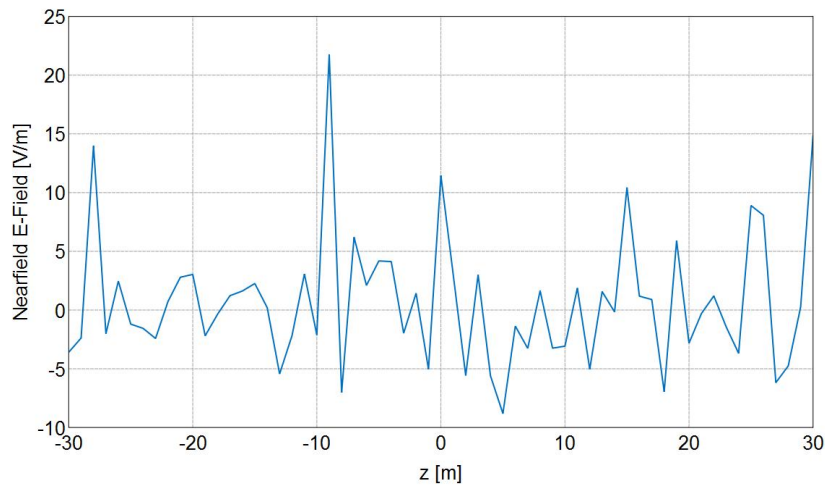
Imaginary Z H-Field [Frequency = 100 Hz; x = 0 m; y = 0 m] - Vertical well orthogonal fracture 5 m CH

Figure A2.4: Imaginary component of magnetic field in the Z-direction for a orthogonal fracture of half-length 5 m in a vertical wellbore through steel casing



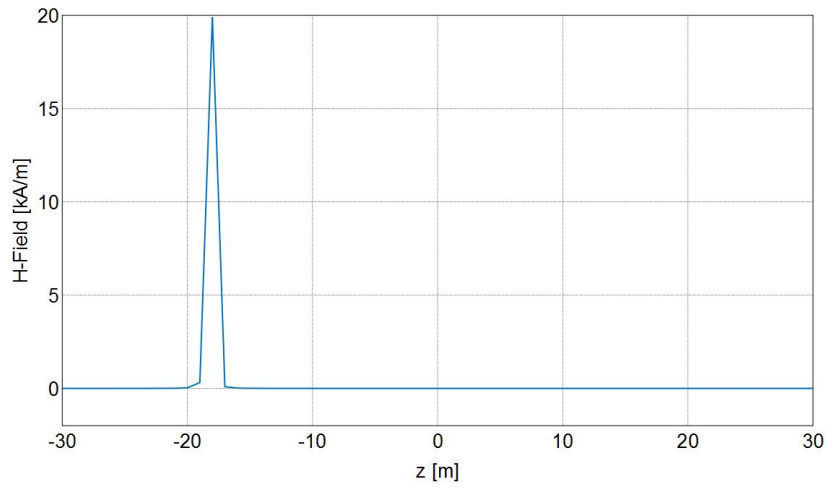
Real Z E-Field [Frequency = 100 Hz; x = 0 m; y = 0 m] - Vertical well orthogonal fracture 10 m CH

Figure A2.5: Real component of electric field in the Z-direction for a orthogonal fracture of half-length 10 m in a vertical wellbore through steel casing



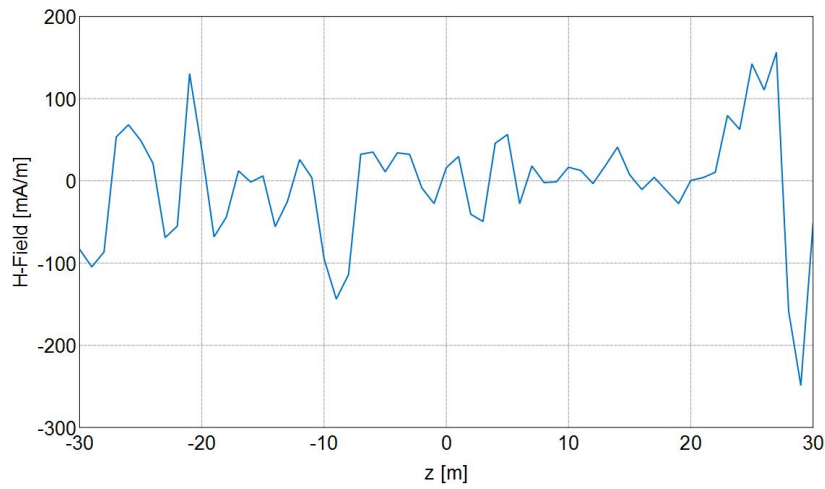
Imaginary Z E-Field [Frequency = 100 Hz; x = 0 m; y = 0 m] - Vertical well orthogonal fracture 10 m C

Figure A2.6: Imaginary component of electric field in the Z-direction for a orthogonal fracture of half-length 10 m in a vertical wellbore through steel casing



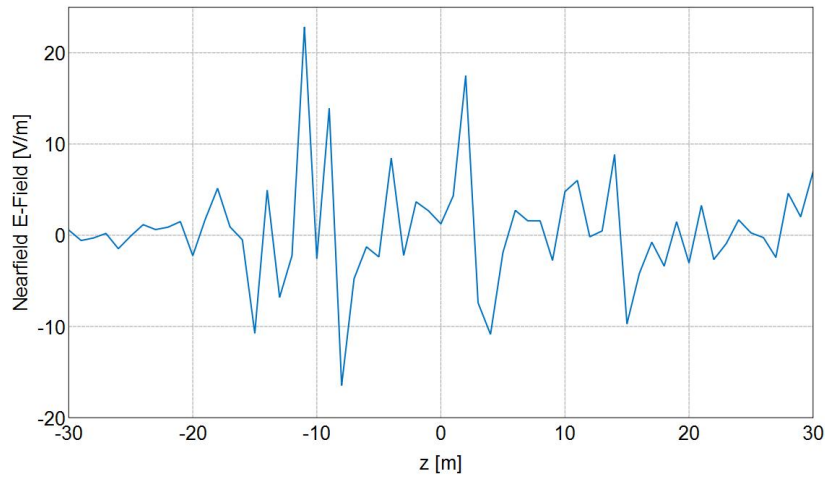
Real Z H-Field [Frequency = 100 Hz; x = 0 m; y = 0 m] - Vertical well orthogonal fracture 10 m CH

Figure A2.7: Real component of magnetic field in the Z-direction for a orthogonal fracture of half-length 10 m in a vertical wellbore through steel casing



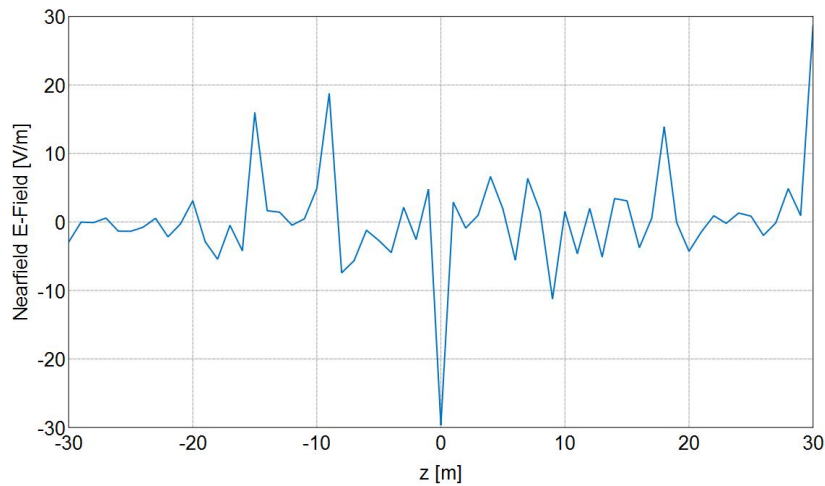
Imaginary Z H-Field [Frequency = 100 Hz; x = 0 m; y = 0 m] - Vertical well orthogonal fracture 10 m C

Figure A2.8: Imaginary component of magnetic field in the Z-direction for a orthogonal fracture of half-length 10 m in a vertical wellbore through steel casing



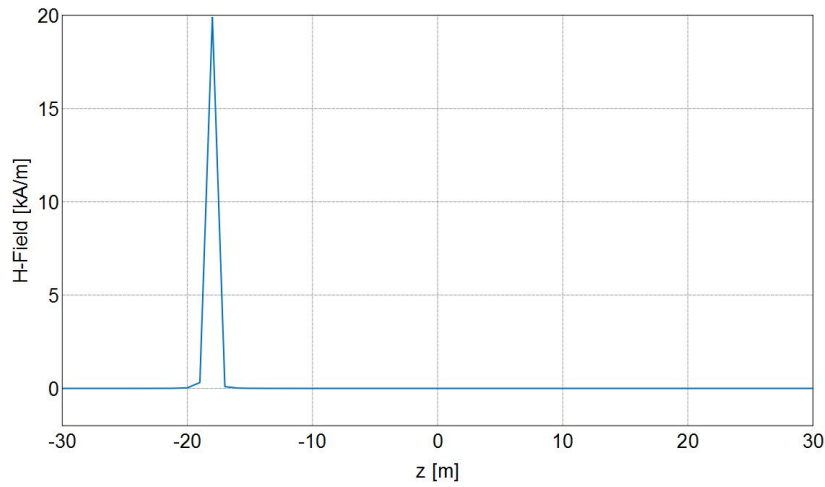
Real Z E-Field [Frequency = 100 Hz; x = 0 m; y = 0 m] - Vertical well orthogonal fracture 15 m CH

Figure A2.9: Real component of electric field in the Z-direction for a orthogonal fracture of half-length 15 m in a vertical wellbore through steel casing



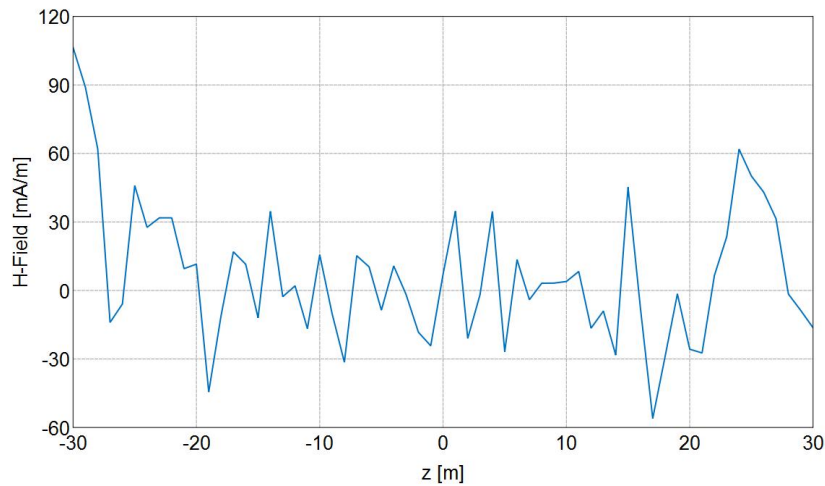
Imaginary Z E-Field [Frequency = 100 Hz; x = 0 m; y = 0 m] - Vertical well orthogonal fracture 15 m C

Figure A2.10: Imaginary component of electric field in the Z-direction for a orthogonal fracture of half-length 15 m in a vertical wellbore through steel casing



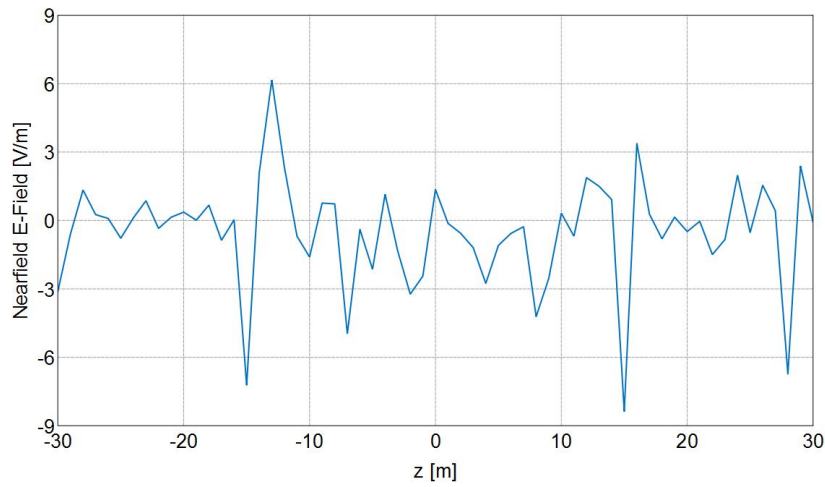
Real Z H-Field [Frequency = 100 Hz; x = 0 m; y = 0 m] - Vertical well orthogonal fracture 15 m CH

Figure A2.11: Real component of magnetic field in the Z-direction for a orthogonal fracture of half-length 15 m in a vertical wellbore through steel casing



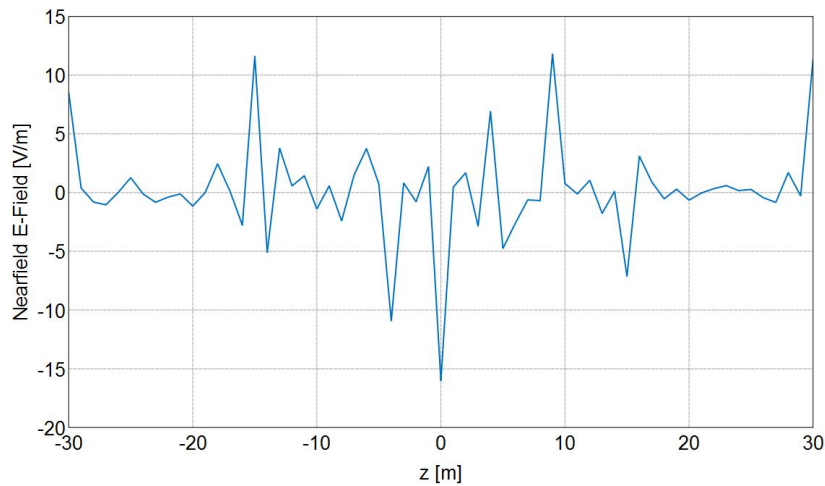
Imaginary Z H-Field [Frequency = 100 Hz; x = 0 m; y = 0 m] - Vertical well orthogonal fracture 15 m C

Figure A2.12: Imaginary component of magnetic field in the Z-direction for a orthogonal fracture of half-length 15 m in a vertical wellbore through steel casing



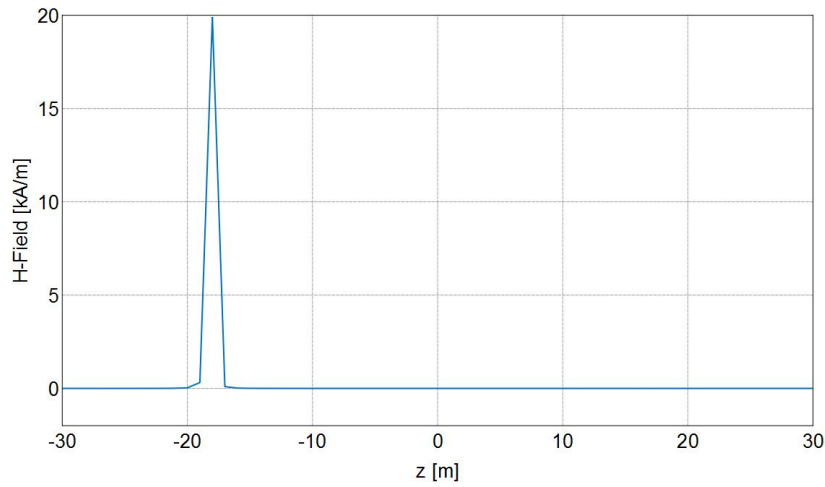
Real Z E-Field [Frequency = 100 Hz; x = 0 m; y = 0 m] - Vertical well orthogonal fracture 20 m CH

Figure A2.13: Real component of electric field in the Z-direction for a orthogonal fracture of half-length 20 m in a vertical wellbore through steel casing



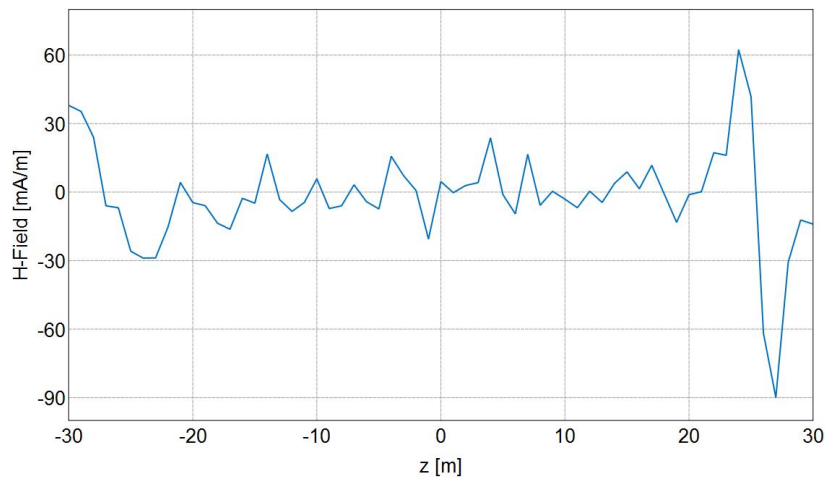
Imaginary Z E-Field [Frequency = 100 Hz; x = 0 m; y = 0 m] - Vertical well orthogonal fracture 20 m C

Figure A2.14: Imaginary component of electric field in the Z-direction for a orthogonal fracture of half-length 20 m in a vertical wellbore through steel casing



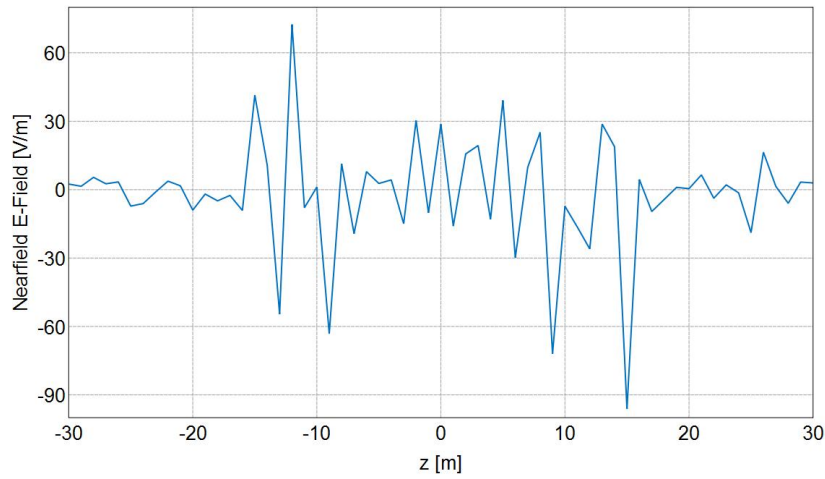
Real Z H-Field [Frequency = 100 Hz; x = 0 m; y = 0 m] - Vertical well orthogonal fracture 20 m CH

Figure A2.15: Real component of magnetic field in the Z-direction for a orthogonal fracture of half-length 20 m in a vertical wellbore through steel casing



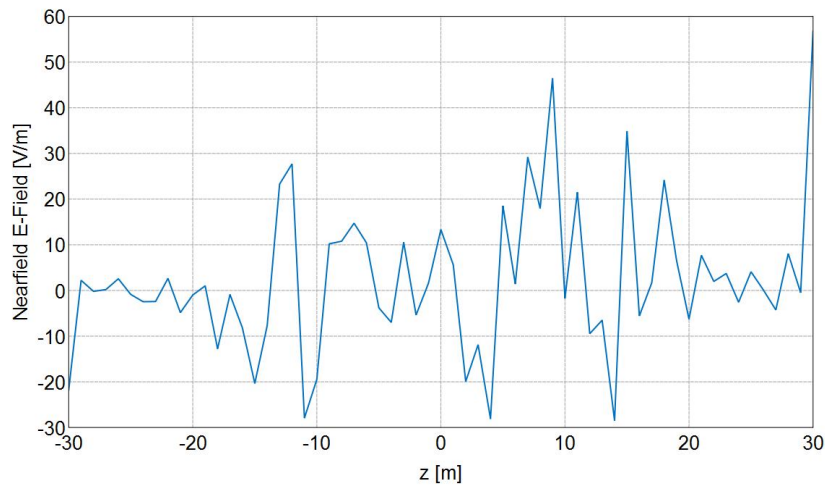
Imaginary Z H-Field [Frequency = 100 Hz; x = 0 m; y = 0 m] - Vertical well orthogonal fracture 20 m C

Figure A2.16: Imaginary component of magnetic field in the Z-direction for a orthogonal fracture of half-length 20 m in a vertical wellbore through steel casing



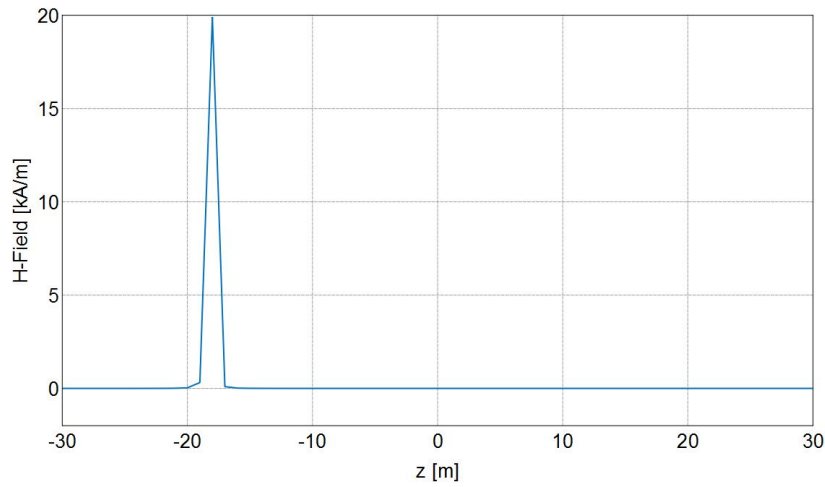
Real Z E-Field [Frequency = 100 Hz; x = 0 m; y = 0 m] - Vertical well orthogonal fracture 25 m CH

Figure A2.17: Real component of electric field in the Z-direction for a orthogonal fracture of half-length 25 m in a vertical wellbore through steel casing



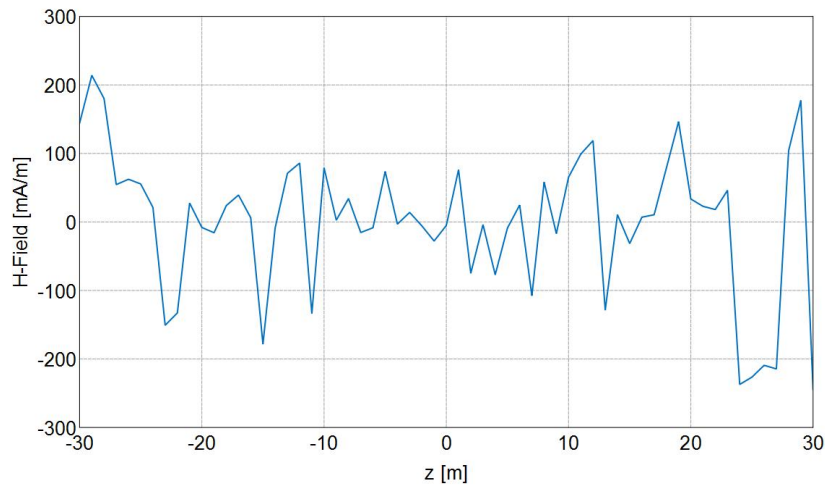
Imaginary Z E-Field [Frequency = 100 Hz; x = 0 m; y = 0 m] - Vertical well orthogonal fracture 25 m C

Figure A2.18: Imaginary component of electric field in the Z-direction for a orthogonal fracture of half-length 25 m in a vertical wellbore through steel casing



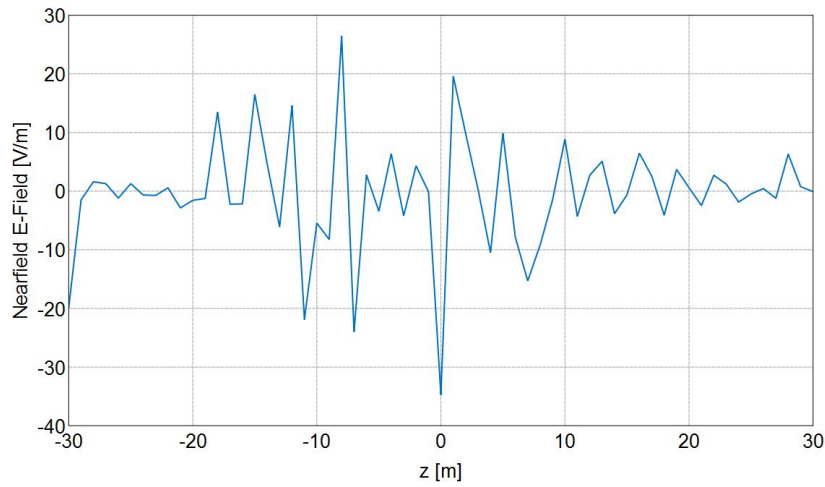
Real Z H-Field [Frequency = 100 Hz; x = 0 m; y = 0 m] - Vertical well orthogonal fracture 25 m CH

Figure A2.19: Real component of magnetic field in the Z-direction for a orthogonal fracture of half-length 25 m in a vertical wellbore through steel casing



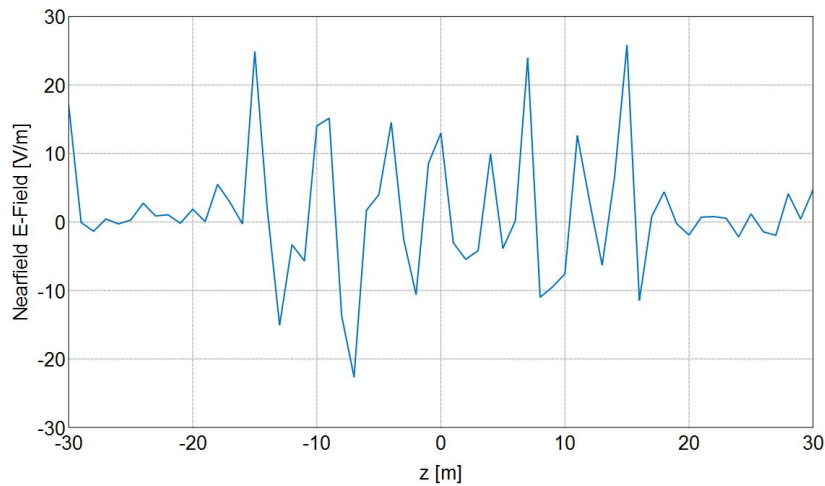
Imaginary Z H-Field [Frequency = 100 Hz; x = 0 m; y = 0 m] - Vertical well orthogonal fracture 25 m C

Figure A2.20: Imaginary component of magnetic field in the Z-direction for a orthogonal fracture of half-length 25 m in a vertical wellbore through steel casing



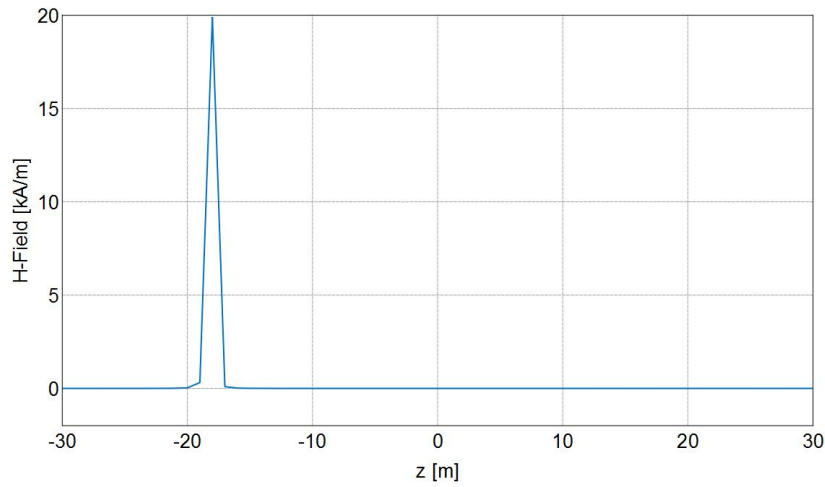
Real Z E-Field [Frequency = 100 Hz; x = 0 m; y = 0 m] - Vertical well orthogonal fracture 30 m CH

Figure A2.21: Real component of electric field in the Z-direction for a orthogonal fracture of half-length 30 m in a vertical wellbore through steel casing



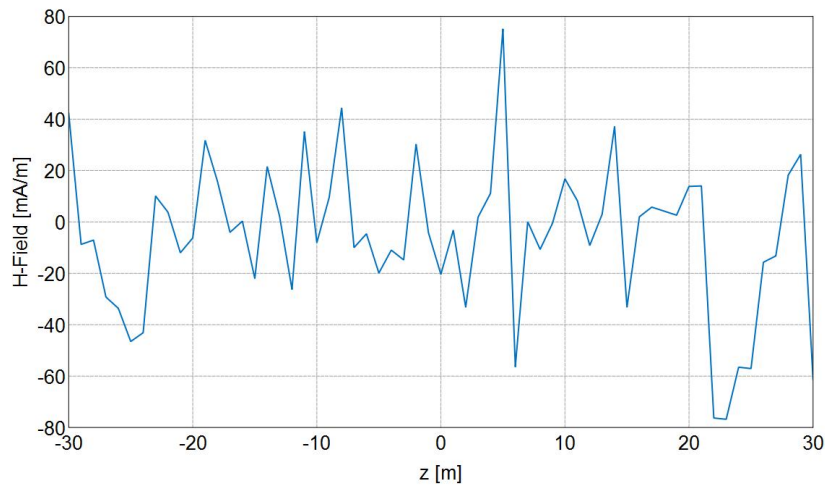
Imaginary Z E-Field [Frequency = 100 Hz; x = 0 m; y = 0 m] - Vertical well orthogonal fracture 30 m C

Figure A2.22: Imaginary component of electric field in the Z-direction for a orthogonal fracture of half-length 30 m in a vertical wellbore through steel casing



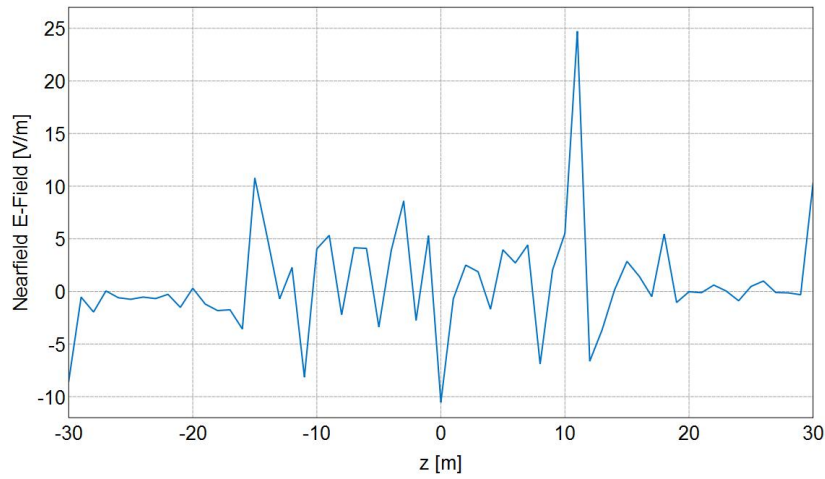
Real Z H-Field [Frequency = 100 Hz; x = 0 m; y = 0 m] - Vertical well orthogonal fracture 30 m CH

Figure A2.23: Real component of magnetic field in the Z-direction for a orthogonal fracture of half-length 30 m in a vertical wellbore through steel casing



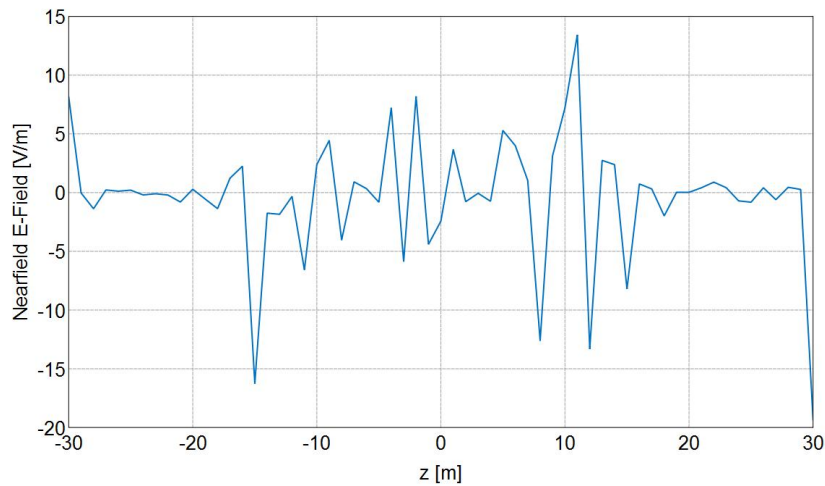
Imaginary Z H-Field [Frequency = 100 Hz; x = 0 m; y = 0 m] - Vertical well orthogonal fracture 30 m C

Figure A2.24: Imaginary component of magnetic field in the Z-direction for a orthogonal fracture of half-length 30 m in a vertical wellbore through steel casing



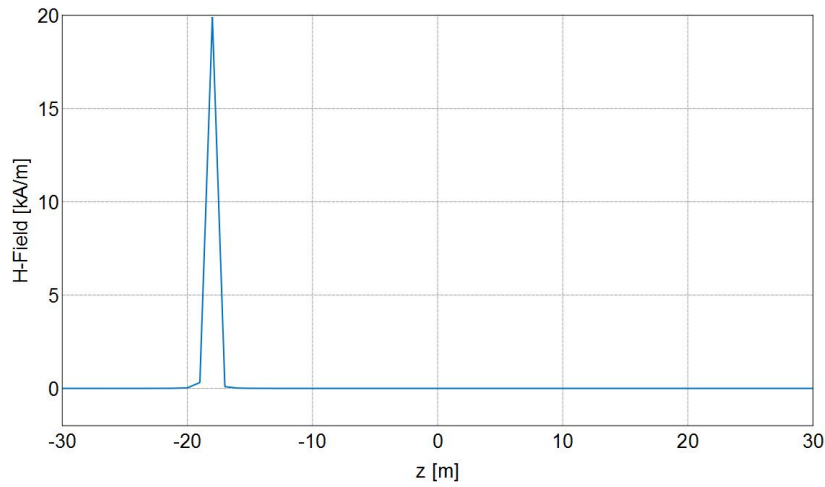
Real Z E-Field [Frequency = 100 Hz; x = 0 m; y = 0 m] - Vertical well orthogonal fracture 35 m CH

Figure A2.25: Real component of electric field in the Z-direction for a orthogonal fracture of half-length 35 m in a vertical wellbore through steel casing



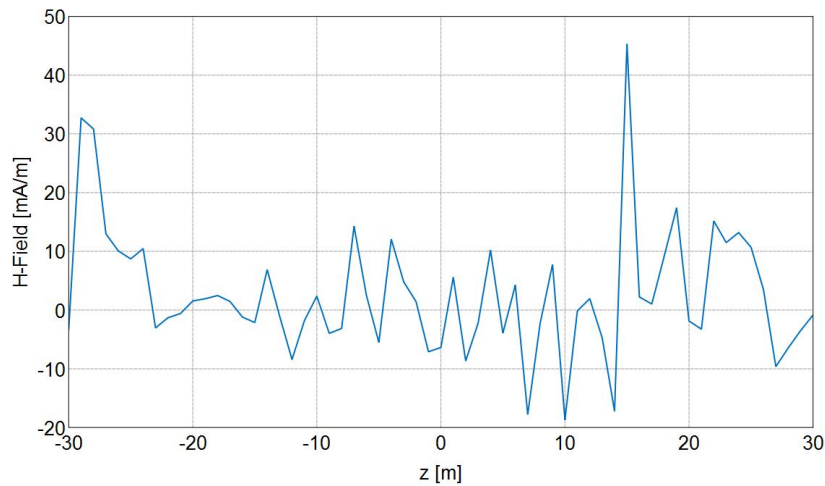
Imaginary Z E-Field [Frequency = 100 Hz; x = 0 m; y = 0 m] - Vertical well orthogonal fracture 35 m C

Figure A2.26: Imaginary component of electric field in the Z-direction for a orthogonal fracture of half-length 35 m in a vertical wellbore through steel casing



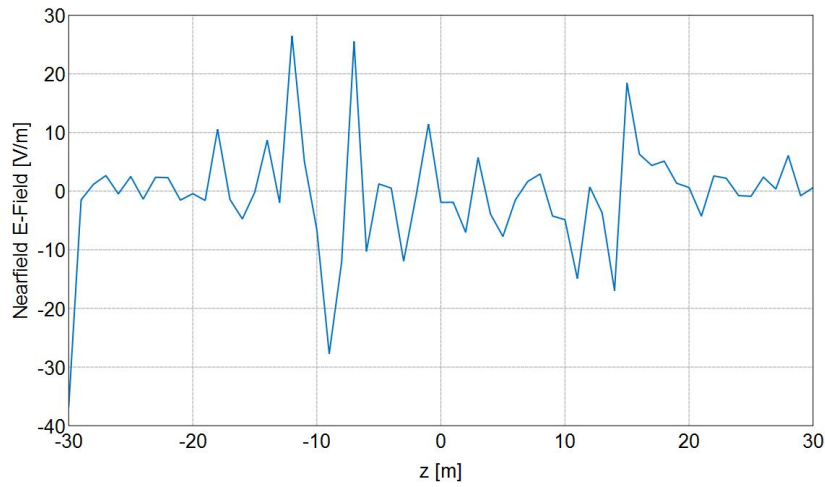
Real Z H-Field [Frequency = 100 Hz; x = 0 m; y = 0 m] - Vertical well orthogonal fracture 35 m CH

Figure A2.27: Real component of magnetic field in the Z-direction for a orthogonal fracture of half-length 35 m in a vertical wellbore through steel casing



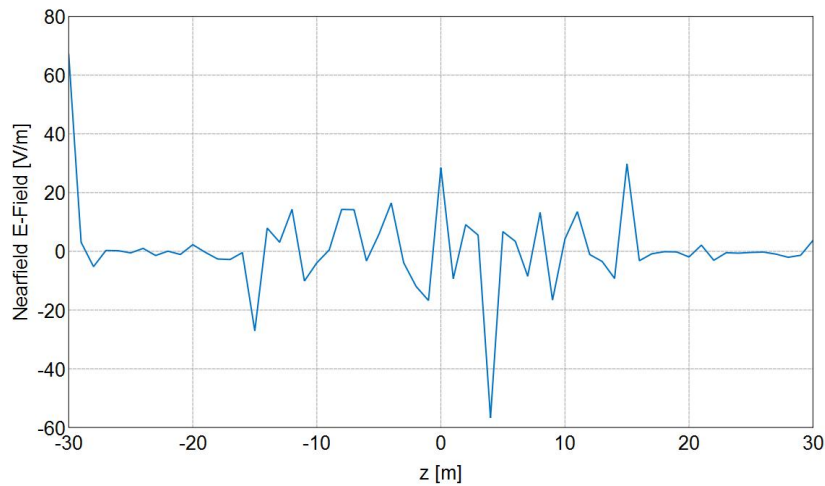
Imaginary Z H-Field [Frequency = 100 Hz; x = 0 m; y = 0 m] - Vertical well orthogonal fracture 35 m C

Figure A2.28: Imaginary component of magnetic field in the Z-direction for a orthogonal fracture of half-length 35 m in a vertical wellbore through steel casing



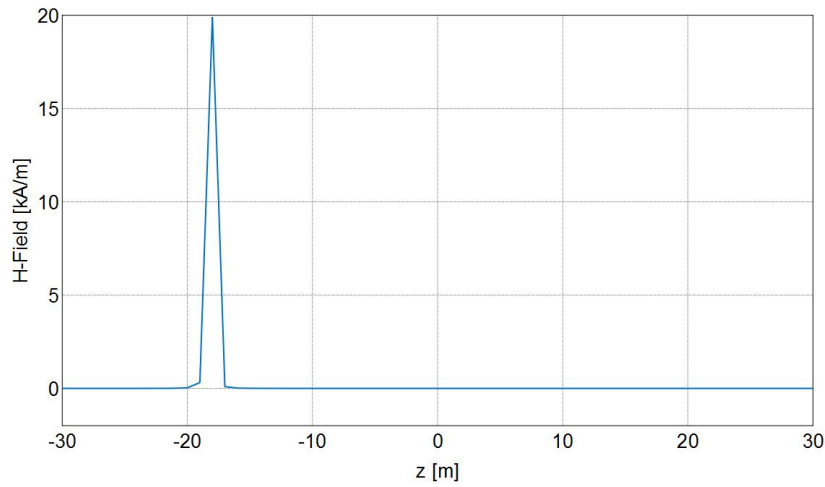
Real Z E-Field [Frequency = 100 Hz; x = 0 m; y = 0 m] - Vertical well orthogonal fracture 40 m CH

Figure A2.29: Real component of electric field in the Z-direction for a orthogonal fracture of half-length 40 m in a vertical wellbore through steel casing



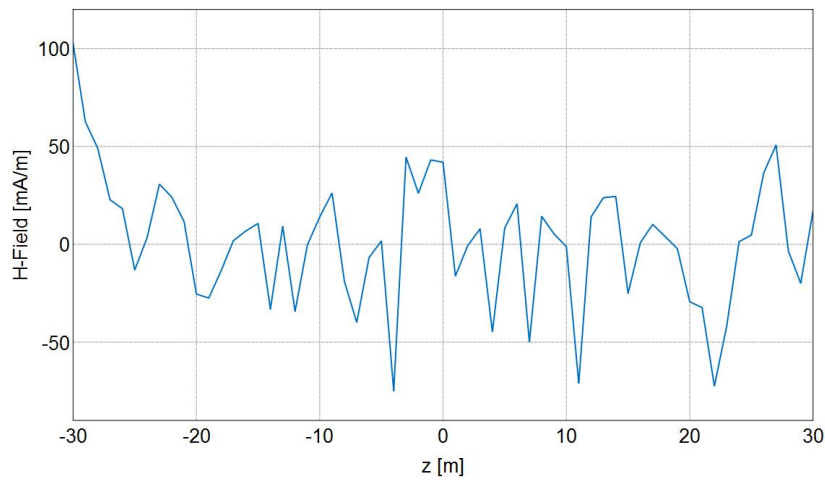
Imaginary Z E-Field [Frequency = 100 Hz; x = 0 m; y = 0 m] - Vertical well orthogonal fracture 40 m C

Figure A2.30: Imaginary component of electric field in the Z-direction for a orthogonal fracture of half-length 40 m in a vertical wellbore through steel casing



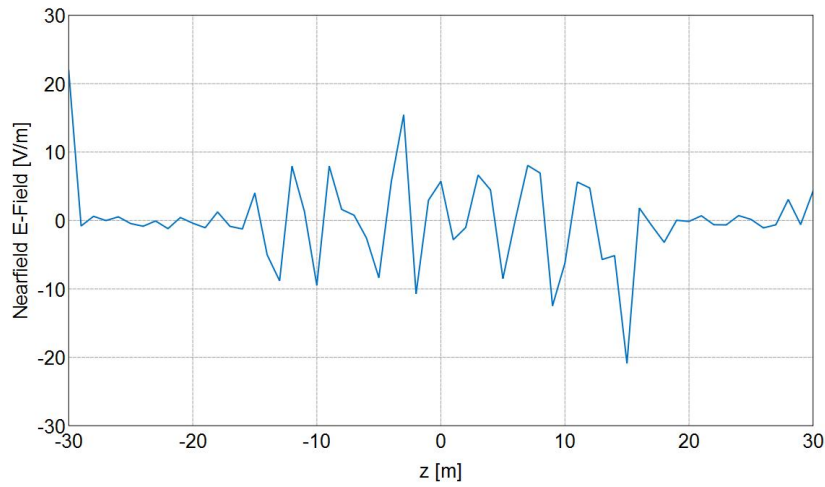
Real Z H-Field [Frequency = 100 Hz; x = 0 m; y = 0 m] - Vertical well orthogonal fracture 40 m CH

Figure A2.31: Real component of magnetic field in the Z-direction for a orthogonal fracture of half-length 40 m in a vertical wellbore through steel casing



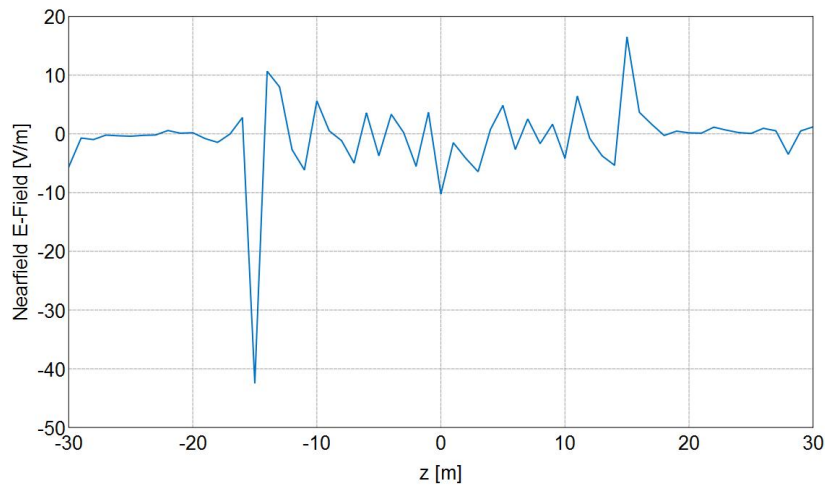
Imaginary Z H-Field [Frequency = 100 Hz; x = 0 m; y = 0 m] - Vertical well orthogonal fracture 40 m C

Figure A2.32: Imaginary component of magnetic field in the Z-direction for a orthogonal fracture of half-length 40 m in a vertical wellbore through steel casing



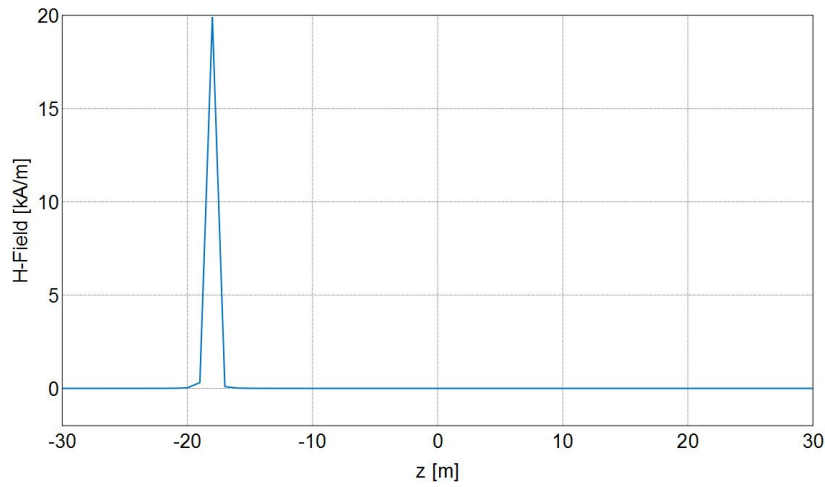
Real Z E-Field [Frequency = 100 Hz; x = 0 m; y = 0 m] - Vertical well orthogonal fracture 45 m CH

Figure A2.33: Real component of electric field in the Z-direction for a orthogonal fracture of half-length 45 m in a vertical wellbore through steel casing



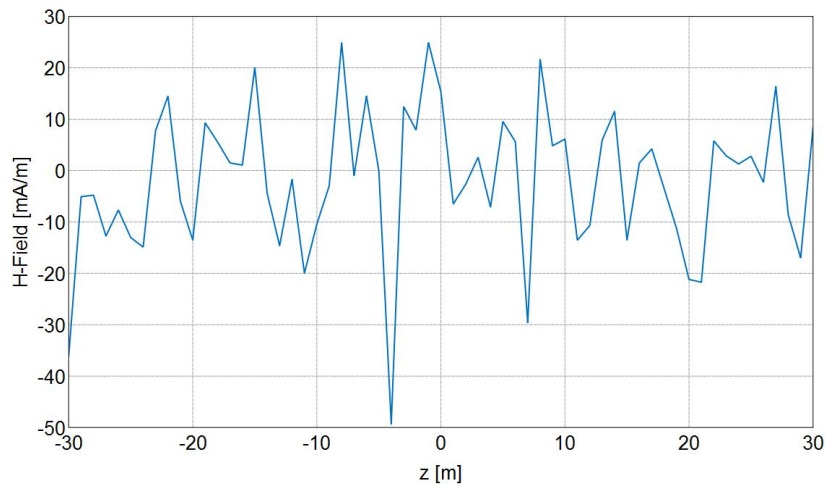
Imaginary Z E-Field [Frequency = 100 Hz; x = 0 m; y = 0 m] - Vertical well orthogonal fracture 45 m C

Figure A2.34: Imaginary component of electric field in the Z-direction for a orthogonal fracture of half-length 45 m in a vertical wellbore through steel casing



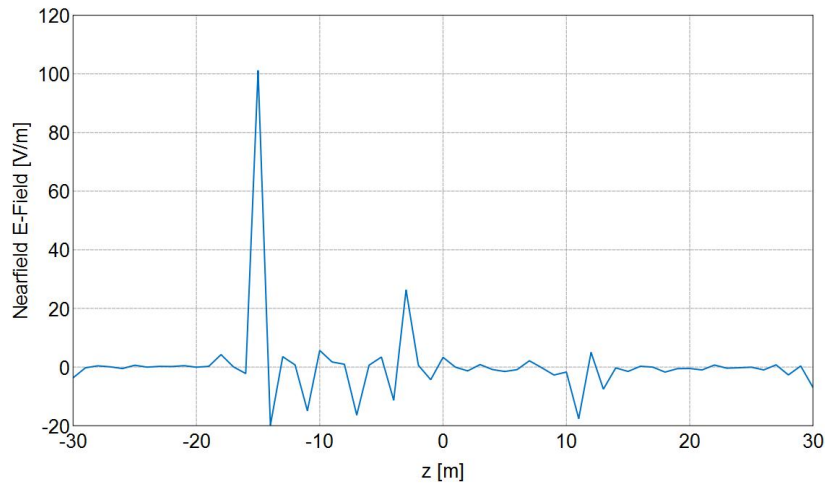
Real Z H-Field [Frequency = 100 Hz; x = 0 m; y = 0 m] - Vertical well orthogonal fracture 45 m CH

Figure A2.35: Real component of magnetic field in the Z-direction for a orthogonal fracture of half-length 45 m in a vertical wellbore through steel casing



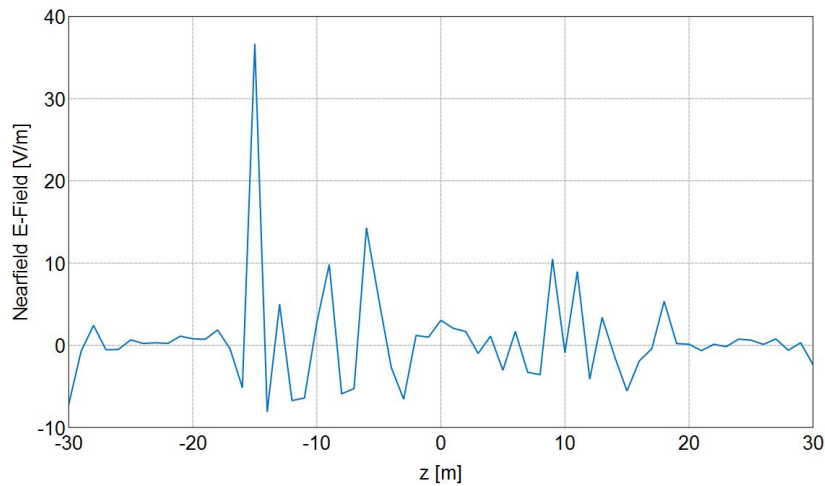
Imaginary Z H-Field [Frequency = 100 Hz; x = 0 m; y = 0 m] - Vertical well orthogonal fracture 45 m C

Figure A2.36: Imaginary component of magnetic field in the Z-direction for a orthogonal fracture of half-length 45 m in a vertical wellbore through steel casing



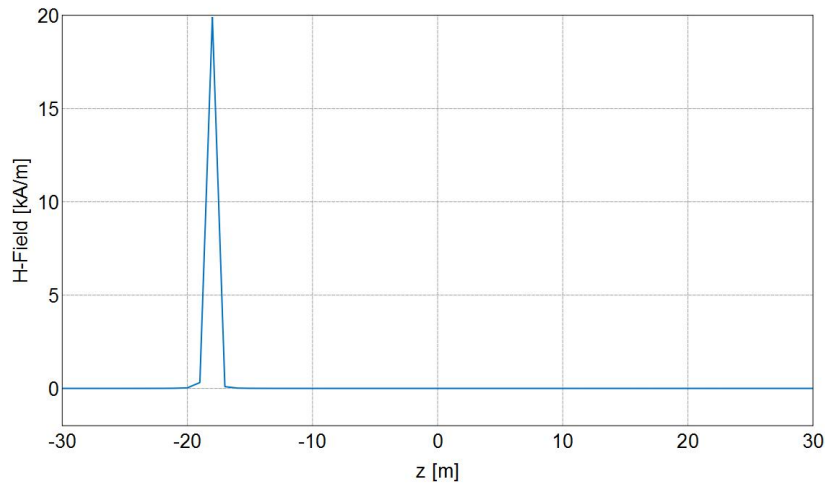
Real Z E-Field [Frequency = 100 Hz; x = 0 m; y = 0 m] - Vertical well orthogonal fracture 60 m CH

Figure A2.37: Real component of electric field in the Z-direction for a orthogonal fracture of half-length 60 m in a vertical wellbore through steel casing



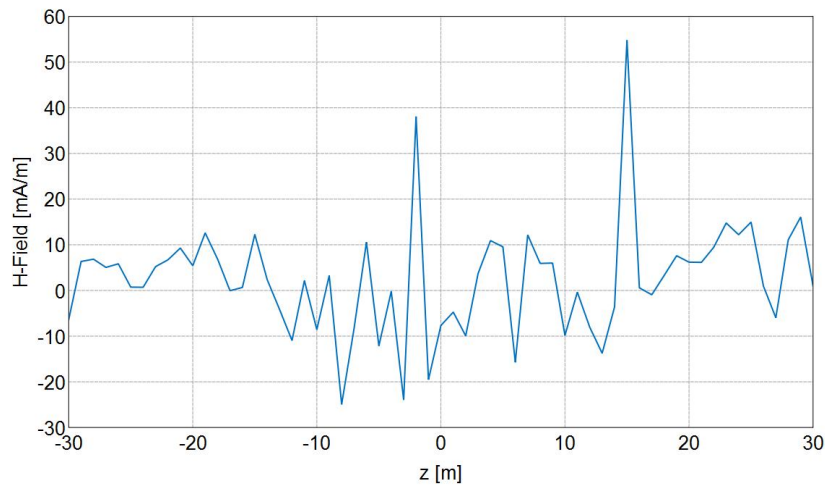
Imaginary Z E-Field [Frequency = 100 Hz; x = 0 m; y = 0 m] - Vertical well orthogonal fracture 60 m C

Figure A2.38: Imaginary component of electric field in the Z-direction for a orthogonal fracture of half-length 60 m in a vertical wellbore through steel casing



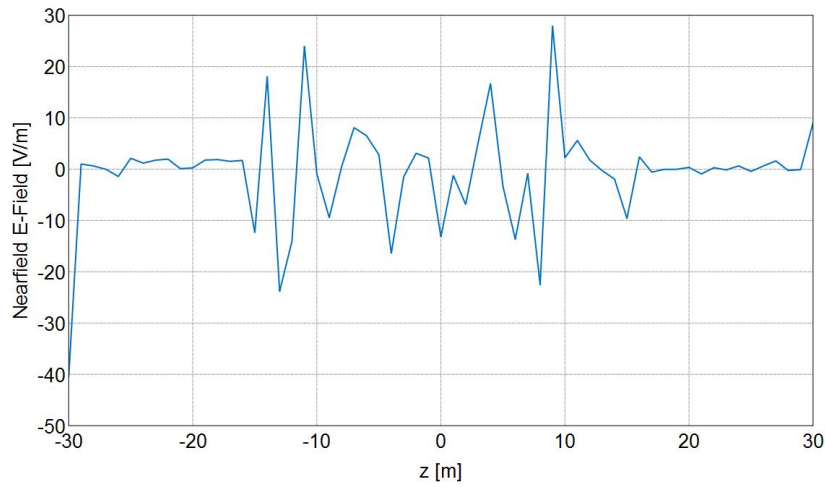
Real Z H-Field [Frequency = 100 Hz; x = 0 m; y = 0 m] - Vertical well orthogonal fracture 60 m CH

Figure A2.39: Real component of magnetic field in the Z-direction for a orthogonal fracture of half-length 60 m in a vertical wellbore through steel casing



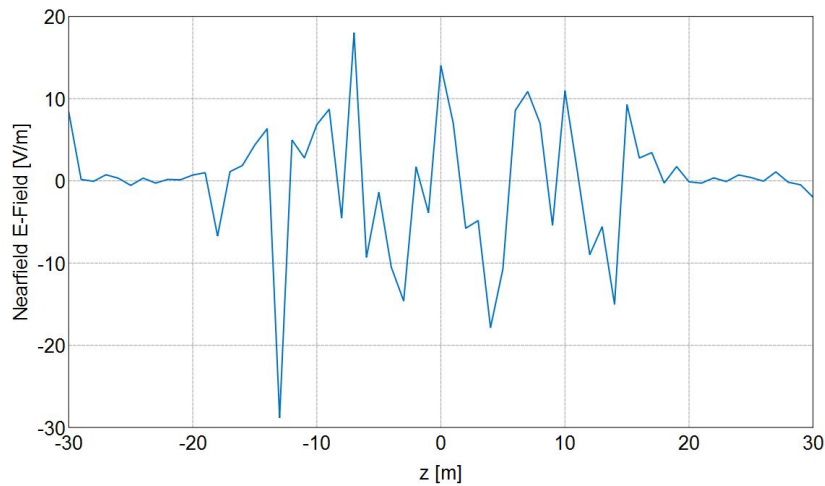
Imaginary Z H-Field [Frequency = 100 Hz; x = 0 m; y = 0 m] - Vertical well orthogonal fracture 60 m C

Figure A2.40: Imaginary component of magnetic field in the Z-direction for a orthogonal fracture of half-length 60 m in a vertical wellbore through steel casing



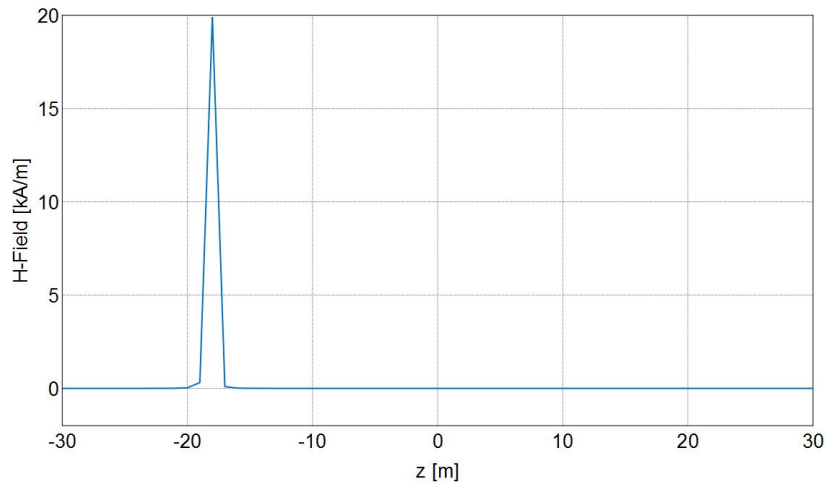
Real Z E-Field [Frequency = 100 Hz; x = 0 m; y = 0 m] - Vertical well orthogonal fracture 75 m CH

Figure A2.41: Real component of electric field in the Z-direction for a orthogonal fracture of half-length 75 m in a vertical wellbore through steel casing



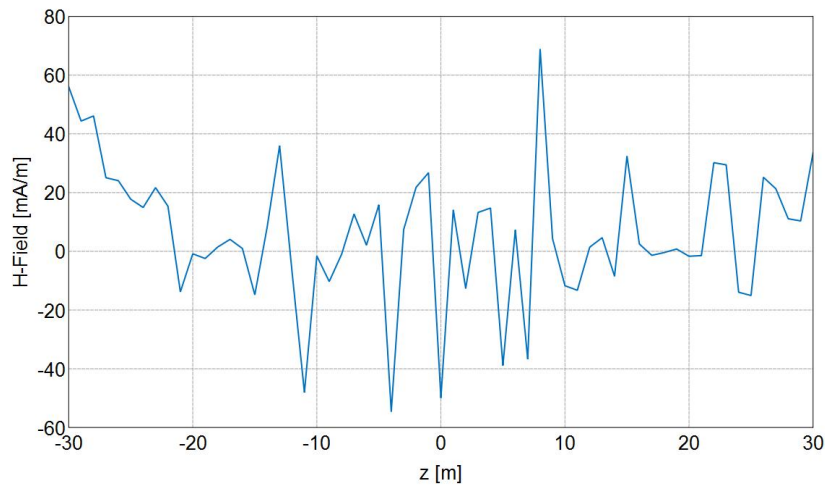
Imaginary Z E-Field [Frequency = 100 Hz; x = 0 m; y = 0 m] - Vertical well orthogonal fracture 75 m C

Figure A2.42: Imaginary component of electric field in the Z-direction for a orthogonal fracture of half-length 75 m in a vertical wellbore through steel casing



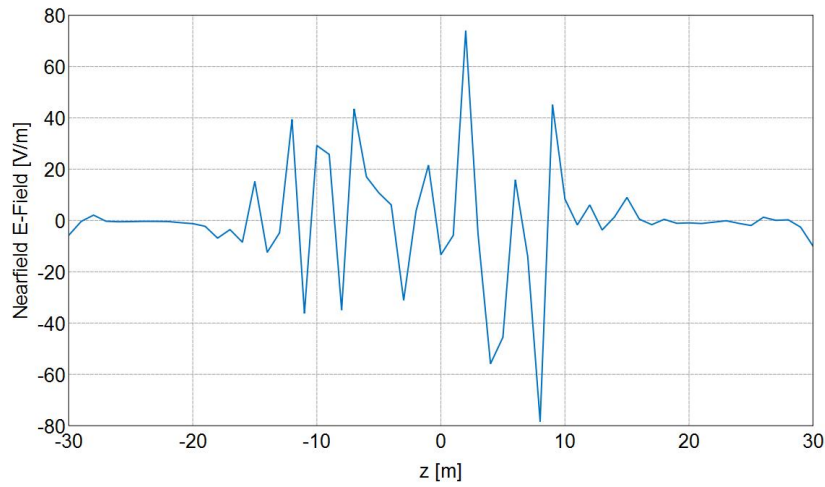
Real Z H-Field [Frequency = 100 Hz; x = 0 m; y = 0 m] - Vertical well orthogonal fracture 75 m CH

Figure A2.43: Real component of magnetic field in the Z-direction for a orthogonal fracture of half-length 75 m in a vertical wellbore through steel casing



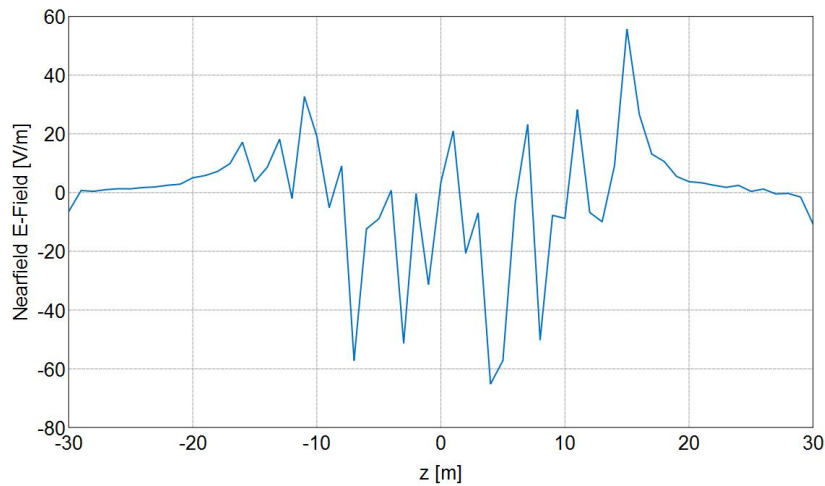
Imaginary Z H-Field [Frequency = 100 Hz; x = 0 m; y = 0 m] - Vertical well orthogonal fracture 75 m C

Figure A2.44: Imaginary component of magnetic field in the Z-direction for a orthogonal fracture of half-length 75 m in a vertical wellbore through steel casing



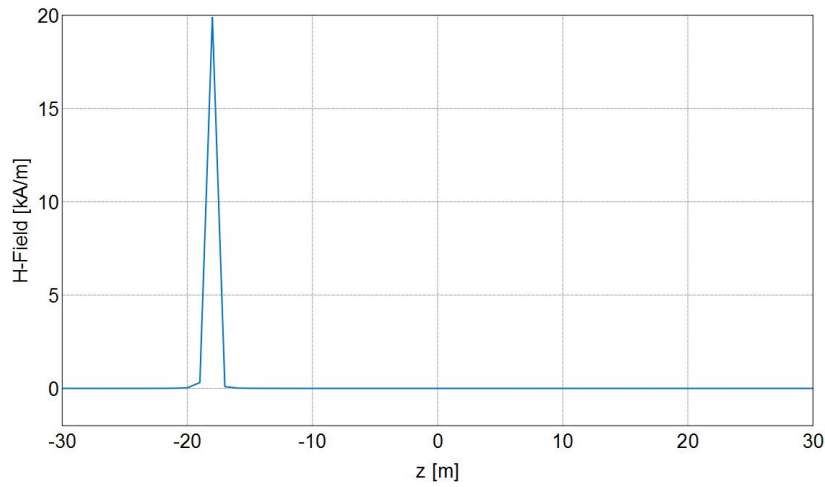
Real Z E-Field [Frequency = 100 Hz; x = 0 m; y = 0 m] - Vertical well orthogonal fracture 100 m CH

Figure A2.45: Real component of electric field in the Z-direction for a orthogonal fracture of half-length 100 m in a vertical wellbore through steel casing



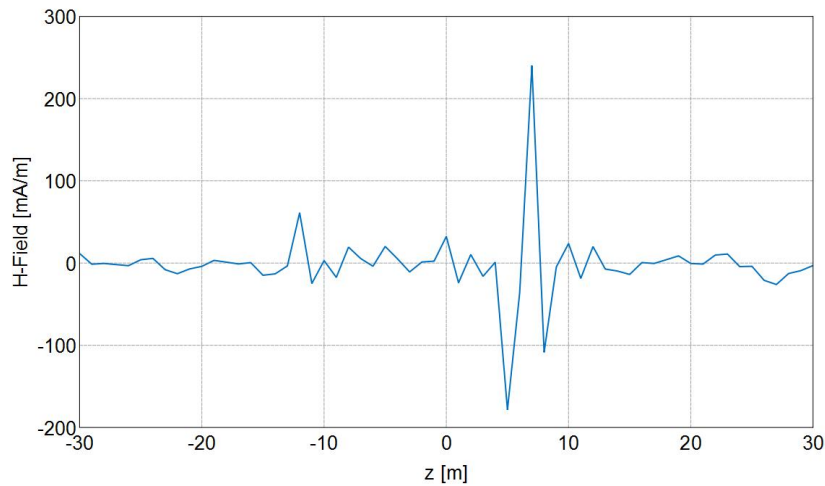
Imaginary Z E-Field [Frequency = 100 Hz; x = 0 m; y = 0 m] - Vertical well orthogonal fracture 100 m C

Figure A2.46: Imaginary component of electric field in the Z-direction for a orthogonal fracture of half-length 100 m in a vertical wellbore through steel casing



Real Z H-Field [Frequency = 100 Hz; x = 0 m; y = 0 m] - Vertical well orthogonal fracture 100 m CH

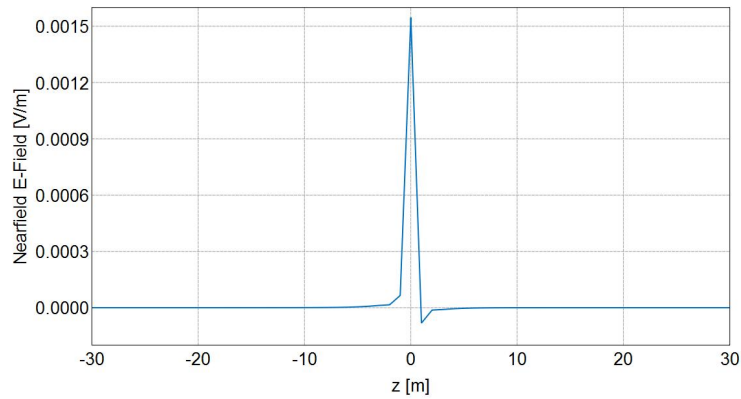
Figure A2.47: Real component of magnetic field in the Z-direction for a orthogonal fracture of half-length 100 m in a vertical wellbore through steel casing



Imaginary Z H-Field [Frequency = 100 Hz; x = 0 m; y = 0 m] - Vertical well orthogonal fracture 100 m CH

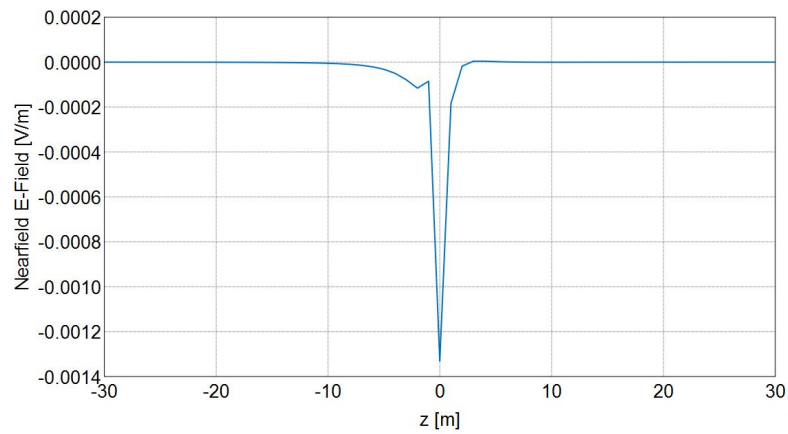
Figure A2.48: Imaginary component of magnetic field in the Z-direction for a orthogonal fracture of half-length 100 m in a vertical wellbore through steel casing

### A3. RAW ELECTRIC AND MAGNETIC FIELD RESPONSES FOR AN ORTHOGONAL FRACTURE IN HORIZONTAL WELL (OPEN HOLE COMPLETION)



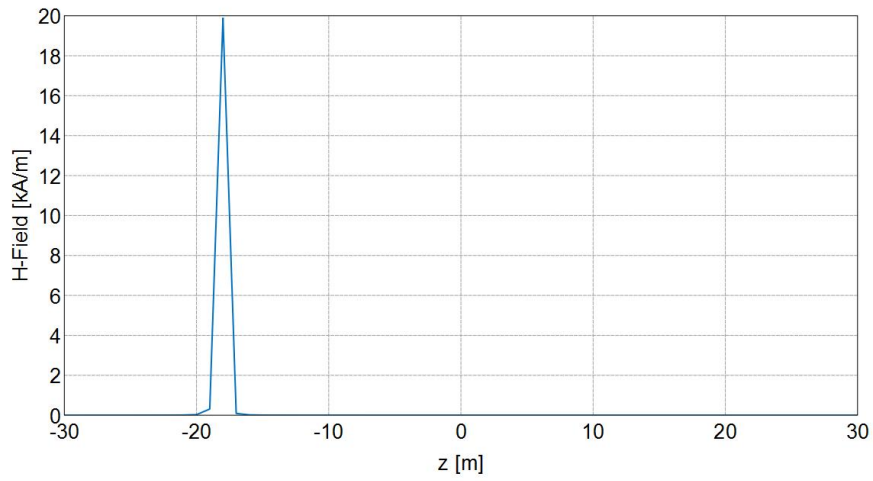
Real Z E-Field [Frequency = 100 Hz; x = 0 m; y = 0 m] - Horizontal well orthogonal fracture 5 m

Figure A3.1: Real component of electric field in the Z-direction for a orthogonal fracture of half-length 5 m in a horizontal wellbore



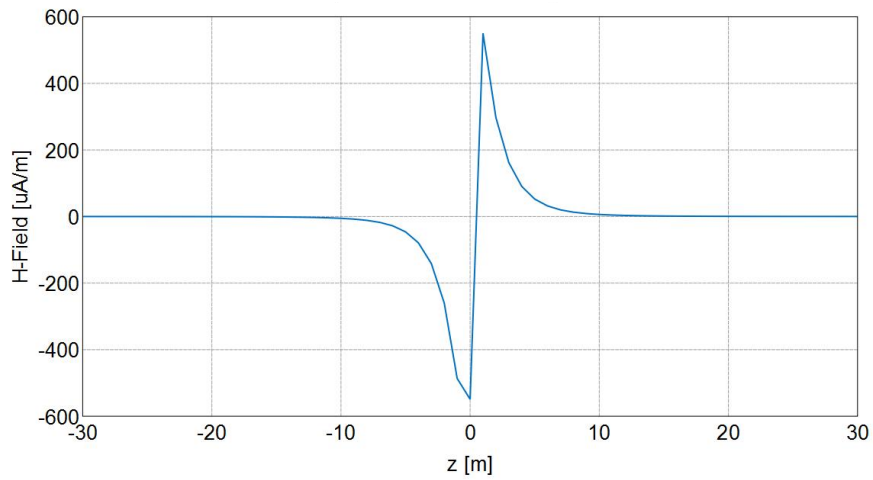
maginary Z E-Field [Frequency = 100 Hz; x = 0 m; y = 0 m] - Horizontal well orthogonal fracture 5 m

Figure A3.2: Imaginary component of electric field in the Z-direction for a orthogonal fracture of half-length 5 m in a horizontal wellbore



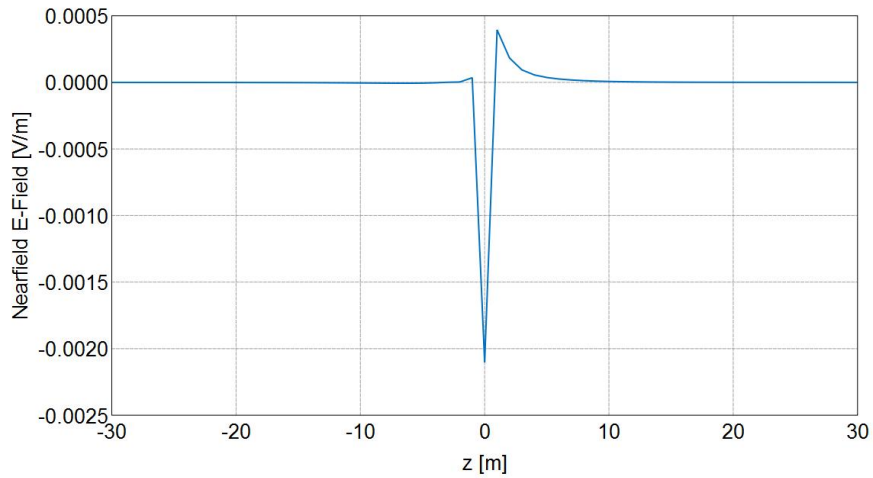
Real Z H-Field [Frequency = 100 Hz; x = 0 m; y = 0 m] - Horizontal well orthogonal fracture 5 m

Figure A3.3: Real component of magnetic field in the Z-direction for a orthogonal fracture of half-length 5 m in a horizontal wellbore



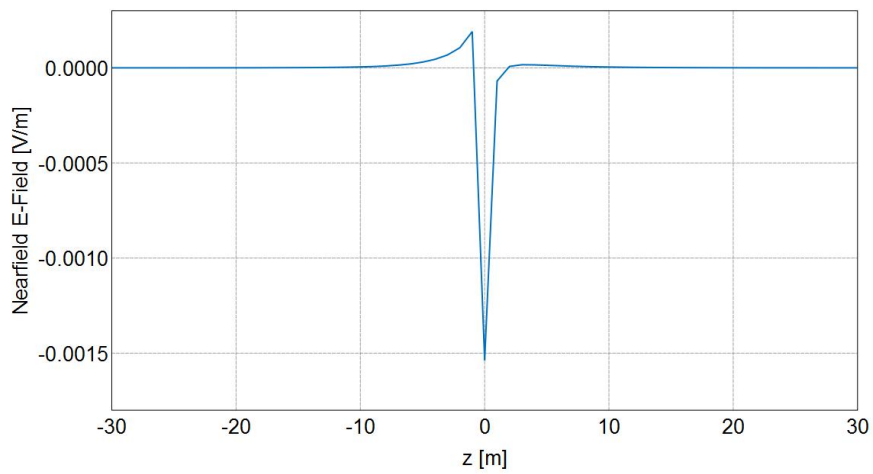
maginary Z H-Field [Frequency = 100 Hz; x = 0 m; y = 0 m] - Horizontal well orthogonal fracture 5 m

Figure A3.4: Imaginary component of magnetic field in the Z-direction for a orthogonal fracture of half-length 5 m in a horizontal wellbore



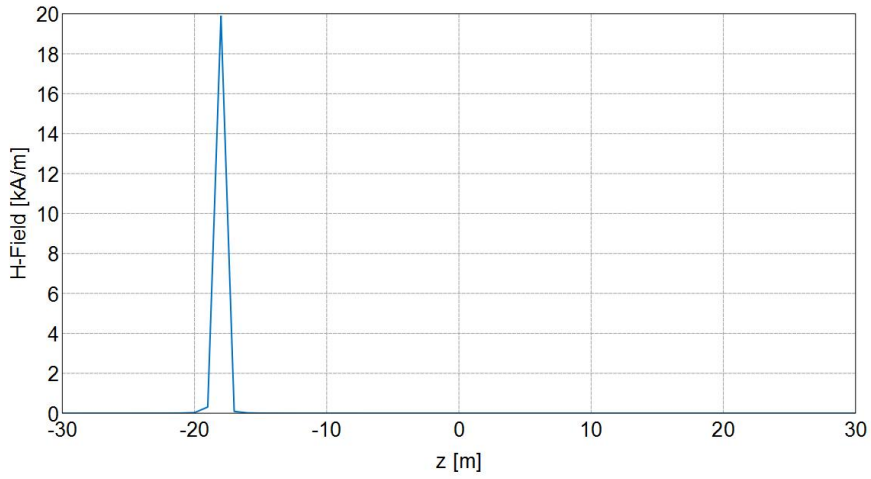
Real Z E-Field [Frequency = 100 Hz; x = 0 m; y = 0 m] - Horizontal well orthogonal fracture 10 m

Figure A3.5: Real component of electric field in the Z-direction for a orthogonal fracture of half-length 10 m in a horizontal wellbore



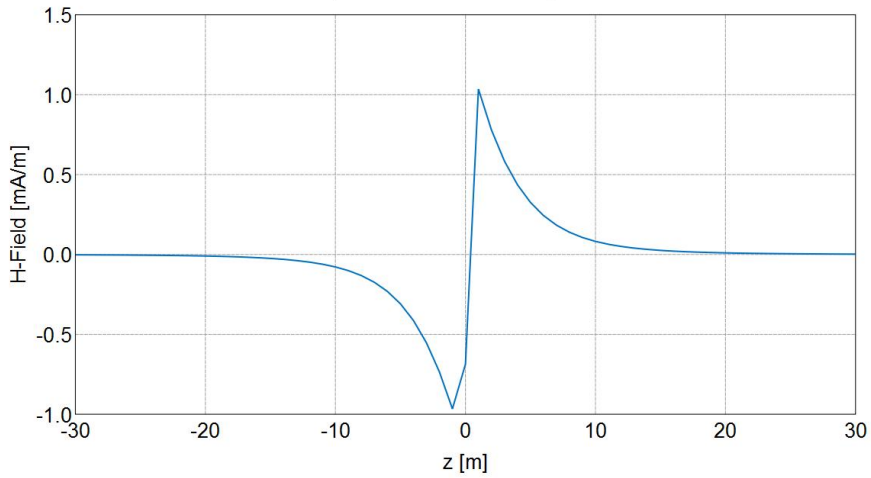
maginary Z E-Field [Frequency = 100 Hz; x = 0 m; y = 0 m] - Horizontal well orthogonal fracture 10 r

Figure A3.6: Imaginary component of electric field in the Z-direction for a orthogonal fracture of half-length 10 m in a horizontal wellbore



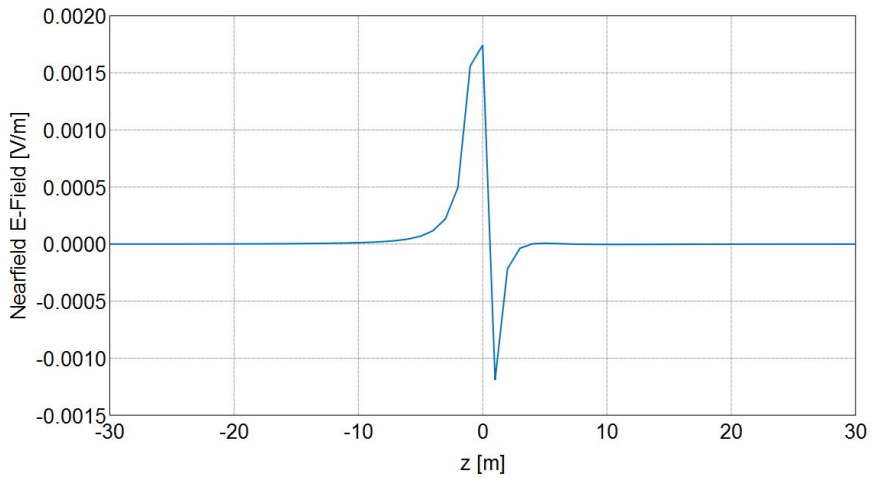
Real Z H-Field [Frequency = 100 Hz; x = 0 m; y = 0 m] - Horizontal well orthogonal fracture 10 m

Figure A3.7: Real component of magnetic field in the Z-direction for a orthogonal fracture of half-length 10 m in a horizontal wellbore



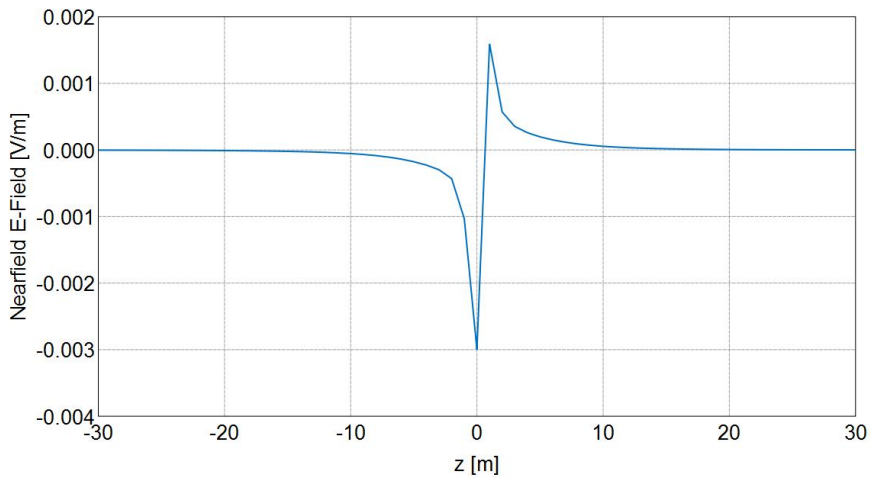
Imaginary Z H-Field [Frequency = 100 Hz; x = 0 m; y = 0 m] - Horizontal well orthogonal fracture 10 m

Figure A3.8: Imaginary component of magnetic field in the Z-direction for a orthogonal fracture of half-length 10 m in a horizontal wellbore



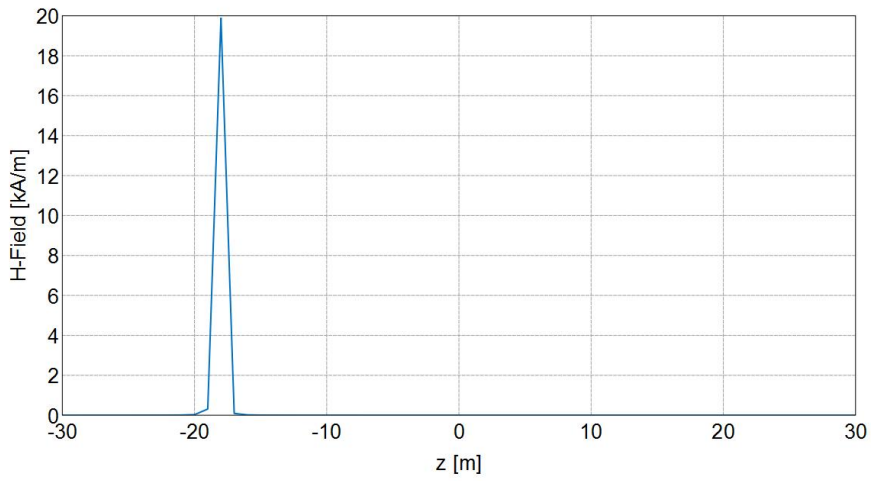
Real Z E-Field [Frequency = 100 Hz; x = 0 m; y = 0 m] - Horizontal well orthogonal fracture 15 m

Figure A3.9: Real component of electric field in the Z-direction for a orthogonal fracture of half-length 15 m in a horizontal wellbore



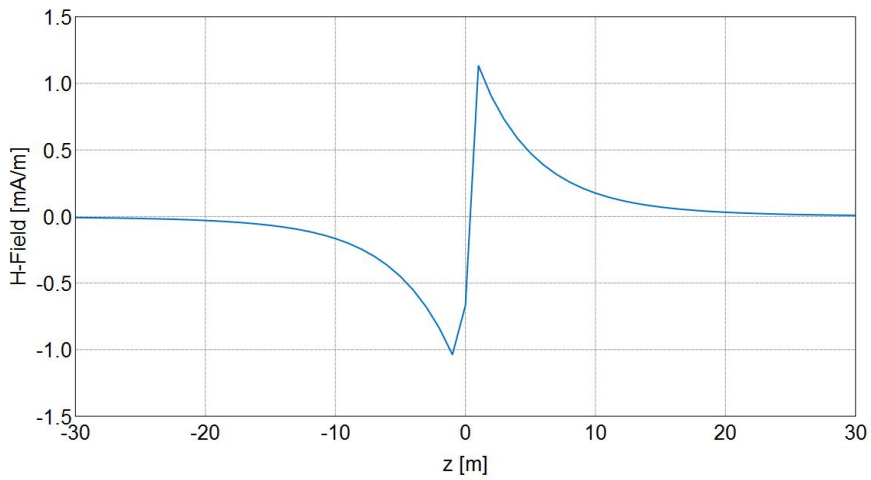
Imaginary Z E-Field [Frequency = 100 Hz; x = 0 m; y = 0 m] - Horizontal well orthogonal fracture 15 m

Figure A3.10: Imaginary component of electric field in the Z-direction for a orthogonal fracture of half-length 15 m in a horizontal wellbore



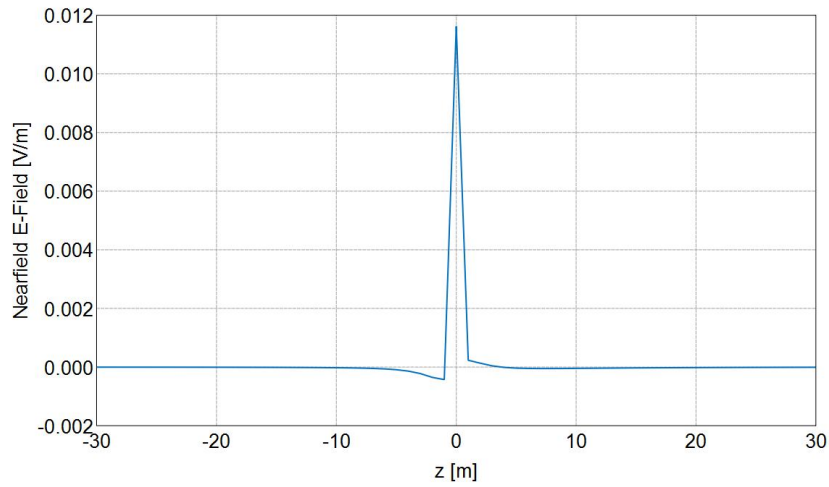
Real Z H-Field [Frequency = 100 Hz; x = 0 m; y = 0 m] - Horizontal well orthogonal fracture 15 m

Figure A3.11: Real component of magnetic field in the Z-direction for a orthogonal fracture of half-length 15 m in a horizontal wellbore



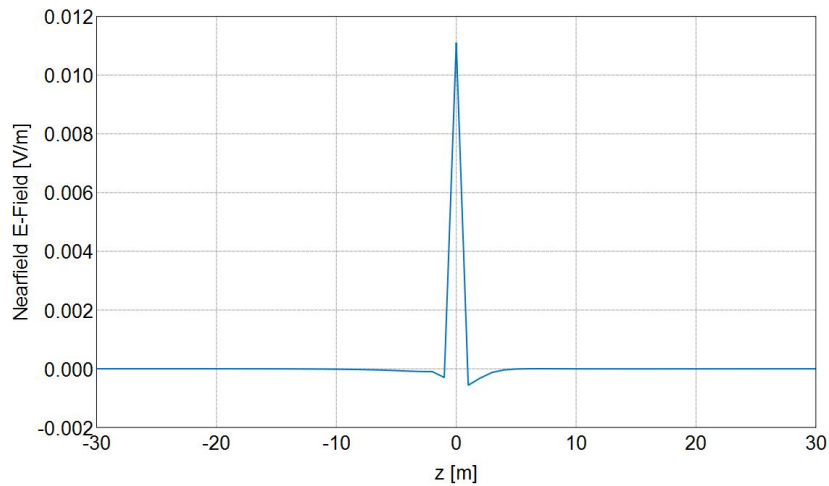
Imaginary Z H-Field [Frequency = 100 Hz; x = 0 m; y = 0 m] - Horizontal well orthogonal fracture 15 m

Figure A3.12: Imaginary component of magnetic field in the Z-direction for a orthogonal fracture of half-length 15 m in a horizontal wellbore



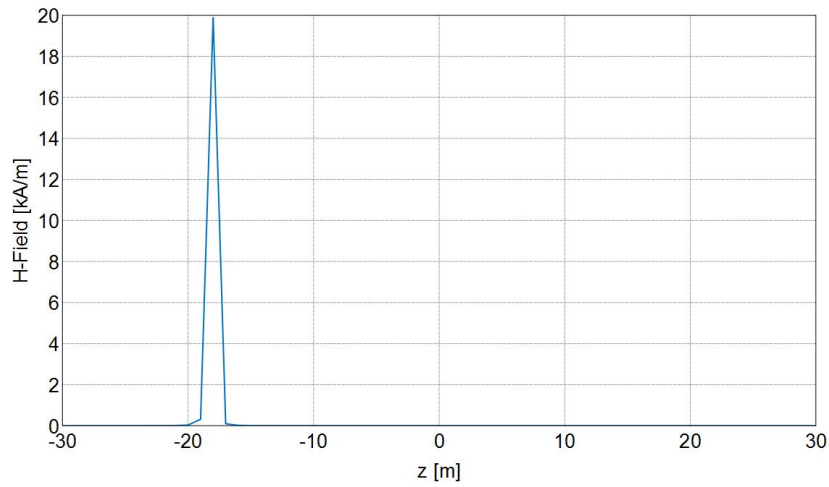
Real Z E-Field [Frequency = 100 Hz; x = 0 m; y = 0 m] - Horizontal well orthogonal fracture 20 m

Figure A3.13: Real component of electric field in the Z-direction for a orthogonal fracture of half-length 20 m in a horizontal wellbore



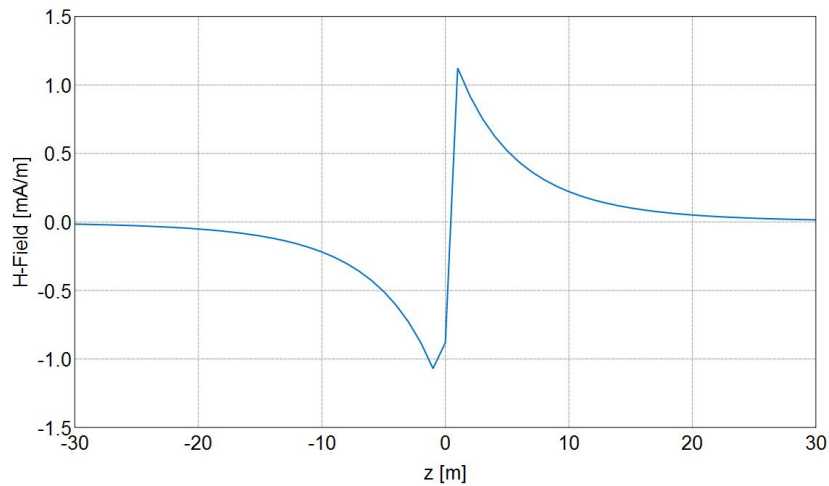
Imaginary Z E-Field [Frequency = 100 Hz; x = 0 m; y = 0 m] - Horizontal well orthogonal fracture 20 m

Figure A3.14: Imaginary component of electric field in the Z-direction for a orthogonal fracture of half-length 20 m in a horizontal wellbore



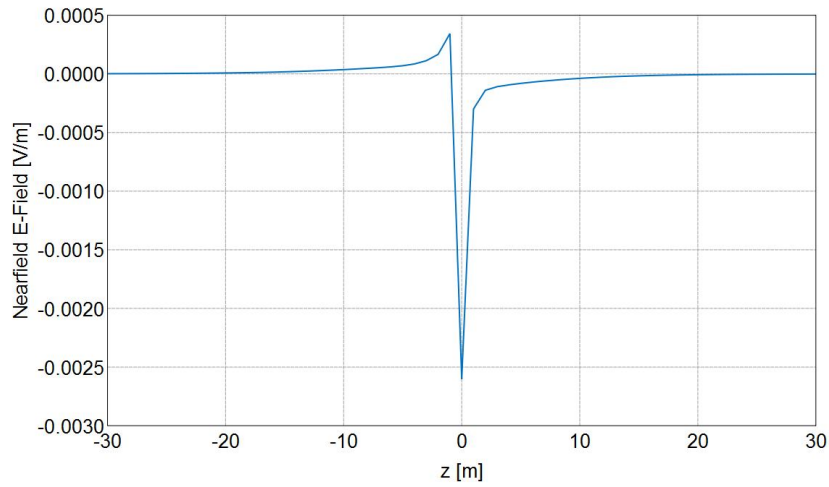
Real Z H-Field [Frequency = 100 Hz; x = 0 m; y = 0 m] - Horizontal well orthogonal fracture 20 m

Figure A3.15: Real component of magnetic field in the Z-direction for a orthogonal fracture of half-length 20 m in a horizontal wellbore



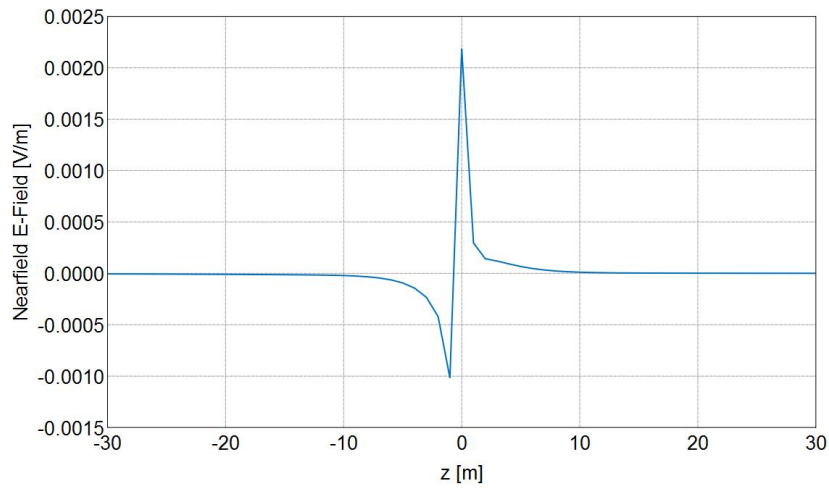
Imaginary Z H-Field [Frequency = 100 Hz; x = 0 m; y = 0 m] - Horizontal well orthogonal fracture 20 m

Figure A3.16: Imaginary component of magnetic field in the Z-direction for a orthogonal fracture of half-length 20 m in a horizontal wellbore



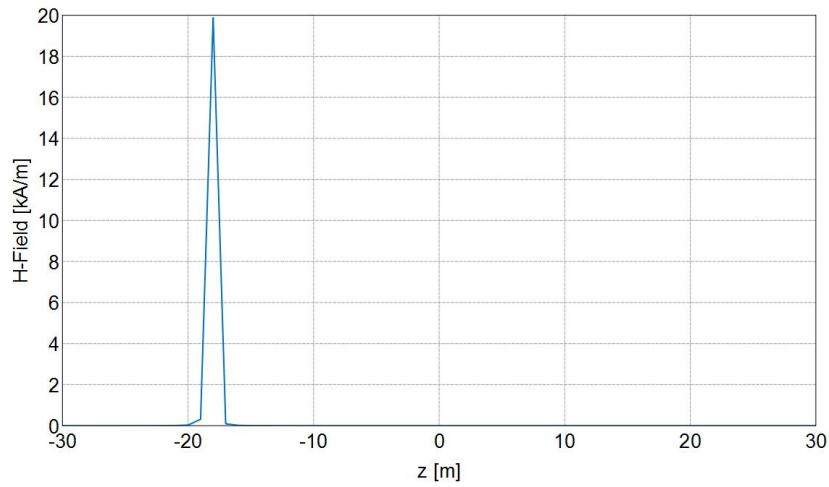
Real Z E-Field [Frequency = 100 Hz; x = 0 m; y = 0 m] - Horizontal well orthogonal fracture 25 m

Figure A3.17: Real component of electric field in the Z-direction for a orthogonal fracture of half-length 25 m in a horizontal wellbore



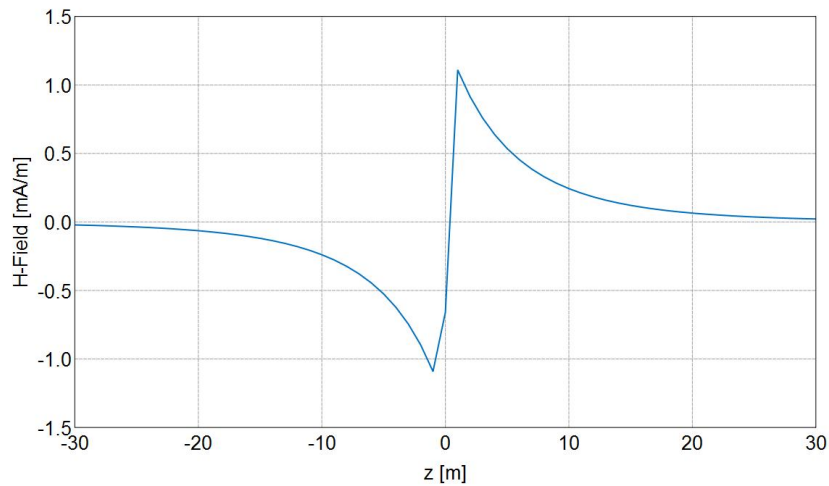
Imaginary Z E-Field [Frequency = 100 Hz; x = 0 m; y = 0 m] - Horizontal well orthogonal fracture 25 m

Figure A3.18: Imaginary component of electric field in the Z-direction for a orthogonal fracture of half-length 25 m in a horizontal wellbore



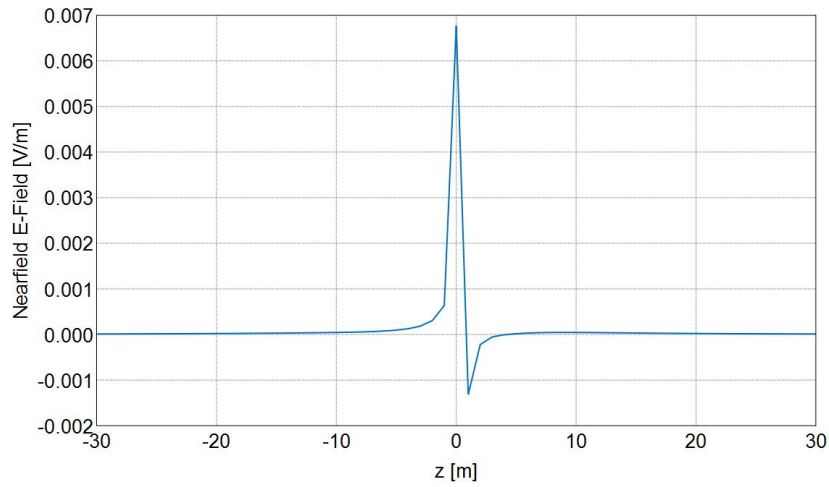
Real Z H-Field [Frequency = 100 Hz; x = 0 m; y = 0 m] - Horizontal well orthogonal fracture 25 m

Figure A3.19: Real component of magnetic field in the Z-direction for a orthogonal fracture of half-length 25 m in a horizontal wellbore



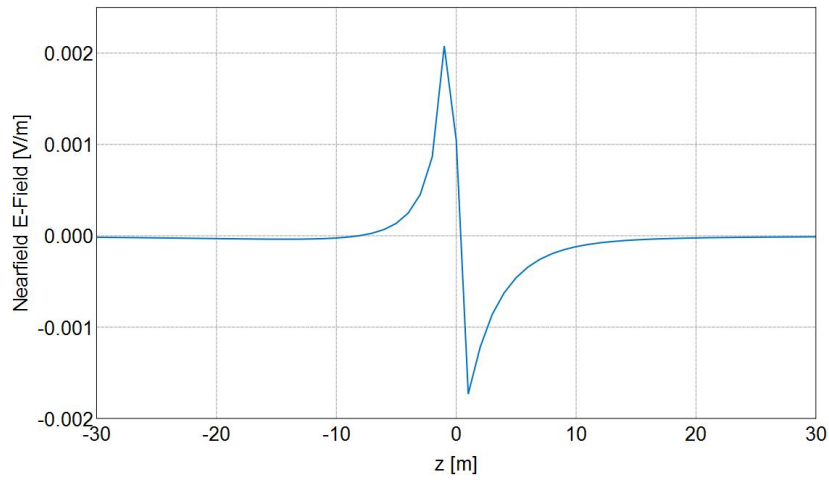
Imaginary Z H-Field [Frequency = 100 Hz; x = 0 m; y = 0 m] - Horizontal well orthogonal fracture 25 m

Figure A3.20: Imaginary component of magnetic field in the Z-direction for a orthogonal fracture of half-length 25 m in a horizontal wellbore



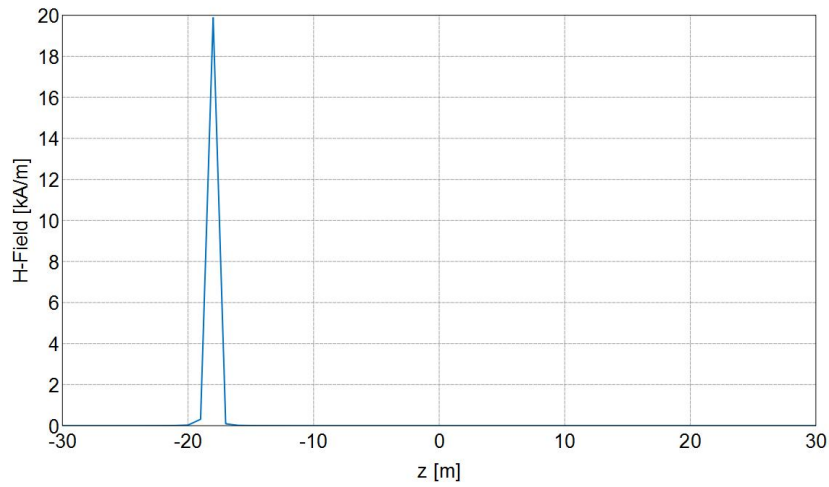
Real Z E-Field [Frequency = 100 Hz; x = 0 m; y = 0 m] - Horizontal well orthogonal fracture 30 m

Figure A3.21: Real component of electric field in the Z-direction for a orthogonal fracture of half-length 30 m in a horizontal wellbore



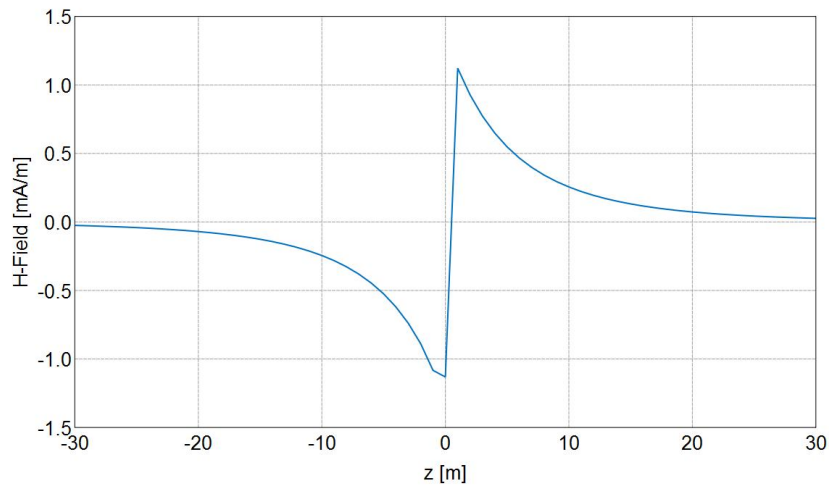
Imaginary Z E-Field [Frequency = 100 Hz; x = 0 m; y = 0 m] - Horizontal well orthogonal fracture 30 m

Figure A3.22: Imaginary component of electric field in the Z-direction for a orthogonal fracture of half-length 30 m in a horizontal wellbore



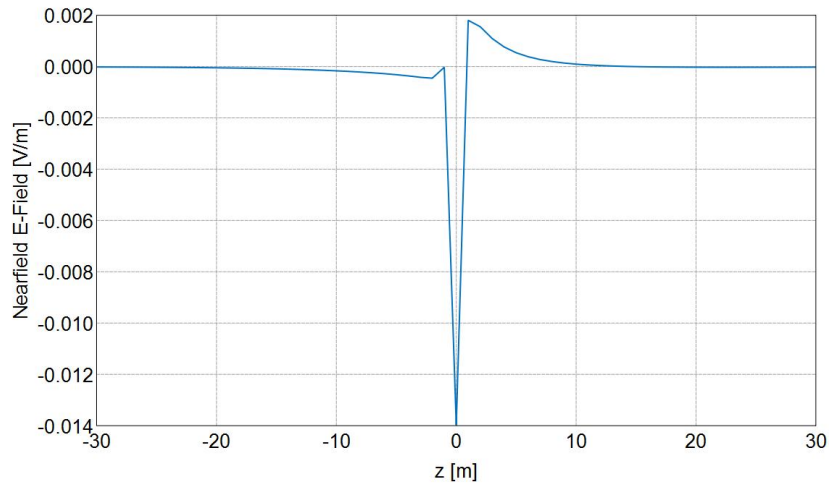
Real Z H-Field [Frequency = 100 Hz; x = 0 m; y = 0 m] - Horizontal well orthogonal fracture 30 m

Figure A3.23: Real component of magnetic field in the Z-direction for a orthogonal fracture of half-length 30 m in a horizontal wellbore



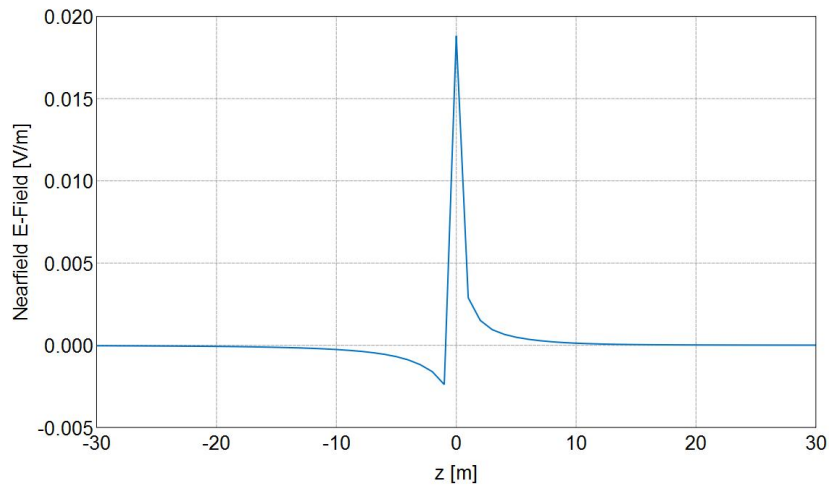
Imaginary Z H-Field [Frequency = 100 Hz; x = 0 m; y = 0 m] - Horizontal well orthogonal fracture 30 m

Figure A3.24: Imaginary component of magnetic field in the Z-direction for a orthogonal fracture of half-length 30 m in a horizontal wellbore



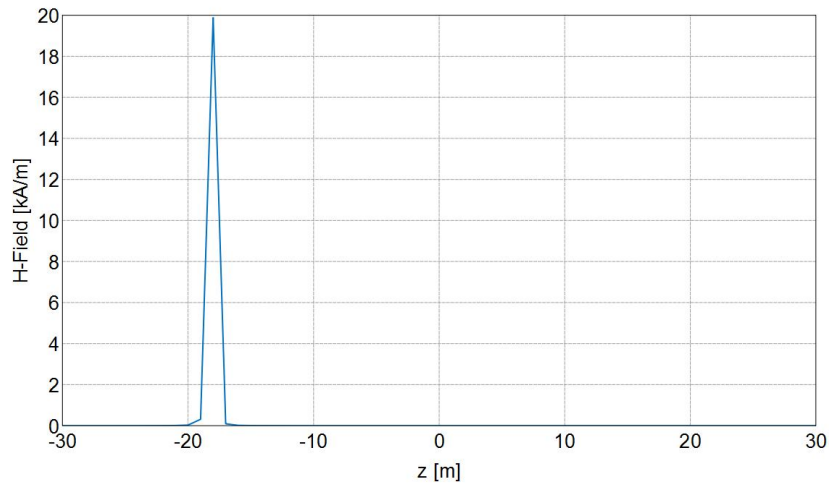
Real Z E-Field [Frequency = 100 Hz; x = 0 m; y = 0 m] - Horizontal well orthogonal fracture 35 m

Figure A3.25: Real component of electric field in the Z-direction for a orthogonal fracture of half-length 35 m in a horizontal wellbore



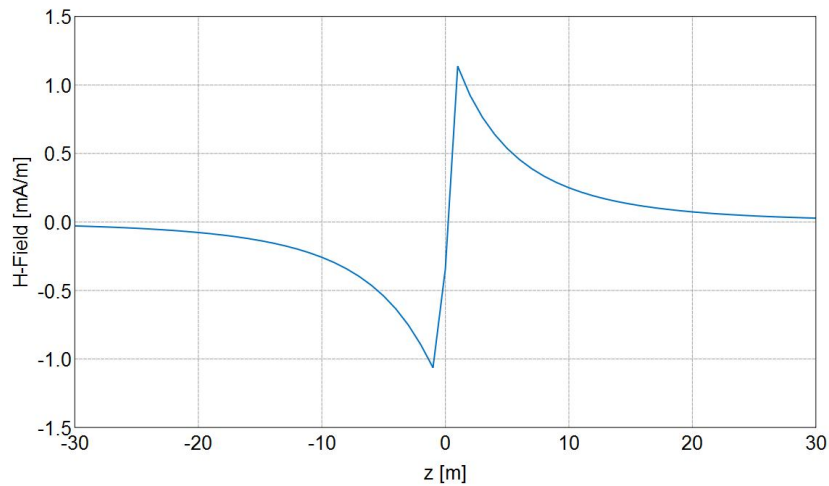
Imaginary Z E-Field [Frequency = 100 Hz; x = 0 m; y = 0 m] - Horizontal well orthogonal fracture 35 m

Figure A3.26: Imaginary component of electric field in the Z-direction for a orthogonal fracture of half-length 35 m in a horizontal wellbore



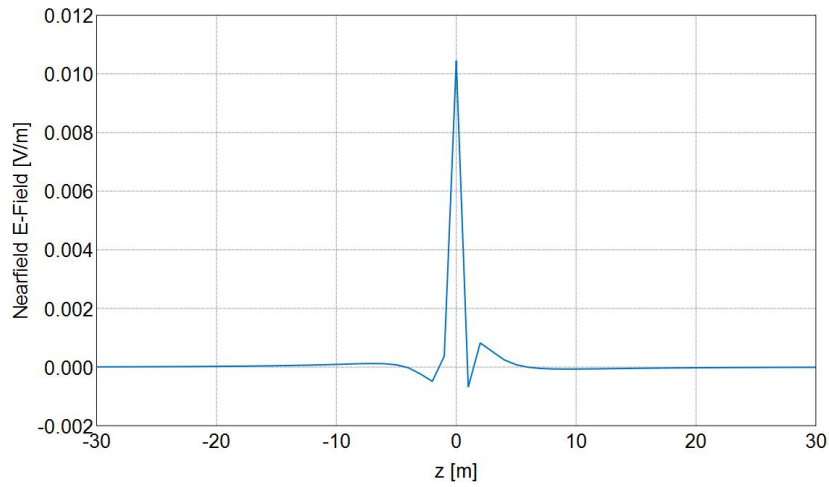
Real Z H-Field [Frequency = 100 Hz; x = 0 m; y = 0 m] - Horizontal well orthogonal fracture 35 m

Figure A3.27: Real component of magnetic field in the Z-direction for a orthogonal fracture of half-length 35 m in a horizontal wellbore



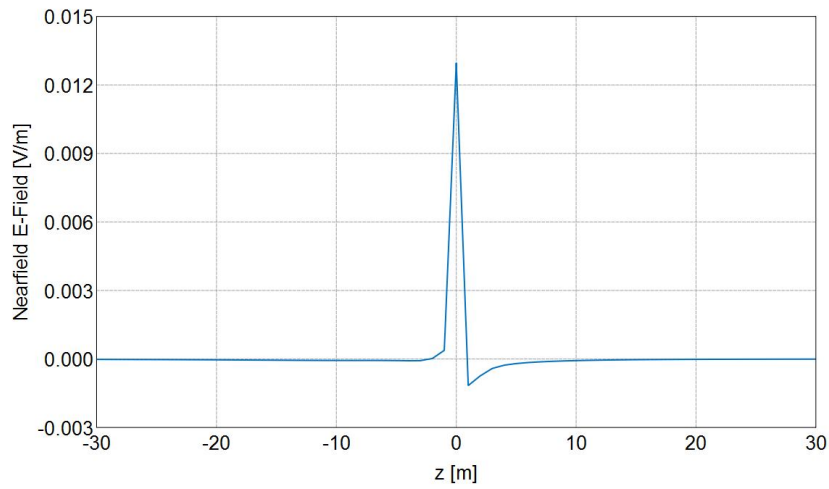
Imaginary Z H-Field [Frequency = 100 Hz; x = 0 m; y = 0 m] - Horizontal well orthogonal fracture 35 m

Figure A3.28: Imaginary component of magnetic field in the Z-direction for a orthogonal fracture of half-length 35 m in a horizontal wellbore



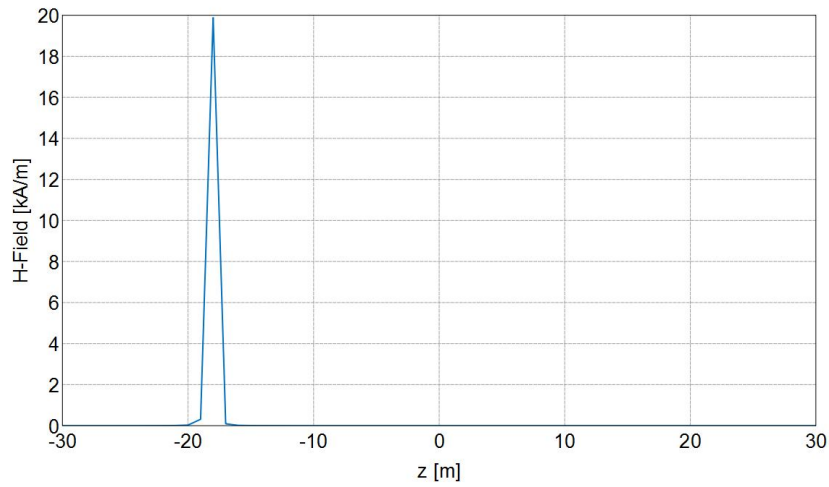
Real Z E-Field [Frequency = 100 Hz; x = 0 m; y = 0 m] - Horizontal well orthogonal fracture 40 m

Figure A3.29: Real component of electric field in the Z-direction for a orthogonal fracture of half-length 40 m in a horizontal wellbore



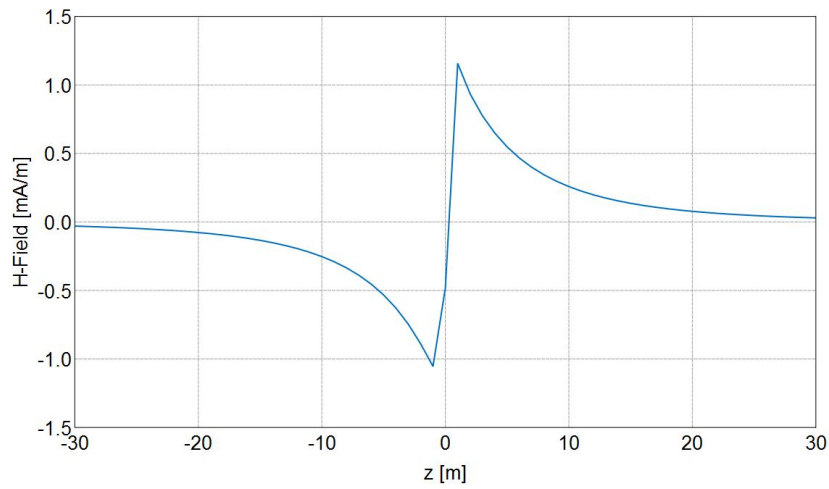
Imaginary Z E-Field [Frequency = 100 Hz; x = 0 m; y = 0 m] - Horizontal well orthogonal fracture 40 m

Figure A3.30: Imaginary component of electric field in the Z-direction for a orthogonal fracture of half-length 40 m in a horizontal wellbore



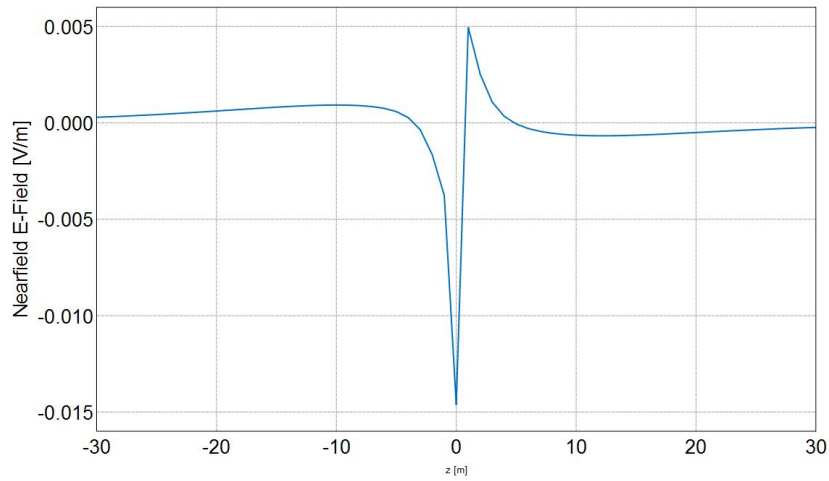
Real Z H-Field [Frequency = 100 Hz; x = 0 m; y = 0 m] - Horizontal well orthogonal fracture 40 m

Figure A3.31: Real component of magnetic field in the Z-direction for a orthogonal fracture of half-length 40 m in a horizontal wellbore



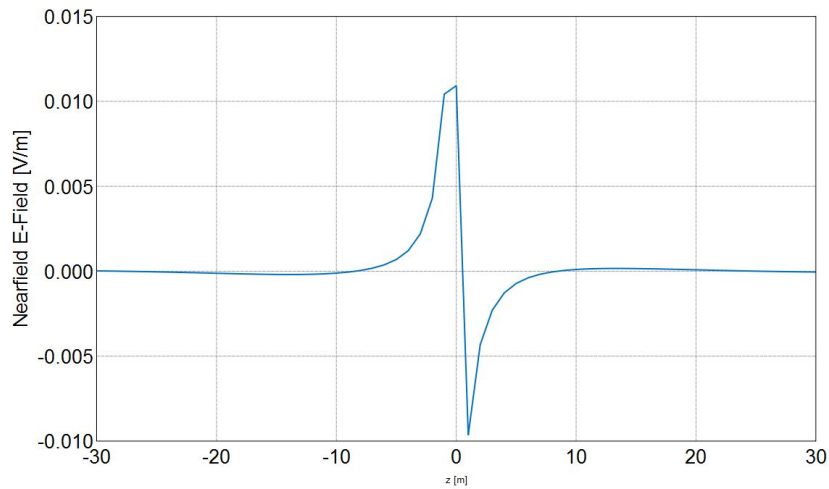
Imaginary Z H-Field [Frequency = 100 Hz; x = 0 m; y = 0 m] - Horizontal well orthogonal fracture 40 m

Figure A3.32: Imaginary component of magnetic field in the Z-direction for a orthogonal fracture of half-length 40 m in a horizontal wellbore



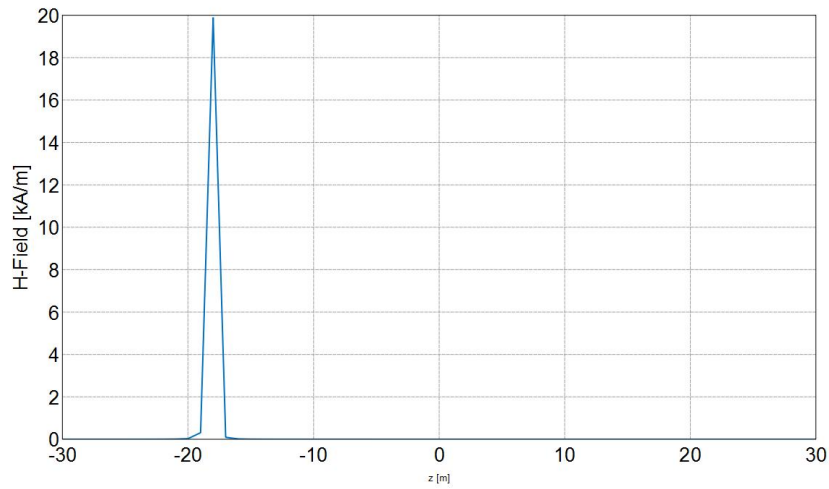
Real Z E-Field [Frequency = 100 Hz; x = 0 m; y = 0 m] - Horizontal well orthogonal fracture 45 m

Figure A3.33: Real component of electric field in the Z-direction for a orthogonal fracture of half-length 45 m in a horizontal wellbore



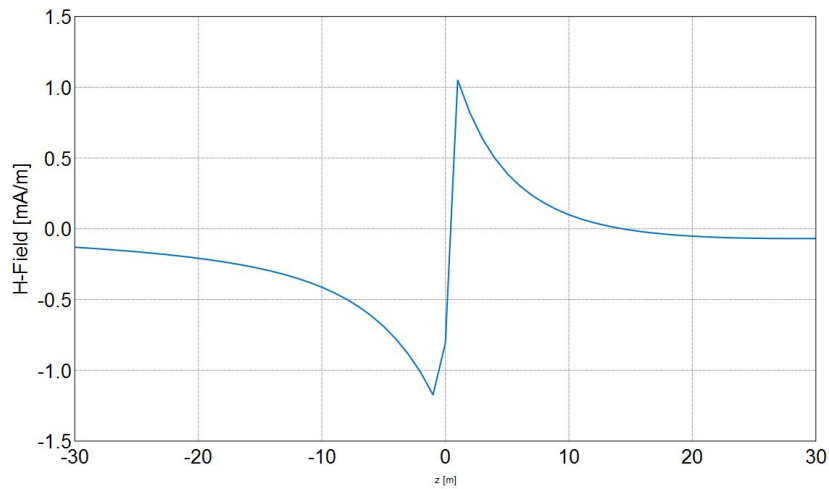
Imaginary Z E-Field [Frequency = 100 Hz; x = 0 m; y = 0 m] - Horizontal well orthogonal fracture 45 m

Figure A3.34: Imaginary component of electric field in the Z-direction for a orthogonal fracture of half-length 45 m in a horizontal wellbore



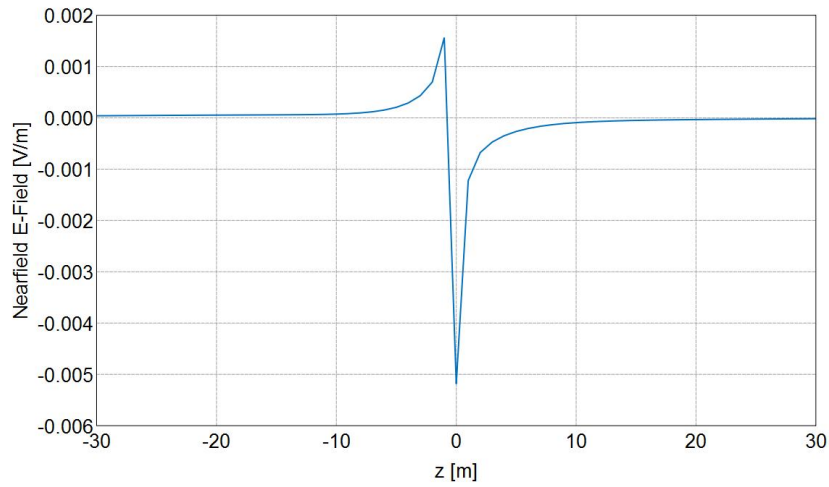
Real Z H-Field [Frequency = 100 Hz; x = 0 m; y = 0 m] - Horizontal well orthogonal fracture 45 m

Figure A3.35: Real component of magnetic field in the Z-direction for a orthogonal fracture of half-length 45 m in a horizontal wellbore



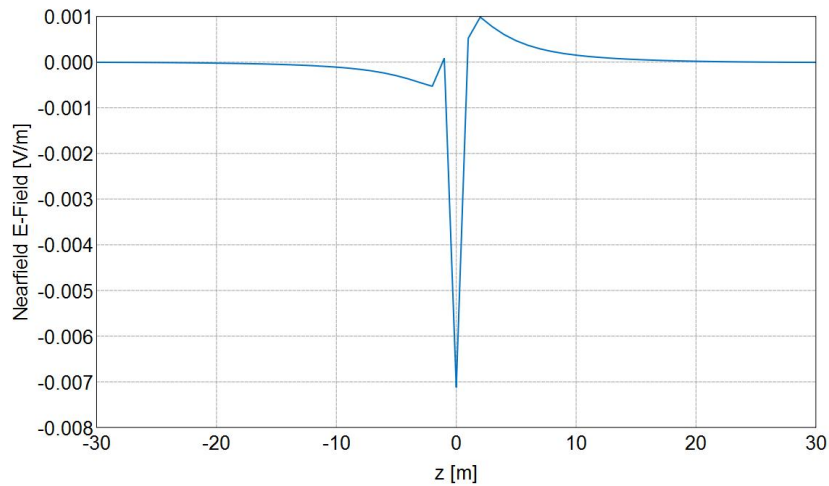
Imaginary Z H-Field [Frequency = 100 Hz; x = 0 m; y = 0 m] - Horizontal well orthogonal fracture 45 m

Figure A3.36: Imaginary component of magnetic field in the Z-direction for a orthogonal fracture of half-length 45 m in a horizontal wellbore



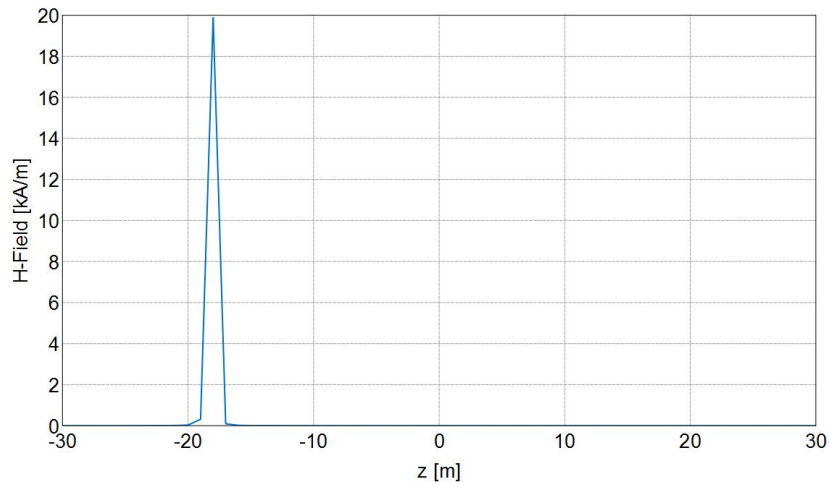
Real Z E-Field [Frequency = 100 Hz; x = 0 m; y = 0 m] - Horizontal well orthogonal fracture 60 m

Figure A3.37: Real component of electric field in the Z-direction for a orthogonal fracture of half-length 60 m in a horizontal wellbore



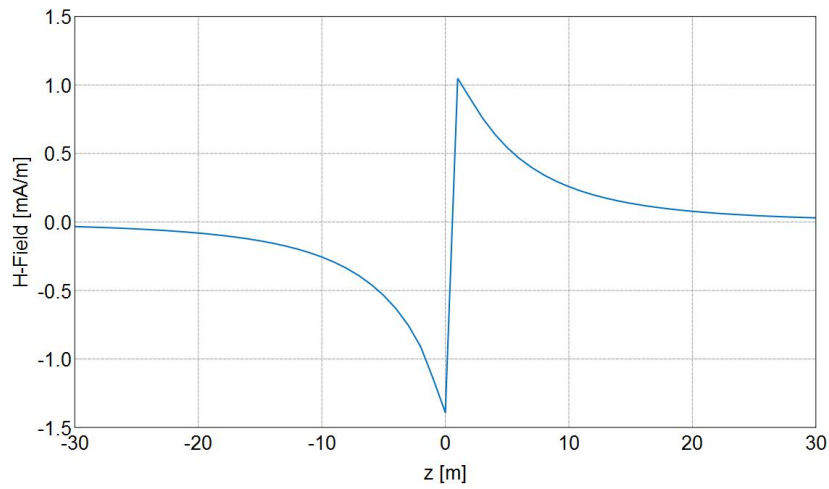
Imaginary Z E-Field [Frequency = 100 Hz; x = 0 m; y = 0 m] - Horizontal well orthogonal fracture 60 m

Figure A3.38: Imaginary component of electric field in the Z-direction for a orthogonal fracture of half-length 60 m in a horizontal wellbore



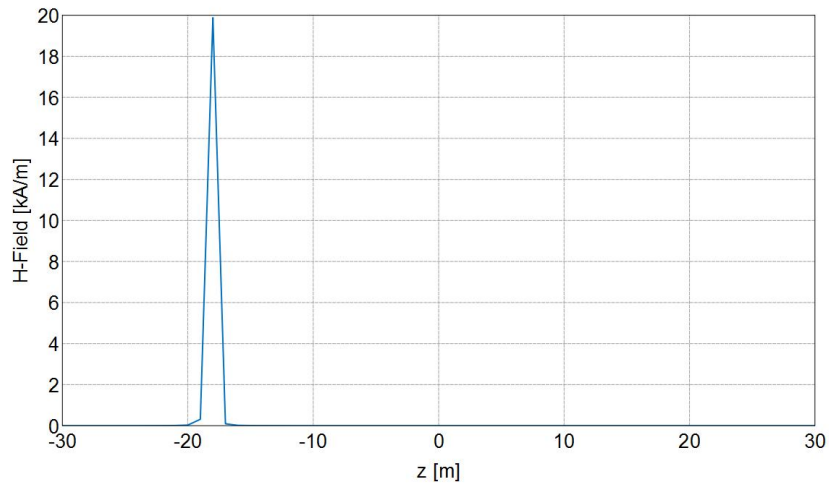
Real Z H-Field [Frequency = 100 Hz; x = 0 m; y = 0 m] - Horizontal well orthogonal fracture 60 m

Figure A3.39: Real component of magnetic field in the Z-direction for a orthogonal fracture of half-length 60 m in a horizontal wellbore



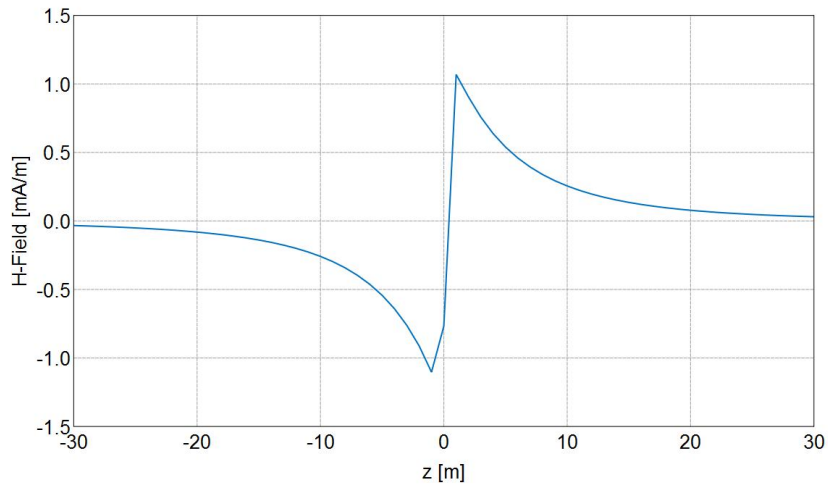
Imaginary Z H-Field [Frequency = 100 Hz; x = 0 m; y = 0 m] - Horizontal well orthogonal fracture 60 m

Figure A3.40: Imaginary component of magnetic field in the Z-direction for a orthogonal fracture of half-length 60 m in a horizontal wellbore



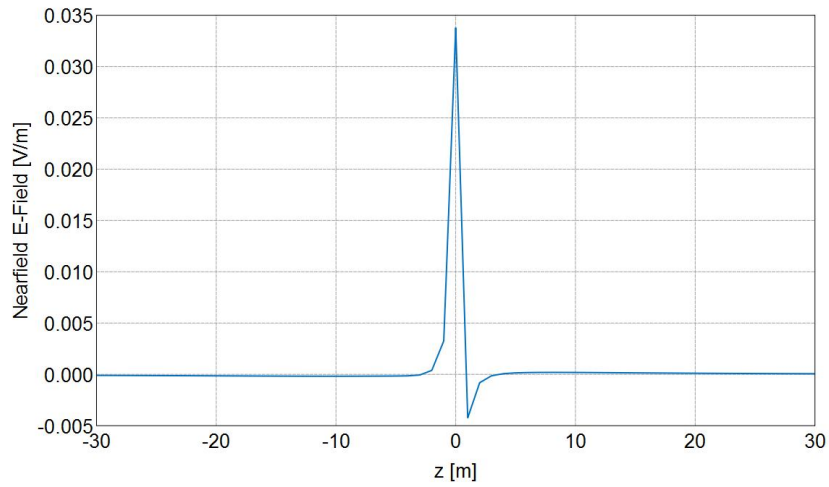
Real Z H-Field [Frequency = 100 Hz; x = 0 m; y = 0 m] - Horizontal well orthogonal fracture 75 m

Figure A3.41: Real component of magnetic field in the Z-direction for a orthogonal fracture of half-length 75 m in a horizontal wellbore



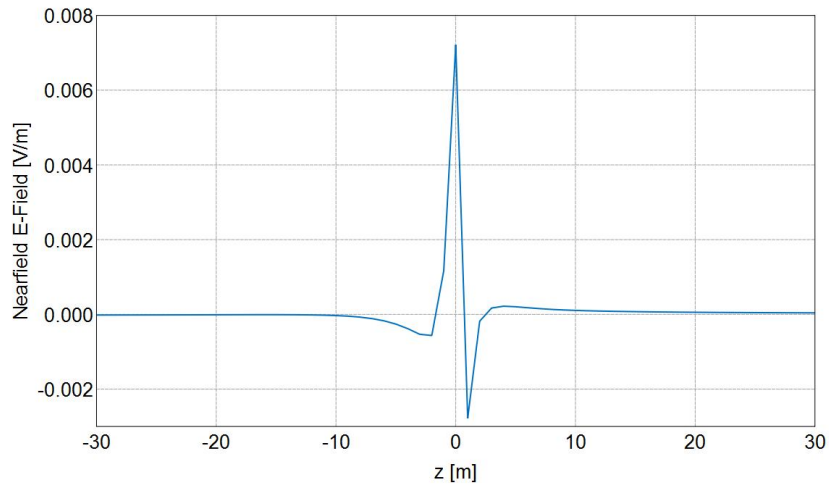
Imaginary Z H-Field [Frequency = 100 Hz; x = 0 m; y = 0 m] - Horizontal well orthogonal fracture 75 m

Figure A3.42: Imaginary component of magnetic field in the Z-direction for a orthogonal fracture of half-length 75 m in a horizontal wellbore



Real Z E-Field [Frequency = 100 Hz; x = 0 m; y = 0 m] - Horizontal well orthogonal fracture 75 m

Figure A3.43: Real component of electric field in the Z-direction for a orthogonal fracture of half-length 75 m in a horizontal wellbore



Imaginary Z E-Field [Frequency = 100 Hz; x = 0 m; y = 0 m] - Horizontal well orthogonal fracture 75 m

Figure A3.44: Imaginary component of electric field in the Z-direction for a orthogonal fracture of half-length 75 m in a horizontal wellbore

#### A4. ELECTRIC AND MAGNETIC FIELD RESPONSES FOR AN ORTHOGONAL FRACTURE IN HORIZONTAL WELL (CASED HOLE COMPLETION)

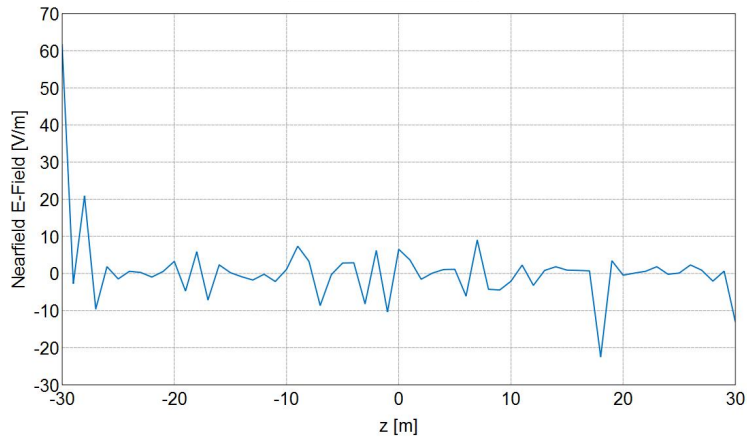


Figure A4.1: Real component of electric field in the Z-direction for a orthogonal fracture of half-length 5 m in a horizontal wellbore in steel casing

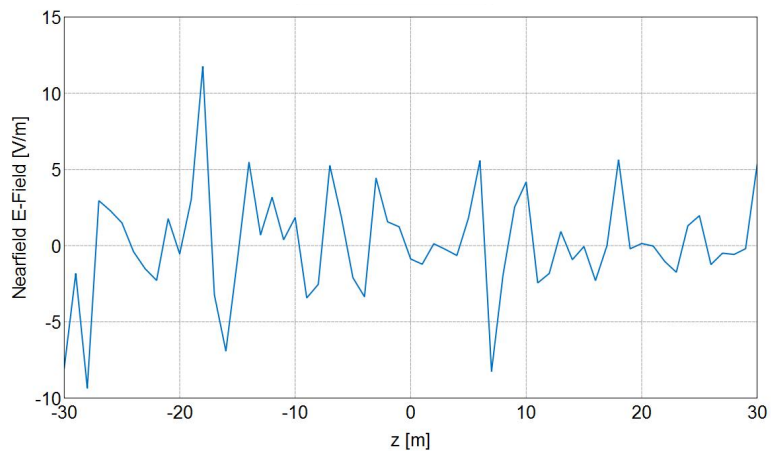
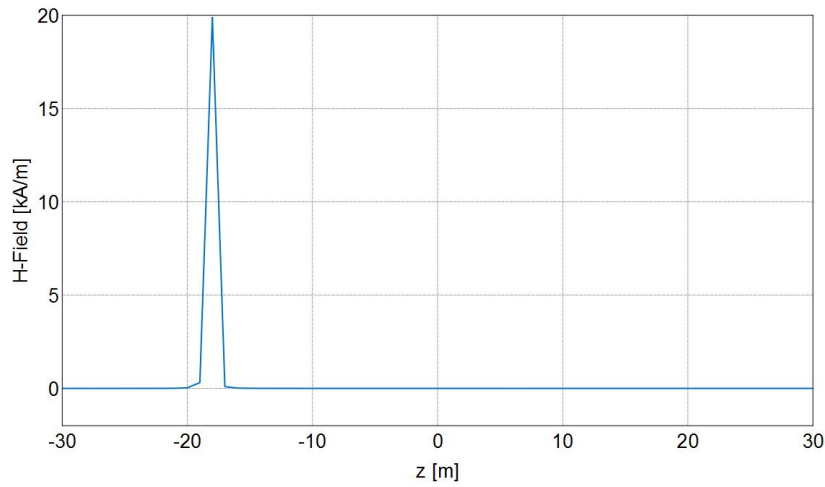
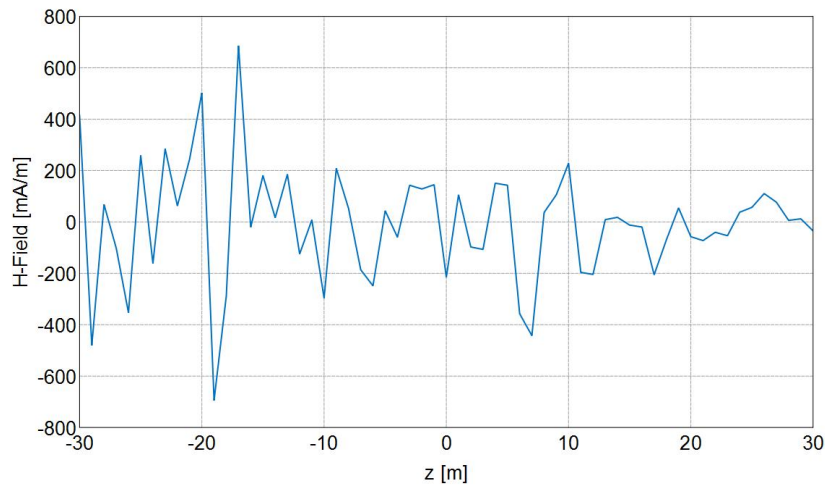


Figure A4.2: Imaginary component of electric field in the Z-direction for a orthogonal fracture of half-length 5 m in a horizontal wellbore in steel casing



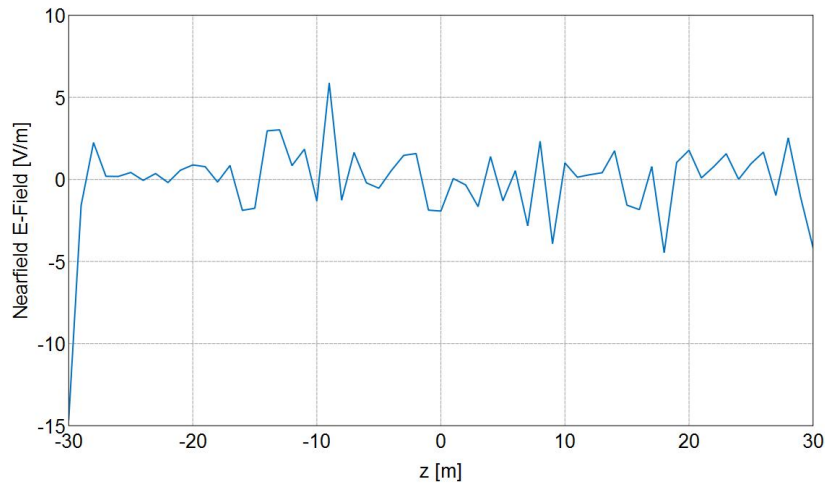
Real Z H-Field [Frequency = 100 Hz; x = 0 m; y = 0 m] - Horizontal well orthogonal fracture 5 m CH

Figure A4.3: Real component of magnetic field in the Z-direction for a orthogonal fracture of half-length 5 m in a horizontal wellbore in steel casing



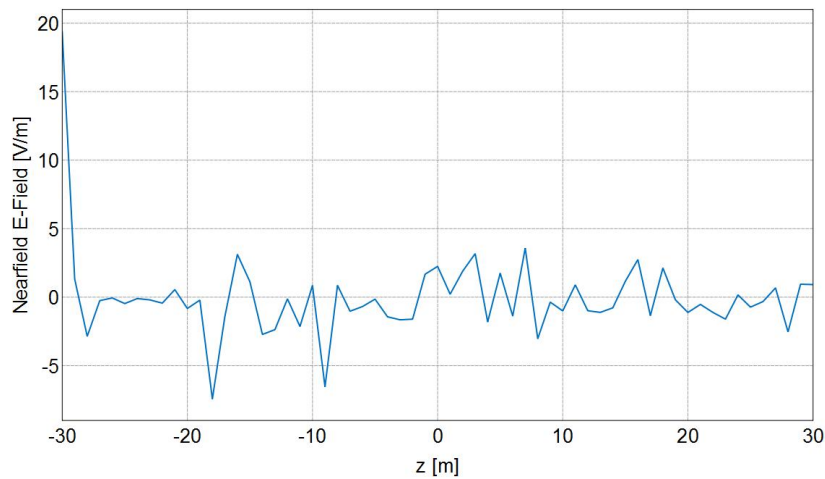
Imaginary Z H-Field [Frequency = 100 Hz; x = 0 m; y = 0 m] - Horizontal well orthogonal fracture 5 m CH

Figure A4.4: Imaginary component of magnetic field in the Z-direction for a orthogonal fracture of half-length 5 m in a horizontal wellbore in steel casing



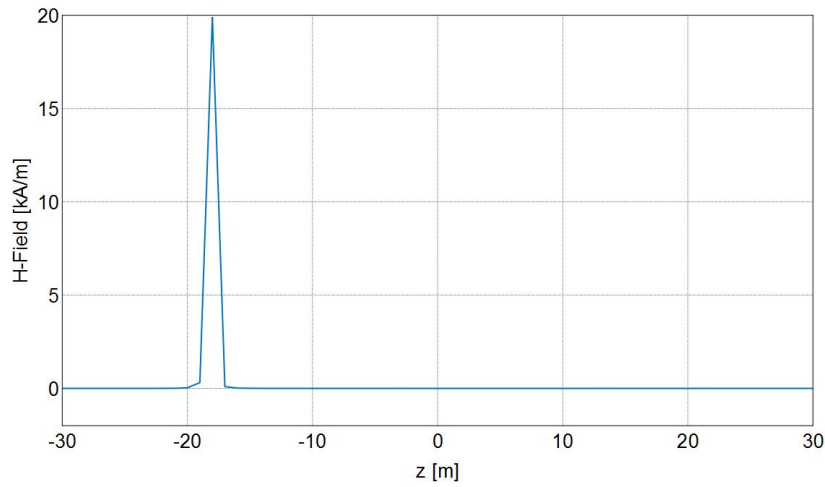
Real Z E-Field [Frequency = 100 Hz; x = 0 m; y = 0 m] - Horizontal well orthogonal fracture 10 m CH

Figure A4.5: Real component of electric field in the Z-direction for a orthogonal fracture of half-length 10 m in a horizontal wellbore in steel casing



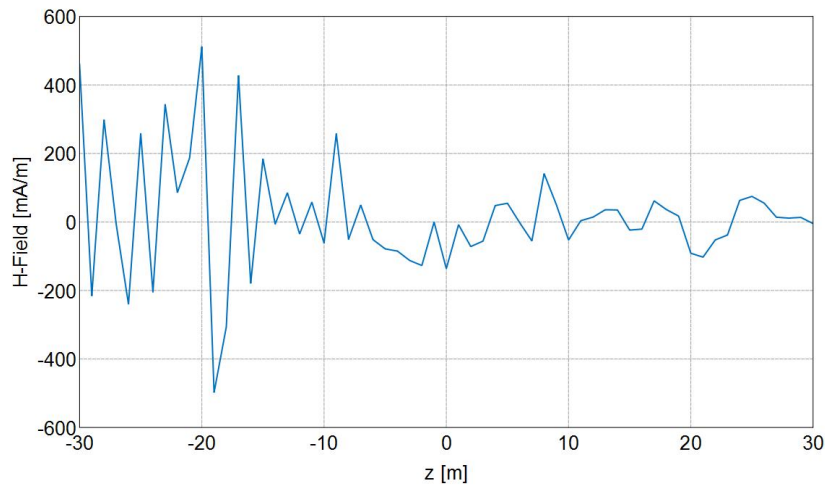
Imaginary Z E-Field [Frequency = 100 Hz; x = 0 m; y = 0 m] - Horizontal well orthogonal fracture 10 m CH

Figure A4.6: Imaginary component of electric field in the Z-direction for a orthogonal fracture of half-length 10 m in a horizontal wellbore in steel casing



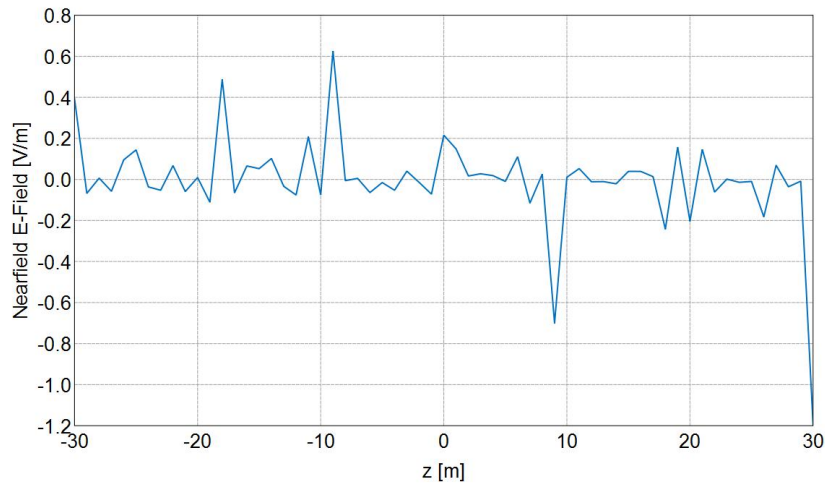
Real Z H-Field [Frequency = 100 Hz; x = 0 m; y = 0 m] - Horizontal well orthogonal fracture 10 m CH

Figure A4.7: Real component of magnetic field in the Z-direction for a orthogonal fracture of half-length 10 m in a horizontal wellbore in steel casing



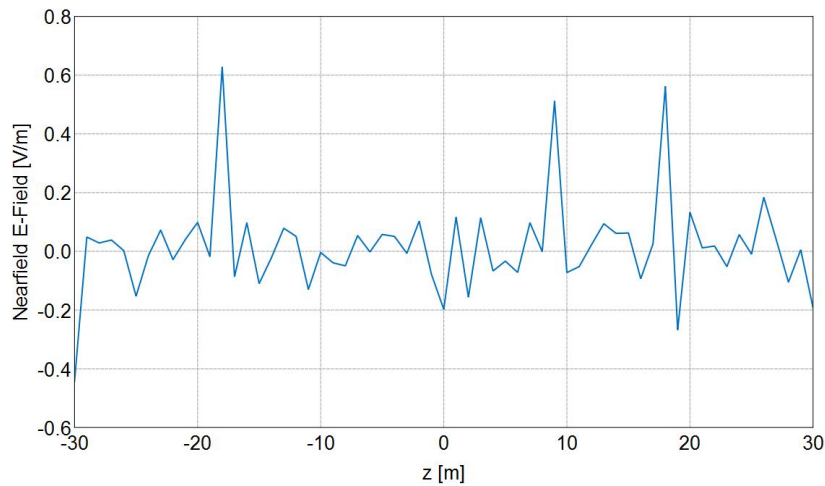
Imaginary Z H-Field [Frequency = 100 Hz; x = 0 m; y = 0 m] - Horizontal well orthogonal fracture 10 m CH

Figure A4.8: Imaginary component of magnetic field in the Z-direction for a orthogonal fracture of half-length 10 m in a horizontal wellbore in steel casing



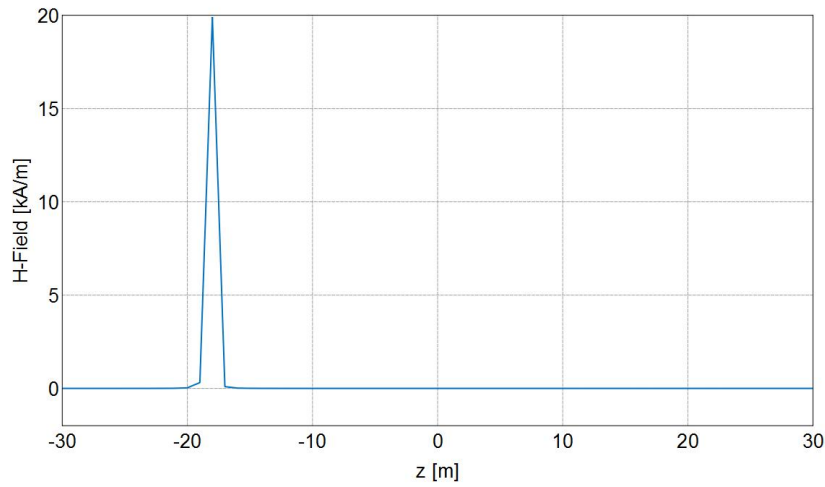
Real Z E-Field [Frequency = 100 Hz; x = 0 m; y = 0 m] - Horizontal well orthogonal fracture 15 m CH

Figure A4.9: Real component of electric field in the Z-direction for a orthogonal fracture of half-length 15 m in a horizontal wellbore in steel casing



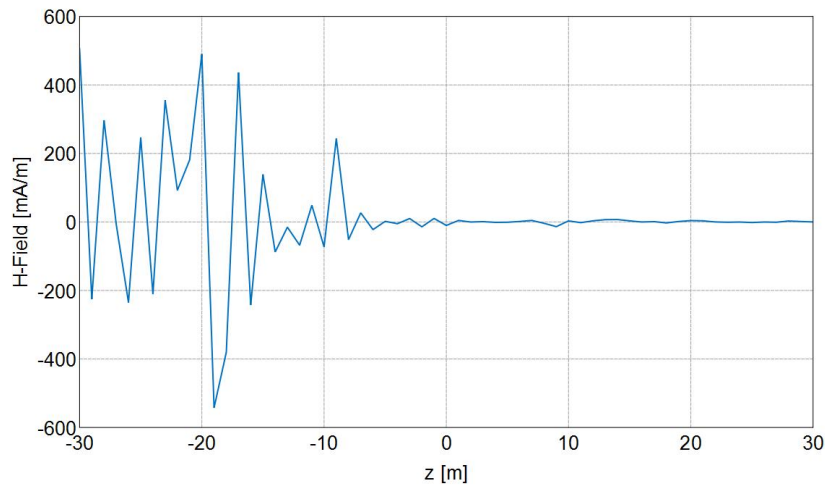
Imaginary Z E-Field [Frequency = 100 Hz; x = 0 m; y = 0 m] - Horizontal well orthogonal fracture 15 m CH

Figure A4.10: Imaginary component of electric field in the Z-direction for a orthogonal fracture of half-length 15 m in a horizontal wellbore in steel casing



Real Z H-Field [Frequency = 100 Hz; x = 0 m; y = 0 m] - Horizontal well orthogonal fracture 15 m CH

Figure A4.11: Real component of magnetic field in the Z-direction for a orthogonal fracture of half-length 15 m in a horizontal wellbore in steel casing



Imaginary Z H-Field [Frequency = 100 Hz; x = 0 m; y = 0 m] - Horizontal well orthogonal fracture 15 m CH

Figure A4.12: Imaginary component of magnetic field in the Z-direction for a orthogonal fracture of half-length 15 m in a horizontal wellbore in steel casing

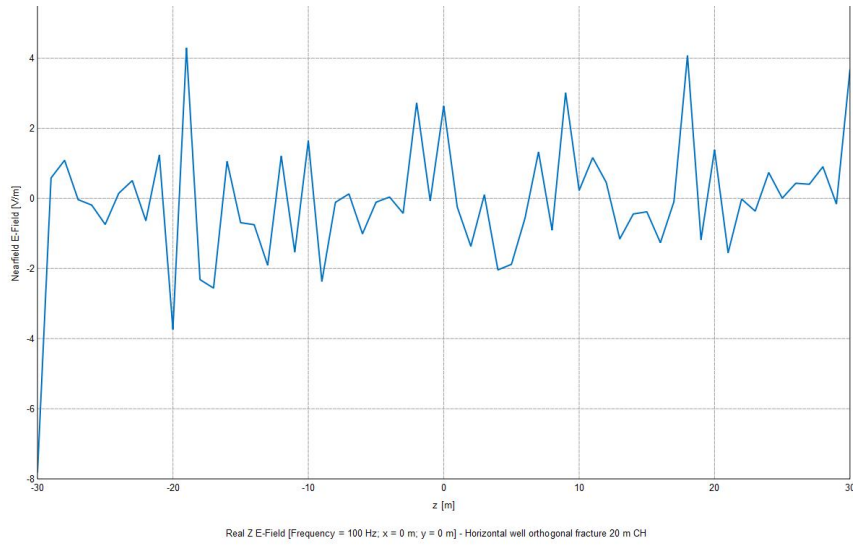


Figure A4.13: Real component of electric field in the Z-direction for a orthogonal fracture of half-length 20 m in a horizontal wellbore in steel casing

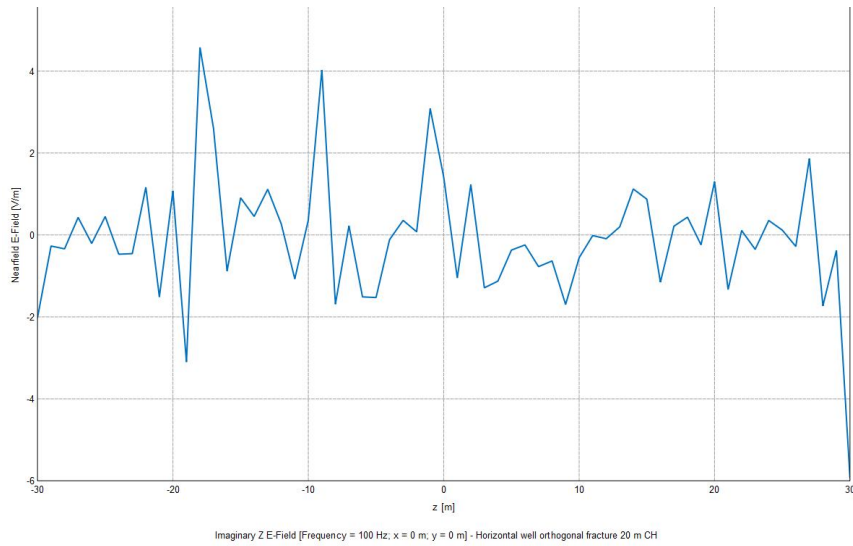


Figure A4.14: Imaginary component of electric field in the Z-direction for a orthogonal fracture of half-length 20 m in a horizontal wellbore in steel casing

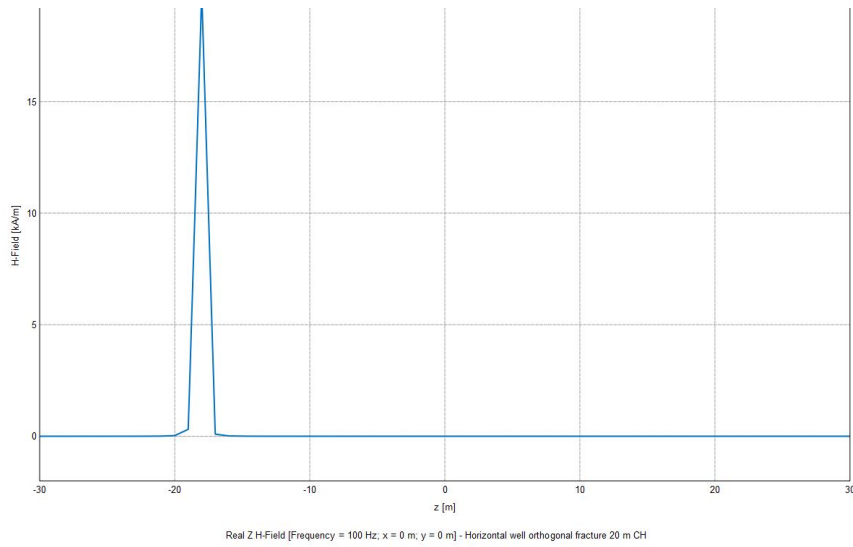


Figure A4.15: Real component of magnetic field in the Z-direction for a orthogonal fracture of half-length 20 m in a horizontal wellbore in steel casing

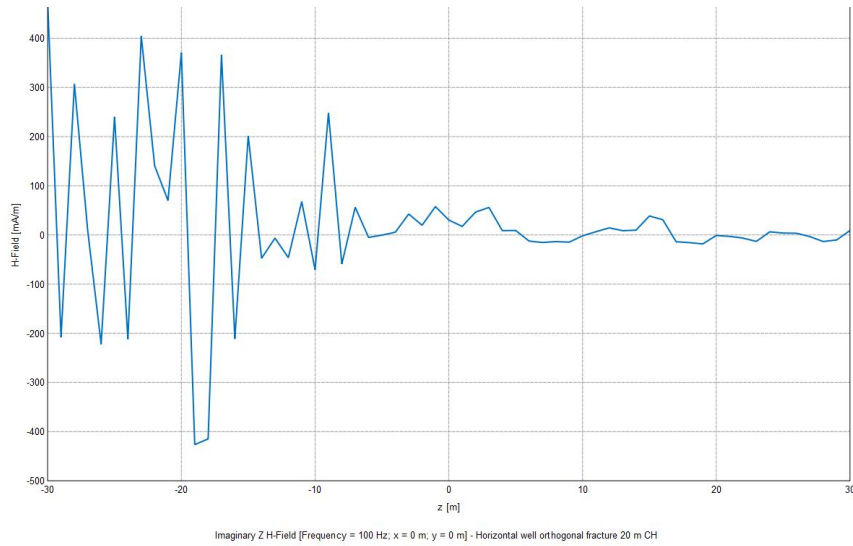
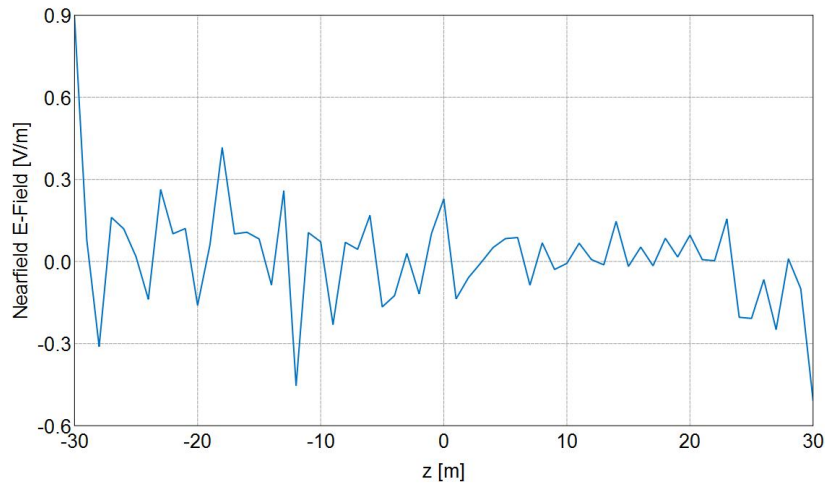
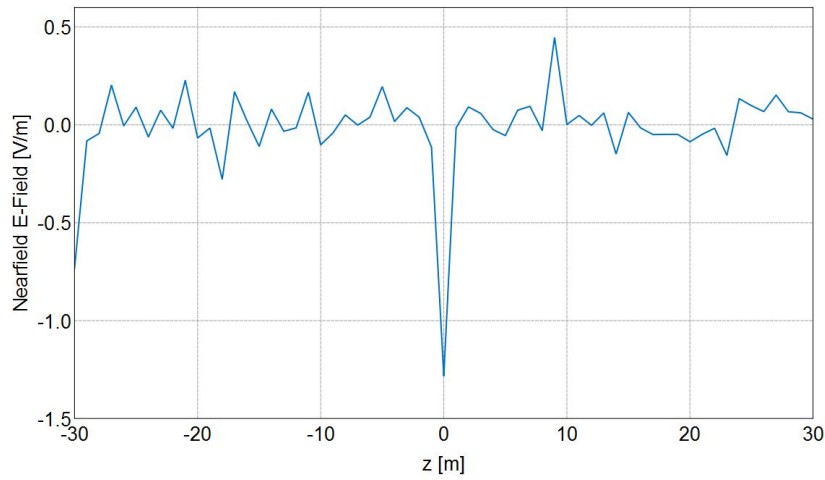


Figure A4.16: Imaginary component of magnetic field in the Z-direction for a orthogonal fracture of half-length 20 m in a horizontal wellbore in steel casing



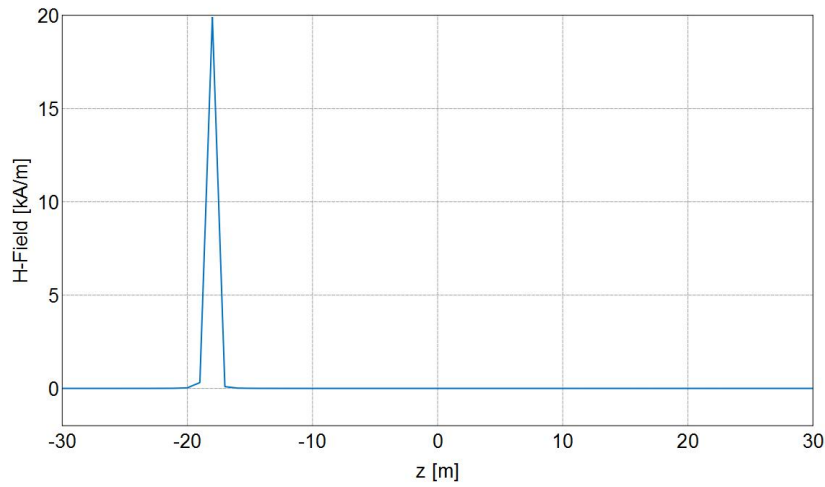
Real Z E-Field [Frequency = 100 Hz; x = 0 m; y = 0 m] - Horizontal well orthogonal fracture 25 m CH

Figure A4.17: Real component of electric field in the Z-direction for a orthogonal fracture of half-length 25 m in a horizontal wellbore in steel casing



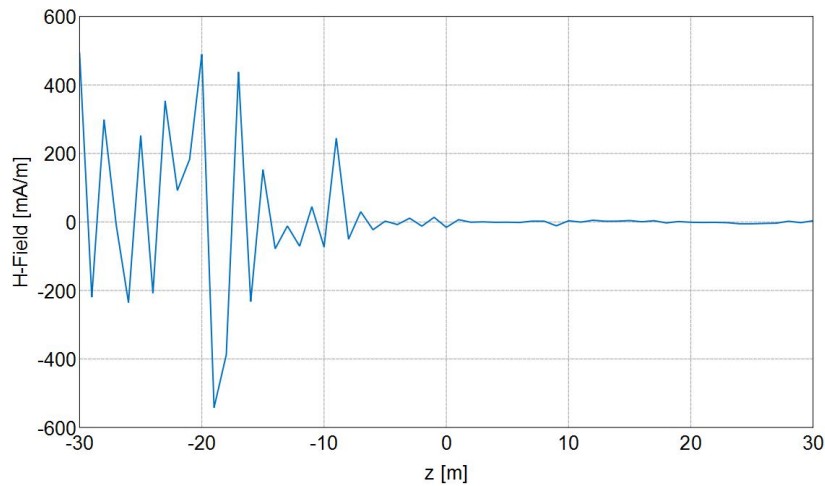
Imaginary Z E-Field [Frequency = 100 Hz; x = 0 m; y = 0 m] - Horizontal well orthogonal fracture 25 m CH

Figure A4.18: Imaginary component of electric field in the Z-direction for a orthogonal fracture of half-length 25 m in a horizontal wellbore in steel casing



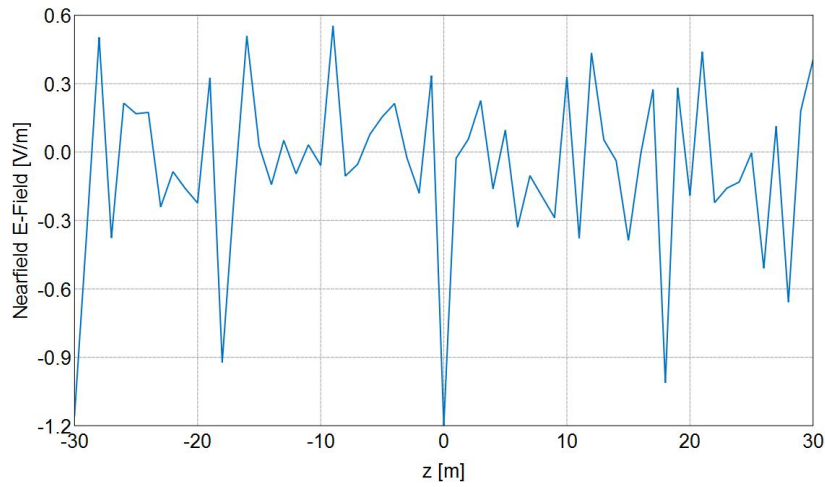
Real Z H-Field [Frequency = 100 Hz; x = 0 m; y = 0 m] - Horizontal well orthogonal fracture 25 m CH

Figure A4.19: Real component of magnetic field in the Z-direction for a orthogonal fracture of half-length 25 m in a horizontal wellbore in steel casing



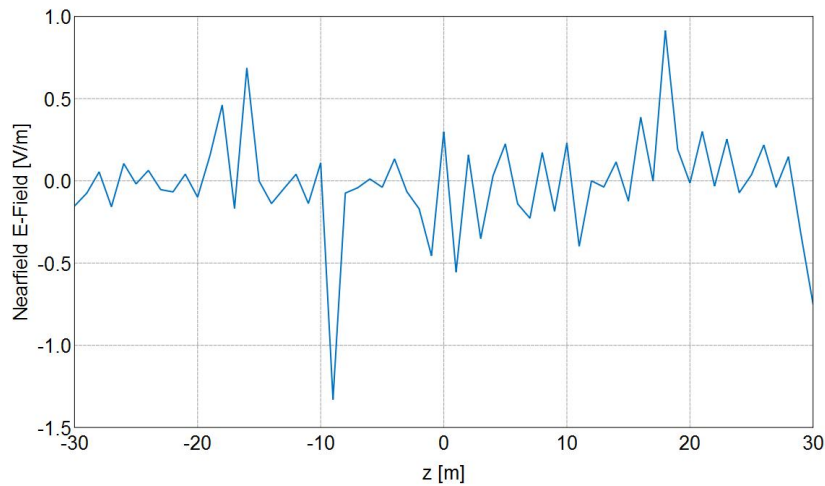
Imaginary Z H-Field [Frequency = 100 Hz; x = 0 m; y = 0 m] - Horizontal well orthogonal fracture 25 m CH

Figure A4.20: Imaginary component of magnetic field in the Z-direction for a orthogonal fracture of half-length 25 m in a horizontal wellbore in steel casing



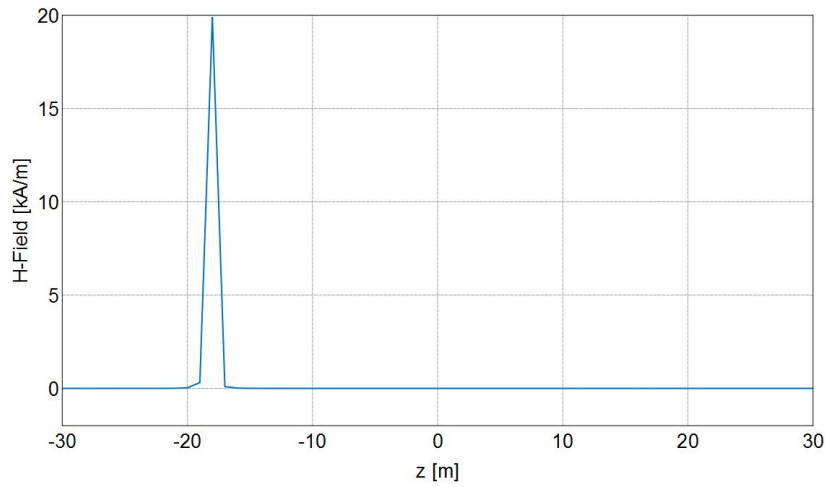
Real Z E-Field [Frequency = 100 Hz; x = 0 m; y = 0 m] - Horizontal well orthogonal fracture 30 m CH

Figure A4.21: Real component of electric field in the Z-direction for a orthogonal fracture of half-length 30 m in a horizontal wellbore in steel casing



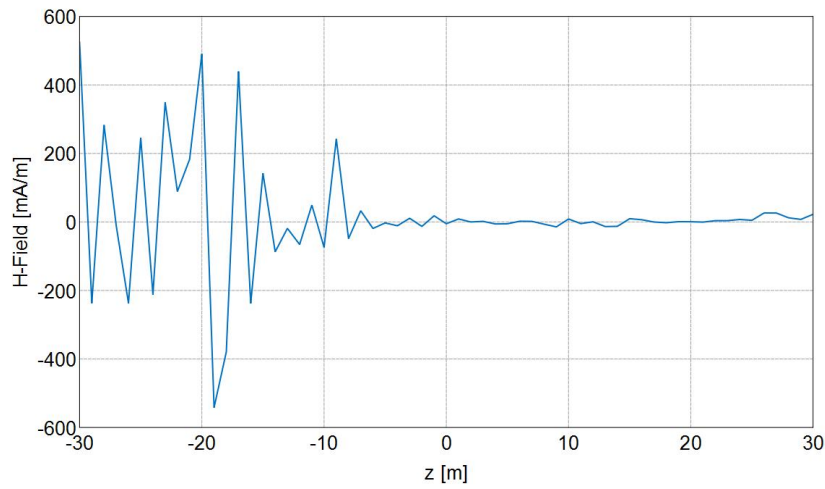
Imaginary Z E-Field [Frequency = 100 Hz; x = 0 m; y = 0 m] - Horizontal well orthogonal fracture 30 m CH

Figure A4.22: Imaginary component of electric field in the Z-direction for a orthogonal fracture of half-length 30 m in a horizontal wellbore in steel casing



Real Z H-Field [Frequency = 100 Hz; x = 0 m; y = 0 m] - Horizontal well orthogonal fracture 30 m CH

Figure A4.23: Real component of magnetic field in the Z-direction for a orthogonal fracture of half-length 30 m in a horizontal wellbore in steel casing



Imaginary Z H-Field [Frequency = 100 Hz; x = 0 m; y = 0 m] - Horizontal well orthogonal fracture 30 m CH

Figure A4.24: Imaginary component of magnetic field in the Z-direction for a orthogonal fracture of half-length 30 m in a horizontal wellbore in steel casing

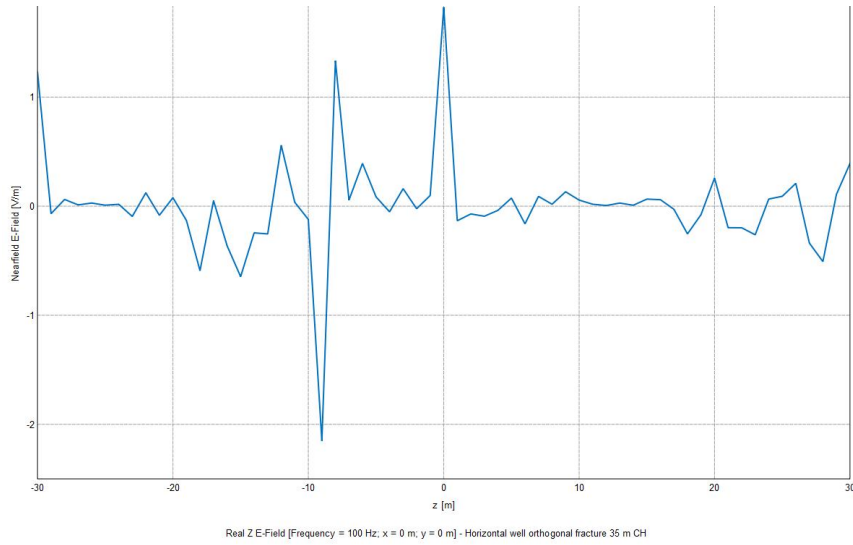


Figure A4.25: Real component of electric field in the Z-direction for a orthogonal fracture of half-length 35 m in a horizontal wellbore in steel casing

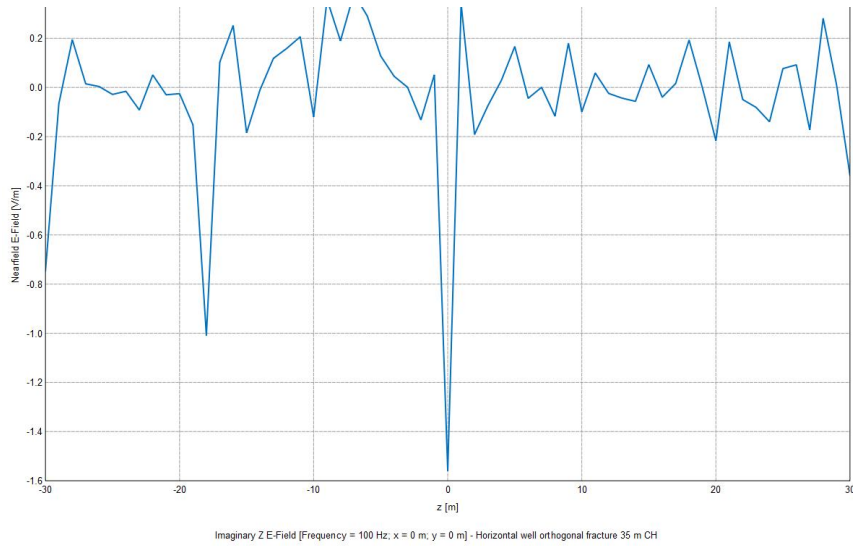


Figure A4.26: Imaginary component of electric field in the Z-direction for a orthogonal fracture of half-length 35 m in a horizontal wellbore in steel casing

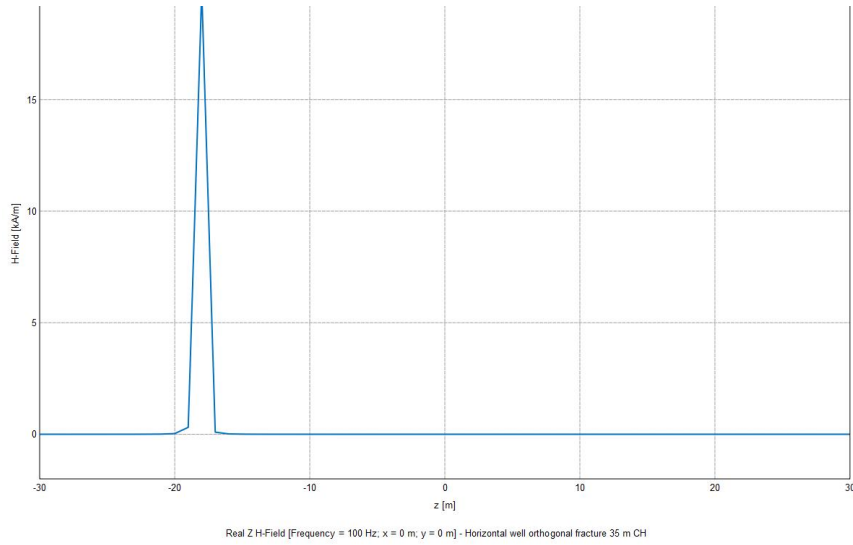


Figure A4.27: Real component of magnetic field in the Z-direction for a orthogonal fracture of half-length 35 m in a horizontal wellbore in steel casing

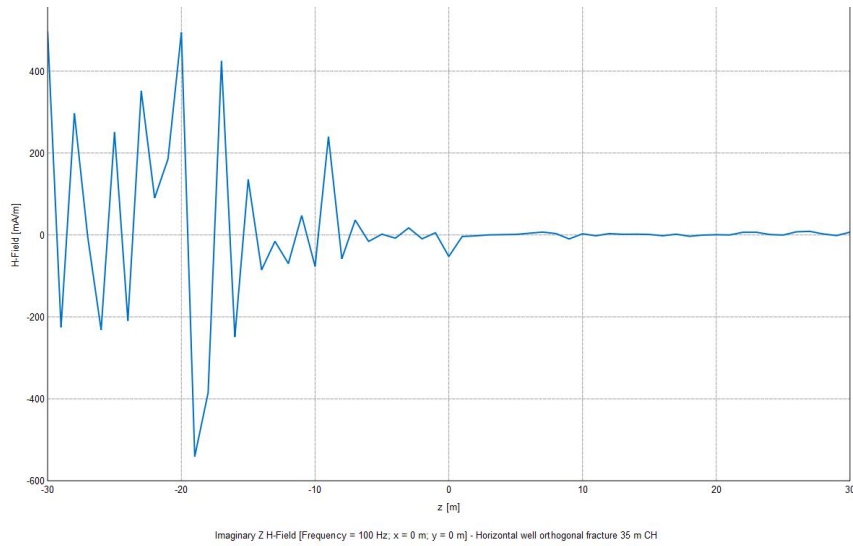
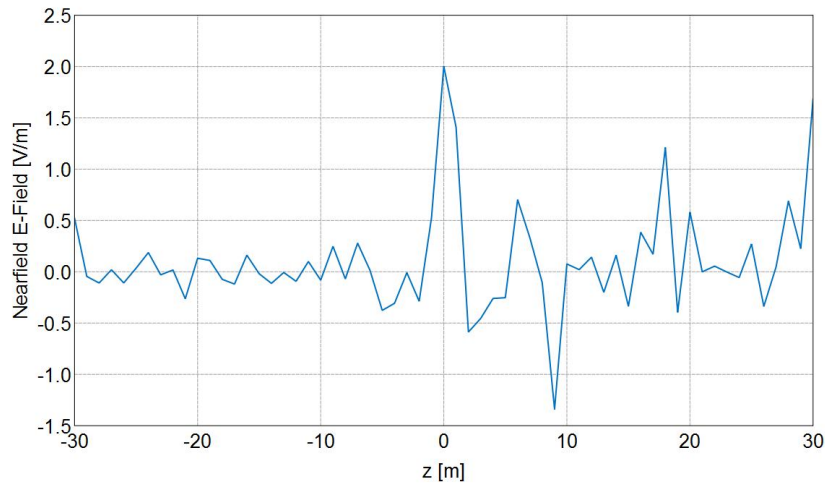
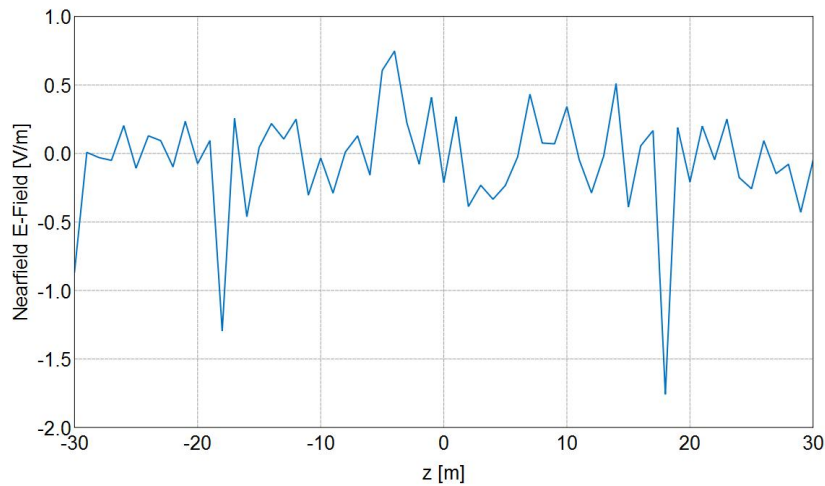


Figure A4.28: Imaginary component of magnetic field in the Z-direction for a orthogonal fracture of half-length 35 m in a horizontal wellbore in steel casing



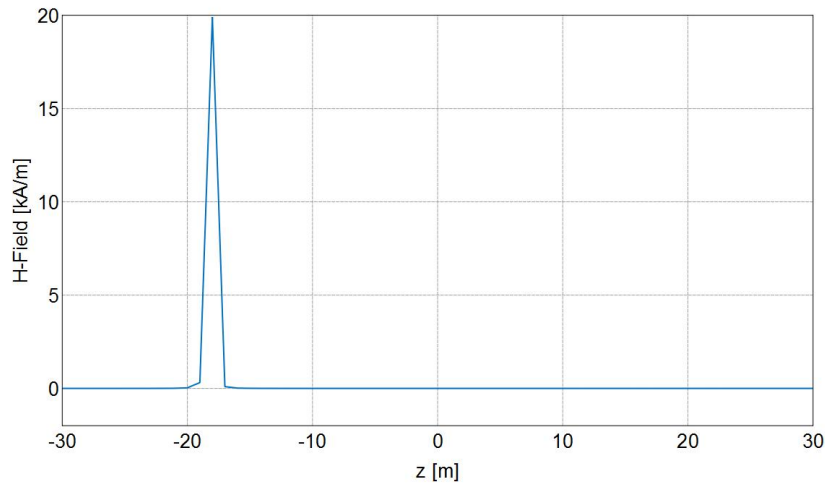
Real Z E-Field [Frequency = 100 Hz; x = 0 m; y = 0 m] - Horizontal well orthogonal fracture 40 m CH

Figure A4.29: Real component of electric field in the Z-direction for a orthogonal fracture of half-length 40 m in a horizontal wellbore in steel casing



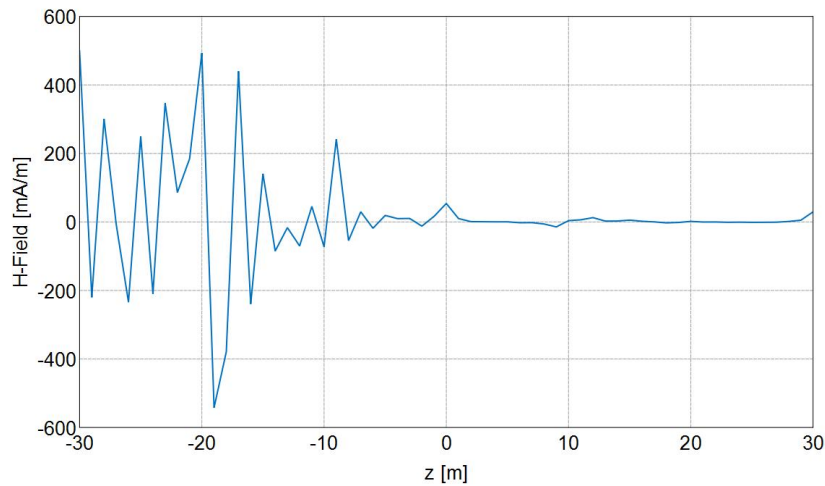
Imaginary Z E-Field [Frequency = 100 Hz; x = 0 m; y = 0 m] - Horizontal well orthogonal fracture 40 m CH

Figure A4.30: Imaginary component of electric field in the Z-direction for a orthogonal fracture of half-length 40 m in a horizontal wellbore in steel casing



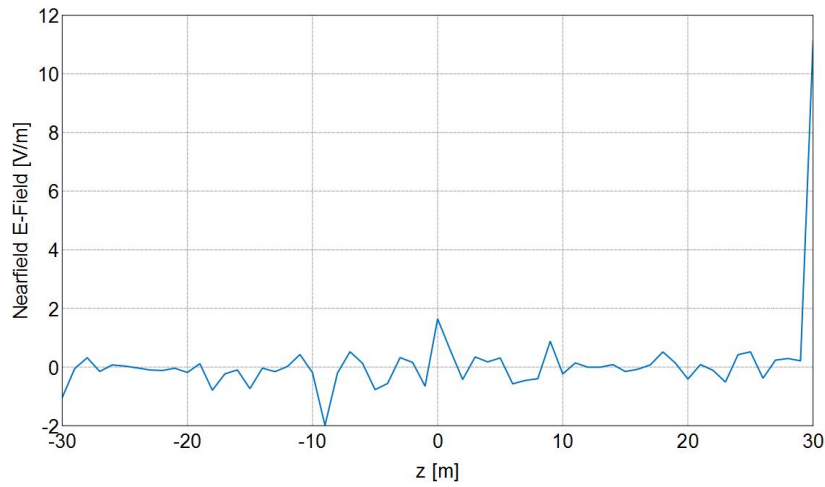
Real Z H-Field [Frequency = 100 Hz; x = 0 m; y = 0 m] - Horizontal well orthogonal fracture 40 m CH

Figure A4.31: Real component of magnetic field in the Z-direction for a orthogonal fracture of half-length 40 m in a horizontal wellbore in steel casing



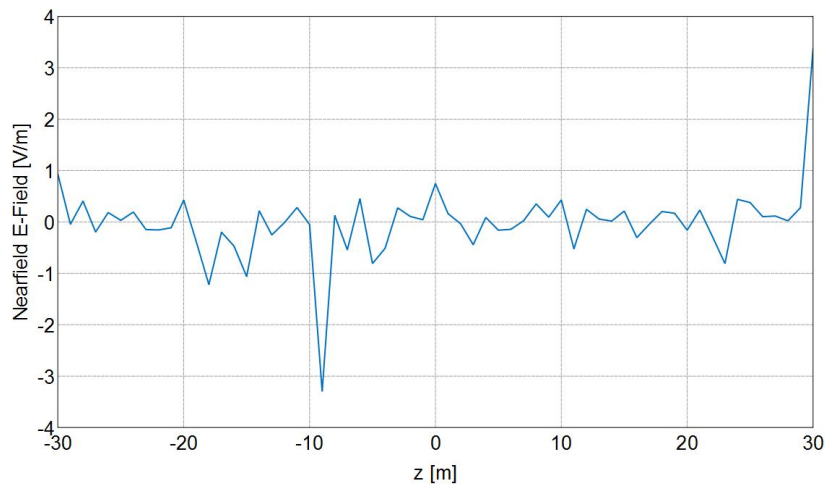
Imaginary Z H-Field [Frequency = 100 Hz; x = 0 m; y = 0 m] - Horizontal well orthogonal fracture 40 m CH

Figure A4.32: Imaginary component of magnetic field in the Z-direction for a orthogonal fracture of half-length 40 m in a horizontal wellbore in steel casing



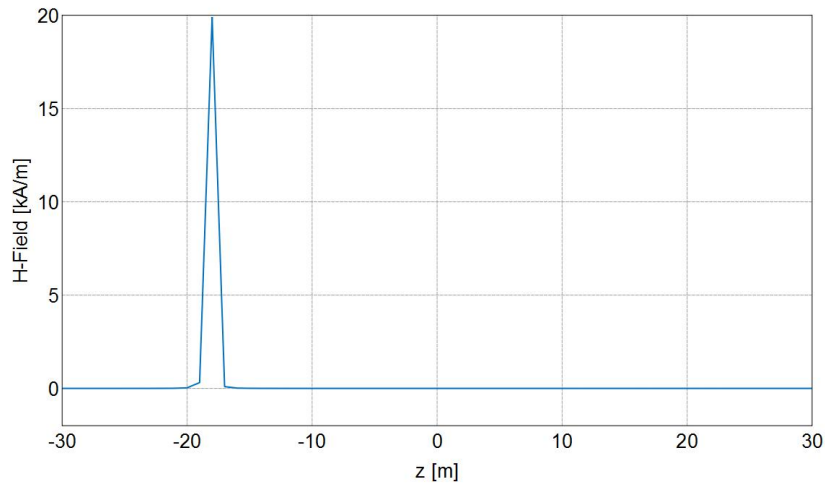
Real Z E-Field [Frequency = 100 Hz; x = 0 m; y = 0 m] - Horizontal well orthogonal fracture 45 m CH

Figure A4.33: Real component of electric field in the Z-direction for a orthogonal fracture of half-length 45 m in a horizontal wellbore in steel casing



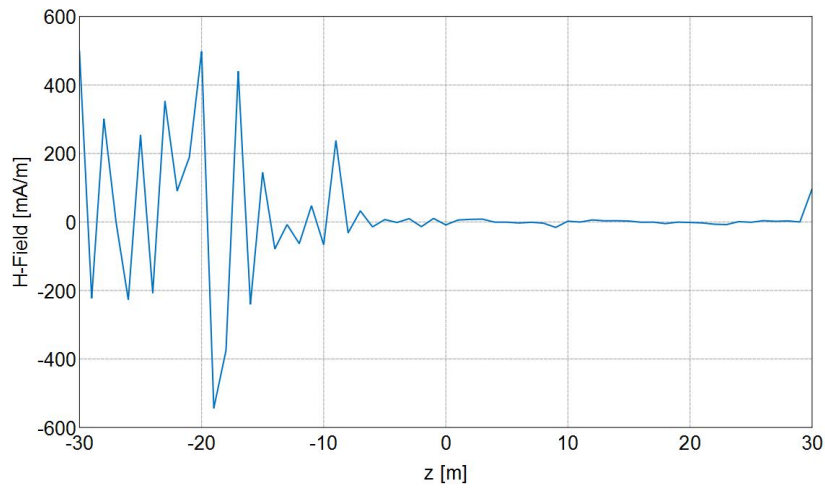
Imaginary Z E-Field [Frequency = 100 Hz; x = 0 m; y = 0 m] - Horizontal well orthogonal fracture 45 m CH

Figure A4.34: Imaginary component of electric field in the Z-direction for a orthogonal fracture of half-length 45 m in a horizontal wellbore in steel casing



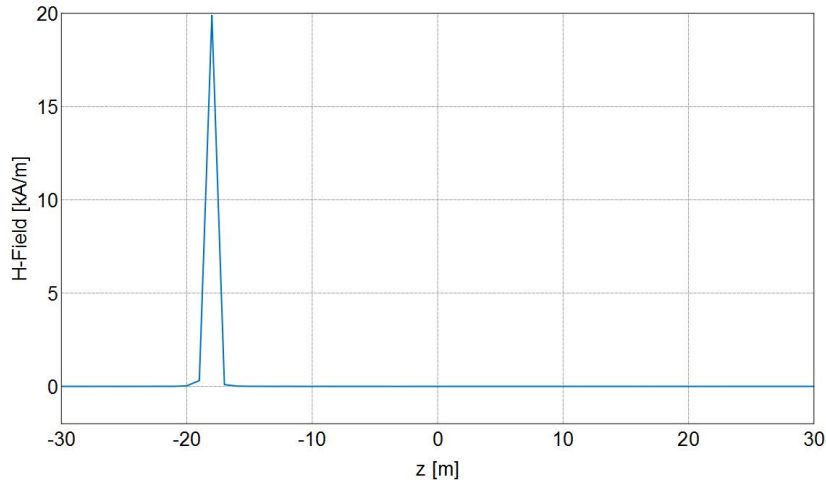
Real Z H-Field [Frequency = 100 Hz; x = 0 m; y = 0 m] - Horizontal well orthogonal fracture 45 m CH

Figure A4.35: Real component of magnetic field in the Z-direction for a orthogonal fracture of half-length 45 m in a horizontal wellbore in steel casing



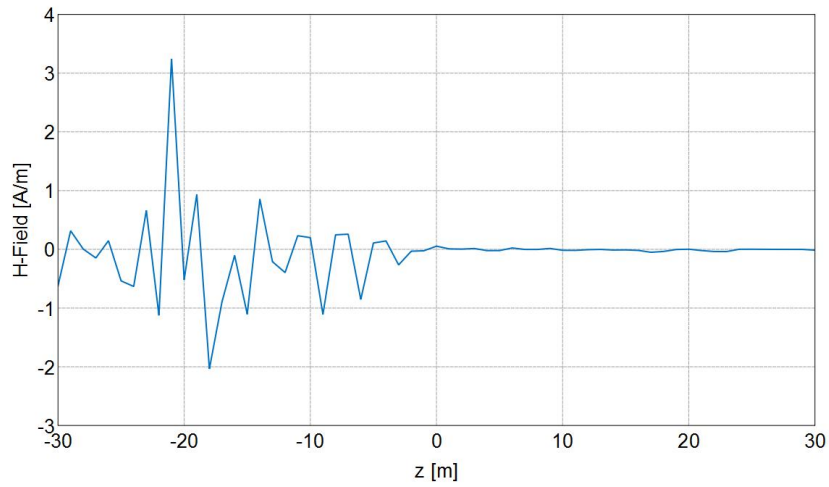
Imaginary Z H-Field [Frequency = 100 Hz; x = 0 m; y = 0 m] - Horizontal well orthogonal fracture 45 m CH

Figure A4.36: Imaginary component of Magnetic field in the Z-direction for a orthogonal fracture of half-length 45 m in a horizontal wellbore in steel casing



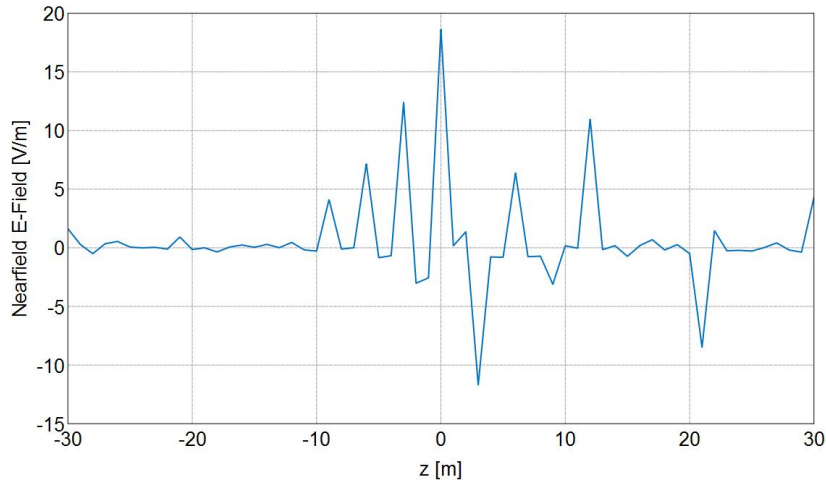
Real Z H-Field [Frequency = 100 Hz; x = 0 m; y = 0 m] - Horizontal well orthogonal fracture 60 m CH

Figure A4.37: Real component of magnetic field in the Z-direction for a orthogonal fracture of half-length 60 m in a horizontal wellbore in steel casing



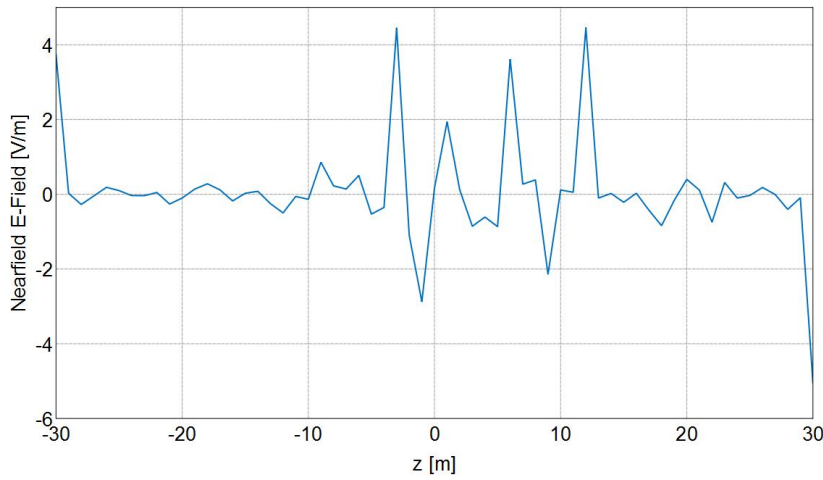
Imaginary Z H-Field [Frequency = 100 Hz; x = 0 m; y = 0 m] - Horizontal well orthogonal fracture 60 m CH

Figure A4.38: Imaginary component of magnetic field in the Z-direction for a orthogonal fracture of half-length 60 m in a horizontal wellbore in steel casing



Real Z E-Field [Frequency = 100 Hz; x = 0 m; y = 0 m] - Horizontal well orthogonal fracture 60 m CH

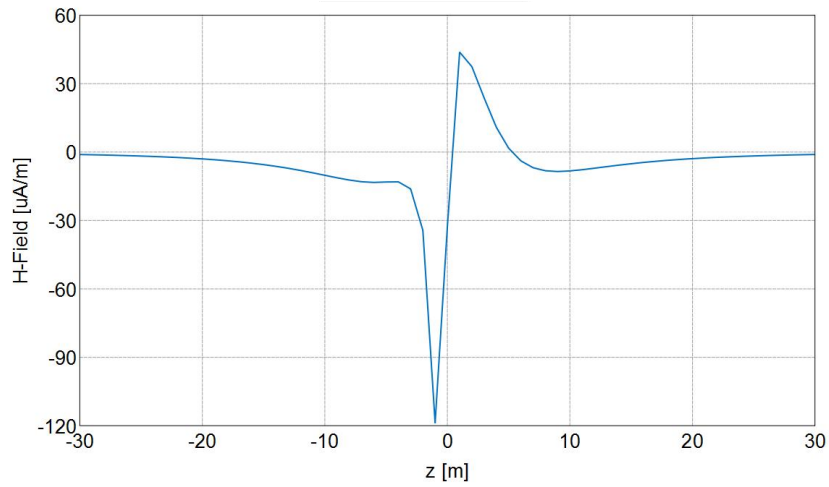
Figure A4.39: Real component of electric field in the Z-direction for a orthogonal fracture of half-length 60 m in a horizontal wellbore in steel casing



Imaginary Z E-Field [Frequency = 100 Hz; x = 0 m; y = 0 m] - Horizontal well orthogonal fracture 60 m CH

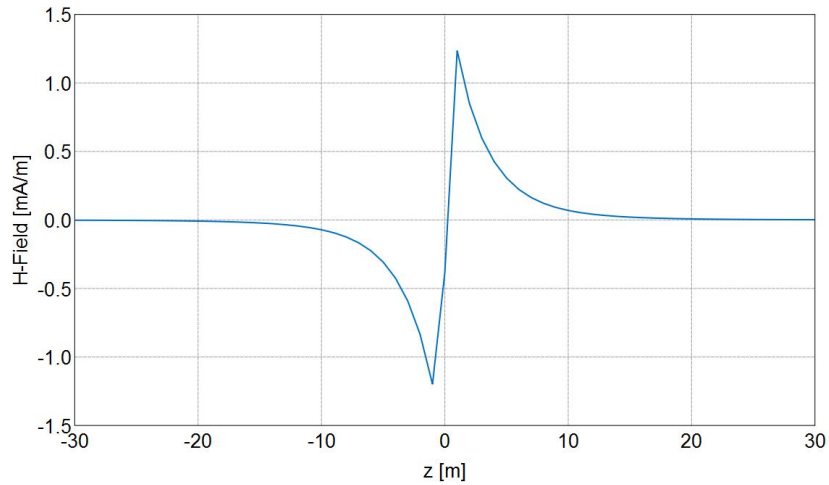
Figure A4.40: Imaginary component of electric field in the Z-direction for a orthogonal fracture of half-length 60 m in a horizontal wellbore in steel casing

**A5. RAW ELECTRIC AND MAGNETIC FIELD RESPONSES FOR NON SYMMETRICAL BI-WING FRACTURE IN HORIZONTAL WELL (OPEN HOLE COMPLETION)**



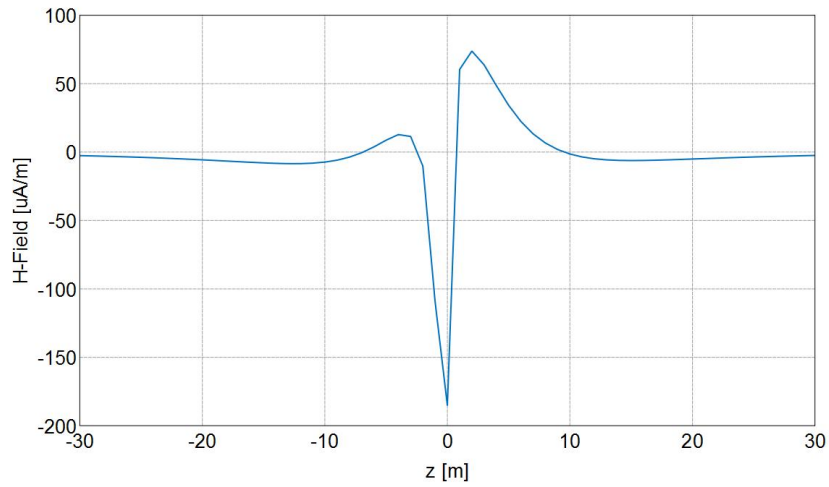
Imaginary Y H-Field [Frequency = 100 Hz; x = 0 m; y = 0 m] - NS frac 5 10

Figure A5.1: Imaginary component of magnetic field in Y- direction for a non-symmetrical fracture of wings of half length 5m and 10m on either side



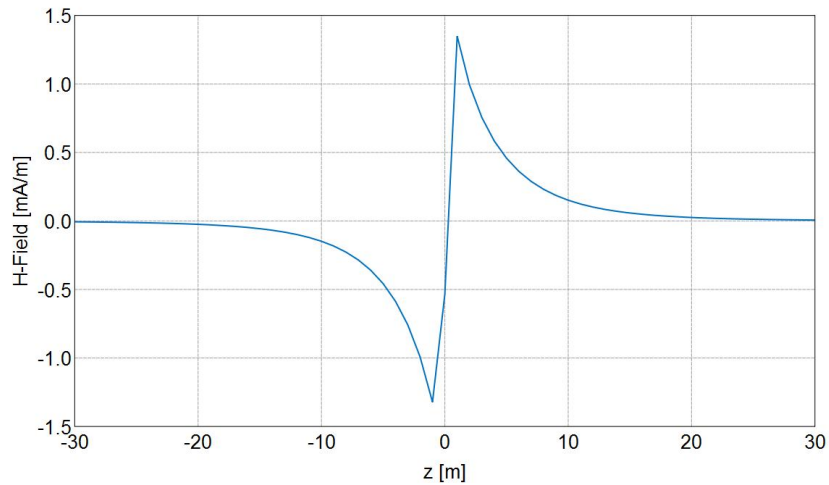
Imaginary Z H-Field [Frequency = 100 Hz; x = 0 m; y = 0 m] - NS frac 5 10

Figure A5.2: Imaginary component of magnetic field in Z- direction for a non-symmetrical fracture of wings of half length 5m and 10m on either side



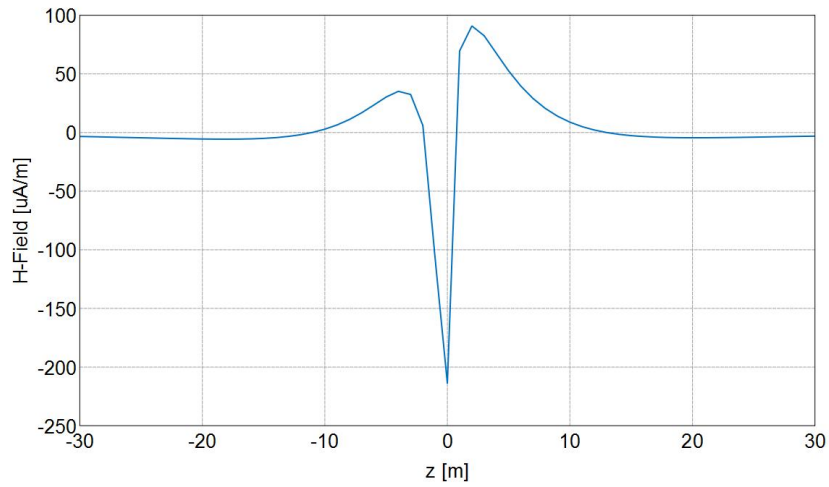
Imaginary Y H-Field [Frequency = 100 Hz; x = 0 m; y = 0 m] - NS frac 5 15

Figure A5.3: Imaginary component of magnetic field in Y- direction for a non-symmetrical fracture of wings of half length 5m and 15m on either side



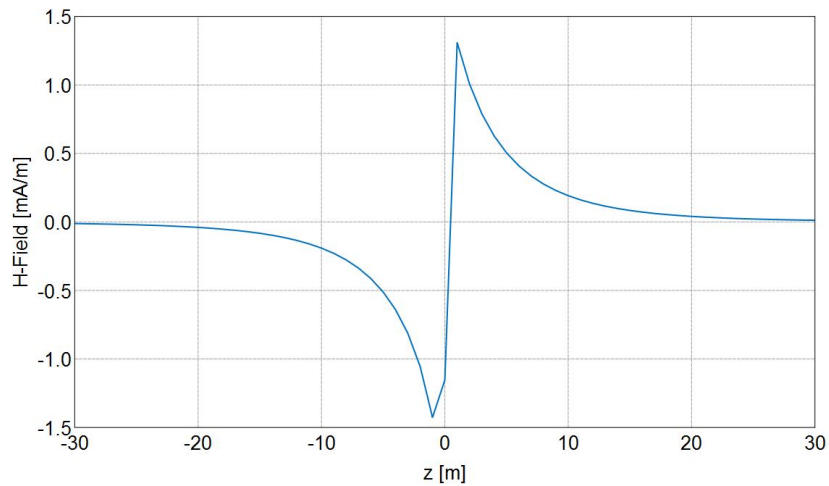
Imaginary Z H-Field [Frequency = 100 Hz; x = 0 m; y = 0 m] - NS frac 5 15

Figure A5.4: Imaginary component of magnetic field in Z- direction for a non-symmetrical fracture of wings of half length 5m and 15m on either side



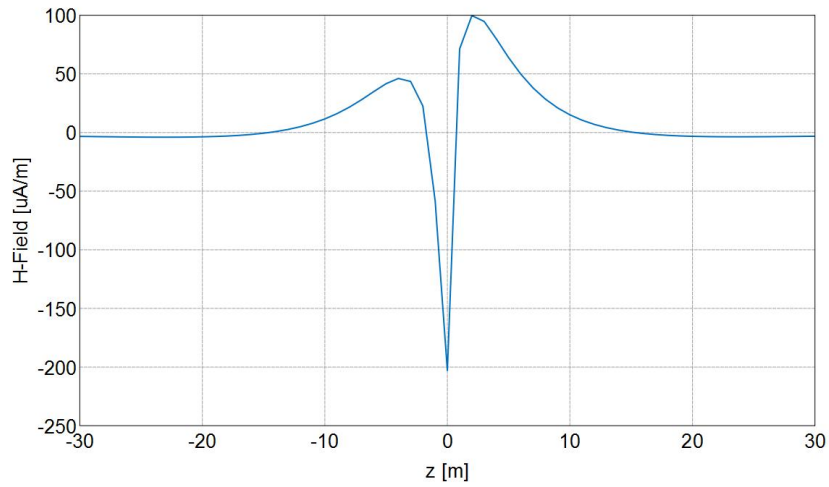
Imaginary Y H-Field [Frequency = 100 Hz; x = 0 m; y = 0 m] - NS frac 5 20

Figure A5.5: Imaginary component of magnetic field in Y- direction for a non-symmetrical fracture of wings of half length 5m and 20m on either side



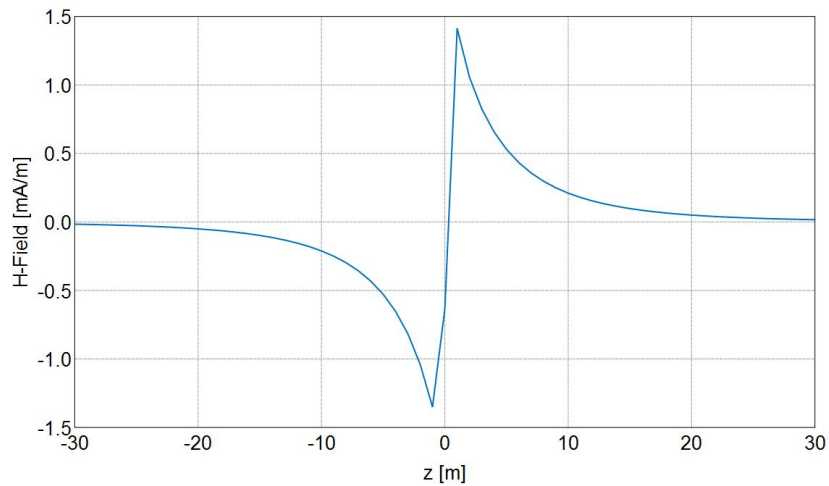
Imaginary Z H-Field [Frequency = 100 Hz; x = 0 m; y = 0 m] - NS frac 5 20

Figure A5.6: Imaginary component of magnetic field in Z- direction for a non-symmetrical fracture of wings of half length 5m and 20m on either side



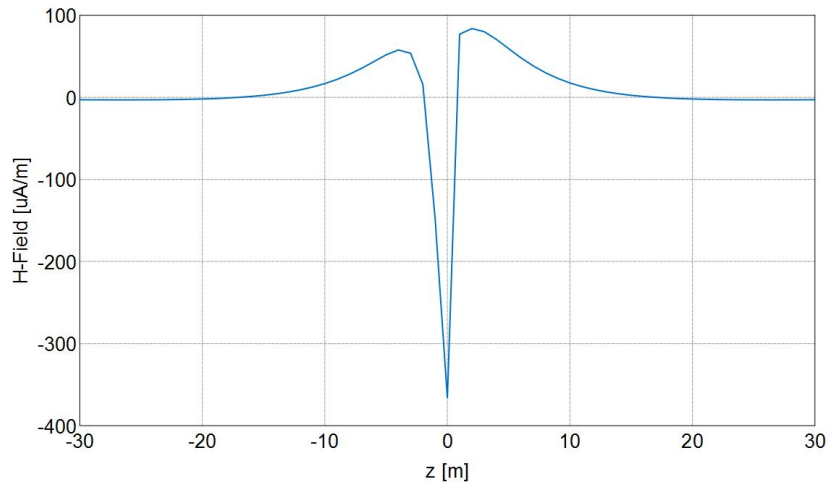
Imaginary Y H-Field [Frequency = 100 Hz; x = 0 m; y = 0 m] - NS frac 5 25

Figure A5.7: Imaginary component of Magnetic field in Y- direction for a non-symmetrical fracture of wings of half length 5m and 25m on either side



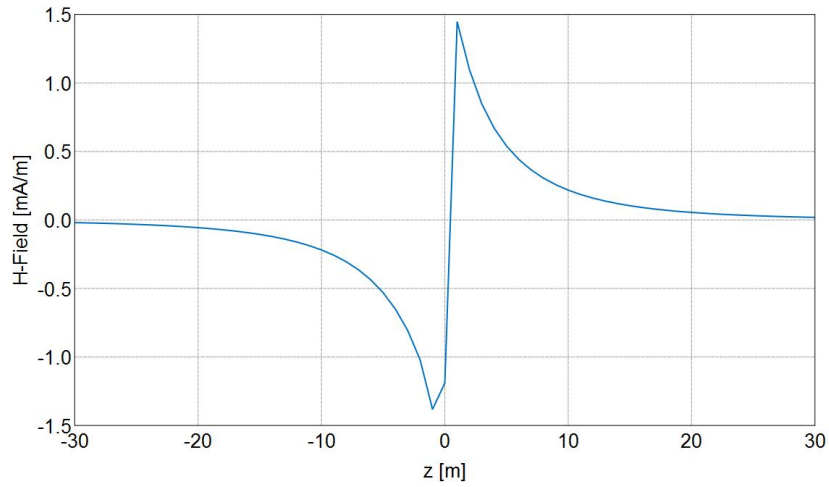
Imaginary Z H-Field [Frequency = 100 Hz; x = 0 m; y = 0 m] - NS frac 5 25

Figure A5.8: Imaginary component of magnetic field in Z- direction for a non-symmetrical fracture of wings of half length 5m and 25m on either side



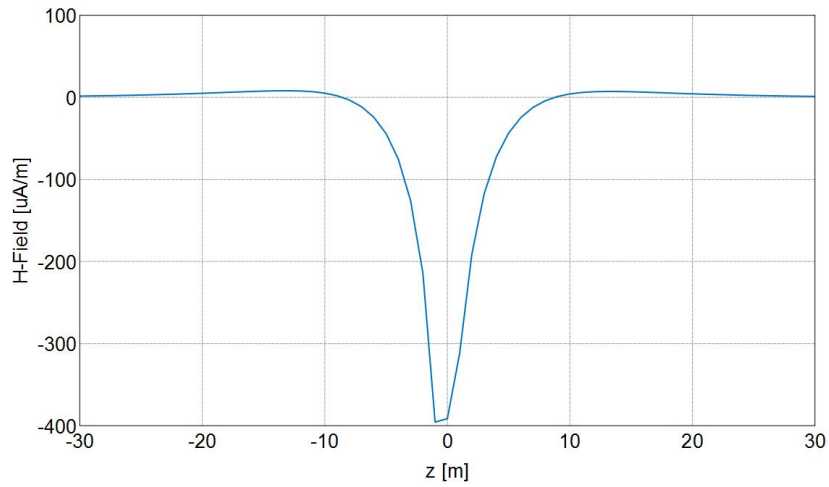
Imaginary Y H-Field [Frequency = 100 Hz; x = 0 m; y = 0 m] - NS frac 5 30

Figure A5.9: Imaginary component of magnetic field in Y- direction for a non-symmetrical fracture of wings of half length 5m and 30m on either side



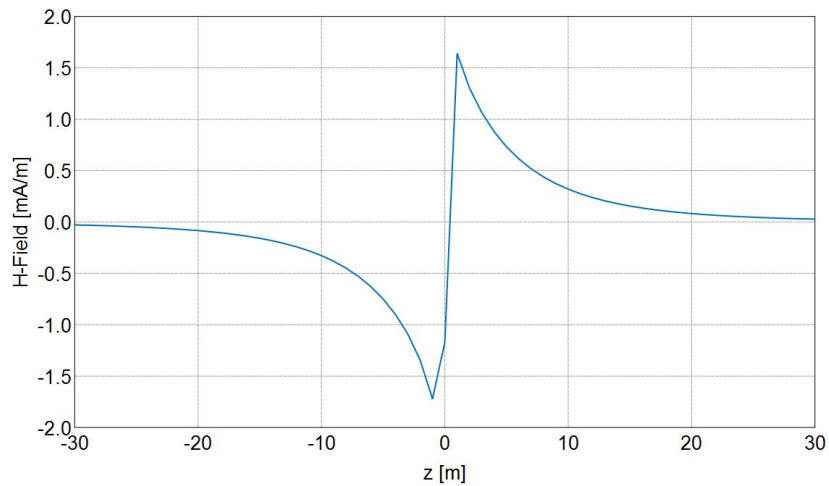
Imaginary Z H-Field [Frequency = 100 Hz; x = 0 m; y = 0 m] - NS frac 5 30

Figure A5.10: Imaginary component of magnetic field in Z- direction for a non-symmetrical fracture of wings of half length 5m and 30m on either side



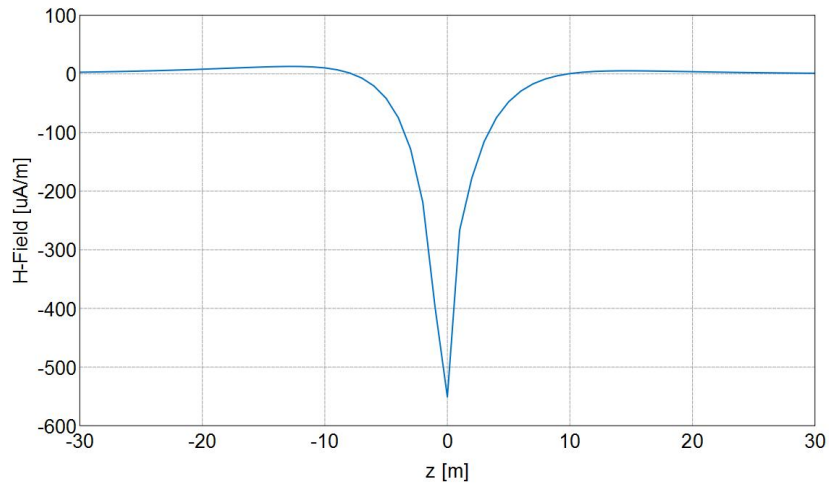
Imaginary Y H-Field [Frequency = 100 Hz; x = 0 m; y = 0 m] - NS frac 15 30

Figure A5.11: Imaginary component of magnetic field in Y- direction for a non-symmetrical fracture of wings of half length 15m and 30m on either side



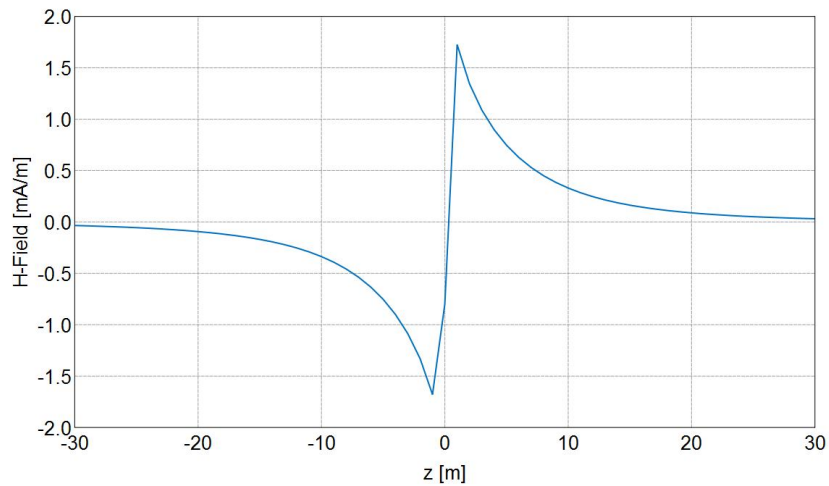
Imaginary Z H-Field [Frequency = 100 Hz; x = 0 m; y = 0 m] - NS frac 15 30

Figure A5.12: Imaginary component of magnetic field in Z- direction for a non-symmetrical fracture of wings of half length 15m and 30m on either side



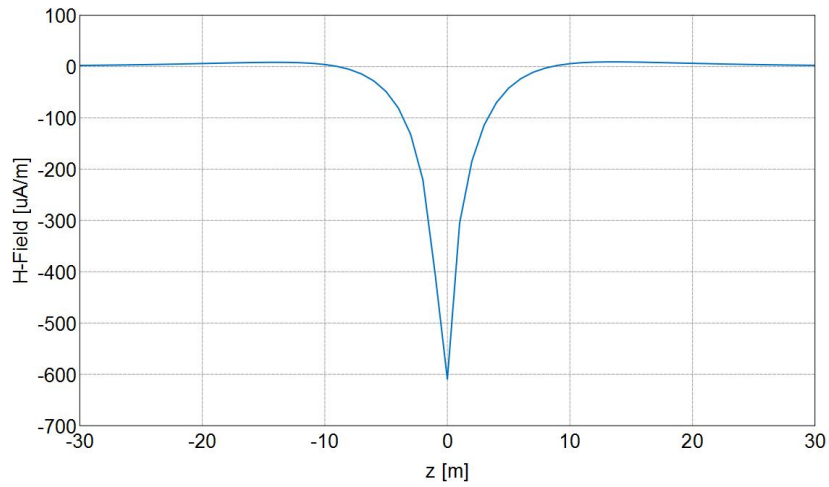
Imaginary Y H-Field [Frequency = 100 Hz; x = 0 m; y = 0 m] - NS frac 15 45

Figure A5.13: Imaginary component of magnetic field in Y- direction for a non-symmetrical fracture of wings of half length 15m and 45m on either side



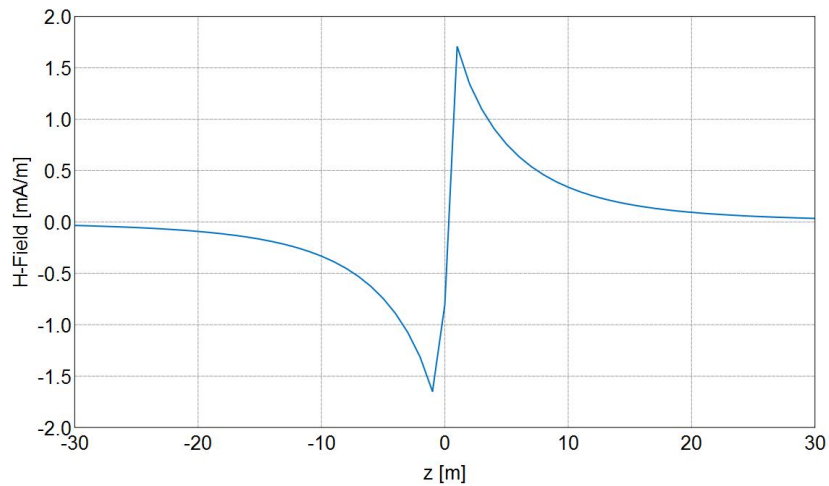
Imaginary Z H-Field [Frequency = 100 Hz; x = 0 m; y = 0 m] - NS frac 15 45

Figure A5.14: Imaginary component of magnetic field in Z- direction for a non-symmetrical fracture of wings of half length 15m and 45m on either side



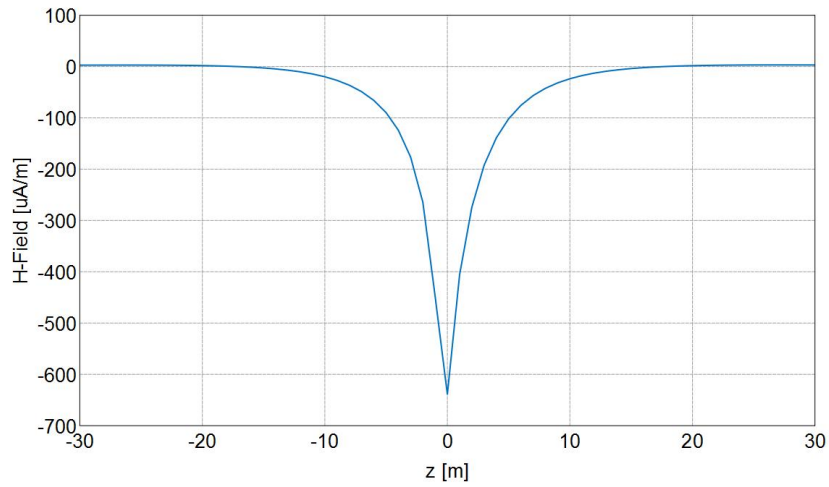
Imaginary Y H-Field [Frequency = 100 Hz; x = 0 m; y = 0 m] - NS frac 15 60

Figure A5.15: Imaginary component of magnetic field in Y- direction for a non-symmetrical fracture of wings of half length 15m and 60m on either side



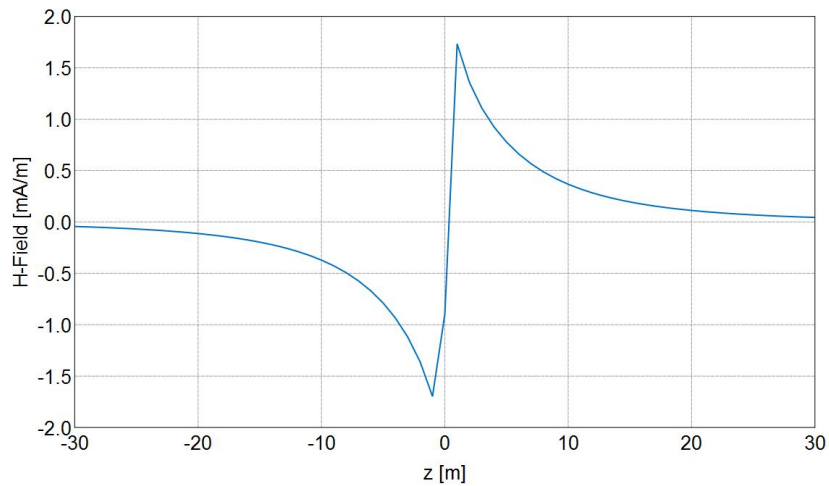
Imaginary Z H-Field [Frequency = 100 Hz; x = 0 m; y = 0 m] - NS frac 15 60

Figure A5.16: Imaginary component of magnetic field in Z- direction for a non-symmetrical fracture of wings of half length 15m and 60m on either side



Imaginary Y H-Field [Frequency = 100 Hz; x = 0 m; y = 0 m] - NS frac 30 60

Figure A5.17: Imaginary component of magnetic field in Y- direction for a non-symmetrical fracture of wings of half length 30m and 60m on either side



Imaginary Z H-Field [Frequency = 100 Hz; x = 0 m; y = 0 m] - NS frac 30 60

Figure A5.18: Imaginary component of magnetic field in Z- direction for a non-symmetrical fracture of wings of half length 30m and 60m on either side

## References

- Anderson, B. and Barber, T. 1995. *Induction Logging*. Houston, Texas: Schlumberger.
- Anderson, B.I. and Barber, T.D. 1999. Deconvolution and Boosting parameters for Obsolete Schlumberger Induction Tools. *The Log Analyst* **40** (1): 133.
- Attali, G. 1969. Methods and Apparatus for Investigating Earth Formations Including Measuring the Resistivity of Radially Different Formation Zones. US Patent No. 3,453,530.
- Barber, T., Orban, A., Hazen, G. et al. 1995. A Multiarray Induction Tool Optimized for Efficient Wellsite Operation. Presented at the SPE Annual Technical Conference and Exhibition, Dallas, Texas, 22-25 October 1995. SPE-30583-MS. <http://dx.doi.org/10.2118/30583-MS>
- Barber, T.D. 1985. Introduction to the Phasor Dual Induction Tool. *J Pet Technol* **37** (9): 1699-1706. SPE-12049-PA. <http://dx.doi.org/10.2118/12049-PA>
- Barber, T.D. 1998. Interpretation of AIT-Family Logs in Invaded Formations at High Relative Dip Angles. Paper A presented at the 1998 SPWLA Annual Logging Symposium, Keystone, Colorado, 26-29 May.
- Barber, T.D. and Minerbo, G.N. 2002. An Analytic Method for Producing Multiarray Induction Logs That Are Free of Dip Effect. Presented at the SPE Annual Technical Conference and Exhibition, San Antonio, Texas, 29 September-2 October 2002. SPE-77718-MS. <http://dx.doi.org/10.2118/77718-MS>
- Barber, T.D. and Rosthal, R.A. 1991. Using a Multiarray Induction Tool To Achieve High-Resolution Logs With Minimum Environmental Effects. Presented at the SPE Annual Technical Conference and Exhibition, Dallas, Texas, 6-9 October 1991. SPE-22725-MS. <http://dx.doi.org/10.2118/22725-MS>
- Beard, D., Zhou, Q., and Bigelow, E. 1996. Practical Applications of a New Multichannel and Fully Digital Spectrum Induction System. Presented at the SPE Annual Technical Conference and Exhibition, Denver, Colorado, 6-9 October 1996. SPE-36504-MS. <http://dx.doi.org/10.2118/36504-MS>.
- Beste, R., King, G., Strickland, R. et al. 2000. A New High Resolution Array Induction Tool. Presented at the SPWLA 41st Annual Logging Symposium, 2000. SPWLA-2000-C.
- Cipolla, C.L. and Wright, C.A. 2000. State-of-the-Art in Hydraulic Fracture Diagnostics. Presented at the SPE Asia Pacific Oil and Gas Conference and Exhibition, Brisbane, Australia, 16-18 October. SPE-64434-MS.
- Crary, S., Jacobsen, S., Rasmus, J.C. et al. 2001. Effect of Resistive Invasion on Resistivity Logs. Presented at the SPE Annual Technical Conference and

- Exhibition, New Orleans, Louisiana, 30 September-3 October 2001. SPE-71708-MS. <http://dx.doi.org/10.2118/71708-MS>.
- Doll, H.G. 1949. Introduction to Induction Logging and Application to Logging of Wells Drilled With Oil Base Mud. *J Pet Technol* **1** (6): 148-162. SPE-949148-G. <http://dx.doi.org/10.2118/949148-G>
- Griffiths, R., Barber, T., and Faivre, O. 2000. Optimal Evaluation of Formation Resistivities Using Array Induction and Array Laterolog Tools. Paper BBB presented at the 2000 SPWLA Annual Logging Symposium, Dallas, 4–7 June.
- Grove, G.P. and Minerbo, G.N. 1991. An Adaptive Borehole Correction Scheme For Array Induction Tools. Paper P presented at the 1991 SPWLA Annual Logging Symposium, Midland, Texas, 16–19 June.
- Hunka, J.F., Barber, T.D., Rosthal, R.A. et al. 1990. A New Resistivity Measurement System for Deep Formation Imaging and High-Resolution Formation Evaluation. Presented at the SPE Annual Technical Conference and Exhibition, New Orleans, Louisiana, 23-26 September 1990. SPE-20559-MS. <http://dx.doi.org/10.2118/20559-MS>
- Kienitz, C. et al. 1986. Accurate Logging in Large Boreholes. Paper III presented at the 1986 SPWLA Annual Logging Symposium, Houston, 9–13 June.
- King, G.E. 2010. Thirty Years of Gas Shale Fracturing: What Have We Learned? Paper 133556 presented at the 2010 SPE Annual Technical Conference and Exhibition, Florence, Italy, 19-22 September.
- La Vigne, J., Barber, T.D., and Bratton, T. 1997. Strange Invasion Profiles: What Multiarray Induction Logs Can Tell Us About How Oil-Based Mud Affects The Invasion Process and Wellbore Stability. Presented at the SPWLA 38th Annual Logging Symposium, Houston, Texas, 15–18 June. 1997-B.
- Martin, D.W., Spencer, M.C., and Patel, H.K. 1984. The Digital Induction - A New Approach to Improving the Response of the Induction Measurement. Presented at the SPWLA 25th Annual Logging Symposium, 1984. SPWLA-1984-M.
- Moran, J.H. and Kunz, K.S. 1962. Basic Theory of Induction Logging and Application to Study of Two-Coil Sondes. *Geophysics* **44** (7): 829-858. <http://dx.doi.org/10.1190/1.1439108>
- Samworth, J.R. et al. 1994. The Array Induction Tool Advances Slim-hole Logging Technology. Presented at the SPWLA European Formation Evaluation Symposium, Aberdeen, 11–13 October. SPWLA-1994-Y.
- Tanguy, D.R. 1962. Induction Well Logging. US No. Patent 3,067,383.
- Tanguy, D.R. 1967. Methods and Apparatus for Investigating Earth Formations Featuring Simultaneous Focused Coil and Electrode System Measurements. US Patent No. 3,329,889.